TRANSLATIONAL MODELLING OF TRAUMATIC AXONAL AND VASCULAR INJURY USING CHIMERA (CLOSED HEAD IMPACT MODEL OF ENGINEERED ROTATIONAL ACCELERATION)

by

Asma Bashir

B.A. Hons, Boston University, 2014

A THESIS SUBMITTED IN PARTIAL FULFILLMENT OF

THE REQUIREMENTS FOR THE DEGREE OF

DOCTOR OF PHILOSOPHY

in

THE FACULTY OF GRADUATE AND POSTDOCTORAL STUDIES

(Neuroscience)

THE UNIVERSITY OF BRITISH COLUMBIA

(Vancouver)

December 2019

The following individuals certify that they have read, and recommend to the Faculty of Graduate and Postdoctoral Studies for acceptance, the dissertation entitled:

Translational modelling of traumatic axonal and vascular injury using CHIMERA

submitted by Asma Bashir in partial fulfillment of the requirements for

the degree of Doctor of Philosophy

in Neuroscience

Examining Committee:

Cheryl Wellington, Pathology and Laboratory Medicine
Supervisor

Thalia Field, Neurology
Supervisory Committee Member

Edward Conway, Medicine
Supervisory Committee Member

Anthony Phillips, Neuroscience
University Examiner

Fabio Rossi, Medical Genetics
University Examiner

Additional Supervisory Committee Members:

Katerina Dorovini-Zis, Pathology and Laboratory Medicine
Supervisory Committee Member

Abstract

Traumatic brain injury (TBI) is a leading cause of death and disability in modern societies. Diffuse axonal and vascular injury are nearly universal consequences of mechanical energy impacting the head, and are major contributors to disability throughout the spectrum of injury severity. Designing a rodent model of head injury that recapitulates the hallmarks of human TBI is important to delineate biological mechanisms of TBI, to help pinpoint targets for future therapeutic strategies.

We developed CHIMERA (Closed Head Impact Model of Engineered Rotational Acceleration), a non-surgical, impact-acceleration model of rodent TBI that reliably produces diffuse axonal injury characterized by white matter inflammation and axonal damage at 0.5J. In this thesis, we begin by investigating the behavioral and neuropathological phenotypes induced by single CHIMERA TBI up to 0.7J. We demonstrate the capability of CHIMERA to induce proportionate outcomes based on biomechanical inputs, as single CHIMERA TBI at 0.6 and 0.7J in wild-type mice induced neurological and motor deficits, and triggered white matter damage and inflammation in a dose-dependent manner. Subsequently, we expanded CHIMERA's capacity to induce more severe injuries with evidence of vascular damage and grey matter inflammation, in the hopes that therapies can be developed for TBIs across the injury spectrum. We report that interface-assisted single CHIMERA TBI at 2.5J in wild-type mice induced neurological deficits, elevated plasma total tau and neurofilament-light levels, transiently increased proinflammatory cytokines in brain, blood-brain barrier leakage and vascular abnormalities, as well as grey matter microgliosis. Finally, we expanded the CHIMERA platform to rats, to better understand the relationship between repetitive TBI (rTBI), impulsivity and neuropathology. Compared to sham

controls, rats with rTBI displayed progressive impairment in impulsive choice. In addition to histological changes sustained by the mesolimbic dopaminergic system, grey and white matter inflammation along with tau immunoreactivity were observed.

In summary, we have developed a valuable rodent model of human TBI, replicating many of the hallmarks of clinical and neuropathological TBI in both mouse and rat models. We therefore hope that this platform can be used to validate promising drug targets that may ameliorate the inflammatory and behavioral sequelae of human TBI.

Lay Summary

Almost 3 million new cases of traumatic brain injury (TBI) are reported each year in North America and represent a leading cause of death and disability. There is still a lot we do not know about what happens to the brain after it has sustained a hit, and for this thesis, we wished to characterize the pathological changes that ensue after injury. By characterizing what happens after TBI, we hope to be able to pinpoint possible preventative strategies and evaluate therapies that can be then applied after head injury in humans. Using our model of TBI, we induced single and repetitive head injury in mice and rats, and detected changes in behavioral outcomes, particularly in memory and impulsivity. The work outlined in this thesis has the potential to fill in missing information on changes within the brain after TBI, therefore providing the foundation necessary to study the usefulness of therapies.

Preface

The works contained within this thesis were conducted at the University of British Columbia, namely the Djavad Mowafaghian Centre for Brain Health and the Centre for Disease Modelling. All the projects were approved by the University of British Columbia's Research Ethics Board and procedures were carried out in strict accordance with the Canadian Council on Animal Care guidelines:

- Animal care protocols: A15-0096 (mice) and A15-0040 (rats).
- Personal animal care and safety certificates: Canadian Council on Animal Care (7713-16); Introduction to Working with Rodents in Research (IWRR-M-P-70-16); Rodent Restraint and Subcutaneous/Intraperitoneal Injections (RSCIP-M-P-64-16); Introduction to Rodent Anesthesia - Inhalational and Injectable (RA-P-76-16); Biological Safety (2016-vvU7Q); Chemical Safety (2016-KfMR4). I was also certified for live physical euthanasia by Animal Care Services at the University of British Columbia.

A version of Chapter 1 has been published in Sandsmark D*, **Bashir A*,** Wellington C[#], Diaz-Arrastia R[#]. (2019). Cerebral microvascular injury: a potentially treatable endophenotype of traumatic brain injury-induced neurodegeneration. *Neuron* 103(3):367-379. I am a co-first author of this article and wrote sections reviewing cerebral microvascular injury in pre-clinical studies and designing the illustrative figures. Danielle Sandsmark wrote the sections on clinical changes in the cerebrovasculature after traumatic brain injury, with contributions from Asma Bashir, Cheryl Wellington and Ramon Diaz-Arrastia. Conception of the article was by Cheryl Wellington and Ramon Diaz-Arrastia.

Sections of Chapter 1 are in preparation for an invited mini-review article, **Bashir A***, Cheng WH, McInnes, KA, Cripton PA, and Wellington, CL. (2020) The Evolution of CHIMERA (Closed Head Impact Model of Engineered Rotational Acceleration): a translationally relevant, biofidelic platform of mild traumatic brain injury in rodents. I am first author of this article and wrote sections on the CHIMERA platform and the neuropathological phenotypes of various traumatic brain injury models, while Wai Hang Cheng and Kurt McInnes contributed to the introduction and biomechanical sections. Conception of the article was by Asma Bashir, Wai Hang Cheng, Kurt McInnes, Peter Cripton and Cheryl Wellington.

A version of Chapter 2 has been published in Namjoshi DR*, Cheng WH, **Bashir A**, Wilkinson A, Stukas S, Martens KM, Whyte T, Abebe ZA, McInnes KA, Cripton PA, Wellington CL. (2017). Defining the biomechanical and biological threshold of murine mild traumatic brain injury using CHIMERA (Closed Head Impact Model of Engineered Rotational Acceleration). *Exp Neurol* 292:80-91. I am a co-author of this article. Dhananjay Namjoshi was the post-doctoral fellow responsible for coordinating experiments. Behavioral assays were performed by Dhananjay Namjoshi, Wai Hang Cheng, Asma Bashir, and Kris Martens. Head kinematic analysis was performed by Wai Hang Cheng and Asma Bashir, with expert advice from Zelalem Abebe, Kurt McInnes, Tom Whyte, and Peter Cripton. Histology experiments were conducted and analyzed by Dhananjay Namjoshi, Asma Bashir, and Wai Hang Cheng, with support from Anna Wilkinson. Biochemical assays were conducted by Sophie Stukas and Anna Wilkinson. The manuscript was prepared by Dhananjay Namjoshi and Cheryl Wellington, and edited by Wai Hang Cheng and Asma Bashir. Cheryl Wellington and Peter Cripton were the supervisory

authors on this project and were involved throughout the project in concept formation and manuscript edits. As this work was highly collaborative, with major direction sought from Dhananjay Namjoshi, the work described in Chapter 2 is also present in the doctoral thesis of Wai Hang Cheng.

A version of Chapter 3 has been published in **Bashir A***, Abebe ZA, McInnes KA, Tatarnikov I, Button EB, Cheng WH, Haber M, Wilkinson A, Barron C, Diaz-Arrastia R, Stukas S, Cripton PA, Wellington CL. (2020) Increased severity of the CHIMERA model induces acute vascular injury, sub-acute deficits in memory recall, and chronic white matter gliosis. *Exp Neurol* 324: pre-print. I am first author of this manuscript and was responsible for designing and conducting experiments and analyzing results. Interface was designed by Kurt McInnes and Zelalem Abebe. Behavioral assays were performed by Asma Bashir. Head kinematic analysis was performed by Zelalem Abebe. Electrophysiological experiments were conducted by Asma Bashir and Igor Tatarnikov. Histology experiments were conducted and analyzed by Asma Bashir, with support from Anna Wilkinson and Wai Hang Cheng. Electron micrographs were obtained by Margalit Haber under the supervision of Ramon Diaz-Arrastia. Biochemical assays were conducted by Sophie Stukas and Emily Button. Carlos Barron oversaw the care of the animals post-procedure. The manuscript was prepared by Asma Bashir. Cheryl Wellington and Peter Cripton were the supervisory authors on this project and were involved in concept formation and manuscript edits.

A version of Chapter 4 has been published in Vonder Haar C*, Martens KM*, **Bashir A*,** McInnes KA, Cheng WH, Cheung H, Stukas S, Barron C, Ladner T, Welch KA, Cripton PA, Winstanley CA, and Wellington CL. (2019) Repetitive closed-head impact model of engineered

rotational acceleration (CHIMERA) injury in rats increases impulsivity, decreases dopaminergic innervation in the ventral striatum and generates white matter inflammation, tau phosphorylation and degeneration. *Exp Neurol* 317:87-99. I am a co-first author of this article. Rat CHIMERA was designed and built by Kurt McInnes. Behavioral experiments were conducted and analyzed by Cole Vonder Haar and Kris Martens. Histology experiments were conducted and analyzed by Asma Bashir, with support from Wai Hang Cheng and Honor Cheung. Biochemical assays were conducted and analyzed by Sophie Stukas. Carlos Barron oversaw the care of the animals post-procedure, with support from Tessa Ladner and Kassandra Welch. The manuscript was prepared by Cole Vonder Haar, Kris Martens, Asma Bashir, and Cheryl Wellington. Cheryl Wellington, Catharine Winstanley and Peter Cripton were the supervisory authors on this project and were involved in concept formation and manuscript edits.

Table of Contents

List of Tables

List of Figures

List of Symbols

°	degree
d	day
F	female
fps	frames per second
g	gram
g	gravitational acceleration
h	hour
J	joules
kg	kilogram
M	male
m	meter
m/s	meters per second
mg	milligram
mL	milliliter
mm	millimeter
mOsm	milliosmole
ms	millisecond
N	number
pg	picogram
s	second
v	version
µA	microamp

μm	micrometer
w	week

List of Abbreviations

ACSF	artificial cerebrospinal fluid
AD	Alzheimer's disease
apoE	apolipoprotein E
AQP-4	aquaporin-4
ASL	arterial spin labeling
AUC	area under the curve
Aβ	amyloid-beta
BBB	blood-brain barrier
BCA	bicinchoninic acid
CBF	cerebral blood flow
CCI	controlled cortical impact
CDC	Center for Disease Control and Prevention
CHI	closed head impact
CHIMERA	closed head impact model of engineered rotational acceleration
CNS	central nervous system
CSF	cerebrospinal fluid
CT	computed tomography
CTE	chronic traumatic encephalopathy
CVR	cerebrovascular reactivity
DAB	3,3’ diaminobenzidine
DAI	diffuse axonal injury
DAPI	4′,6-diamidino-2-phenylindole

DAT	dopamine transporter
DDT	delay discounting task
DTI	diffusion tensor imaging
EEG	electroencephalography
ELISA	enzyme-linked immunosorbent assay
EM	electron microscopy
EPM	elevated plus maze
FDG-PET	fluorodeoxyglucose-positron emission tomography
fEPSP	field excitatory post-synaptic potential
fMRI	functional magnetic resonance imaging
FPI	fluid percussion injury
FST	forced swim test
GCS	Glasgow Coma Scale
GFAP	glial fibrillary acidic protein
hTau	human tau
Iba1	ionized calcium-binding adapter molecule 1
IgG	immunoglobulin G
IL-1β	interleukin-1β
IL-6	interleukin-6
ITI	intertrial interval
LRR	loss of righting reflex
LTP	long term potentiation
MMP	matrix metallopeptidase

MRI	magnetic resonance imaging
mTBI	mild traumatic brain injury
NF-L	neurofilament-light
NGS	normal goat serum
NIRS	near-infrared spectroscopy
NSS	neurological severity score
NVU	neurovascular unit
PBS	phosphate buffered saline
PD	Parkinson's disease
PDGF	platelet-derived growth factor
PFA	paraformaldehyde
PLA	polylactic acid
p-tau	phosphorylated-tau
RIPA	radioimmunoprecipitation assay
ROI	region of interest
RT	room temperature
rmTBI	repetitive mild traumatic brain injury
rTBI	repetitive traumatic brain injury
SEM	standard error of the mean
SD	standard deviation
SPECT	single photon emission computed tomography
TBI	traumatic brain injury
TCD	transcranial doppler

TH	tyrosine hydroxylase
TMVI	traumatic microvascular injury
TNFα	tumor necrosis factor-α
UCHL-1	Ubiquitin C-Terminal Hydrolase L1
VEGF	vascular endothelial growth factor
VTA	ventral tegmental area
WD	weight drop

Acknowledgements

It is undoubtedly incumbent upon me to express my sincerest gratitude to everyone who partook in this great endeavor with me. First and foremost, I would like to thank my supervisor, Dr Cheryl Wellington, a pillar of wisdom, strength, and integrity. She has been an incredible mentor, offering me countless opportunities to grow as a scientist. I would also like to thank past and present members of the Wellington laboratory for their intellectual support and kindness: research associates Drs Sophie Stukas, Tara Caffrey, Iva Kulic, and Jianjia Fan; postdoctoral fellows Drs Tom Cheng, Jérôme Robert, Dhananjay Namjoshi, and Kris Martens; graduate trainees (soon to be Dr) Emily Button, Jasmine Gill, and Sonja Soo; undergraduate students Claire Huang, Kassandra Welch, Rachel Zhao, Cameron Parro, Emma Martin, Honor Cheung, and Amanda Clark; and technicians Carlos Barron, Anna Wilkinson, Wenchen Zhao, Andrew Agbay, Megan Gilmour, Guilaine Boyce, and Jeniffer Chan. The CHIMERA team has the honor of working very closely with a phenomenal group of biomechanical engineers, Dr Peter Cripton, Kurt McInnes, and Zelalem Abebe. I would like to thank them for humoring my naivete in the field of biomechanics, answering my incessant questions, and supporting all of the projects presented in this thesis.

I would next like to thank the members of my supervisory committee – Drs Edward Conway, Katerina Dorovini-Zis, and Thalia Field – for their incredible zeal and breadth of ideas. I would also like to express my thanks to members of the Graduate Program in Neuroscience, especially my classmates and members of the Neuroscience Graduate Student Association. At the administrative level, I would like to thank Dr Liisa Galea, Dr Tim O'Connor, Jennifer Campbell, and Allen Yang for their support throughout my degree.

Importantly, I would like to thank the professor who unveiled the world of neuroscience to me as an undergraduate at Boston University. Dr Paul Lipton was the first domino in this phenomenal journey that I have been on for the last years. In many ways, I wouldn't be here without him.

My family makes up so much of who I am, so I would be remiss if I did not thank my mother, father and brother for their undying support. I am blessed to have extraordinary individuals in my life, people who care for me with love and offer their protection. Sincere thanks are owed to (in alphabetical order, for the sake of fairness) Ana, Corinne, Emma, Kassi, Leena, Okwui, Parand, Silvia, Winnie, and Yameen (Bear). I cannot thank you enough for consoling me when the ever-present turmoil around the world was getting to me.

I owe an immense level of gratitude to my partner. It is safe to say I could not have predicted our remarkable journey together when we began our graduate degrees in 2015. Thank you, حبيبي, for bringing a rose-tinted hue to my life.

Lastly, I would like to thank the following organizations for funding support: The University of British Columbia for the Four Year Doctoral Fellowship and Faculty of Medicine Awards, the Canadian Institutes of Health Research for the Canada Graduate Scholarship – Master's Award, the National Neurotrauma Society for the Diversity Award, and the Weston Brain Institute for the Transformational Grant awarded to Dr Wellington.

For the incredible women whose treacherous paths I walk on with ease,

simply because I came after them,

and for my great-grandmother, whose spirit lives in my bones.

Chapter 1: Introduction

1.1 Overview of TBI epidemiology

Traumatic Brain Injury (TBI) refers to "an alteration in brain function, or other evidence of brain pathology, caused by an external force" (Menon et al., 2010). Under this definition, the "alteration in brain function" includes clinical signs such as a decreased level or loss of consciousness, post-traumatic amnesia, neurological deficits, or any alteration in mental state at the time of injury. In short, a TBI occurs when any mechanical force acting on the head leads to a change in neurological functions or mental state.

TBI has traditionally been conceptualized as a primary injury event, caused by an initial mechanical impact, followed by secondary insults due to the molecular and cellular responses in reaction to the primary injury. Secondary injury can propagate a trauma-induced cascade in the surrounding brain tissue. This secondary injury, even in the most severe cases, was thought to extend only for a few weeks or at most a month, followed by a trajectory of recovery that was generally thought to be largely complete within months or at most, one year. Evidence accumulated over the past decade has led to a recognition that for many patients, the consequences of TBI continue to evolve long after the acute period of initial recovery (Wilson et al., 2017). Longitudinal studies have shown that outcomes following TBI are not fixed, but as there can be improvement and/or deterioration in neurological functioning many years after injury (Corrigan and Hammond, 2013; Wilson et al., 2017). TBI can therefore be best conceptualized as a chronic health condition triggered by the injury which initiates long-lasting and still poorly understood downstream events that can impact brain functioning for decades

(Corrigan and Hammond, 2013), having life-long effects on multiple health outcomes (Masel and DeWitt, 2010).

1.1.1 Incidence and social burden of TBI

TBI has a high incidence rate and incurs a tremendous socio-economic cost worldwide. In North America, the annual incidence of TBI is estimated to be over 3 million. (Statistics Canada 2015, Centers for Disease Control and Prevention 2016). Every year, there are 2 million recorded emergency room visits following TBI in the US (715 per 100,000). The incidence of TBI is disproportionately higher in low and middle-income countries, where TBIs are the leading cause of death and disability in young adults (Maas et al., 2017). Because head injuries often affect young people in their most productive years, the cumulative loss of productivity is high compared to other injuries and illnesses (Max et al., 1991).

Some TBI cases result in death or long-term disabilities. In the US, the annual number of TBI-induced death and long-term disability cases are 50,000 (17 per 100,000) and 120,000 (43 per 100,000), respectively. While up to 80% of individuals with mild TBI (mTBI) recover spontaneously, a significant number experience enduring symptoms (Schwarzbold et al., 2008), including headaches, mild cognitive dysfunction, emotional lability, psychiatric symptoms, and an increased risk of neurodegenerative disease (Broshek et al., 2015; McKee and Daneshvar, 2015).

1.1.2 Economic burden of TBI

TBI has been estimated to incur an annual economic cost of over $60 billion in the US and €33 billion in Europe (Corso et al., 2006; Olesen et al., 2012). Despite such alarming figures, TBI is often referred to as a "silent epidemic" (Rusnak, 2013), and currently there are no effective pharmacological treatments (Menon and Maas, 2015). Thus far, all TBI therapeutic agents have failed phase III clinical trials, including the highly anticipated progesterone studies (Skolnick et al., 2014). The lack of any effective pharmacological intervention further emphasizes the dire need to research and improve our understanding on the pathophysiology of TBI for both acute and chronic time periods, in order to determine potential targets for therapeutics.

1.2 Classification of TBI severity

Acute TBI is clinically characterized using the Glasgow Coma Scale (GCS), which was published in 1974 by neurosurgeons Graham Teasdale and Bryan Jennett. The scale is a numerical rubric that contains eye, verbal and motor components, assessing the patient's level of consciousness and responsiveness. With respect to TBI, GCS 13-15 is classified as mild, 9-12 as moderate, and 3-8 as severe (Maas et al., 2017). When applicable, latency of loss of consciousness is also incorporated into the assessment of TBI severity: 0-30 minutes of unconsciousness is considered mild, 30 minutes to 24 hours is moderate, and greater than 24 hours is severe. Ever since the implementation of the GCS in clinics around the world, little has changed in TBI diagnostic methods. The shortcomings of these measures lie in the GCS's inability to detect cognitive, psychosocial and physiological abnormalities, especially in the mild category, and that it is inaccurate when patients are intubated or sedated after injury.

1.3 Causes of TBI

The cause of TBI is highly heterogeneous. According to the classification system used by the Centers for Disease Control and Prevention (CDC) (Faul et al., 2010), the major causes of TBI are:

- Falls (35.2%)
- Motor vehicle-traffic accidents (17.3%)
- Struck by/against (16.5%)
- Assault (10%)
- Other/Unknown (~20%)

Sports-related TBI, which can be classified as "falls" or "struck by/against" under the CDC system, accounts for roughly 10% of all TBI (**Figure 1.1,** Selassie et al., 2013). Although any person can sustain a TBI at any age, three particular age groups are at the highest risk: very young children (0-4 years old), followed by older adolescents (15-24 years old) and older adults (>65 years) (Faul et al., 2010). However, the highest rates of TBI-related hospitalization and death are found among older patients. Further, reports have also shown that TBI occurs 1.4 times more in males than in females (Faul et al., 2010).

1.4 Acute features of TBI

The mechanical force occurring during TBI may result in immediate (primary) or delayed (secondary) macroscopic or microscopic tissue damage to the skull, brain, or blood vessels. Tissue stress or strains due to blunt or inertial TBI may induce gross pathologies such as skull fracture, subdural, epidural, and subarachnoid hemorrhages, cerebral contusion, intracerebral

hemorrhage, and edema (Silver and Lux, 1994). These gross pathologies are prevalent in severe and fatal TBI, but less common in mTBI. On the other hand, microscopic pathologies, such as diffuse axonal injury, inflammatory changes, and excitotoxicity, are frequent occurrences in all forms of TBI.

1.5 Chronic features of TBI

In addition to the acute macroscopic and microscopic changes, TBI may have chronic consequences such as premature mortality, long-term disability, epilepsy, and behavioral changes (Myburgh et al., 2008; Sariaslan et al., 2016; Skolnick et al., 2014). Many studies have shown that TBI, particularly moderate and severe TBI, may increase long-term risk for dementia (Gardner et al., 2014), Alzheimer's Disease (AD) (Guo et al., 2000; Plassman et al., 2000), or parkinsonism (Crane et al., 2016).

1.5.1 TBI-related neurodegeneration

Neurodegenerative disease following TBI was first described in professional boxers in the 1920s who sustained repeated head trauma (Martland, 1928). Termed dementia pugilistica, it was appreciated that a history of head impacts is associated with the development of AD and other dementias (Barnes et al., 2018; Gardner et al., 2014), Parkinson's disease (PD) (Gardner et al., 2018), and/or amyotrophic lateral sclerosis (Sweeney et al., 2018a) later in life. Though far from universal (Weiner et al., 2017), the possibility of these long-term consequences are understandably of great concern to patients and their families. Epidemiological studies aimed at better understanding this relationship have been mixed. It has long been recognized that moderate and severe TBI in early and mid-life is associated with an increased risk of late-life

dementia, with relative risks (RRs) in the order of 2.5-5.0 (Fleminger et al., 2003; Guo et al., 2000; Plassman et al., 2000). Several prospective observational studies failed to establish a relationship between mTBI, which is a far more common injury, and later-life dementia (Dams-O'Connor et al., 2013; Mehta et al., 1999; Weiner et al., 2017). More recently, careful epidemiologic studies indicate that mTBI is also associated with increased risk of dementia, with RRs in the order of 1.3–2.0 (Gardner et al., 2014; Nordström et al., 2014; Wang et al., 2012). RRs for those who sustain multiple mild TBIs approach those associated with a single severe TBI (Nordström et al., 2014). Additional, detailed prospective studies will be critical to better understand the patient and injury characteristics that associate with later neurodegeneration.

It is often asserted that TBI-associated dementia is similar to Alzheimer's disease (AD) (Fleminger et al., 2003), which is the most common type of dementia in the general population. However, prior studies on the etiology of dementia associated with TBI have used chart reviews or clinical interviews for dementia ascertainment, which are recognized to have a low specificity (Kukull et al., 1990). No prior study of TBI-associated dementia has used pathologic confirmation of the dementia subtype, which is recognized as the gold standard. Furthermore, no prior studies have used modern neurodiagnostic tools such as neuroimaging or biomarker assays in cerebrospinal fluid, serum or plasma, which are recognized to provide refinements over the clinical diagnosis alone (Jack et al., 2011, 2018; Walhovd et al., 2010; Zetterberg and Burnham, 2019). Despite the substantial social burden imposed by the long-term neurodegeneration after TBI, very little is known about the pathophysiology involved, there are no biomarkers that are prognostic for identifying individuals at risk for progressive neurodegeneration, and as a consequence, there are no effective therapies to prevent or slow this process. It is unclear

whether brain trauma in early or mid-life leads to an acceleration and higher risk of AD-type pathology, or whether TBI-associated dementia is a distinct pathologic entity.

1.5.1.1 Chronic traumatic encephalopathy (CTE)

Much recent attention has focused on the neurodegenerative sequelae of those exposed to mild repetitive subconcussive injuries, such as those sustained as a result of multiple sport-related impacts similar to those diagnosed with dementia pugilistica in Martland's original case series (Changa et al., 2018). Now called CTE, the diagnosis can only be made upon neuropathological examination after death. While there has been much lay media attention on the clinical features of CTE, which can include memory impairments, personality changes, and neuropsychiatric disturbances, the clinical criteria have not been rigorously defined. The importance of accurately portraying the diagnostic challenges of CTE has recently been highlighted (Stewart et al., 2019). The neuropathology of CTE is similarly complex, consisting of deposits of tau and amyloid-β (Aβ), neuronal and axonal loss, and gliosis. The most consistent neuropathological characteristic of CTE neuropathology is accumulation of phosphorylated tau protein (p-tau) in perivascular regions and at sulcal depths (McKee et al., 2016). Although Aβ pathology can be observed following TBI, tau pathology is prominent both in CTE and in long-term survivors after a single moderate-severe TBI. Aβ plaques can be seen after acute TBI (Gentleman et al., 1997; Graham et al., 1995), but are more rarely seen in long-term survivors and, when present, are more likely to be in a mature fibrillary form (Johnson et al., 2012). Emerging preclinical evidence suggests that this variability in pathology may be influenced by the age at injury and underlying genetic factors (Cheng et al., 2018, 2019).

1.6 Diffuse axonal injury

Diffuse axonal injury (DAI) – a result of rapid acceleration and deceleration forces sustained by the head – is one of the hallmark features of TBI reported in mild, moderate, and severe cases. Rapid acceleration and deceleration can result in shearing forces, damaging the axonal cytoskeleton and leading to altered axonal transport and, in the worst cases, degeneration. DAI was originally considered a primary injury event, however, there is emerging evidence that the neurobiochemical cascades that occur in response to the primary injury contribute significantly to the damaged axons.

1.6.1 Electrophysiological changes following TBI

Physical disruption to the axonal membrane causes mechanically-sensitive sodium channels to open, triggering axonal depolarization, and causing voltage-gated calcium channels to open. The subsequent influx of calcium ions can initiate a number of cascades, including neurotransmitter release and activating secondary messengers (Siedler et al., 2014). Excitotoxicity, which can be caused by the over-release or impaired reuptake of the excitatory neurotransmitter glutamate, is another mechanism by which DAI is exacerbated. Further, the influx of intracellular calcium can also lead to the proteolysis of cytoskeletal proteins neurofilament, microtubule associated proteins (which include tau), and tubulin.

1.6.2 Structural methods to study axonal damage

To visualize the extent of structural injury in the clinic, computed tomography (CT) and magnetic resonance (MR) imaging are used, however evidence of damage is not often visible, especially at the mild level of injury (Sener et al., 2016). Diffusion tensor imaging (DTI), which

also uses MR technology, has emerged as the premier technique for assessing white matter integrity as axonal pathways are not well visualized using conventional neuroimaging techniques. Results of a clinical investigation into the efficacy of DTI in predicting survival after sustaining a severe TBI are very promising, suggesting that changes at a microstructural level are tightly correlated with outcome (Sener et al., 2016).

1.6.3 Functional methods to study electrophysiological changes

Electrophysiological methods are currently being investigated as potential diagnostic and prognostic tools following injury (Gosselin et al., 2012; Rapp et al., 2015). Electroencephalography (EEG) measures the electrical potential differences between two electrodes, requiring millions of neurons to fire in synchrony (Rapp et al., 2015). After TBI, axonal damage can reduce this synchrony, primarily within the cortex, increasing the occurrence of slower-wave frequencies (Modarres et al., 2017). Conversely, bursts of higher amplitude activity following mild injury have also been reported (Geets and Louette, 1985). The benefit of incorporating EEG into the TBI diagnostic catalogue is its high temporal resolution (at the sub-millisecond scale). MR and CT however, have much better spatial resolution, but are "temporally static" (Rapp et al., 2015).

1.7 Microglial and astrocytic activation

Neuroinflammation is a dynamic response to damage and injury, largely involving resident microglia and astrocytes (Burda et al., 2017; Karve et al., 2016; Streit, 2000). The microglial and astrocytic response to injury involves secretion of pro- and anti-inflammatory cytokines, as well as phagocytosis of cellular debris (Karve et al., 2016). The glial response to injury is highly

pleiotropic, as they can act as facilitators of inflammation resolution and exacerbation (Johnson et al., 2013).

1.7.1 Astrocytes

Astrocytes are responsible for a number of homeostatic processes within the brain parenchyma, including the maintenance of neural circuitry and neurovascular coupling (described in brief in **Section 1.8.1**). Astrocytes are known to become hypertrophic following injury, which involves swelling of the cell body and an active extension and retraction of processes. This phenomenon is speculated to arise from the activation of mechanosensitive ion channels following membrane deformation (Bowman et al., 1992). Another speculation is that adenosine triphosphate (ATP), released by injured and dying cells, triggers a sudden rise in cytoplasmic calcium in nearby astrocytes (Burda et al., 2017). This intracellular increase in calcium triggers the polarization of astrocyte processes towards the injured tissue. In milder cases of TBI, perturbations within the CNS can be easily resolved by astrocytes, and a return to homeostasis soon follows. However, astrocyte can remain hyperactive at chronic stages if the sustained damage is more severe (Bylicky et al., 2018). One key homeostatic process that astrocytes perform under healthy conditions is glutamate uptake following excitatory neurotransmission (Bylicky et al., 2018; Myer et al., 2006). Following moderate and severe TBI, astrocytes display reduced glutamate uptake, which can create an excitotoxic environment leading to seizure activity and cell death (Ouyang et al., 2007).

1.7.2 Microglia

Microglia also become rapidly activated following injury, significantly altering their morphology. Microglial morphology is thought to indicate their activation states, which were hypothesized to exist on a spectrum between M1 or (classically activated) or M2 (alternatively activated) (Ransohoff, 2016; Tang and Le, 2016). The M1 activation state is considered pro-inflammatory, favoring the production and release of cytokines in response to injury. The M2 activation state is associated with repair, promoting the release of neurotrophic factors and phagocytosis (Donat et al., 2017). Emerging evidence suggests that microglia can take on mixed activation states, suggesting that the M1/M2 categorizations may be too simplistic (Ransohoff, 2016). Nonetheless, microglia remaining in a state of chronic activation following injury can contribute unfavorable outcomes following TBI (Faden and Loane, 2015). Recently, studies have demonstrated that chronic elevations of pro-inflammatory cytokines in serum or correlated strongly with changes in behavior (Juengst et al., 2014). Further, chronic inflammation is now thought to underpin neurodegenerative diseases such as AD (Eikelenboom et al., 2010) and CTE (Saing et al., 2011).

1.8 Neurovascular injury

1.8.1 The neurovascular unit

The brain is critically dependent on a steady blood supply that is acutely responsive to the constantly changing metabolic demands of the brain tissue. To accomplish this, the brain parenchyma is served by a vascular network of arteries, arterioles, capillaries, venules, and veins that runs approximately 400 miles in length (Sweeney et al., 2018a). Several cell types distributed along this network act in concert to regulate cerebral blood flow, vascular

permeability, and micronutrient supply. Collectively, these cells are termed the neurovascular unit (NVU) (Shlosberg et al., 2010). The NVU consists of the endothelial lining of the blood vessels, smooth muscle cells (at the artery/arteriole/venule levels), pericytes (at the capillary level), and perivascular glial and neuronal cells (**Figure 1.2 A**), which help to regulate vascular tone. The endothelial cells form a monolayer consisting of intercellular tight and adherens junctions to form the blood-brain barrier (BBB), 85% of which is provided by the capillary endothelium (Sweeney et al., 2018b). This BBB forms an exquisitely regulated barrier between the systemic vasculature and the brain parenchyma. All components of the NVU undergo continuous crosstalk under normal physiological conditions to form an integrated and keenly responsive system to changing cerebral and systemic factors. This process, termed neurovascular coupling, ensures consistent cerebral blood flow and micronutrient supply across the BBB as a function of neuronal activity.

1.8.2 The neurovascular unit following injury

Following brain injury, these normal patterns of communication among the elements of the NVU can be severely altered (**Figure 1.2 B**). Disturbed NVU functioning leads to inappropriate changes in cerebral blood flow in response to the altered metabolic demands of the injured brain. Dysfunction of the BBB disrupts the extracellular environment due to protein and electrolyte leakage and can trigger other downstream processes, like microglia activation and recruitment (Shlosberg et al., 2010; Zlokovic, 2011). Emerging evidence, as we discuss below, indicates that these disruptions last far longer than previously assumed and may contribute to ongoing neuropathology long after the primary injury.

1.8.3 Functional methods to study microvascular injury

1.8.3.1 Cerebral blood flow

Cerebral blood flow (CBF) has been extensively studied after TBI in humans, mostly in the acute period within a few days of injury (Furuya et al., 2003; Menon, 2006) although several studies have examined CBF weeks to years after TBI (Kim et al., 2010). There is a consistent body of literature in humans indicating that deficits in CBF are common after TBI, including repetitive mTBI (Bonne et al., 2003). Studies using single photon emission computed tomography (SPECT) to measure regional CBF in patients with chronic TBI (Barkai et al., 2004; Bonne et al., 2003; Lewine et al., 2007) have consistently found regions of hypoperfusion in a subset of symptomatic TBI subjects (Raji et al., 2014). SPECT perfusion changes significantly correlated with neuropsychological or neurological deficits. Studies using Xenon-CT report similar findings (Lewine et al., 2007). In addition to nuclear medicine studies, advanced MRI techniques have also been helpful in evaluating traumatic microvascular injury. Arterial Spin Labelling (ASL) reveals alterations in global and regional resting CBF in TBI patients of all severities. Kim et al. showed that patients with chronic moderate-to-severe TBI have reduced global CBF, as well as decreased regional perfusion in the thalamus, posterior cingulate cortex, and frontal cortex (Kim et al., 2010). Regions with decreased resting CBF also had altered task-related activation during an ASL fMRI working memory paradigm in chronically injured subjects. Regional relative CBF can also be measured with perfusion-weighted imaging (Bartnik-Olson et al., 2014). The exact causes of these alterations in CBF following TBI are unclear. Decreased CBF may result from a lower metabolic demand from injured tissue, resulting in an appropriate matched reduction in blood flow. However, studies using fluorodeoxyglucose positron emission tomography (FDG-PET) have suggested that glucose metabolism is disrupted following TBI, but can be increased,

decreased, or unchanged in ways that do not clearly correlate with structural abnormalities (Ito et al., 2016; Yamaki et al., 2018).

1.8.3.2 Cerebrovascular reserve

Cerebrovascular reserve, or the ability of the cerebral vasculature to react to vasodilatory or vasoconstrictive stimuli, termed cerebrovascular reactivity (CVR), can be altered after TBI. Breath holding (resulting in induced hypercapnia), hyperventilation, CO_2 inhalation, or acetazolamide administration can be used in conjunction with non-invasive imaging techniques to assess CVR (Kassner and Roberts, 2004). Transcranial Doppler (TCD) ultrasound, near infra-red spectroscopy (NIRS) and magnetic resonance imaging (MRI) have been the most popular methods to examine post-TBI CVR in recent studies. TCD offers the advantage of very high temporal resolution but suffers from poor spatial resolution. A large prospective study of 299 acute TBI patients assessed the incidence of cerebral vasospasm via TCD (Oertel et al., 2005). Nearly half of the patients met at least one TCD criterion for vasospasm. After the acute stage, studies of professional boxers exposed to repetitive mild TBI showed that CVR was reduced in the subacute period when measured with both TCD and NIRS particularly in boxers who had experienced the highest mTBI exposures (Bailey et al., 2013). In the boxers, lower CVR measurements correlate with worse neurocognitive dysfunction and were inversely correlated with head injury exposure. A recent meta-analysis identified three studies examining sport-related concussion and CVR via TCD in 42 athletes (primarily boxers and hockey players) and 33 healthy controls (Gardner et al., 2015). All three studies found decreased CVR in the acute period after a mTBI.

NIRS has been used to study CVR after TBI as well as other neurologic conditions (Lee et al., 2009; Rodriguez Merzagora et al., 2014; Zweifel et al., 2010a, 2010b). Changes in CBF and associated changes in tissue concentrations of oxy- and deoxy-hemoglobin can be measured by NIRS. Like TCD, NIRS offers a very high temporal resolution, and while spatial resolution is superior to TCD, it is not as high as MRI. NIRS allows for reliable CVR measurements over time during dynamic challenges that are independent of hemoglobin concentration, skull thickness and extracranial circulation (Kainerstorfer et al., 2015). NIRS has been used to assess the CVR index in 37 acute TBI patients in the intensive care unit (Diedler et al., 2011). NIRS has also been carried out in the chronic stage of TBI. In chronic moderate and severe TBI patients (mean 18 years after TBI), CVR remained significantly reduced compared to 15 age-sex matched controls (Rodriguez Merzagora et al., 2014), indicating that CVR disruption is a long-lasting deficit in at least a subset of patients. Notably, CVR abnormalities corresponded to cognitive performance.

CVR can also be measured with MRI coupled with a hypercapnia challenge (Amyot et al., 2018; Mutch et al., 2016a, 2016b). CVR is more sensitive than CBF for discriminating between injured and uninjured participants. Even in the absence of frank structural or CBF abnormality, impaired response to induced hypercapnia (end-tidal CO_2 = 50 mmHg) can be observed years after even relatively minor injuries (Amyot et al., 2018; Haber et al., 2018), indicating that cerebrovascular reserve is chronically impaired in some patients following TBI. It should be noted that, while these responses are abnormal in TBI subjects compared to healthy, uninjured control subjects, they do not address whether the brain tissue served by these vessels experiences metabolic distress in the form of impaired oxygen and glucose delivery.

1.9 Gaps in clinical research

A major gap in clinical TBI research, especially for mTBI, is the lack of human brain specimens to study, as human brain tissues are only available under extreme life-threatening circumstances, or at postmortem where the time between injury and autopsy can be highly variable. Cerebrospinal fluid (CSF), which has been invaluable for the development of biomarkers of neurodegenerative disease, is rarely obtained after TBI. Blood specimens are being collected in several clinical TBI studies and several promising blood TBI biomarkers are emerging (Shahim et al., 2016; Zetterberg and Blennow, 2016). Still, how blood biomarkers may reflect brain changes after TBI is not yet clear.

1.9.1 The necessity for animal models

Given the complexity of TBI, there is an urgent need to better understand the specific pathophysiological mechanisms contributing to TBI-related dysfunction in both the acute and chronic phases of disease. In particular, the absence of an effective pharmacological treatment for TBI is an enormous concern, and pinpoints the knowledge gap in our understanding of TBI pathophysiology (Menon and Maas, 2015). Animal models of head injury have been crucial to broadening our understanding of the neuropathological sequelae of TBI. In animal models, interventions aimed at molecular targets involved in secondary injury have been successful in limiting the extent of injury and improving neurologic recovery (McIntosh et al., 1998). These results provide convincing proof of principle that effective therapeutic intervention is possible, but therapeutic efficacy has yet to be achieved in the human condition.

Importantly, the selection of a TBI model requires considering the neuropathological phenotypes associated with each model. An often-overlooked aspect of choosing an appropriate model is the injury-related biomechanics of each platform, which we postulate may contribute significantly to the fidelity of any injury model.

1.10 Animal models of injury

Experimental TBI animal models from which pre-injury and longitudinal data can be obtained and from which brain biospecimens can be collected under controlled conditions have considerable potential to address a multitude of questions about the tissue level mechanisms of TBI and the factors that modulate TBI recovery and repair.

1.10.1 Fluid percussion

Fluid Percussion (FP) models use a pulse of fluid (typically saline), injected into the space between the skull and the dura mater through a hole in the skull, to injure the brain [reviewed in (Lyeth, 2016)]. There are two major variants of this injury model: midline and lateral. With the midline FP model, which was developed first in larger animals (cats/dogs) with the trephination centered on the midline of the brain, the fluid pulse produces a diffuse pressure wave that does not create significant localized strains in the brain tissue on the incident side. Instead, it distributes the pressure/force across a large area and causes motion of the brain within the skull. This results in strains developing in the brain tissues upon impact or compression of the brain on the contralateral side, commonly referred to as a contra-coup injury. In addition, the motion of the brain in these models also creates significant strains in the brain stem, as the gross motion of the brain is not only constrained by the skull cavity but also by the spinal cord to which it is

tethered. The histopathology associated with the lateral FP model includes cell death around the impact site, grey and white matter atrophy, as well as cerebrovascular damage, which has been reported in multiple regions of interest (ROIs), including the corpus callosum, thalamus, fimbria, and brain stem (Bramlett et al., 1997; Cortez et al., 1989; Graham et al., 2000). These phenotypes suggest that FP models induce focal injuries with diffuse components.

1.10.2 Controlled Cortical Impact

Controlled Cortical Impact (CCI) models use an impactor driven by a pneumatic or electromagnetic system to apply a force to the brain or skull whose head has been immobilized [reviewed in (Osier and Dixon, 2017)]. This model is distinguished by its capacity to precisely control the individual impact parameters of the tip, namely depth, velocity, and compression duration. Initially, this model was used to create a focal lesion in the brain tissue by directly impacting on the dura mater of the brain following craniotomy. These focal lesions subsequently cause cell death and inflammation surrounding the injury site, axonal injury, and breach of the BBB (demonstrated by measuring albumin extravasation). Interestingly, it has more recently been adapted to be used to impact the intact skull and produce a CHI. The type and nature of the injuries produced by these two variants are quite different. Due to the mechanical properties of brain tissue (viscous with low elasticity), impacting directly on the brain with a small diameter tip will produce massive strains in the tissue adjacent to the impactor while having a minimal effect on the rest of the brain. In the CHI variant, the device is using a larger diameter, compliant tip impacting on the skull, which, having a much higher stiffness, will distribute the impactor's force over a larger area as it compresses/flexes. Since the head is immobilized, the strains will develop in response to the skull compression and resulting shape change of the skull cavity. The

glio-inflammatory pathology generated using the CHI variant is more diffuse (Luo et al., 2014; Tucker et al., 2019; Velosky et al., 2017; Villapol et al., 2017), akin to most cases of TBI in the clinic, given the distribution of biomechanical forces. Nonetheless, restricting head motion induced by impact is a biomechanical limitation, as we believe both linear and rotational kinematics are necessary to produce a holistic concussive event.

1.10.3 Weight drop

Weight Drop (WD) models use gravity to accelerate an impactor from a given height down towards the animal's head. There are number of different versions of WD models that utilize different animal restraint conditions and impactor shapes/masses dropped from precise heights determined by their particular configuration to produce the desired level of injury. A typical configuration would have the animal lying prone on a compliant surface (foam) with a metal disc (helmet) glued to its exposed skull with a cylindrical weight being guided downward in free-fall within an acrylic tube to strike the disc on the dorsal aspect of the head (Flierl et al., 2009; Kallakuri et al., 2015; Kane et al., 2012). The impact parameters are all coupled to each other and fully defined by the impactor characteristics and the drop height, producing a repeatable impact velocity, impact energy, and momentum exchange between the weight and the animal head. Since the animal is resting on a compliant surface, the impact creates a combination of diffuse skull compression and a short acceleration-deceleration impulse (primarily linear) to the head. The resulting brain tissue damage will be a combination of the components attributed to the compression resulting from skull deformation and the inertial forces caused by the head acceleration-deceleration. Given the kinematics associated with WD injuries, gliosis is often detected surrounding the injury site at acute and sub-acute time-points (Namjoshi et al., 2013).

Additionally, mild axonal damage has been reported in large white matter structures, namely within the corpus callosum and optic tracts (Namjoshi et al., 2013).

1.10.4 Inertial loading

Inertial loading models have been developed to accelerate the head in the absence of a skull impact in order to isolate the injury components caused by brain motion relative to the skull from those caused by deformations of the skull (Cullen et al., 2016; Johnson et al., 2018). A number of different types of inertial loading models exist, but the majority are focused on producing rotational acceleration in either the sagittal or coronal plane. The locations and magnitudes of strain experienced by the brain tissues in this type of loading are highly dependent on the skull and brain geometry, which can vary quite significantly from species to species. This is because the tissue strains are created solely through the interaction between the brain and skull architecture. In gyrencephalic models, the neuropathology associated with inertial loading is largely dependent on the direction of rotation. Injuries in the sagittal and axial planes produce the most significant neuropathology, including bleeding and inflammation at the sulcal depths, subdural hematomas, and accumulation of blood within the ventricles at acute time-points (Johnson et al., 2018). Further, protein aggregates of α-synuclein, the neuronal protein that, when misfolded, is associated with the development of Parkinson's disease, is also detected in higher quantities following inertial loading injuries (Cullen et al., 2016). APP and neurofilament staining also revealed axonal damage one week after inertial loading injury (Cullen et al., 2016).

1.10.5 Boston University (BU) Lateral Impact Acceleration Model

Tagge et al. developed a custom impact-acceleration device that delivers an impulse to the lateral aspect of the head of a chemically sedated mouse restrained in the prone position (Tagge et al., 2018). This results in the head experiencing linear acceleration in the direction of the impulse followed by rotational acceleration in the transverse plane about a point between the shoulder blades once the neck and shoulders are engaged. The impulse is applied via a soft pad such that it is not suspected to significantly deform the skull. As previously noted with regards to inertial loading, the direction/axis of acceleration and geometry of the skull/brain are the critical factors in creating brain tissue strains. Since this device produces rotations about the transverse axis, it is not surprising that the brain injury pathology produced by this device is quite distinct from the other inertial loading platforms that produce rotations about the other axes. This device produces an asymmetrical injury pattern without skull fracture, with tissue strains concentrated on the ipsilateral side: axonopathy and phosphorylated tauopathy are reported at 24h and 5.5 months post-injury, respectively. Neuronal loss in the perirhinal cortex was significantly elevated after injury. Breach of the cerebrovasculature was also localized to the site of injury, and surrounding areas (the perirhinal, insular, entorhinal, and piriform cortices, as deep as the basolateral amygdala). Increased GFAP immunoreactivity was also detected in the aforementioned regions and in the hippocampus, suggesting rapid astrogliosis following a change in BBB permeability (Tagge et al., 2018). The neuropathology generated by this platform is largely constrained within the perirhinal cortex, however the displacement, velocity and acceleration of the unrestricted head also triggers some diffuse changes (Tagge et al., 2018).

1.10.6 Blast

Animal models of TBI using a high-pressure blast wave were developed to mimic the injury mechanism for TBI sustained by military personnel from exposure to explosives during combat (Koliatsos et al., 2011; Lucke-Wold et al., 2016; Meabon et al., 2016). These blast models have a unique injury profile as the tissue damage is caused by a combination of inertial loading and a transient pressure gradient. Since the pressure wave distributes force evenly over the head's surface area, there are no large stress concentrations or localized deformations created during the acceleration of the head. In contrast to the rotational inertial loading devices, this will induce primarily linear head accelerations unless other constraints to the body are implemented that cause the head to rotate about an axis defined by the physiology. Additionally, the pressure gradient may cause additional tissue damage as it propagates through the brain. The neuropathology associated with blast injuries affects grey and white matter structures in a diffuse manner. Necrosis has been detected in frontal lobes and within the hippocampus, while astrogliosis has been observed surrounding the ventricles and blood vessels, in addition to the frontal lobes and hippocampus (Goldstein et al., 2012). Silver uptake, indicating axonal degeneration, has been detected in the optic tract, olfactory nerve layer, brachium of superior colliculus and cerebellum, while an increase in APP staining was observed in the corpus callosum (Goldstein et al., 2012).

1.10.7 CHIMERA

The Closed Head Impact Model of Engineered Rotational Acceleration (CHIMERA) produces an impact-acceleration injury with a particular emphasis on the acceleration component by allowing unrestricted head motion post-impact. Its initial intent was to mimic the clinical

scenario presented during the majority of mild TBI/concussions. The original design had a pneumatically driven piston with a rubber tip impacting the dorsal part of the intact skull of a mouse restrained by its chest and abdomen in a supine position. This produced an injury from a combination of skull compression and inertial forces. Using the same pneumatically-driven, velocity-controlled piston, subsequent injury models were developed employing different injury mechanisms. In order to model TBI with greater severity, a new version of CHIMERA will utilize an impact interface to distribute the load across the entire surface of the skull, thereby minimizing the skull compression aspect of the injury and creating brain tissue loading scenarios similar to whiplash or helmeted impacts (to be discussed in Chapter 3). Another already published modification to the CHIMERA (modCHIMERA) braces the head, neck, and torso, limiting the amount of flexion possible, thereby reducing the angular acceleration of head and increasing the effective mass of the head (Sauerbeck et al., 2018). This model was used in conjunction with a semi-compliant helmet to protect against skull fracture as they used higher impact energies than the original design. This model will load the brain tissue primarily by a diffuse skull compression in combination with linear acceleration inertial forces. The key neuropathological phenotype associated with the CHIMERA platform is diffuse axonal injury (DAI) and inflammation. With the addition of the semi-compliant helmet, grey matter microgliosis (in the cortex and hippocampus) as well as neuronal necrosis, have also been reported. The neuropathological phenotypes associated with the listed TBI models are summarized in **Figure 1.3**.

1.10.7.1 Development and progress of the CHIMERA platform

The CHIMERA system currently includes mouse, rat and ferret variants, each with their own benefits and drawbacks for modelling key clinical aspects of TBI. Mice are optimal for studying the intersections of TBI and neurodegeneration through transgenic modelling. They also have the advantage of lower housing costs and being supported by most animal facilities. However, behavioral assessments are limited to the relatively simple sensorimotor and memory tasks that mice can be trained on. Rats are more suitable for the study of complex behaviors, including those that measure chronic deficits that can persist long after the initial injury, such as reward sensitivity and disinhibition. While using rodents in pre-clinical TBI research is practical, the major limitation to their use is based on neuroanatomical differences between rodents and human. Mice and rats possess lissencephalic brains (i.e. lacking folds and fissures), while human, non-human primate, porcine and ferret brains are gyrencephalic in nature (i.e. with convolutions). The development of the ferret CHIMERA was important for this reason, and for the similarity of grey:white ratios between ferrets and humans. We predict understanding ferret tissue mechanics and deformation will lay the groundwork for clinically relevant investigations into the sequelae of sulcal and perivascular damage, as well as white matter pathology, following TBI.

1.10.7.1.1 Mouse CHIMERA

The mouse CHIMERA was specifically developed to fill the void of a non-surgical model of impact-acceleration concussive injury, maintaining the reproducibility associated with FP and CCI, while incorporating the linear and rotational head movement that is associated with clinical TBI. To assess the reproducibility of head impacts, the inaugural CHIMERA study - published in

2014 - was designed as a double-impact paradigm, using high speed videography to record head motions and calculate the kinematic response to 0.5J impacts (50g piston with 4.47m/s impact velocity) spaced 24h apart (Namjoshi et al., 2014). Head kinematic analysis demonstrated consistency and reproducibility in impact delivery, head trajectories, and peak velocity and acceleration across testing days. Further, the mice displayed features of human TBI immediately after impact, including prolonged loss of consciousness and neurological deficits using neurological severity score (NSS). Working and spatial memory deficits were observed in the animals subjected to two CHIMERA injuries (0.5J), evidenced by their behavior on the passive avoidance task and Barnes maze. Histopathological evaluation of brain tissues revealed diffuse axonal injury and inflammation within major white matter tracts: the olfactory nerve layer in olfactory bulb, corpus callosum, optic tract and brachium of superior colliculus. Subsequently, in collaboration with Haber et al., we carried out *ex vivo* magnetic resonance and diffusion tensor imaging at 7d post-CHIMERA repetitive TBI (two 0.5J or 0.65J impacts at 24 hours apart), to determine if the TBI-related histological changes detected in cryo-sections could also be detected using highly translational imaging techniques (Haber et al., 2017). Reduced fractional anisotropy was observed in white matter areas including anterior corpus callosum, optic tract, and brachium of superior colliculus, as well as in the grey matter hippocampus. Significant histological changes were found in the same matching white matter areas, including astrocytes (GFAP), microglia (Iba1), retraction bulbs and axonal varicosities (neurofilament), and axonal injury (silver stain). These pathological findings overlap with clinical TBI features. They showed that CHIMERA TBI induces pathological changes that are detectable by both standard histological methods and highly translational imaging techniques such as DTI. In a separate study, we further showed that the white matter changes of CHIMERA rTBI (two 0.5J impacts at 24 hours apart),

including axonal injury and microgliosis, were exacerbated by an 8-week pre-injury exposure to androgenic anabolic steroid cocktail (a mixture of testosterone, nandrolone and 17α-methyltestosterone) (Namjoshi et al., 2016). These findings highlight the importance of potential deleterious drug interactions in determining concussion outcomes.

Since its inception, the mouse platform has been distributed to fifteen academic institutions and industry sites worldwide, and a consensus in injury outcomes has emerged. Chen et al. utilized a repeated injury paradigm, delivering three CHIMERA impacts at 0.6J in young C57Bl/6 mice (Chen et al., 2017a). Their findings included acute behavioral and inflammatory changes that were congruent with previously published results using CHIMERA, including LRR, motor deficit, and acute gliosis in major white matter structures (optic tract and corpus callosum). Additionally, Chen et al found that CHIMERA rTBI produced chronic gliosis in both white matter and grey matter (hippocampus and cortex) and cognitive learning and memory impairments that lasted up to 6.5 months after the initial injuries (Chen et al., 2017a). In particular, injured mice required more time to travel to the visible platform during the Morris Water Maze, also spending less time in the platform quadrant during probe trials when the platform had been removed. Their findings demonstrate the capacity for CHIMERA to model long-lasting effects following repetitive CHI events.

1.10.7.1.2 Rat CHIMERA

We adapted the CHIMERA system to rats, to first understand the relationship between repetitive TBI, impulsivity, and neuropathology. Our hope for this platform was to help pinpoint a biological basis of complex neuropsychiatric phenotypes after brain injury. The development of

this model, as well as the results from our inaugural study, will be discussed in greater detail in Chapter 4.

1.10.7.1.3 Ferret CHIMERA

Studies using the ferret CHIMERA are yet to be published, however, pilot investigations suggest a susceptibility for inflammation within the sulcal depths. Chronic studies will be crucial to elucidate the sequelae of inflammation, cerebrovascular damage, and tau pathology following CHIMERA TBI in the ferret. Pilot studies using the ferret CHIMERA will be discussed in brief in Chapter 5.

1.11 Inconclusive findings for effective TBI therapies

While a number of recent therapies have shown promise in treating TBI outcomes in the pre-clinical setting, none have translated into effective intervention for the human condition (Stein, 2015). The consensus of several expert panels convened to improve TBI-related clinical trials have emphasized the urgent need for TBI imaging and molecular biomarkers that facilitate (1) the identification of subgroups of TBI patients with specific brain pathologies which can be selected for targeted therapeutic trials, (2) confirmation that the therapy is engaging the proposed molecular target, (3) measurement of pharmacodynamics and therapeutic efficacy (Diaz-Arrastia et al., 2014; Saatman et al., 2008). In this regard, biomarkers of BBB breakdown and other vascular pathology are also being developed. The most common biofluid biomarker of BBB breakdown is the CSF:serum albumin ratio which is altered in mild cognitive impairment, Alzheimer's disease, and severe TBI (Bhowmick et al., 2019; Saw et al., 2014), but not clearly altered in milder forms of TBI (Papa et al., 2015). Soluble PDGF receptor-β is shed from

pericytes and can be used to distinguish pericyte injury from injury to brain endothelial or vascular smooth muscle cells (Sagare et al., 2015). Development of markers for these other vascular cell types will be important, as will determining if biofluid levels of soluble PDGF receptor-β correlate with TBI-related neurodegeneration, as was recently demonstrated for CSF levels in those with mild cognitive impairment (Nation et al., 2019). We also need to develop and leverage imaging biomarkers that can assess vascular damage and BBB permeability, using available techniques like NIRS, ASL, and CVR. Additional studies are required to assess longitudinal changes in these imaging markers so that they can be used to identify patients with vascular dysfunction and monitor their response to vascular-directed therapeutics. The validation and implementation of such biomarkers will be absolutely critical to make studies of long-term outcomes practically feasible.

Another reason behind the lack of translational success may lie in the difficulty of modelling traumatic brain injury in a rodent or porcine model. Rodents in particular possess a more resilient cerebrovasculature than humans, a hypothesized consequence of differing circulating lipoproteins that affect vascular health. Specifically, as wild-type mice do not express cholesteryl ester transfer protein, they have far higher levels of vasoprotective high density lipoproteins compared to humans, and are therefore resistant to atherosclerosis (Marotti et al., 1993). Further, the method of inducing head injury is an equally important consideration. Though no single animal model has been able to capture the entire spectrum of neuropathological outcomes of human TBI, rotational platforms are showing promise (Clevenger et al., 2015; Johnson et al., 2018). From a biomechanical perspective, few models are able to capture the head kinematics that contribute to TBI-induced tissue deformation. We speculate that impact-acceleration and

rotation are key biomechanical features that would increase the likelihood of a pre-clinical model being sufficient to reproduce the complex pathophysiology following TBI.

1.12 Summary

The preparation of biospecimens using experimental TBI models is critical to address the questions surrounding molecular and systemic mechanisms of TBI, as well as to evaluate therapeutic approaches to promote recovery. Injury-induced neuropathology has frequently been a targeted end-point for evaluating therapies, with preferred platforms having as many of the clinical TBI hallmarks as possible, including but not limited to increased loss of consciousness, greater neurological deficits, and behavioral impairments.

CHIMERA is a model of non-surgical impact-acceleration head injury that triggers behavioral deficits and, importantly, diffuse axonal injury at acute, sub-acute, and chronic time-points, mimicking the phenotypes found in the majority of clinical TBI cases. Therefore, CHIMERA performs remarkably well as a model of concussive or sub-concussive injury, optimal for modelling consistently reproducible single or repetitive injuries. Importantly, this platform only requires isoflurane anesthesia, thus behavioral tests can be performed immediately after the animal has regained consciousness. The capacity of CHIMERA to generate injuries in the mild spectrum is a limitation. We have found that impacts greater than 0.7J in wild-type mice lead to skull fracture, an ethical concern and a limitation in clinical relevance. The work in Chapter 3 describe our efforts to expand the platform to include moderate-severe phenotypes in the mouse and rat models, in the hopes that increasing linear and angular velocity and acceleration will be sufficient to trigger multi-focal BBB breach and grey matter inflammation.

With the push towards the use of biomarkers in the clinic, it will be imperative that preclinical TBI research follows suit, by pinpointing biomarker endpoints that can be validated in animal models and used as a measure of target engagement in therapeutic studies. Our ultimate goal is for CHIMERA to be a useful translational platform to investigate genetic contributions and future therapeutics for TBI.

1.13 Study aims, design and thesis organization

The specific aims of this thesis are 1) to establish CHIMERA settings to reliably generate mild TBI in C57Bl/6 mice using kinematics, behavior and neuropathophysiological outcomes to define the threshold of injury; 2) to expand CHIMERA to reliably generate moderate-severe TBI behavioral and neuropathological phenotypes in C57Bl/6 mice with use of an interface to protect the murine skull; and 3) to use CHIMERA to explore the correlations of repetitive head trauma, impulsivity, and neuropathology in rats.

In Chapter 2, I will discuss the characterization of CHIMERA at the mild spectrum of injury, between 0.1J and 0.7J. In this study, male mice were exposed to single CHIMERA TBI and assessed for behavioral, histological, biochemical changes. The severity of injury was found to correlate strongly with neurological deficits, diffuse axonal inflammation, and white matter inflammation. Impact energies of 0.4 J or below produced no significant phenotype (subthreshold), 0.5 J led to significant changes for one or more phenotypes (threshold), and 0.6 and 0.7 J resulted in significant changes in all outcomes assessed (mTBI). We also show that

linear head kinematics were correlated most with duration of unconsciousness, severity of neurological deficits, white matter injury, and microgliosis following single TBI.

In Chapter 3, I will discuss the introduction of physical interfaces to the mouse CHIMERA platform to enable impacts up to 2.5J without causing skull fracture. This line of investigation is particularly important for future therapeutic studies directed at treating moderate-severe TBI. In the pilot experiments for this study, male and female mice were exposed to single CHIMERA TBI at 2.5J and assessed for changes in plasma biomarkers and damage to the blood-brain barrier. Impacts at 2.5J were found to elevate plasma proteins tau and neurofilament-light at an acute time-point. Damage to the BBB was also detected. I will then discuss the data obtained from the behavioral study, where male mice were exposed to single 2.5J injury and assessed for behavioral, functional, and neuropathological changes up to 60 days post-injury. Compared to sham controls, mice with TBI displayed poorer memory recall using Barnes maze, and diminished event amplitudes in the hippocampus by electrophysiology. Histological analysis revealed acute grey matter inflammation, along with sub-acute and chronic white matter damage and inflammation that intensified over time.

In Chapter 4, I will discuss the expansion of the CHIMERA platform to include rats. In this study, male rats were exposed to repetitive CHIMERA TBI and were assessed for trait impulsivity using the delay discounting task and for neuropathology at endpoint. Compared to sham controls, rats with rTBI displayed progressive impairment in impulsive choice. Histological analyses revealed reduced dopaminergic innervation from the ventral tegmental area to the olfactory tubercle, consistent with altered impulsivity neurocircuitry. Consistent with

diffuse axonal injury generated by CHIMERA, white matter inflammation, tau immunoreactivity and degeneration were observed in the optic tract and corpus callosum. Finally, pronounced grey matter microgliosis was observed in the olfactory tubercle.

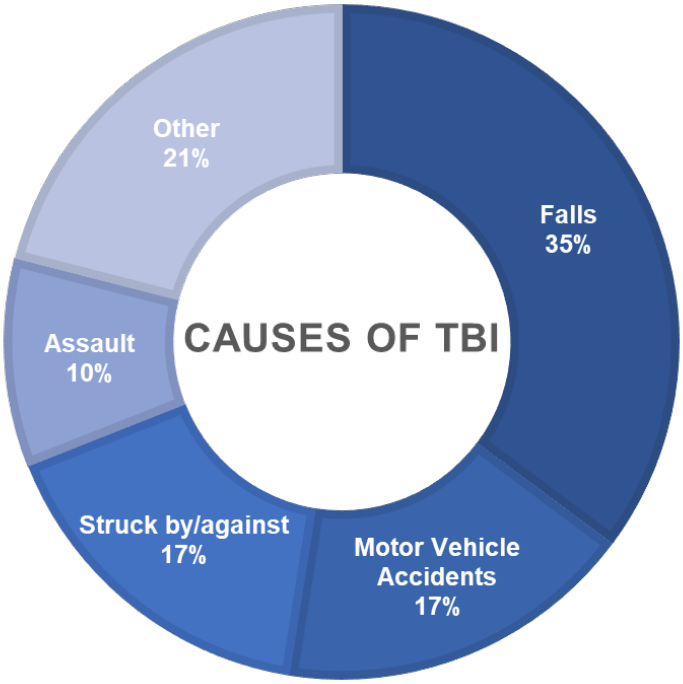

Figure 1.1 Causes of TBI

According to the classification system used in by the Centers for Disease Control and Prevention (CDC), the major cause of TBI is falls (35.2%), followed by motor vehicle-traffic accidents (17.3%), struck by/against (16.5%), and assault (10%). Sports-related TBI, which can be classified as “falls” or “struck by/against” under the CDC system, accounts for roughly 10% of all TBI.

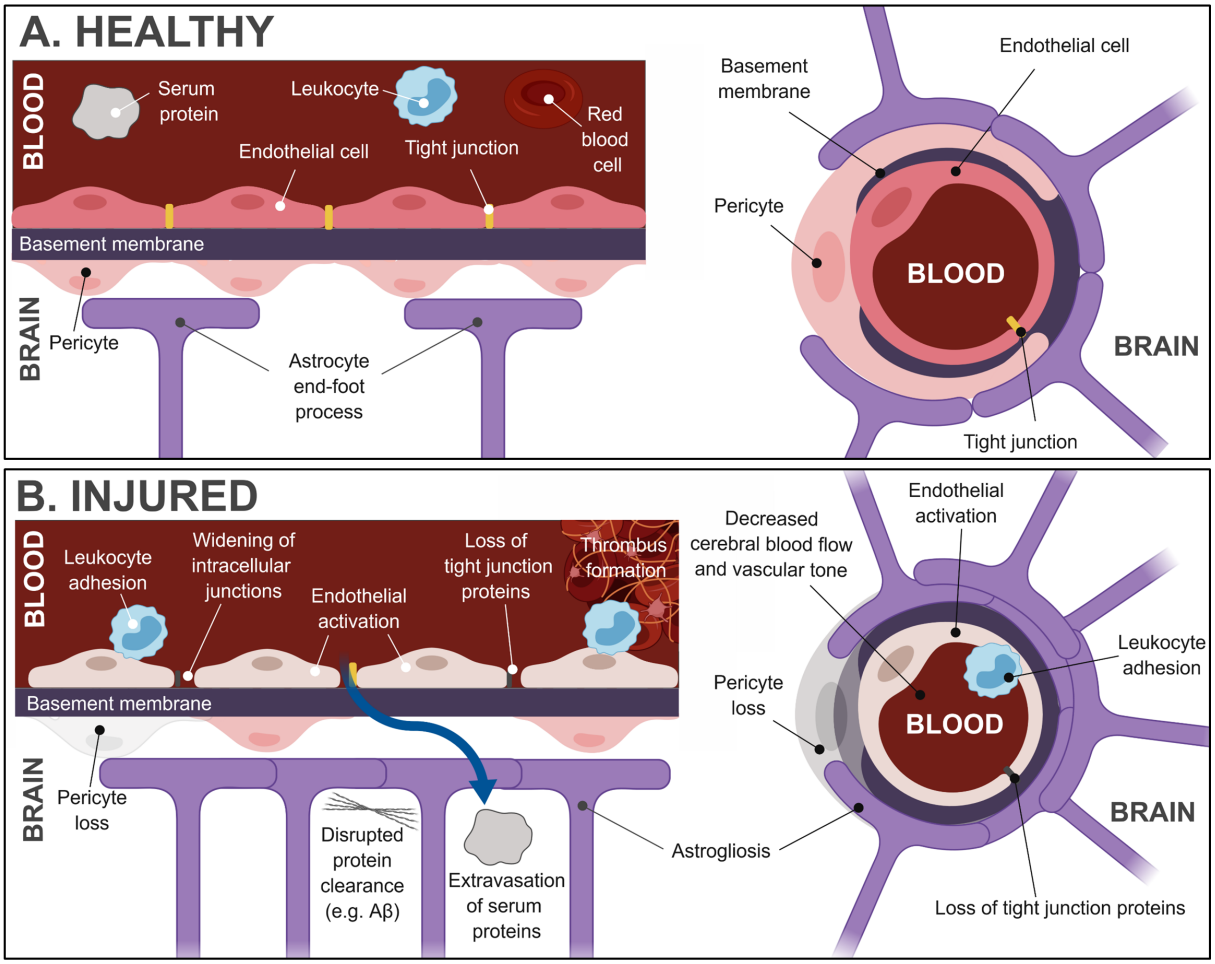

Figure 1.2 Healthy and injured neurovascular unit.

(A) At the capillary level, the neurovascular unit is composed of endothelial cells, perivascular astrocytes, and pericytes. Smooth muscle cells are present at the artery/arteriole/venule levels (not shown). The endothelial cells form a monolayer consisting of intercellular tight junctions to form the blood-brain barrier. (B) Following injury, a number of vascular changes have been reported in preclinical studies, including widening of intracellular junctions, loss of tight junction proteins – both of which contribute to extravasation of serum proteins into the parenchyma – astrogliosis, pericyte loss, endothelial activation, leukocyte adhesion, thrombus formation and disrupted protein clearance.

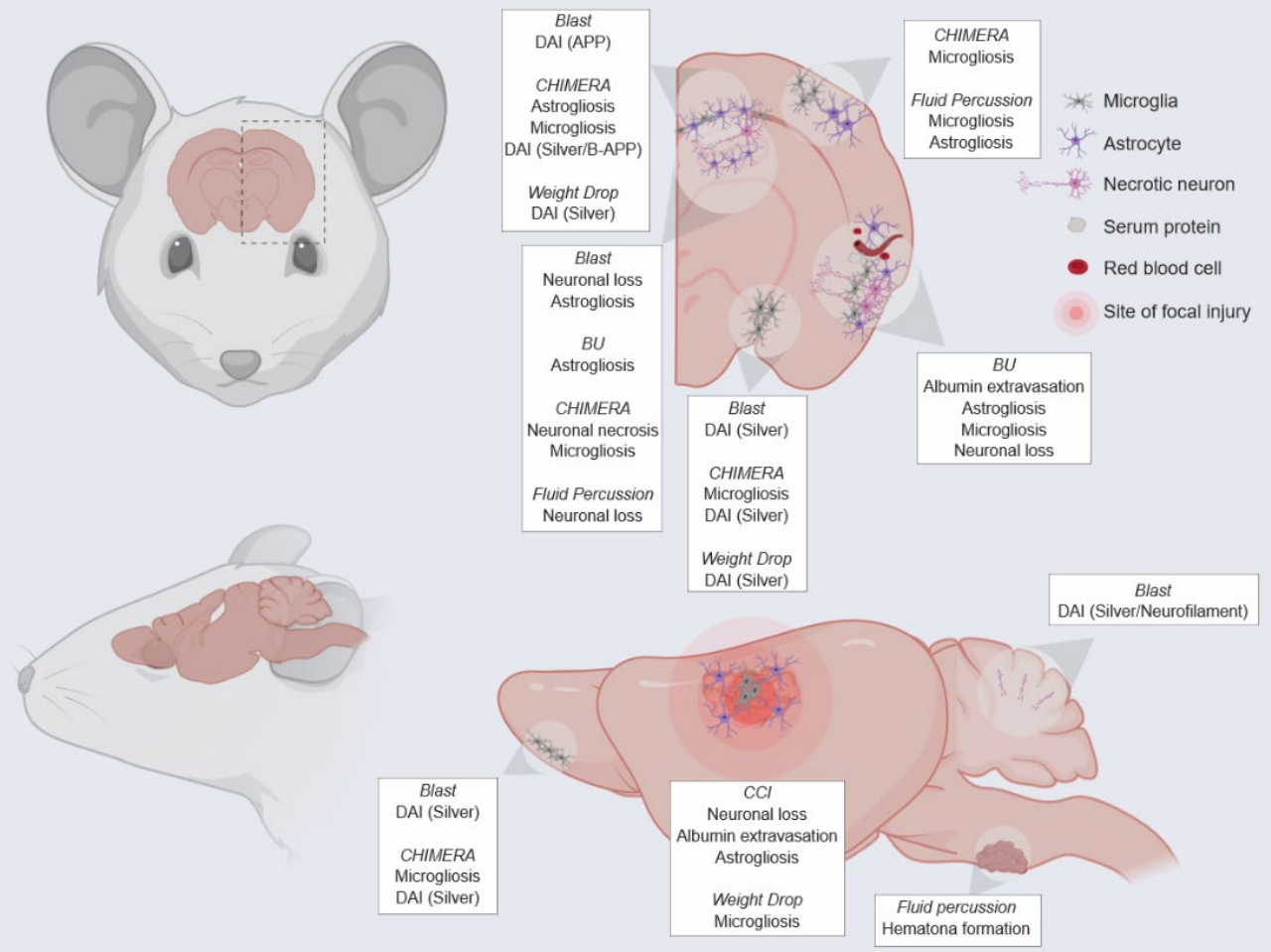

Figure 1.3 Neuropathological outcomes following rodent TBI.

Coronal (top) and sagittal (bottom) views are shown displaying the reported neuropathological outcomes of each platform discussed in Chapter 1. Following blast injuries, diffuse axonal injury in corpus callosum, olfactory nerve layer, optic tract, and cerebellar white matter, neuronal loss and astrogliosis in the hippocampus are reported. Impacts using the BU lateral-impact model cause albumin extravasation, astrogliosis, microgliosis, and neuronal loss in the perirhinal cortex, as well as astrogliosis in the hippocampus. The CCI model elicits neuronal loss, albumin extravasation and astrogliosis around the site of injury. CHIMERA injuries lead to white matter

inflammation and diffuse axonal injury in the corpus callosum, olfactory nerve layer, and optic tract. With the addition of the modCHIMERA apparatus, cortical and hippocampal microgliosis along with hippocampal neuronal loss are reported. Following fluid percussion injuries, neuronal loss in hippocampus, cortical microgliosis and astrogliosis, and hematoma formation on the brain stem are reported. Weight drop injuries cause diffuse axonal injury in corpus callosum and optic tract, with microgliosis constrained around the focal site of injury. Abbreviations: APP: amyloid precursor protein; B-APP: beta-amyloid precursor protein; BU: Boston University; CCI: controlled cortical impact; DAI: diffuse axonal injury.

Table 1.1 Classification of TBI severity

Severity Criteria	**Mild TBI**	**Moderate TBI**	**Severe TBI**
Structural imaging	Normal	Normal or abnormal	Normal or abnormal
Loss of consciousness	0 – 30 min	30 min – 24 h	> 24 h
Altered mental state	<= 24 h	> 24 h s; severity based on other criteria	
Post-trauma amnesia	<= 1 d	1 – 7 d	> 7 d
Glasgow Coma Scale score	13 - 15	9 - 12	<9

Chapter 2: Defining the biomechanical and biological threshold of murine mild TBI using CHIMERA

2.1 Introduction

Although historically considered benign, mTBI can result in significant disability. Most mTBI patients recover without sequelae, yet approximately 10% have intracranial lesions on computed tomography scanning (complicated mTBI) and a minority of these can develop a potential life-threatening condition that requires neurosurgical intervention (Haydel et al., 2000). Additionally, up to 30% of mTBI subjects, despite having normal neuroimaging, can suffer persistent impairment of physical, cognitive, and psychosocial functioning known as post-concussive syndrome (Carroll et al., 2014). The recognized incidence of mTBI complications and poor outcomes is rising, owing to greater awareness and reporting especially for sports-related concussion. Although the monetary cost of TBI varies by severity, the high incidence of mTBI leads to a total cost that is nearly three times that for moderate to severe TBI (Te Ao et al., 2014). The prevalence and socioeconomic burden of mTBI are driving the demand to develop objective diagnostic, prognostic and therapeutic tools to address this large unmet medical need.

We recently developed a neurotrauma animal model called CHIMERA (Closed-Head Impact Model of Engineered Rotational Acceleration) to address the absence of a simple, nonsurgical impact acceleration model of closed head injury that reliably produces DAI and white matter inflammation. Our group previously showed that mice subjected to two mild, closed-head TBIs with an impact energy of 0.5 J using CHIMERA show human-like head kinematics and faithfully reproduce behavioral features and diffuse white matter tract pathology similar to human TBI

(Namjoshi et al., 2014). However, much remains to be learned about the parameters of the nascent CHIMERA technology to substantiate it as a useful platform for the TBI research community. This study was therefore designed to establish the threshold at which skull fracture would occur, then assess behavioral and neuropathological outcomes following impact energies below that threshold. We wished to test the hypothesis that single impact CHIMERA impacts of increasing impact energies would be correlated to behavioral and neuropathological outcomes in mice.

2.2 Methods

2.2.1 CHIMERA TBI procedure and high-speed videography

Male C57Bl/6 mice at 4-5 months of age were housed with a reversed 12h light-12h dark cycle. Animals were prepared for single TBI in the sagittal plane. Mice received isoflurane anesthesia (mean ± SD total isoflurane exposure duration: 278.67 ± 60.77s) and were positioned on the CHIMERA impactor. TBI animals received a single closed-head impact at 0.1, 0.3, 0.4, 0.5, 0.6 or 0.7J of energy using a 50-g stainless steel piston, as animals subject to impact greater than 0.7J led to >50% mortality. Sham animals (0J) received an equivalent isoflurane exposure as TBI animals but experienced no impact. Five to six animals were included per energy group per post-TBI time point (described below). Head kinematics at each impact energy were assessed using high-speed (9,000 fps) videography with two reference points including a snout and a cheek marker, and were analyzed by ProAnalyst motion analysis software (Xcitex Inc., Woburn, MA) as described (Namjoshi et al., 2014).

2.2.2 Behavioral analyses

Duration of loss of righting reflex (LRR) was recorded immediately following head impact. Neurological impairment was assessed using the neurological severity score (NSS) at 1h. NSS is a composite score where a point is awarded for failure to perform any of the following tasks: Failure to exit a 30-cm-diameter circle, loss of startle behavior, loss of seeking behavior, inability to walk in a straight line, inability to walk across a 3-cm, 2-cm or 1-cm beam, inability to balance on a 0.5cm beam, inability to balance on a round stick (0.5 cm in diameter), and presence of mono- or hemi-paresis. Motor function was assessed using the accelerating rotarod test at 1, 2, 7 and 14d post-TBI. Anxiety-like thigmotactic behavior was assessed in an open field at 1 and 7d after TBI. Post-TBI anxiety behavior was further tested with the elevated plus maze (EPM) at 2d post-TBI. For EPM testing, the animal was placed in the central zone of a custom-built EPM and spontaneous activity was recorded using AnyMaze (Stoelting Co., Wood Dale, IL) for 5 min to assess time spent in the open and closed arms.

2.2.3 Euthanasia and tissue collection

Brains were collected at 6h and at 1d, 2d, 7d and 14d post-TBI following anesthesia with ketamine and xylazine and perfusion with ice-cold heparinized phosphate-buffered saline (PBS). Brains were rapidly collected, longitudinally bisected and hemibrains were processed for histology or biochemistry as described below.

2.2.4 Immunohistochemistry

Hemibrains fixed in 4% paraformaldehyde in PBS then cryoprotected with 30% sucrose. 40 μm coronal sections were prepared using a cryostat. Three to five coronal sections per brain

spanning the olfactory bulb to the posterior hippocampus were assessed for histology as described below. Microglial activation and astrocytic reactivity were assessed using Iba1 and GFAP immunohistochemistry, respectively.

Briefly, sections were quenched with hydrogen peroxide for 10 min and blocked with 5% NGS in PBS for 1h at RT. Sections were incubated with primary antibodies (Iba1: Wako 019-19741, 1:1000; GFAP: Abcam, AB 305808, 1:500) overnight at 4°C. Sections were then incubated with biotin-conjugated secondary antibodies (1:1000) and detected using a colorimetric procedure by incubating with ABC reagent (Vector Labs PK-6100, 1:400) before color development with DAB (Sigma D5637-1G). Axonal injury was histologically evaluated by Neurosilver staining (FD Neurotechnologies) following the manufacturer's instructions (Namjoshi et al., 2014)

2.2.5 Imaging of histological sections

All stained sections were digitally imaged at a commercial histology service (Wax-it Histology Services Inc., Vancouver, BC) with a ScanScope CS-R scanner (Aperio Technologies) using a 20x magnification objective lens. From the whole-mount images, 20x magnified images containing regions of interest (ROI) were extracted using the Aperio ImageScope Viewer (v. 12.2.2.2015, Aperio Technologies) software.

2.2.6 Quantification of histological images

Image quantification was carried out with ImageJ (1.51f, NIH). The microglial and astrocytic responses were quantified by counting the number of Iba1 and GFAP positive cells in white matter regions, respectively. White matter ROIs were manually isolated and thresholded. Subsequently, count per area was measured after filtering background noise of particles less than

250-pixel units. Images were scaled to mm^2, then cell density was expressed as number of Iba-1 or GFAP positive cells per mm^2. After white matter ROIs were manually isolated and thresholded, silver staining was assessed by quantifying percent stained area of the region of interest of white matter.

2.2.7 Biochemistry

Half-brains were homogenized in 1.5 ml of ice-cold RIPA lysis buffer containing 0.1 mM phenylmethylsulphonyl fluoride, complete protease inhibitor (Roche Applied Science), and PhosSTOP tablets (Roche Applied Science) in a Tissuemiser homogenizer at full speed for 20s and then sonicated at 20% output for 10 s. After incubating on ice for 10 min, lysates were clarified by centrifugation at 9000 rpm for 10 min at 4ºC and the supernatant was taken for analysis. Levels of IL-6, IL-1β and TNFα were measured on lysates diluted 1:2 using a customized version of the V-PLEX Proinflammatory Panel 1 (mouse) (K152A0H-2, Meso Scale Discovery, Rockville, MD) following the manufacturer's protocol, with the exception that sample incubation was increased to overnight at 4ºC. Levels of total and phosphorylated (Thr231) tau were measured on samples diluted 1:50 using an MSD® MULTI-SPOT assay (K15121D-2, Meso Scale Discovery, Rockville, MD) following the manufacturer's protocol. Plates were read on a Sector S 600 (Meso Scale Discovery, Rockville, MD) and concentrations were normalized to total protein content determine by bicinchoninic acid assay (Pierce).

2.2.8 Data analysis and statistics

All statistical analyses were performed using GraphPad Prism (v. 6.07) unless otherwise stated. Peak head kinematic parameters data were analyzed with one-way ANOVA followed by Tukey

post-hoc tests. LRR and 1h NSS data were analyzed with Kruskal-Wallis test. Rotarod latencies and thigmotaxis index data were analyzed with a linear mixed model using SPSS Statistics (v.23, IBM Corporation). Histological quantification and EPM data were analyzed with two-way ANOVA followed by Tukey post-hoc tests. Correlation analyses were employed to assess the relationships between head kinematic data and post-TBI outcomes including LRR, 1h NSS, silver stain quantification, and Iba1 positive cell count using Spearman's rank correlation coefficient. All data are presented as mean ± SD unless otherwise stated.

The study design is summarized in **Figure 2.1**.

2.3 Results

Pre-TBI body weight, age at TBI and isoflurane exposure duration were comparable across all impact energy groups **(Figure 2.2)**.

2.3.1 Data binning

One of the objectives of the current study was to determine the lower limit of impact energy required to induce significant alteration(s) in one or more of our post-TBI outcomes (kinematics, behavior and neurological deficits, neuropathology and biochemical changes) compared to sham controls. Initial analysis of each energy group showed that impact energies from 0.1 – 0.4 J caused no significant changes in any post-TBI behavioral and neuropathological outcome compared to the uninjured group. Significant changes in at least one measure of behavior and neuropathology were observed at impact energy of 0.5 J, and impact energies of 0.6 and 0.7 J produced significantly more injury than 0.5 J but were not significantly different from each other (not shown). Accordingly, we binned data from the seven energy groups into four categories:

Sham (0J), sub-threshold (0.1, 0.3 and 0.4J), threshold (0.5J) and mild TBI (mTBI, 0.6 and 0.7J). The analyses reported hereafter represent binned data obtained from a total of N=31 mice in the sham category, N=94 mice in the subthreshold category, N=36 mice in the threshold category, and N=65 mice in the mTBI category. The details of sample size for each analysis are presented in **Table 2.1**.

2.3.2 Single impact CHIMERA induces energy dose-dependent changes in head kinematics

We assessed changes in head kinematics by analyzing peak linear (head displacement, velocity and acceleration) and angular (angle, velocity and acceleration) kinematic parameters over increasing impact energies. Each parameter showed an impact energy dose-dependent increase **(Figure 2.3)**. Except for head angle, we observed significant impact energy dose effects for all other head kinematic parameters [Displacement: $p < 0.0001$; Linear Velocity: $p < 0.0001$; Linear Acceleration: $p < 0.0001$; Angle: $p = 0.0966$; Angular Velocity: $p < 0.0001$; Angular Acceleration: $p < 0.0001$; One-way ANOVA followed by Tukey's post-hoc test]. Post-hoc analyses revealed that increasing impact energies caused a significant increase in all head kinematic values except head angle compared to the sub-threshold TBI group **(Figure 2.3)**.

2.3.3 Single impact CHIMERA induces energy dose-dependent increases in righting time, neurological severity, motor deficits and thigmotactic behavior

We recorded LRR duration immediately following closed head impact, which showed an injury dose effect (**Figure 2.4 A**, $p < 0.0001$, Kruskal-Wallis test). Post-hoc analysis showed that LRR durations of the threshold and mTBI groups were significantly longer compared to the sham and

sub-threshold TBI groups (**Figure 2.4 A**). Mice in the mTBI group exhibited the longest post-TBI LRR duration compared all other groups (**Figure 2.4 A**). Similarly, the NSS determined at 1h post-TBI also showed an overall injury dose effect (**Figure 2.4 B**, $p < 0.0001$, Kruskal-Wallis test). Mice in the threshold and mTBI groups exhibited significantly higher NSS values compared to sham controls (**Figure 2.4 B**). Post-TBI anxiety behaviors were assessed with the EPM and open-field thigmotactic behavior. For EPM we compared the number of entries by the animal in the open and closed arms of the maze and found no significant differences across any energy group (**Figure 2.4 C**, $p > 0.05$, two-way ANOVA). By contrast, thigmotactic behavior showed significant impact energy dose ($p = 0.016$) and time ($p < 0.0001$) effects (**Figure 2.4 D**, linear mixed model). Post-hoc analysis showed significantly increased thigmotactic behavior of mice in the mTBI group compared to sham and sub-threshold TBI groups regardless of time. However, thigmotactic behavior did not show a significant impact energy x time interaction ($p = 0.559$, linear mixed model). We assessed post-TBI motor deficits using the accelerating rotarod task. Analysis of rotarod latencies revealed significant effects of impact energy dose ($p < 0.0001$) and time ($p < 0.0001$), and revealed a significant interaction of impact energy dose x time ($p < 0.001$) (**Figure 2.4 E**, linear mixed model). Post-hoc analysis of impact energy dose revealed significantly reduced rotarod latencies of mice in the mTBI group, while fall latencies of mice in sham, sub-threshold and threshold TBI groups were comparable over all post-TBI time points tested. Mice in the mTBI group exhibited sustained motor deficits compared to the sham group over all post-TBI time points except 7 d (**Figure 2.4 E**).

2.3.4 Single impact CHIMERA induces energy dose-dependent increases in microgliosis, astrogliosis and proinflammatory cytokines

The post-TBI microglial response was assessed with Iba1 immunohistochemistry at 6h and 1d, 2d, 7d and 14d post-TBI. Compared to sham brains, injured brains showed significant increases in the number of Iba1-positive microglia in several white mater regions including the olfactory nerve layer (**Figure 2.5**), corpus callosum (**Figure 2.6**), brachium of superior colliculus (**Figure 2.7),** and optic tract (**Figure 2.8**), indicating that CHIMERA injury induced proliferation or recruitment of immune cells. Quantitative analysis of Iba1 images revealed an impact energy dose-dependent increase in the number of Iba1-positive microglia in the olfactory nerve layer (**Figure 2.9 A**, energy dose effect: $p < 0.0001$), corpus callosum (**Figure 2.9 B**, energy dose effect: $p < 0.0001$), brachium of superior colliculus (**Figure 2.9 C**, energy dose effect: $p < 0.0001$) and optic tract (**Figure 2.9 D**, energy dose effect: $p < 0.0001$). Microgliosis was significant in all white matter regions in the mTBI group. Microglia number showed persistent increases over 1-14d in the olfactory nerve layer (**Figure 2.9 A**, Time effect: $p = 0.0004$) and over 2-14d in the corpus callosum (**Figure 2.9 B,** Time effect: $p < 0.0001$), brachium of superior colliculus (**Figure 2.9 C**, Time effect: $p < 0.0001$) and optic tract (**Figure 2.9 D**, $p < 0.0001$). Finally, we observed a significant impact energy x time interaction in microglia number in the corpus callosum (**Figure 2.9 B**, $p = 0.0044$), brachium of superior colliculus (**Figure 2.9 C**, $p = 0.0489$) and optic tract (**Figure 2.9 D**, Time effect: $p < 0.0001$), indicating that increased impact energy doses led to persistently increased microglial proliferation or recruitment over time. The temporal profile of post-TBI microgliosis also showed region-specificity. Thus, microgliosis in the olfactory nerve layer and corpus callosum showed an early peak at 2d post-TBI, while that in the brachium of superior colliculus and optic tract peaked later at 7d (**Figure 2.17**)

We also assessed astrocyte activation at the same post-TBI time points by GFAP immunohistochemistry, and found a significant increase in the number of GFAP-positive astrocytes exclusively in the corpus callosum of injured animals (**Figure 2.10**). Quantitative analysis of GFAP images showed significant effects for impact energy dose (**Figure 2.10 B**, $p < 0.0001$) and time ($p < 0.0001$), and revealed a significant energy dose X time interaction ($p < 0.0001$). Astrogliosis peaked in the threshold and mTBI groups at 2 d, and showed persistent increase in mTBI group up to 7d followed by return to baseline in all groups by day 14 (**Figure 2.10 B**).

In addition to microglial and astrocyte response, we also measured protein levels of proinflammatory cytokines IL-6, IL-1β and TNFα in half-brain homogenates at 6h. Protein levels of all the three proinflammatory cytokines were significantly higher than sham levels (**Figure 2.11**, $p < 0.05$, one-way ANOVA).

2.3.5 Single impact CHIMERA induces energy dose-dependent increases in axonal damage.

We used silver staining to assess axonal pathology as a function of energy level and time after single impact CHIMERA. Compared to the sham group, injured brains showed widespread axonal injury, as indicated by intense punctate and fiber-associated argyrophilic structures in the olfactory nerve layer (**Figure 2.12**), corpus callosum (**Figure 2.13**), and optic tract (**Figure 2.14**). Quantification of silver stained images showed an impact energy dose effect in the olfactory nerve layer (**Figure 2.15 A**, $p < 0.0001$), corpus callosum (**Figure 2.15 B,** $p < 0.0001$)

and optic tract (**Figure 2.15 C**, $p < 0.0001$). Post-hoc testing revealed significantly higher silver uptake in all white matter regions by 2 d post-injury in the mTBI group compared to sham (**Figure 2.15**).

We also noticed region-specific changes in the temporal profile of silver uptake (**Figure 2.15** and **Figure 2.17**). Thus, in mTBI group silver uptake was prominent in the olfactory nerve layer at 1 and 2 d followed by return to sham levels by day 7 (time effect: $p < 0.0001$; impact energy dose x time interaction: $p < 0.0001$). On the other hand, silver uptake in the mTBI group showed a delayed but persistent increase over 2-14d in corpus callosum (time effect: $p = 0.5653$; energy dose x time interaction: $p = 0.0245$) and optic tract (time effect: $p < 0.0001$; energy dose x time interaction, $p = 0.0003$), indicating axonal injury continued to evolve over time with distinct patterns in different white matter tracts.

2.3.6 Total and phosphorylated tau are not altered after single impact CHIMERA TBI up to 0.7 J.

We assessed endogenous levels of total and phosphorylated (Thr231) tau in half brain homogenates using an MSD® MULTI-SPOT assay. No significant changes were observed for total tau, phosphorylated tau, or the ratio of phosphorylated:total tau for any injury group at any time point tested (**Figure 2.16**).

2.3.7 Neurological and neuropathological outcomes following single CHIMERA TBI correlate significantly with linear head kinematics.

We also tested for correlations between changes in the biomechanical response of the head following single impact CHIMERA injury in the sagittal plane with neurological and neuropathological outcomes at 2 d post-injury (**Table 2.2**). We observed a strong positive correlation between linear head kinematic parameters with several post-TBI outcomes. Among all post-TBI outcomes, LRR showed the strongest positive correlation with both linear (displacement, velocity and acceleration) and angular (velocity and acceleration) head kinematic parameters ($p < 0.0001$). NSS at 1h was positively correlated with head displacement ($p = 0.0146$), linear velocity ($p = 0.006$), linear acceleration ($p = 0.0168$) and angular velocity ($p = 0.0011$). The microglial response in all white matter regions showed a significant positive correlation with all three linear kinematic parameters but not with any angular kinematic parameters. Silver stain uptake in the olfactory nerve layer and corpus callosum showed a significant positive correlation with head displacement and linear velocity only, whereas, silver stain uptake in the optic tract showed a strong positive correlation with all three linear kinematic parameters.

2.4 Discussion

This study was designed to leverage the advantages of the CHIMERA platform to define the lower limit of mTBI in mice upon a single impact in the sagittal plane. Here we show that impact energies up to 0.4J, which lead to average peak linear and angular accelerations of 305 *g* and 86.9 krad/s^2 respectively, do not produce any significant phenotype except for Iba1 reactivity in the optic tract and brachium of superior colliculus at 14d, and can thus be considered sub-

threshold. An impact energy of 0.5J, which produced average peak linear and angular accelerations of 510 *g* and 149 krad/s^2 respectively, resulted in significant changes in behavioral (LRR and NSS), and histopathological (Iba1 reactivity in corpus callosum, brachium of superior colliculus and optic tract, and GFAP reactivity in corpus callosum) outcomes, and is defined as the threshold of acute injury for murine CHIMERA. Impact energies of 0.6 and 0.7 J resulted in average peak linear and angular accelerations of 539 *g* and 183 krad/s^2, respectively, and led to significant changes for many behavioral (LRR, NSS, thigmotaxis, rotarod), and histopathological (Iba1 reactivity and silver uptake in all white matter tracts examined, and GFAP reactivity in corpus callosum), and can be considered in the mTBI range. Using the current CHIMERA piston design, impact energies greater than 0.7J resulted in skull fracture and posed an ethical upper limit to our studies. These results demonstrate that single impact CHIMERA in the sagittal plane effectively induces both behavioral and histopathological phenotypes of diffuse axonal injury.

Our results define critical experimental parameters that can now be used to determine how well our categories of subthreshold, threshold and mTBI groups using murine CHIMERA reflect human subconcussive, concussive and mTBI categories. Importantly, current definitions that categorize human mTBI are thus far based on clinical and neuroimaging approaches. Our study employed several behavioral measures reminiscent of clinical measures, including LRR as a proxy of loss of consciousness, NSS as a proxy of neurological outcomes, EPM and open field analyses as proxies for anxiety, and rotarod latency as a proxy of motor function and coordination. We observed that LRR and NSS are the most sensitive behavioral assessments in our current battery, as they distinguish both threshold and mTBI categories from sham and demonstrate significant differences between the threshold and mTBI groups. By contrast,

significant changes in open field thigmotactic behavior and motor competency were observed only in the mTBI category. Although future studies will be needed to refine the animal model behavioral assessments to more closely resemble the clinical criteria used for mTBI classification, the data presented here serve as a starting point for this effort.

Although neuroimaging outcomes were beyond the scope of the present study, we anticipate observing white matter changes using neuroimaging based on our observation of white matter histopathological changes induced by CHIMERA. Consistent with our previous report of axonal damage and white matter inflammation after double TBI at 0.5J (Namjoshi et al., 2014), here we observed impact energy-dependent increases in silver uptake in several white matter regions including the olfactory nerve layer, corpus callosum, and optic tract, with significantly increased argyrophilic axons in all regions examined for the mTBI category. Several white matter regions also displayed significant Iba1 reactivity. Our analyses also revealed that both axonal injury and white matter inflammation continued to evolve over 14 d post-injury. Interestingly, we observed transient but significant increases in the number of GFAP-positive astrocytes only in the corpus callosum within 2-7 days post-TBI, suggesting GFAP may be a less sensitive marker of axonal damage than either Iba1 or silver uptake. Several additional histological markers of axonal injury, including neurofilament, amyloid precursor protein, and tau, will be examined in future studies and related to neuroimaging changes. Future studies will also address time points beyond 14d after injury.

The response of tau to single vs repetitive mTBI now becomes an important question. Perivascular tau deposits, particularly in sulcal depths, is the pathognomonic feature of CTE

(Mckee et al., 2016). Biomarker studies, most commonly performed in studies in athletes who participate in high impact sports, also report that blood tau levels can be used as a diagnostic biomarker for mTBI (Shahim et al., 2016; Zetterberg and Blennow, 2016). Using Western blotting, we previously observed transient phosphorylation of tau in a study that used 2 x 0.5 J impacts, which we now define as the threshold for injury (Namjoshi et al., 2014). Using a more quantitative ELISA assay, here we observed that single impact TBI up to 0.7 J does not lead to significant increases in total or phosphorylated (Thr231) tau, at least in the acute 14 d period studied here, despite significant silver uptake. This observation raises the important question of whether tau changes may occur as a function of cumulative injury, which can be rigorously tested using the CHIMERA platform, or more severe injuries (>0.7J) which will be discussed in Chapter 3.

Our data suggest that not all affected white matter regions recover at the same rate (**Figure 2.17**). The most striking example of this is in the olfactory nerve layer, which displays both a larger dynamic range of histopathologic changes and a faster recovery than any other white matter region studied. On the other end of the spectrum is the corpus callosum, which appears to develop a modest but relatively stable phenotype. In our study, white matter pathology is slowest to develop in the optic tract, which has not yet peaked with respect to silver uptake at the 14d time point used here, and is consistent with our previous report using double 0.5J impacts. Future studies that refine the dynamic range and temporal profiles of additional markers in white matter regions, and relate them to neuroimaging findings, will be an important future avenue of investigation.

Our study is limited to describing the associations of impact energy with acute behavioral, neuropathological and biochemical outcomes using single impact CHIIMERA in the sagittal plane. Under these conditions, we observed that linear kinematic values were better predictors of biological outcomes than angular kinematic values. Future studies will leverage the ability of CHIMERA to precisely deliver impact in any desired plane to investigate the relationships between lateral impact, which will induce head acceleration-deceleration in the coronal plane, and mTBI outcomes. The threshold of injury for mice is 0.5J, which produced an average peak linear head velocity of 6.8 m/s, peak linear acceleration of 524 *g*, peak angular velocity of 326 rad/s, and peak angular acceleration of 149 krad/s^2. Scaling these mechanical insults based on an equal stress equal velocity relationship and single scale factor of 13.8 (λ) (Panzer et al., 2014), results in the following equivalent human head kinematics values: peak linear acceleration of 38 *g*, peak angular velocity of 23.6 rad/s and peak angular acceleration of 782 rad/s^2. Peak linear head acceleration of 38 *g* is below most reported human concussion tolerances generated through instrumented helmet data (Guskiewicz et al., 2007; Rowson et al., 2012) but above measured head accelerations in volunteer soccer heading (23.5 *g*) (Shewchenko et al., 2005) and low speed (16 km/h) rear impact vehicle crashes (17.2 *g*) (Szabo and Welcher, 1996). Scaled peak angular velocity was in the range reported to result in human concussion, however, peak angular acceleration was well below threshold levels developed from analysis of sports collisions. The average sub-concussive impact in an American football study had a rotational acceleration of 1230 rad/s^2 and a rotational velocity of 5.5 rad/s, while the average concussive impact had a rotational acceleration of 5022 rad/s^2 and a rotational velocity of 22.3 rad/s (Rowson et al., 2012). Based on reconstructed head impacts in Australian football, A 50% likelihood for concussion was proposed for peak linear acceleration of 65.1 *g*, peak angular velocity of 22.2

rad/s and peak angular acceleration of 3958 rad/s^2 (McIntosh et al., 2014). One possible interpretation of the present results, given that linear kinematic values were better predictors of biological outcomes than angular kinematics, is that impact in the sagittal plane generates limited rotational motion. As CHIMERA can generate precise impact in additional planes of motion, future studies will be able to address how injury tolerance may vary by anatomical plane of movement. Additional studies will also address current limitations in scaling animal model mechanical insults to humans. Biomechanical scaling techniques, while remarkably successful in some applications, have yet to be experimentally validated across a range of species (Panzer et al., 2014).

The initiation of skull fractures at impact energies greater than 0.7J posed an upper ethical limit to our current experimental protocol. In order to produce pathology indicative of more severe brain injury, it will be necessary to induce larger head accelerations while simultaneously decreasing skull fracture risk. Increased skull stiffness and failure strength of murine cranial bones is expected by distribution of impact forces over a greater area of the mouse skull, as has been demonstrated in human cadaver cranium impact tests (Allsop et al., 1991). Our data support CHIMERA as a useful model of several mTBI subcategories, and confirm DAI as a key neuropathology associated with mTBI. By defining the impact energy parameters at the threshold of mild injury, we are now poised to launch several additional studies to further refine our understanding of the tissue level mechanisms of mTBI and repair.

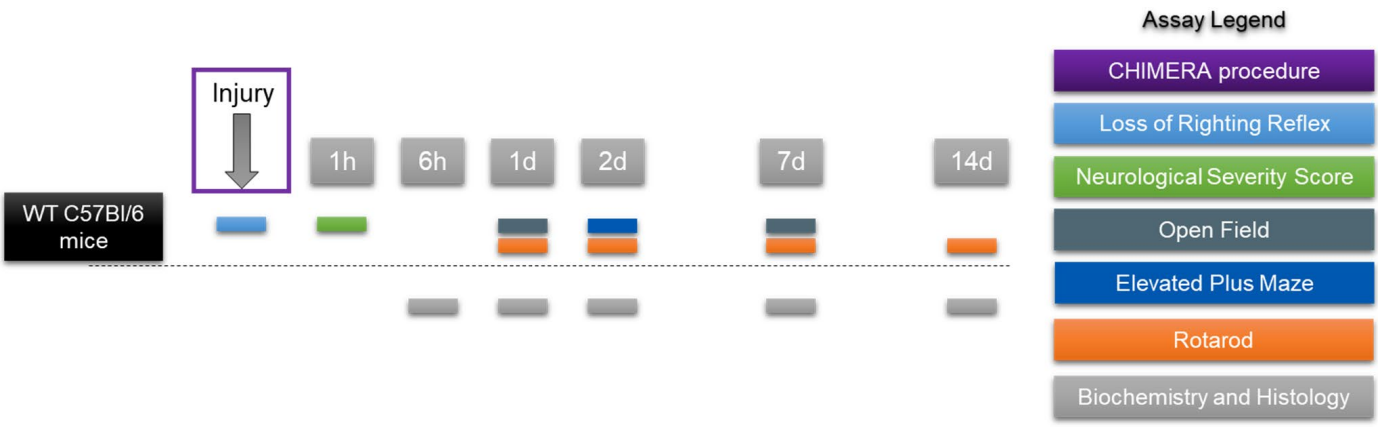

Figure 2.1 Study design.

Injury was induced at T=0, immediately after which LRR latency was recorded. At 1h, neurological severity score testing occurred. Animals underwent open field testing at 1d and 7d post-TBI, and elevated plus maze occurred at 2d. Rotarod tests took place at 1d, 2d, 7d and 14d post-TBI. Terminal collection procedures for biochemical and histological outcomes for this study occurred at 6h, 1d, 2d, 7d, and 14d post-TBI.

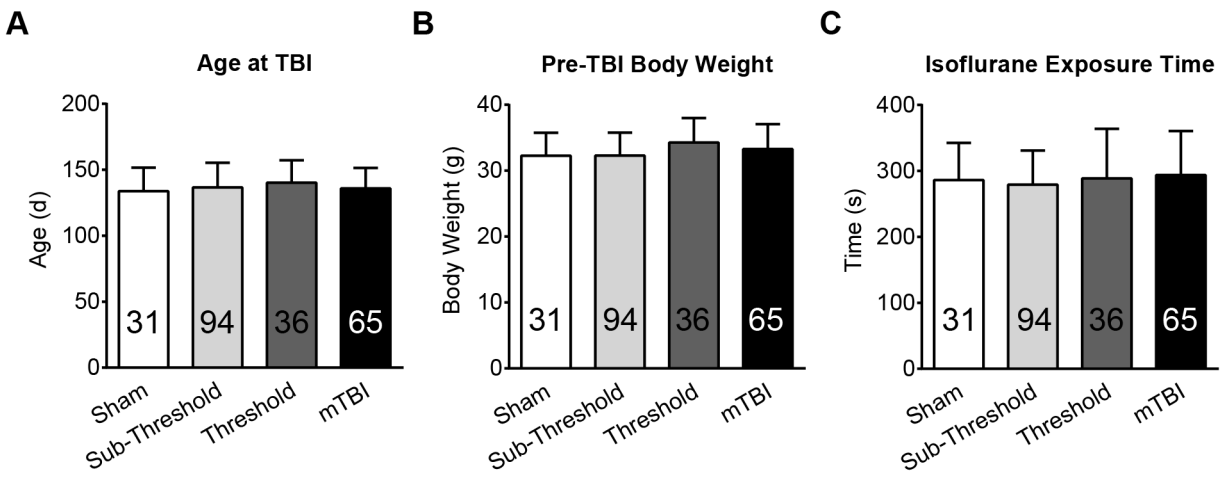

Figure 2.2 Animal morphological data and isoflurane exposure time.

(A) The graph shows age (in days) of animals at the time of TBI across all energy groups. (B) Pre-TBI body weight (in g) of animals in all energy groups. Both age and body weight were comparable across all energy groups. (C) Total isoflurane exposure (in s) during the CHIMERA TBI procedure, which was recorded as the time started with anesthesia induction until head impact when isoflurane delivery was stopped. Numbers within bars indicate sample size.

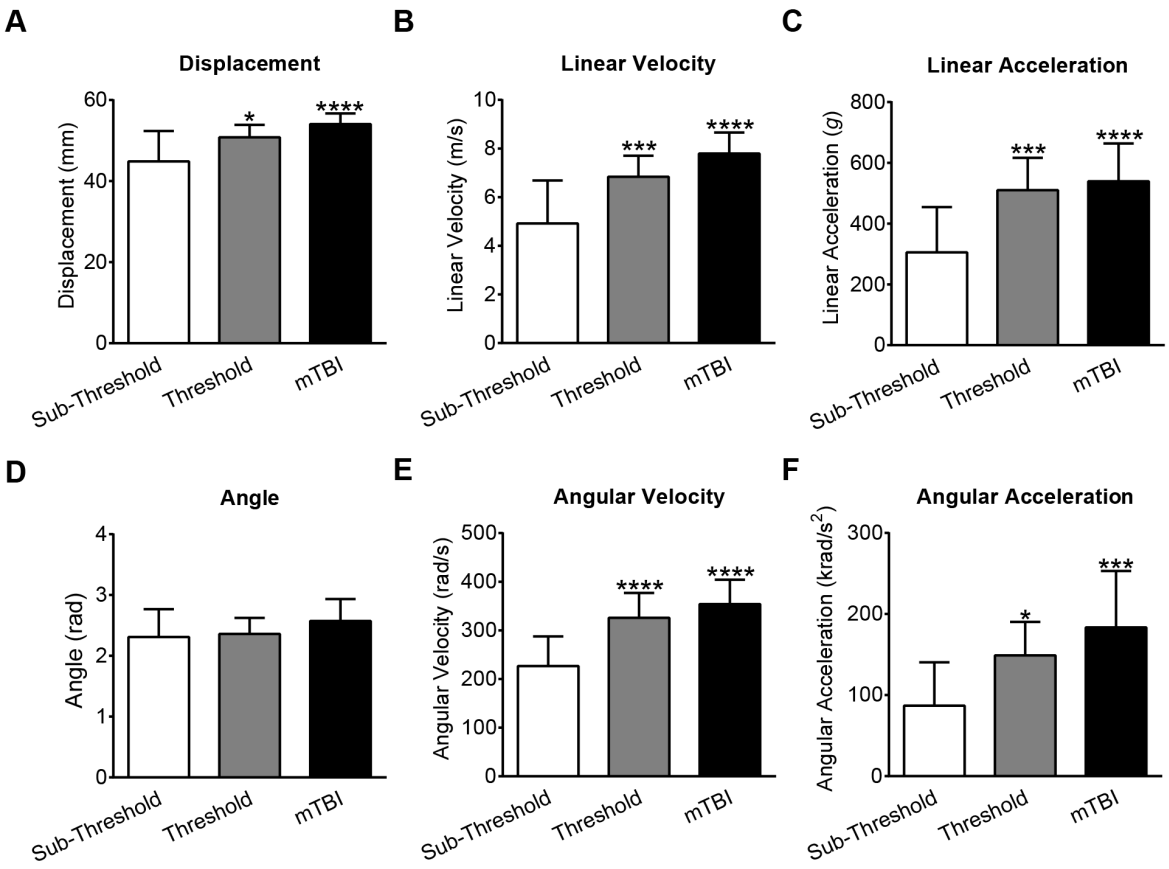

Figure 2.3 Head kinematics during CHIMERA TBI.

Head kinematics during single impact was assessed in mice subjected to single TBI of varying impact energies from 0.1 to 0.7J (N = 8-10/impact energy group), that were binned into categories reflecting subthreshold, threshold and mTBI groups. The graphs depict peak values of linear (A-C) and angular (D-F) head kinematic parameters over different impact energies. Data are presented as mean ± SD. Data were analyzed by one-way ANOVA followed by a Tukey post-hoc test. Asterisks (*) denote significant difference compared to the lowest energy group (i.e., sub-threshold).

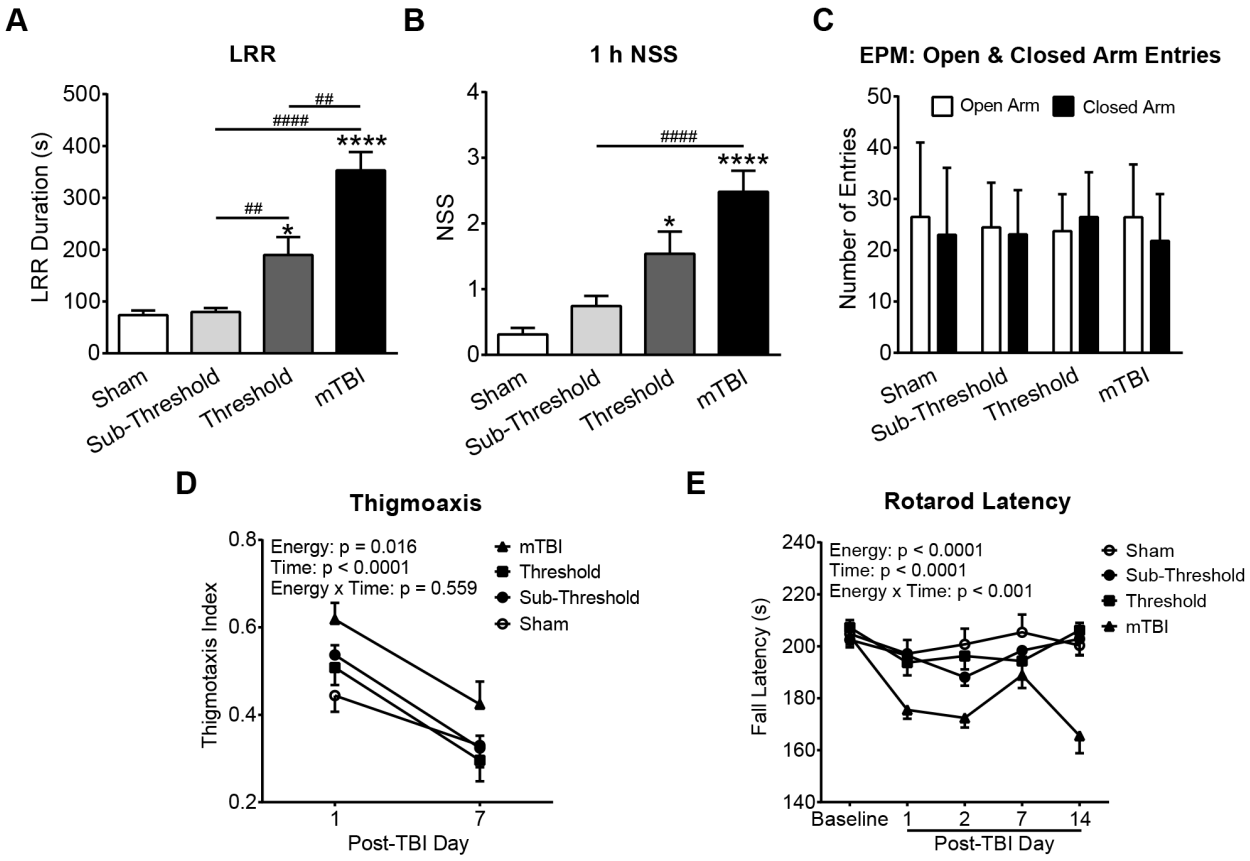

Figure 2.4 Behavior changes after single impact CHIMERA TBI.

(A) Loss of righting reflex (LRR) duration was assessed immediately after single impact. The graph depicts LRR duration over increasing impact energies. (B) Neurological severity score (NSS) was assessed at 1h following single TBI. The graph depicts total NSS value (out of 10) over increasing impact energies. (C, D) Anxiety-like behavior was assessed with elevated plus maze (EPM) at 2 d post-TBI (C) and open field thigmotaxis at 1 and 7 d post-TBI (D). Graphs in (C) and (D) show the time spent by mice from different injury categories in the open and closed arms of the EPM (C), or near the edge of the open field box (D), respectively. Graphs represent the thigmotaxis index of injury categories at 1d and 7d post-TBI. (E) Post-TBI motor performance was assessed with the accelerating rotarod task up to 14d. The graph depicts fall latencies of injury categories at baseline and at different post-TBI time points. LRR and 1h NSS

data are presented as mean ± SEM. All other data are presented as mean ± SD. LRR and NSS data were analyzed by one-way ANOVA on ranks. Rotarod and thigmotaxis data were analyzed by Linear Mixed Model. EPM data were analyzed by one-way ANOVA. For graphs A and B, Asterisks (*) denote significant difference compared to the sham. Hash (#) marks denote significant differences among the groups. For graphs in (A) and (B), * and #: $p < 0.05$, ** and ##: $p < 0.01$, ###: $p < 0.001$, **** and ####: $p < 0.0001$.

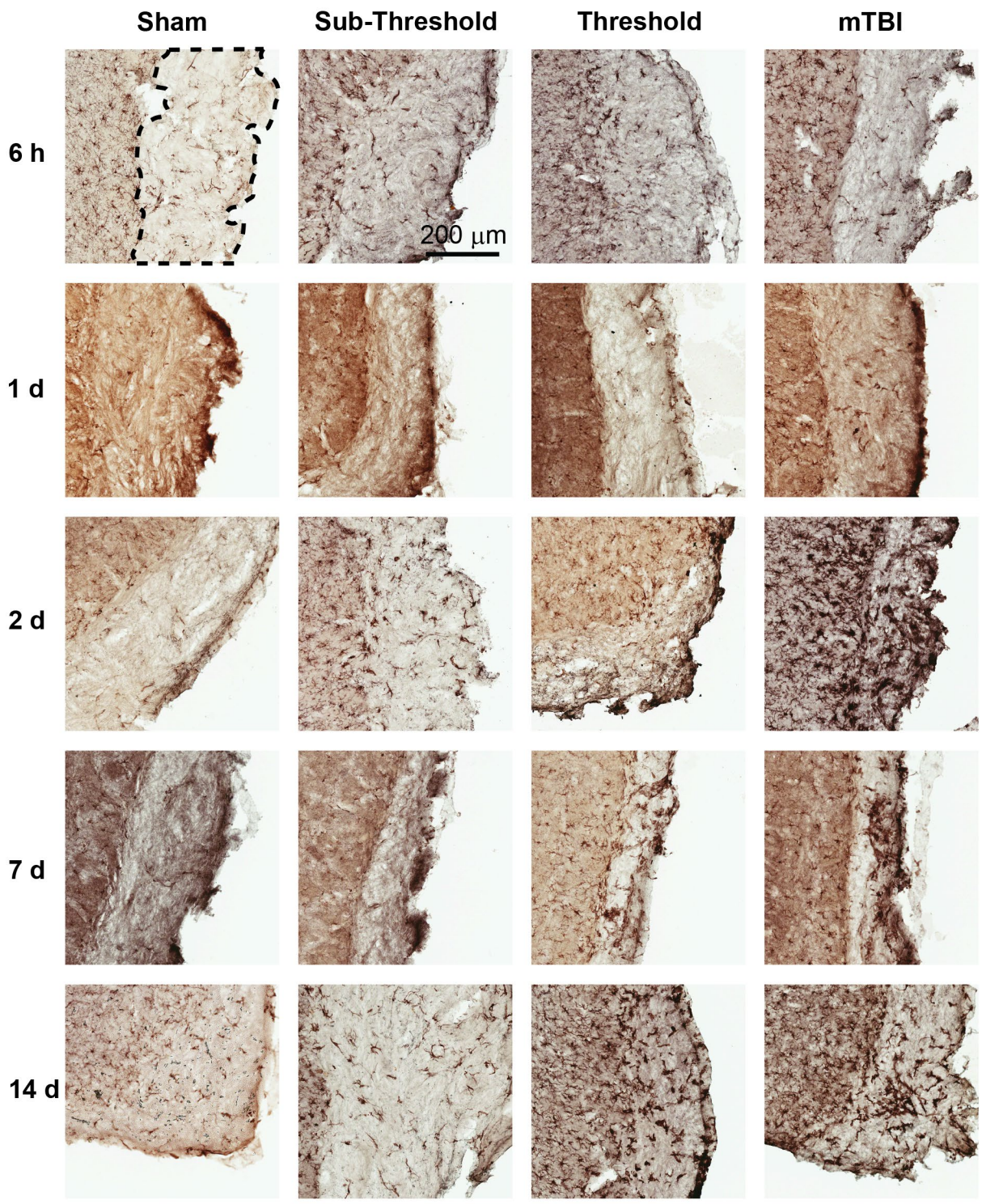

Figure 2.5 Microglial response in the olfactory nerve layer after single impact CHIMERA TBI.

Post-TBI microglial response was assessed using Iba1 immunohistochemistry, presented as representative 20x-magnified images showing the region of interest in the olfactory nerve layer outlined by dotted black lines in the top left corner panel. Energy groups are arranged in rows and time points are arranged in columns.

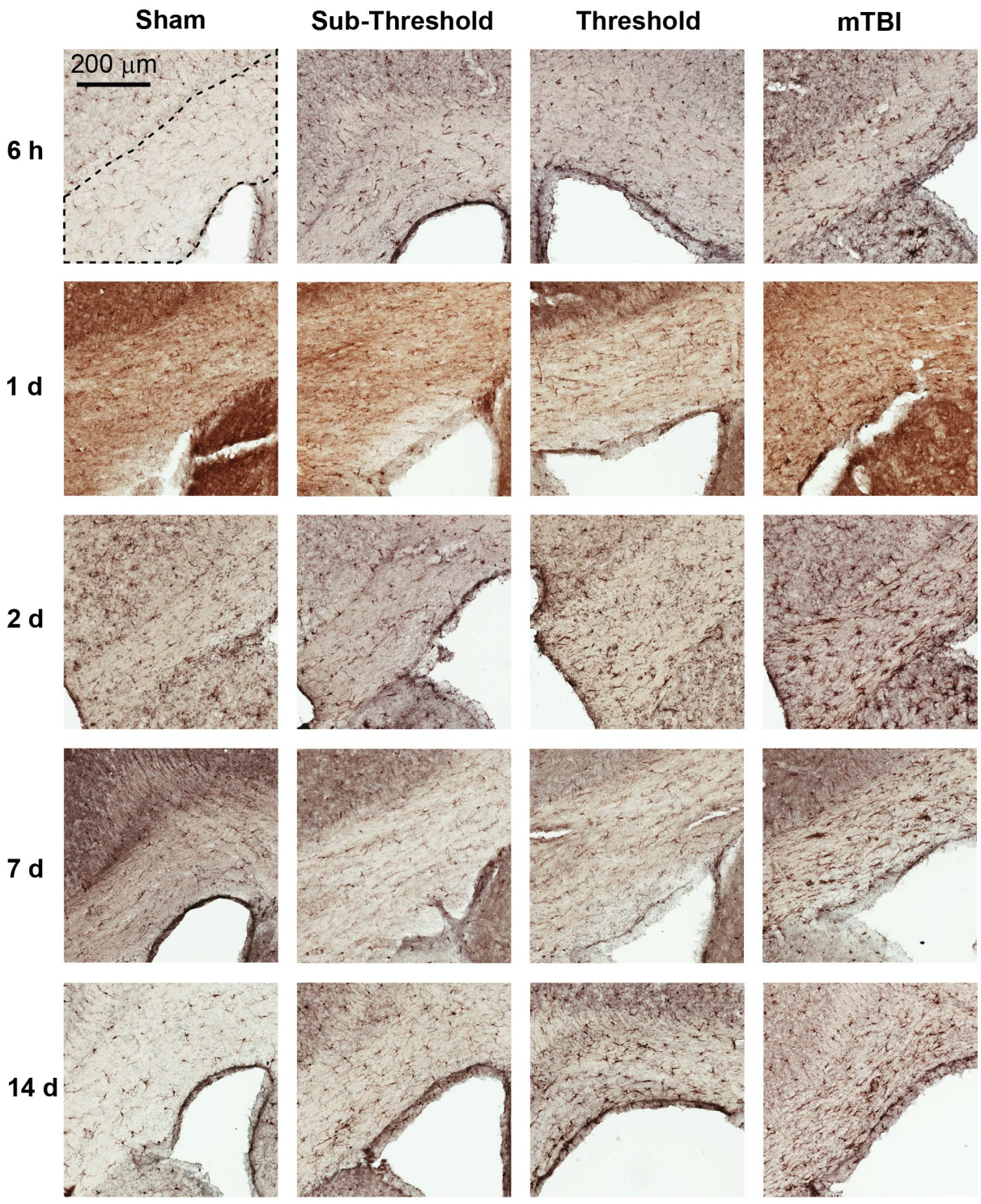

Figure 2.6 Microglial response in the corpus callosum after single impact CHIMERA TBI.

Post-TBI microglial response was assessed using Iba1 immunohistochemistry, presented as representative 20x-magnified images showing the region of interest in the corpus callosum outlined by dotted black lines in the top left corner panel. Energy groups are arranged in rows and time points are arranged in columns.

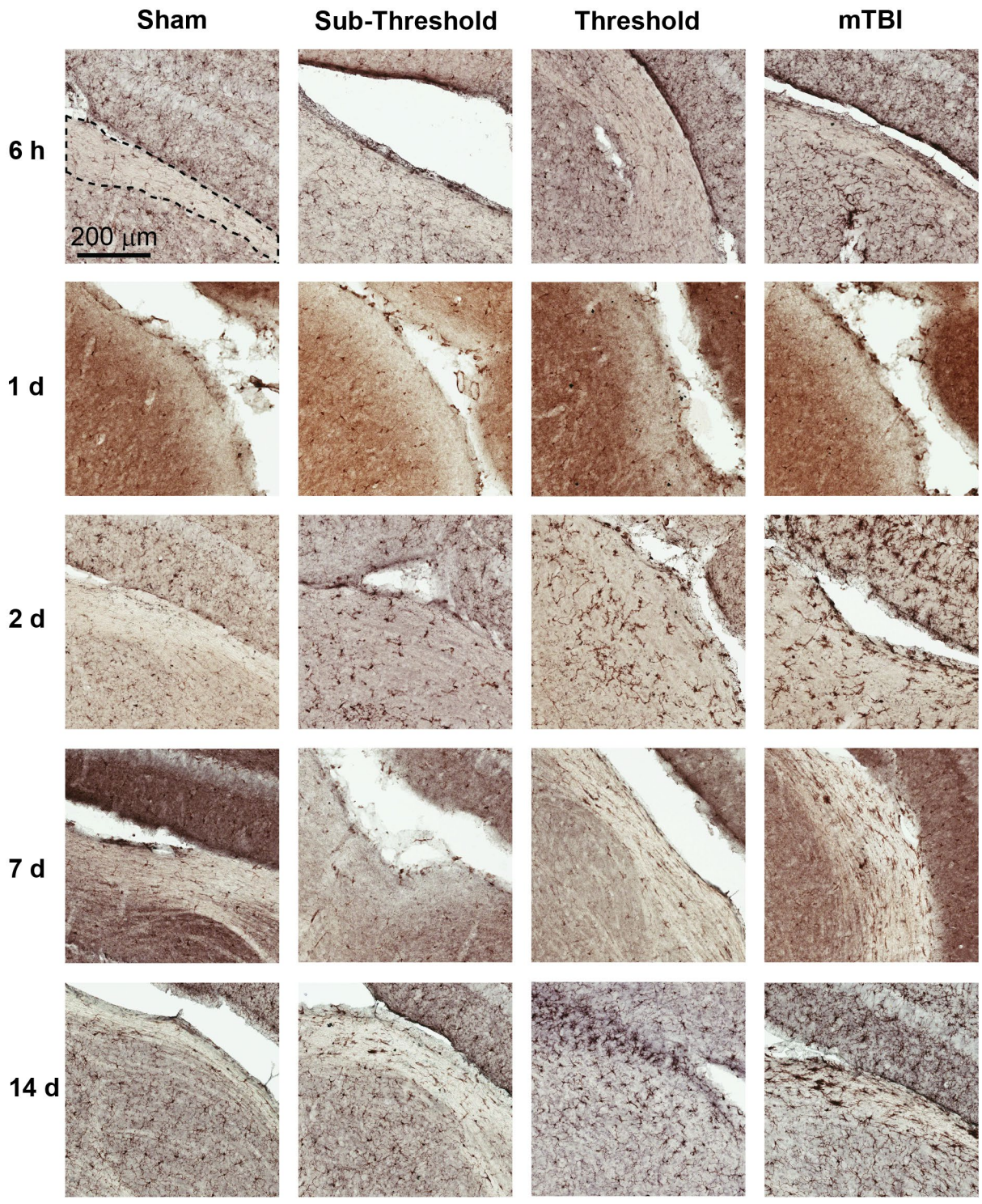

Figure 2.7 Microglial response in the superior colliculus after single impact CHIMERA TBI.

Post-TBI microglial response was assessed using Iba1 immunohistochemistry, presented as representative 20x-magnified images showing the region of interest in the superior colliculus outlined by dotted black lines in the top left corner panel. Energy groups are arranged in rows and time points are arranged in columns.

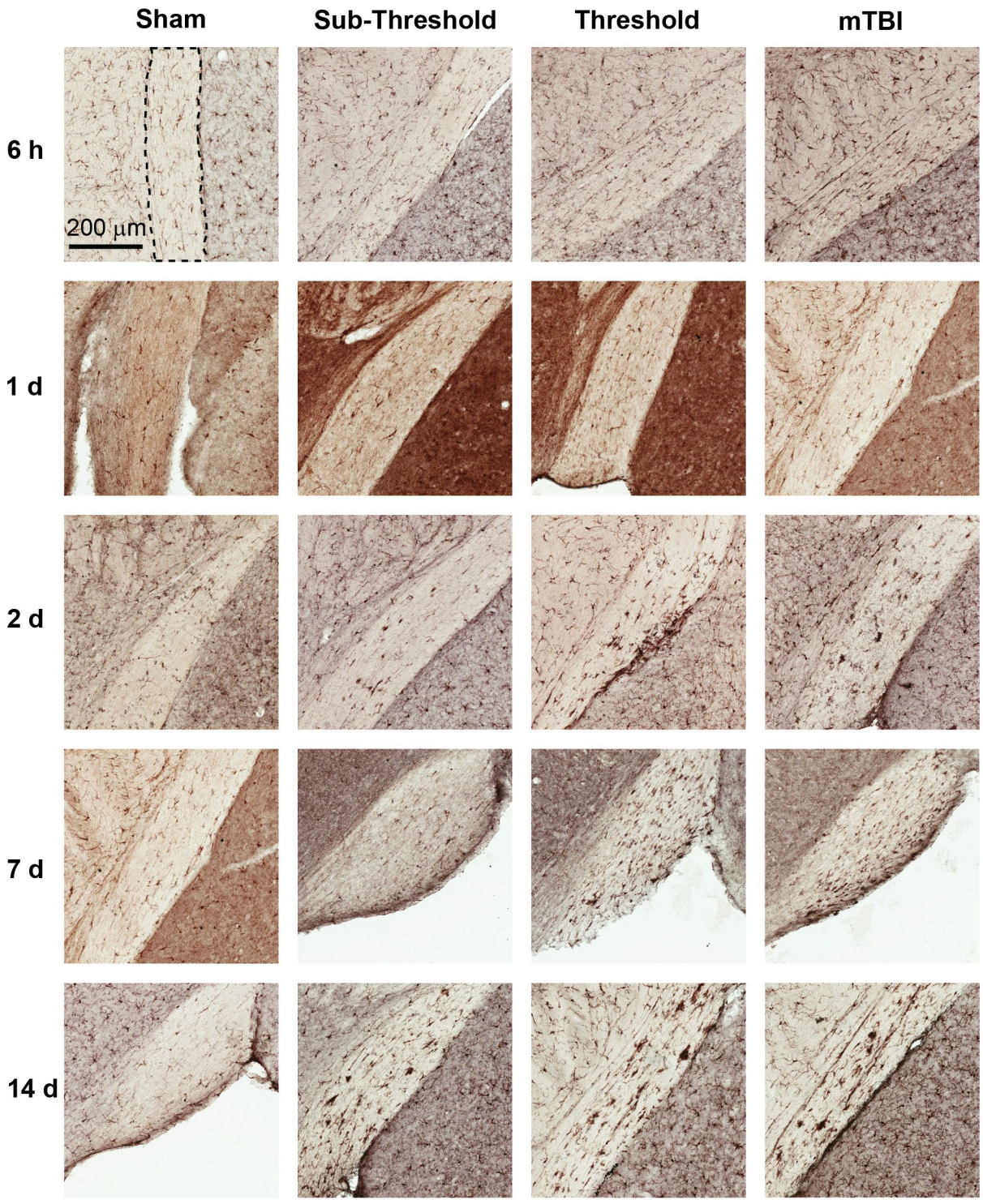

Figure 2.8 Microglial response in the optic tract after single impact CHIMERA TBI.

Microglia were assessed using Iba1 immunohistochemistry in tissue sections prepared from 6h to 14d after single CHIMERA TBI, presented as representative 20X-magnified images. The region of interest in the optic tract is outlined by dotted black lines in the image in the sham 6h panel (top left corner). Injury categories are arranged in rows and time points are arranged in columns.

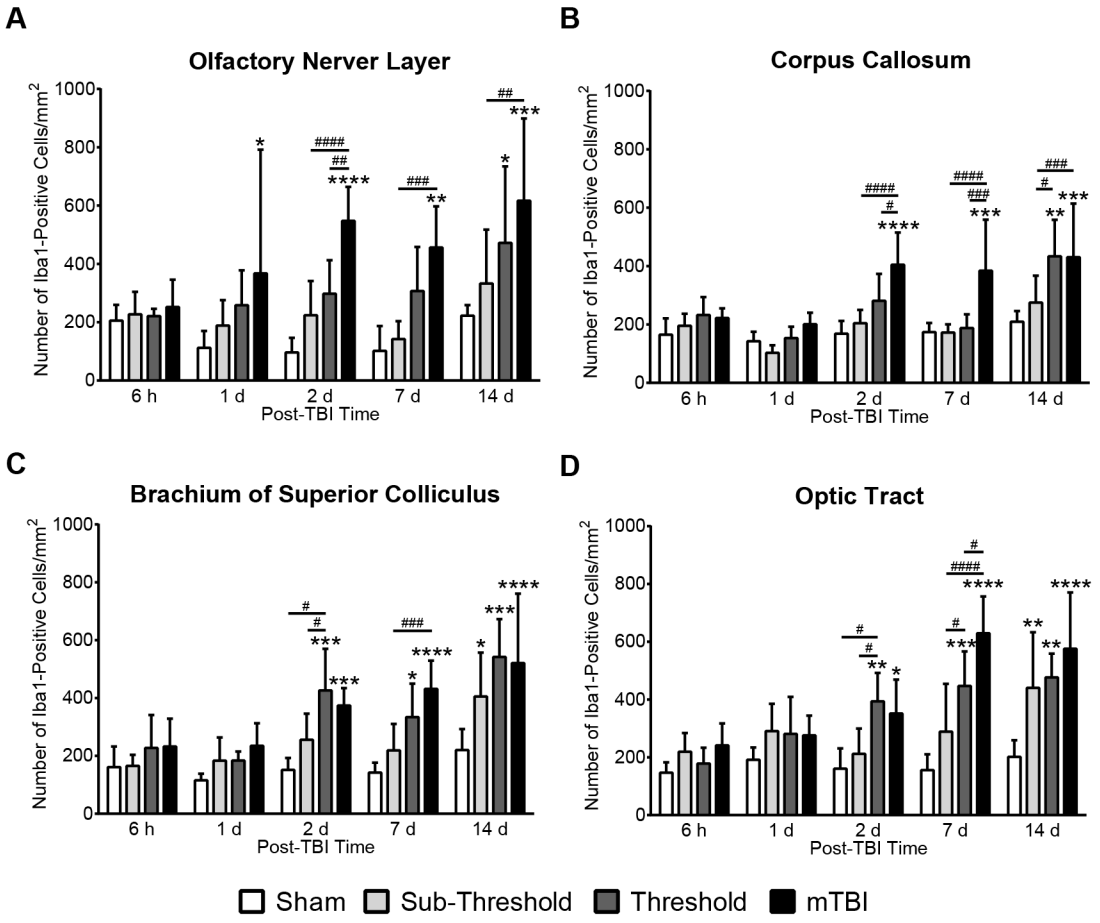

Figure 2.9 Quantification of the post-TBI microglial response to single impact CHIMERA TBI.

The post-TBI microglial response was quantified by counting the number of Iba1-positive cells in white matter regions of interest. Graphs depict the number of Iba1-positive cells over time in the olfactory nerve layer (A), corpus callosum (B), brachium of superior colliculus (C) and optic tract (D). For all graphs, data are presented as mean ± SD. Data were analyzed by two-way ANOVA followed by Tukey post-hoc test. * and #: $p < 0.05$, ** and ##: $p < 0.01$, *** and ###: $p < 0.001$, **** and ####: $p < 0.0001$.

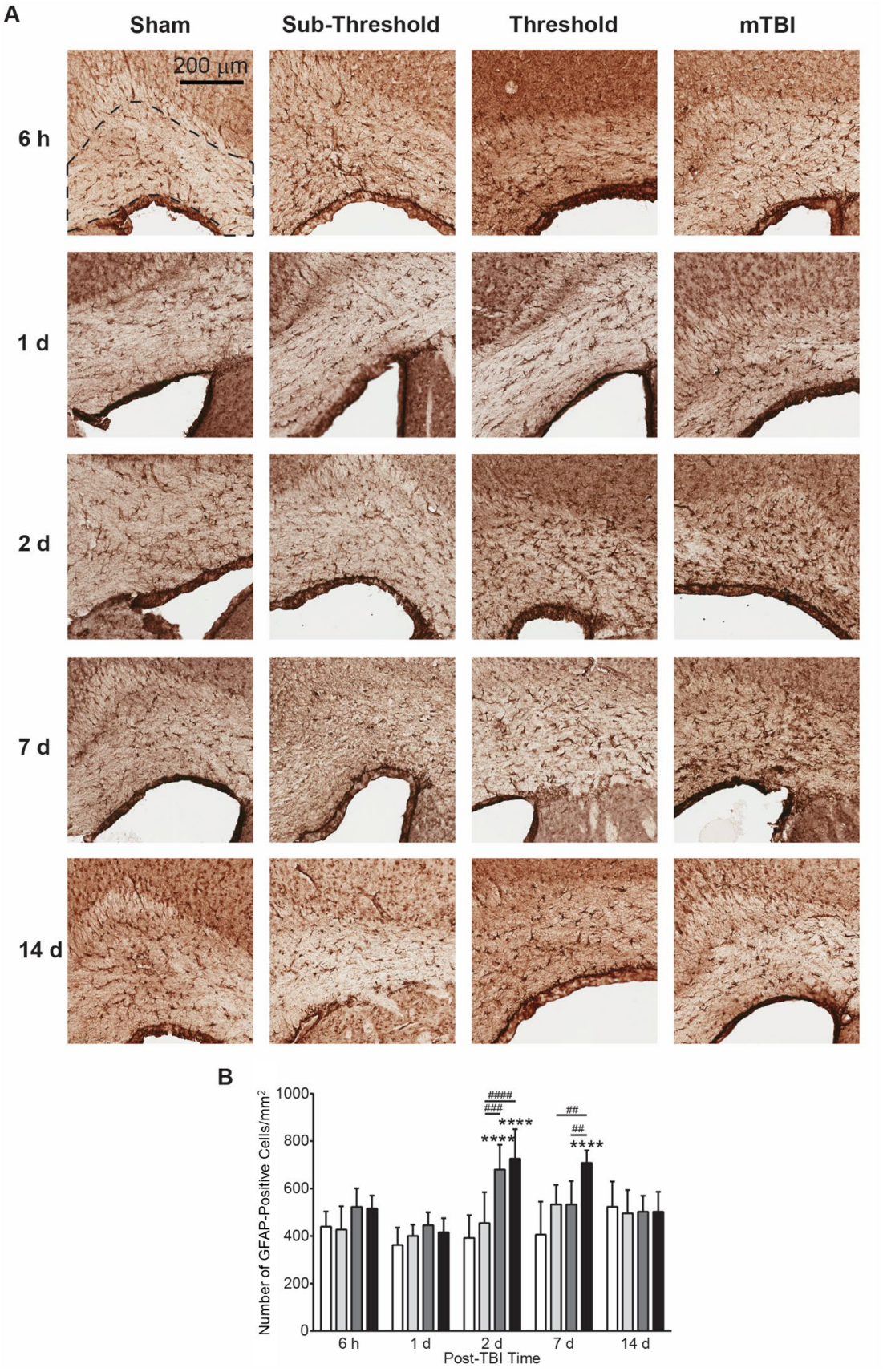
A
Sham
Sub-Threshold
Threshold
mTBI
200 μm
6 h
1 d
2 d
7 d
14 d
B
Number of GFAP-Positive Cells/mm2
1000
800
600
400
200
0
6 h
1 d
2 d
7 d
14 d
Post-TBI Time
####
###
****
****
##
##
****

Figure 2.10 Astrocyte activation in the corpus callosum after single impact CHIMERA TBI.

The post-TBI astrocyte response was assessed using GFAP immunohistochemistry on tissues prepared from 6h to 14d after single CHIMERA TBI. (A) Representative 20x-magnified images of the corpus callosum showing GFAP-positive astrocytes. Injury categories are arranged in rows and time points are arranged in columns. (B) The post-TBI astrocyte response was quantified by counting the number of GFAP-positive cells in the corpus callosum and depicted graphically over time. Data are presented as mean ± SD. Data were analyzed by two-way ANOVA followed by Tukey post-hoc test. * and #: $p < 0.05$, ** and ##: $p < 0.01$, *** and ###: $p < 0.001$, **** and ####: $p < 0.0001$.

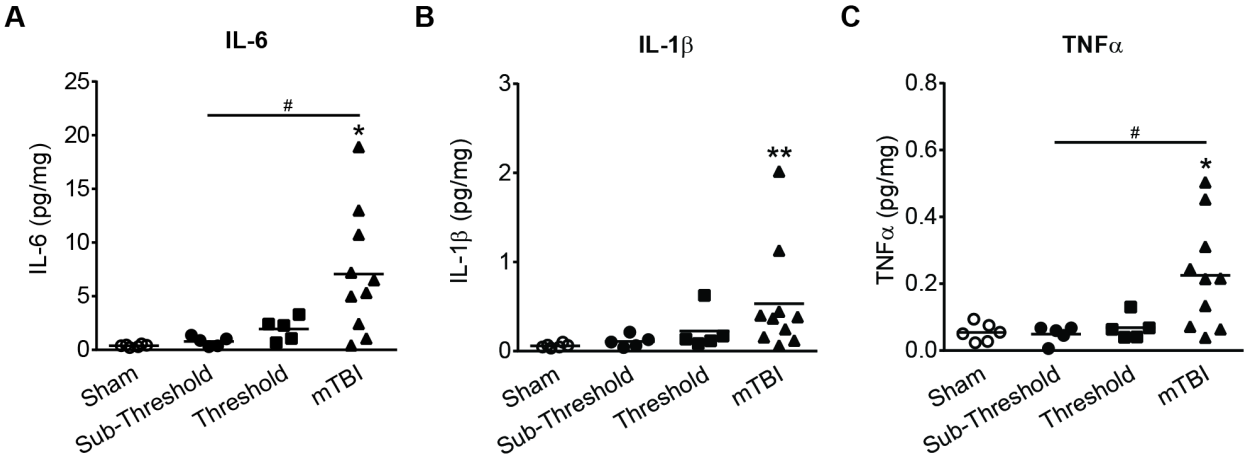

Figure 2.11 Quantification of levels of endogenous proinflammatory cytokines after single impact CHIMERA TBI.

Post-TBI levels of endogenous proinflammatory cytokines were quantified in half-brain lysates at 6 h post-TBI. Data were analyzed by one-way ANOVA followed by Tukey post-hoc test. * and #: $p < 0.05$, **: $p < 0.01$.

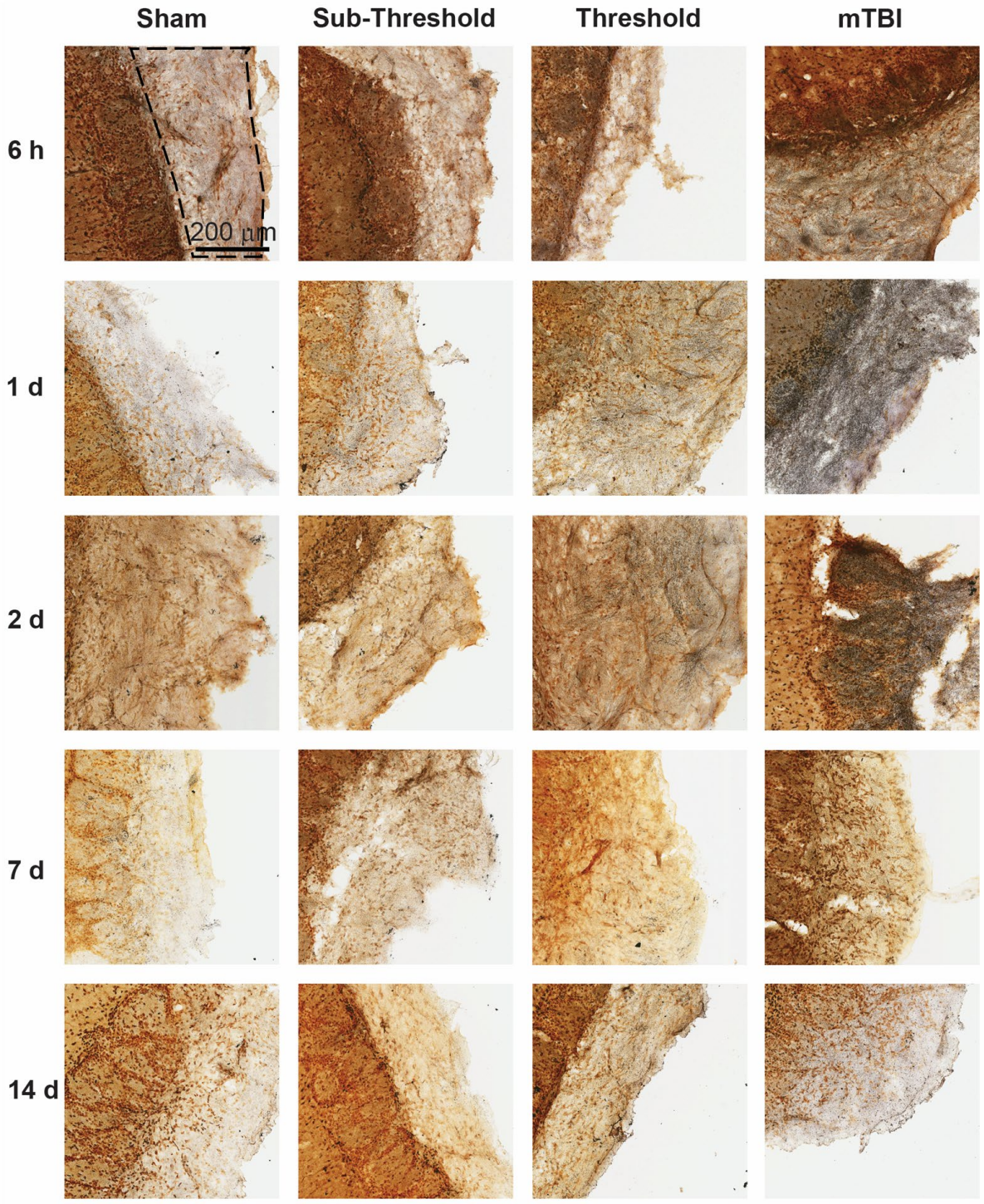

Figure 2.12 Post-TBI axonal pathology in the olfactory nerve layer.

Post-TBI axonal pathology in the olfactory nerve layer was assessed using silver staining, presented as representative 20x-magnified images. Energy groups are arranged in rows and time points are arranged in columns.

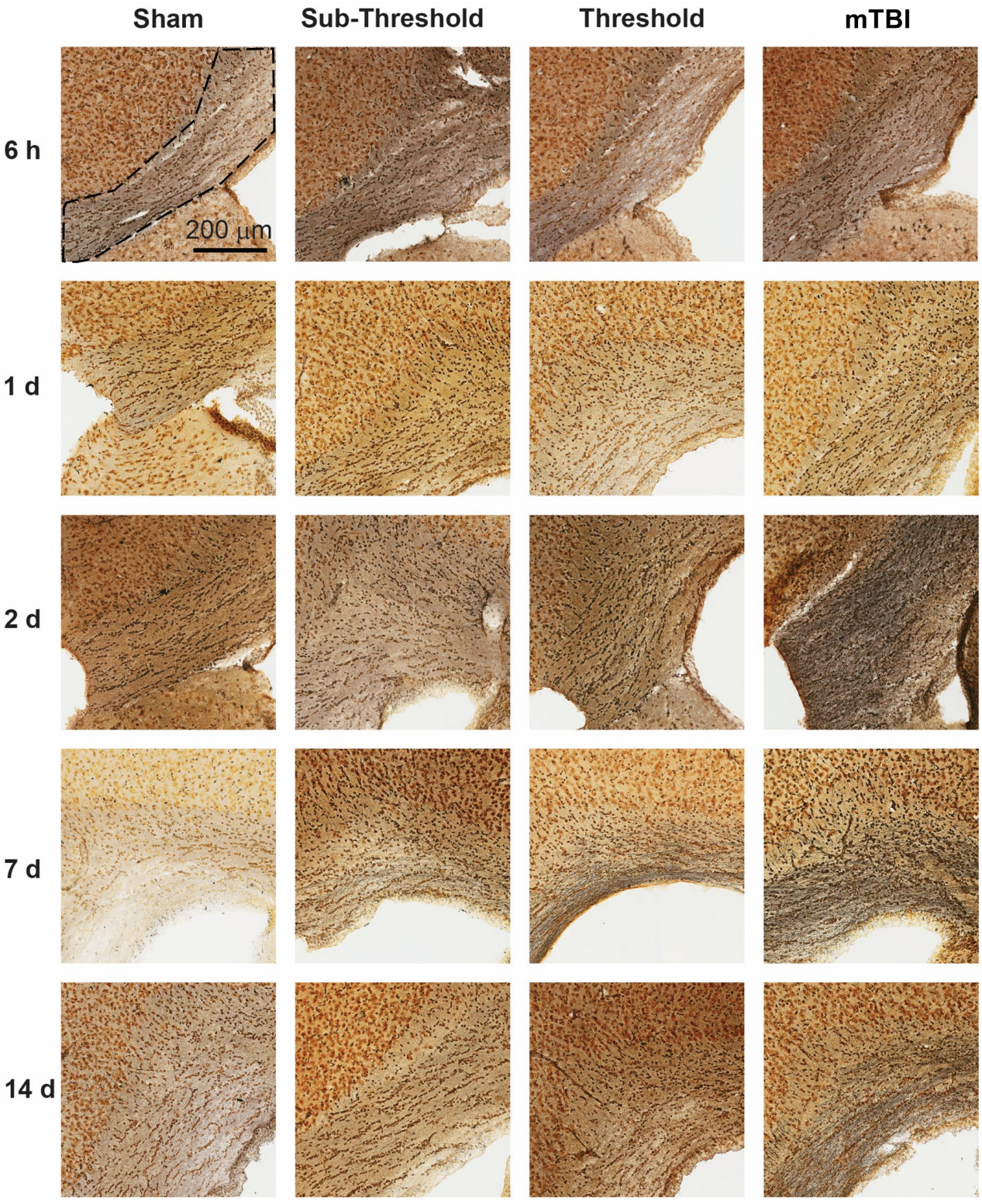
Sham
Sub-Threshold
Threshold
mTBI
6 h
1 d
2 d
7 d
14 d
200 µm

Figure 2.13 Post-TBI axonal pathology in the corpus callosum.

Post-TBI axonal pathology in the corpus callosum was assessed using silver staining, presented as representative 20x-magnified images. Energy groups are arranged in rows and time points are arranged in columns.

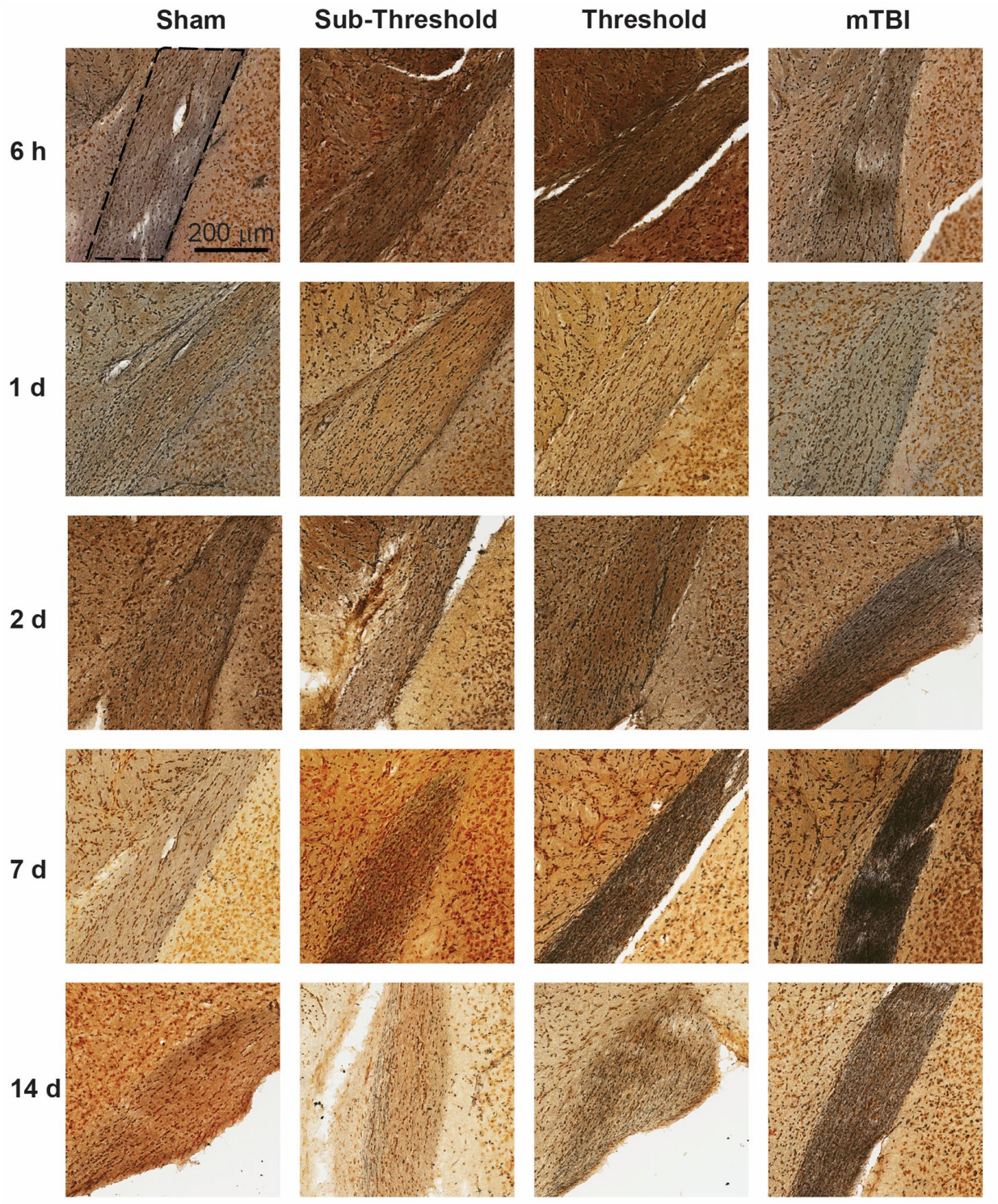

Figure 2.14 Axonal damage in the optic tract after single impact CHIMERA TBI.

Post-TBI axonal pathology was assessed using silver staining on tissues prepared from 6 h to 14 d after single CHIMERA TBI, presented as representative 20x-magnified images of the optic tract showing silver uptake. Injury categories are arranged in rows while time points are arranged in columns.

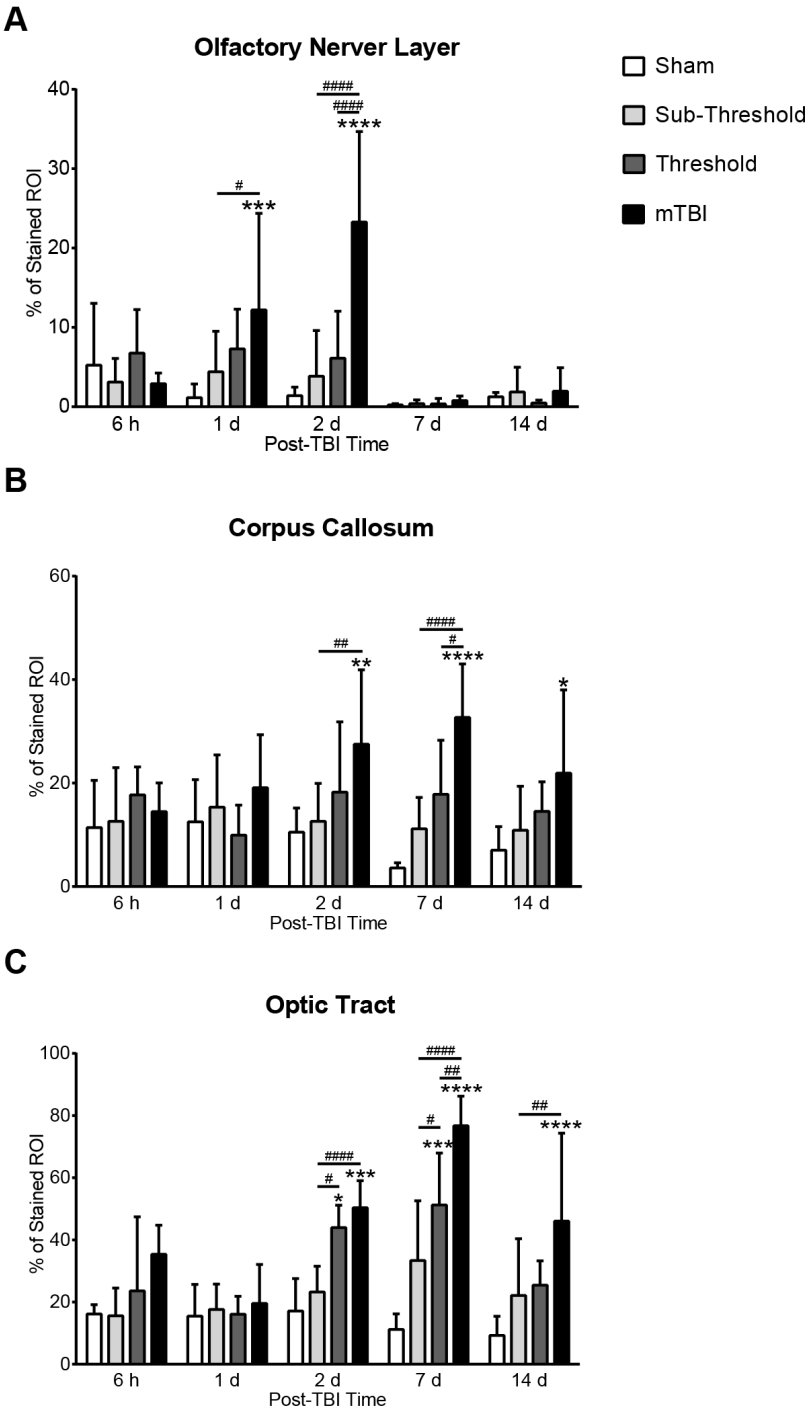

Figure 2.15 Quantitative analysis of axonal pathology after single impact CHIMERA TBI.

Silver stain images were quantified by calculating the % region of interest (ROI) in white matter areas that displayed silver uptake, including the olfactory nerve layer (A), corpus callosum (B)

and optic tract (C). Graphs depict mean ± SD % of the ROI showing in sham and injury categories over time. Data were analyzed by two-way ANOVA followed by Tukey post-hoc test. * and #: $p < 0.05$, ** and ##: $p < 0.01$, *** and ###: $p < 0.001$, **** and ####: $p < 0.0001$.

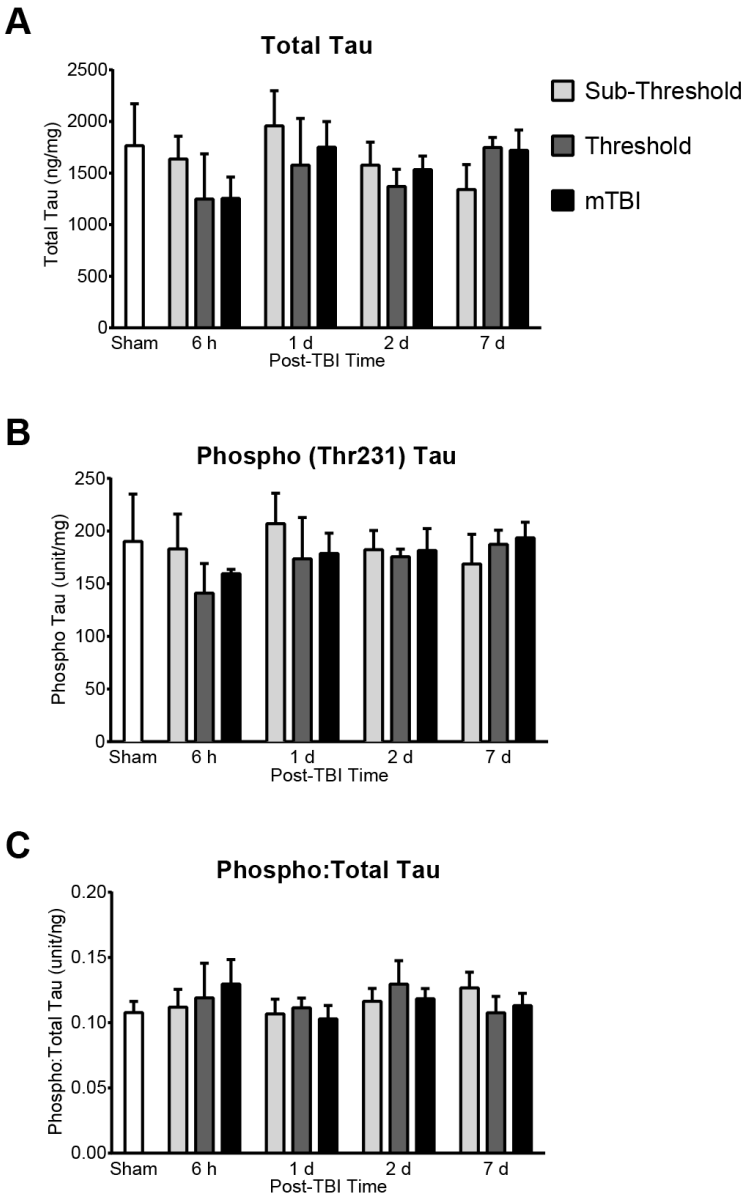

Figure 2.16 Quantification of endogenous tau levels.

Endogenous and phospho (Thr231) tau levels in half-brain homogenates were assessed with an MSD® MULTI-SPOT assay kit. Levels of total tau (A), phospho (Thr231) tau (B) Quantification of and ratio of phospho:total tau (C) are presented as Mean ± SD. Data were analyzed by two-way ANOVA.

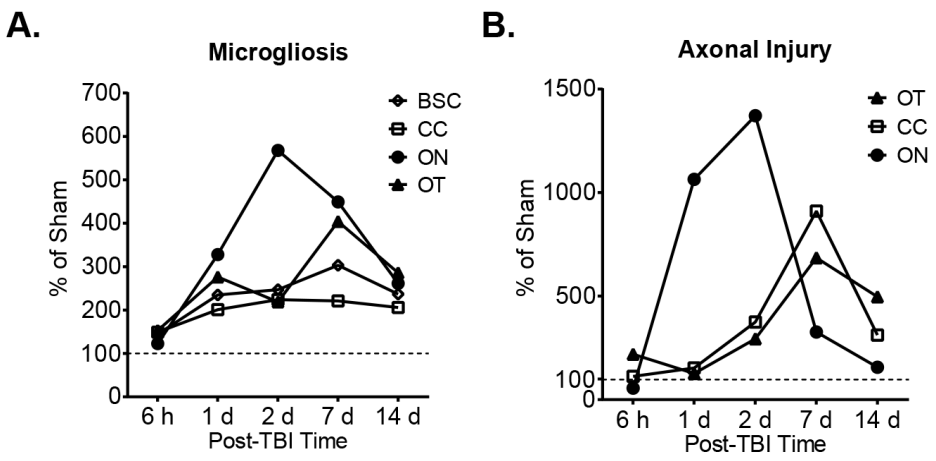

Figure 2.17 Temporal profile of microgliosis and axonal injury following single mTBI.

The graphs depict the temporal profiles of microgliosis (A) and axonal injury (B) in various white matter regions of the mTBI group over 6h to 14d post-TBI. Data are represented as percentage of sham values at the respective time points. BSC: Brachium of superior colliculus, CC: Corpus callosum, ON: Olfactory nerve layer, OT: Optic tract.

Table 2.1 Sample sizes for outcomes

The table details sample number for each post-TBI parameter at the respective post-TBI time point assessed in this study.

Parameter	Time Point	Sham	Sub-Threshold	Threshold	mTBI
Head Kinematics	During/immediately following head impact	-	27	11	18
Loss of Righting Reflex	Immediately following head impact	31	94	36	65
Neurological Severity Score	1 h	29	78	26	54
Elevated Plus Maze	2 d	8	22	11	23
Open Field Thigmotaxis	1 d	20	58	18	36
	7 d	11	34	12	21
Rotarod	1 d	17	58	21	43
	2 d	13	44	19	36
	7 d	10	32	11	20
	14 d	6	15	5	10

Microglial Quantification	6 h	5	14	6	7
	1 d	6	6	6	6
	2 d	6	15	5	9
	7 d	4	8	6	8
	14 d	4	7	4	10
Astrocyte Quantification	6 h	5	5	4	8
	1 d	5	6	5	8
	2 d	5	5	5	10
	7 d	3	9	3	6
	14 d	4	6	4	8
Silver Stain Quantification	6 h	4	13	5	9
	1 d	4	9	5	7
	2 d	5	11	5	8
	7 d	4	15	6	9
	14 d	4	7	5	9

Tau Biochemistry	6 h	2	9	3	6
	1 d	2	9	3	6
	2 d	2	9	3	6
	7 d	2	8	3	6
Cytokine Quantification	6 h	6	5	5	10

Table 2.2 Summary of correlation analyses.

The table summarizes the results of correlation analyses testing associations among linear and angular head kinematic parameters with post-TBI neurological and neuropathological outcomes. For each correlation pair, the respective coefficient of determination is presented in the upper row, while the corresponding *p* value is indicated in lower row. Significant correlations are highlighted in bold.

Post-TBI Outcome		**Linear Parameter**			**Angular Parameter**	
		Displacement	**Velocity**	**Acceleration**	**Velocity**	**Acceleration**
LRR	R^2	0.3400	0.3768	0.2931	0.3036	0.2773
	p	**< 0.0001**	**< 0.0001**	**< 0.0001**	**< 0.0001**	**< 0.0001**
NSS	R^2	0.1401	0.174	0.1347	0.2431	0.0578
	p	**0.0146**	**0.006**	**0.0168**	**0.0011**	0.1301
Iba1 Cell Count						
Olfactory Nerve Layer	R^2	0.5355	0.4231	0.2234	0.1290	0.0073
	p	**0.0006**	**0.0035**	0.0476	0.143	0.7368
Corpus Callosum	R^2	0.3941	0.3312	0.2176	0.0781	0.036
	p	**0.003**	**0.0079**	**0.0381**	0.2326	0.4509

Brachium of Superior Colliculus	R^2	0.1654	0.2487	0.2731	0.1119	0.0259
	p	0.0603	**0.0181**	**0.0126**	0.1281	0.498
Optic Tract	R^2	0.2311	0.436	0.4004	0.1611	0.0000432
	p	**0.0235**	**0.0008**	**0.0016**	0.064	0.9781
Silver Stain % ROI						
Olfactory Nerve Layer	R^2	0.3275	0.3085	0.0158	0.0265	0.002
	p	0.0067	0.009	0.5875	0.4812	0.8533
Corpus Callosum	R^2	0.4563	0.5034	0.1516	0.1103	0.0183
	p	0.0004	0.0002	0.0663	0.1216	0.5591
Optic Tract	R^2	0.541	0.6787	0.3336	0.0159	-0.0588
	p	**0.0001**	**<0.0001**	**0.0061**	0.5866	0.2898

Chapter 3: Increased severity of the CHIMERA TBI model induces acute vascular injury, deficits in memory recall, and chronic white matter inflammation

3.1 Introduction

As described in Chapter 2, we have shown that CHIMERA TBI (up to 0.7J) induces pathologies associated with mild injuries, characterized by mild neurological deficits, white matter injury and microgliosis in a dose-dependent manner. However, impact energies greater than 0.7J lead to skull fracture in >50% of our animals, which presents an ethical and practical concern. As results using CHIMERA show that white matter damage can be induced without any detectable alteration of BBB integrity as assessed by serum albumin extravasation, here we aim to induce injuries that cause cerebrovascular damage and more extensive neurological impairment, thereby mimicking a more severe injury. To impact the murine skull with greater kinetic energy, we developed physical interfaces that would enable vascular injury and grey matter inflammation without causing skull fracture, whilst increasing linear and rotational velocity and acceleration. We hypothesized that increasing impact energy, thereby increasing head kinematic parameters, will elicit breach of blood-brain barrier (BBB) integrity, along with greater neurological impairments, increases in glial proliferation and recruitment, and increases in plasma biomarkers of interest.

The overall purpose of this study was to expand CHIMERA capacity to induce more severe injuries, including vascular and grey matter inflammation without fracturing the skull. In doing

so, we expanded the functionality of the CHIMERA platform beyond inducing diffuse axonal injury, verifying the platform's ability to be used for modelling vascular injury and laying the foundation for CHIMERA to be finetuned to elicit specific TBI endophenotypes that may be of interest in preclinical therapeutic studies.

3.2 Methods

3.2.1 Pilot study

3.2.1.1 Cadaver pilot

Head kinematic analyses were performed on cadaveric animals (n=10-12/group) to determine if interfaced impacts at 2.5J (10.002 m/s) would elicit greater head motion than un-interfaced hits at 0.7J (5.29 m/s). Data were extracted from a novel murine head kinematics tracking system, which consisted of a 3D-printed polylactic acid (PLA) marker carrier fixed rigidly to the upper jaw and incisors with an elastic strap around the snout. Impact videos were recorded using a Phantom V12 high-speed camera (Vision Research® Inc., Wayne, NJ). To ensure that no relative motion between the head and marker would occur, the head marker was glued to the upper incisors with cyanoacrylate (Gorilla® Super Glue, Gorilla Glue Company, Cincinnati OH).

Kinematic analysis of high-speed video was performed using ProAnalyst Motion Analysis Software (Xcitex, Woburn, MA). Velocities were determined by numerically differentiating the head marker position and angle data and accelerations from a second differentiation of the same data. All linear and angular kinematic parameters were filtered using a fifth-order low pass Butterworth filter with a cut-off frequency of 500Hz as determined from frequency analysis of

the raw data. The peak velocities and acceleration values we report here were defined as the maximum value achieved throughout the course of the impact.

3.2.1.2 Live pilot

3.2.1.2.1 CHIMERA TBI procedure

All animal procedures were approved by the University of British Columbia Committee on Animal Care (protocol A15-0096) and were performed in strict compliance with the Canadian Council on Animal Care guidelines. Subjects were male and female wildtype-C57Bl/6 mice aged five-seven months (N=8 male, N=10 female). We planned to have 8 sham and 10 TBI animals for analyses (sham = 3M, 5F; TBI = 5M, 5F), however, two animals (2M) died immediately following impact (see Results). Animals were housed with a reversed 12h light:dark cycle. Animals were prepared for single TBI in the sagittal plane using CHIMERA as described (Namjoshi et al., 2014). Briefly, mice were anesthetized with isoflurane (induction: 5%, maintenance: 2-4% in oxygen 0.8 L/min) during the procedure. Anesthesia was maintained through the nose cone until head impact such that the duration of anesthesia delivery was between 5 and 6 minutes. After mice were positioned on the CHIMERA impactor, meloxicam (1 mg/kg) and saline (10 ml/kg) were administered via subcutaneous injection for pain control and hydration, respectively. Lubricating eye ointment was applied to prevent corneal drying. TBI animals received a single closed-head impact at 2.5J using a 50-g stainless steel piston and the 3D-printed PLA interface. Piston velocities were obtained using photogate sensors on the CHIMERA device. Sham animals received equivalent isoflurane exposure as TBI animals, along with meloxicam and saline, but experienced no impact.

3.2.1.2.2 Loss of righting reflex latency

Loss of righting reflex (LRR) latency was measured from the time of impact, or cessation of isoflurane for sham animals, until the animal became ambulatory in the recovery cage.

3.2.1.2.3 Euthanasia and tissue collection

Brains were collected at 6h post-TBI. Animals were anesthetized with ketamine (150 mg/kg) and xylazine (20 mg/kg). Once a surgical plane of anesthesia was reached, cardiac puncture was performed and whole blood samples were kept on ice in EDTA-lined tubes until centrifugation at 3000g for 10 minutes (RT). After cardiac puncture, 50% of the animals were perfused with ice-cold heparinized phosphate-buffered saline (PBS). The other 50% were not perfused. Brains were rapidly collected, longitudinally bisected and hemibrains were processed for histology.

3.2.1.2.4 Plasma biochemistry

Plasma tau and NF-L levels were measured in EDTA-plasma using the Discovery Mouse Tau Assay (cat no. 102209) and NF-L Advantage Assay (cat no. 102258, Quanterix Corporation) on the Simoa HD-1 Analyzer according to the manufacturer's protocol. Samples were run in singlicate and manually diluted 10x offboard.

3.2.1.2.5 Immunohistochemical staining, imaging, and quantification

Mouse hemibrains were post-fixed in 4% PFA for 2d, then cryoprotected with 30% sucrose in PBS and 0.01% sodium azide for 3-4d, after which 40 μm-thick coronal sections were prepared using a cryotome (Leica Biosystems, Concord, ON). Immunohistochemistry for immunoglobulin G (IgG) to detect blood extravasation was performed on free-floating sections. Briefly, sections

for IgG were washed in PBS and 0.5% Tween-20 for permeabilization, then blocked with 5% normal goat serum (NGS; Millipore Sigma S26-100ML) for 1h at room temperature (RT). Sections were incubated with a pre-conjugated Alexa-Fluor 594 goat anti-mouse IgG antibody (Abcam ab150116, 1:250) for two overnights at 4°C, then mounted. For nuclear co-stain, mounted sections were coverslipped with ProLong Gold Antifade Mountant with 4′,6-diamidino-2-phenylindole (DAPI) (Invitrogen P36935). Histology was performed on both perfused and un-perfused tissue.

Entire coronal sections were imaged using a Zeiss AxioScan Z1 slide scanner at 20x magnification. The anterior commissure size and position relative to the corpus callosum and dorsal/anterior hippocampus were used as anatomical landmarks for consistent coronal section selection. Image quantification was performed using Image J (NIH).

After cortical ROIs were manually isolated, an ImageJ macro script was written to binarize, threshold and convert the images to masks. Subsequently, % area was measured. Comparative quantification was performed such that data from perfused TBI animals were converted into fold change relative to perfused sham animals and data from unperfused TBI animals were converted into fold change relative to unperfused shams.

3.2.1.2.6 Electron microscopy tissue preparation and imaging

Animals were anesthetized with as described above, then perfused with ice-cold heparinized PBS followed by a fixative solution containing 2.5% glutaraldehyde and 2.0% paraformaldehyde in 0.1M sodium cacodylate buffer. Whole brain tissue was then placed in a vial containing the

glutaraldehyde-paraformaldehyde fixative solution overnight at 4ºC. A mouse brain matrix was used to section tissue into 1 mm coronal slices. Cortical regions were identified and isolated into blocks using a dissecting microscope. Tissue blocks were then immersed in the glutaraldehyde-paraformaldehyde fixative solution overnight at 4ºC. After subsequent buffer washes, samples were post-fixed in 2.0% osmium tetroxide for 1 h at RT and rinsed in distilled H_2O prior to *en bloc* staining with 2% uranyl acetate. After dehydration through a graded ethanol series, the tissue was infiltrated and embedded in EMbed-812 (Electron Microscopy Sciences, Fort Washington, PA). Thin sections were stained with uranyl acetate and lead citrate.

Low magnification (40x) images were acquired on a Leica DMi1 microscope with an AmScope MU500 digital camera and AmLite Image Capture Software v3.7. For EM image acquisition at 15,000-25,000x, sections were examined with a JEOL 1010 electron microscope fitted with a Hamamatsu digital camera and AMT Advantage image capture software.

3.2.2 Behavioral study

Upon completion of the pilot study, we proceeded with a behavioral study to elucidate the acute and chronic behavioral and neuropathological effects of single moderate-severe CHIMERA TBI. Subjects were wild-type C57Bl/6 male mice aged five-seven months (n=9-10/group/time-point, randomly assigned to sham or TBI groups). End-points for this study were 6h, 2d, 14d, 30d, and 60d post-TBI. The TBI procedure remained unchanged for the behavioral study, with TBI animals receiving a single closed-head impact at 2.5J using a 50-g stainless steel piston and the 3D-printed PLA interface while anesthetized. Sham animals received equivalent exposure to isoflurane as well as analgesia and positioning on the CHIMERA device.

3.2.2.1 Behavioral analyses

Behavioral analyses were performed as described (Namjoshi et al., 2017). Neurological impairment was assessed using the neurological severity score (NSS) at 1h and 2d post-TBI.

3.2.2.1.1 Barnes maze

To assess spatial learning, memory and cognitive flexibility, we used Barnes maze (BM). BM was purchased from Stoelting (Wood Dale, IL, USA). Acquisition trials of 90s were conducted on D14, D15, D16, D17, and D18 post-injury for 30d animals and on D55, D56, D57, and D58 for 60d animals; 30s probe trials were conducted on D19 and D29 for 30d animals and on D59 for 60d animals. Reverse trials of 90s were conducted the day after each probe trial, prior to sacrifice.

3.2.2.1.2 Forced swim test

The forced swim test (FST) was used to assess depressive-like states. Mice were placed into an inescapable transparent tank (30 cm height x 20 cm diameter) filled with 15 cm of water (23-25°C) and measuring their escape-related mobility. Testing consisted of slowly and gently placing one mouse into the tank of water. Once in the water, the test length for FST was five minutes. Mice were monitored for diving during testing and their performance videotaped. Latency to immobility as well as duration of immobility during the last two minutes of the testing period was measured, as mice that remain immobile for longer periods of time are considered to be more depressed compared to mice that remain mobile. Upon completion of

testing, the mouse was removed and dried gently using paper towels and a heat lamp. After 5 minutes, the animal was returned to its home cage.

3.2.2.2 Ex vivo electrophysiology

Hippocampal field recordings were carried out in a separate cohort of mice to assess functional changes in the pre- and post-synapse at 6h and 14d post TBI. After rapid decapitation, slices (300 μm thick) were prepared on a vibratome, then held and perfused with room temperature artificial cerebrospinal fluid (ACSF) containing (in mM): 125 NaCl, 2.5 KCl, 25 $NaHCO_3$, 1.25 NaH_2PO_4, 2 $MgCl_2$, 2 $CaCl_2$, 10 glucose, pH 7.3–7.4, 300–310 mOsm). Slices were visualized on an Olympus BX51 microscope (4x objective). Structural morphology and location within the dentate gyrus of the hippocampus were identified. A bipolar stimulating electrode was placed in the Schaffer collaterals to deliver input stimuli. A borosilicate glass recording electrode filled with ACSF was positioned in the stratum radiatum of CA1, approximately 200-300 μm from the stimulating electrode. Both electrodes were placed 50–150 μm beneath the slice surface. Data were acquired by Multiclamp 700B amplifier digitized at 10 kHz, filtered at 2 kHz and analyzed in Clampfit10 (Molecular Devices). Stimulus intensities will be set to produce ~60–70% maximum amplitude response for paired-pulses (20–140 ms inter-pulse intervals).

3.2.2.3 Euthanasia and tissue collection

Brains were collected at 6h, 2d, 14d, 30d, and 60d post-TBI as described above. Briefly, animals were anesthetized with ketamine (150 mg/kg) and xylazine (20 mg/kg). After cardiac puncture, all animals were perfused with ice-cold heparinized phosphate-buffered saline (PBS). Brains

were rapidly collected, longitudinally bisected and hemibrains were processed for biochemistry and histology.

3.2.2.4 Brain biochemistry

Unfixed hemibrains were homogenized in 8-volumes of ice-cold radioimmunoprecipitation assay (RIPA) lysis buffer containing protease and phosphatase inhibitor cocktails (Roche, Branford, CT) and centrifuged at 9,000 rpm for 10min at 4°C. The supernatant was extracted and frozen at -80°C until analyzed. Total protein concentration was measured by bicinchoninic acid (BCA) assay (Biorad, Redmond, WA). Half-brain homogenates were diluted 1:2 in dilution buffer provided in the assay kit and incubated overnight (4°C) in a multiplex ELISA to measure IL-1β, IL-6, and TNF-α (V-PLEX Custom Mouse Cytokine kit K152A0H-1, Mesoscale Diagnostics). Levels of total and phosphorylated (Thr231) tau were measured on samples diluted 1:50 using an MSD® MULTI-SPOT assay (K15121D-1, Meso Scale Discovery, Rockville, MD) following the manufacturer's protocol. Cytokine and tau plates were read on a microplate reader (Mesoscale Sector Imager).

3.2.2.5 Immunohistochemical staining, imaging, and quantification

Mouse hemibrains were post-fixed in 4% PFA for 2d, then cryoprotected with 30% sucrose in PBS and 0.01% sodium azide for 3-4d, after which 40 μm-thick coronal sections were prepared using a cryotome (Leica Biosystems, Concord, ON). Immunohistochemistry was performed on free-floating sections and included staining for Iba1 to detect microglia, glial fibrillary acidic protein (GFAP) to detect astrocytes, and silver staining to detect degenerating, argyrophilic axons. Sections stained for Iba1 followed a 3,3' Diaminobenzidine (DAB) staining protocol.

Briefly, sections were quenched with hydrogen peroxide for 10 min and blocked with 5% NGS in PBS for 1h at RT. Sections were incubated with primary antibodies (Wako 019-19741, 1:1000) overnight at 4°C. Sections were then incubated with a biotin-conjugated secondary antibody (1:1000) and detected using a colorimetric procedure by incubating with ABC reagent (Vector Labs PK-6100, 1:400) before color development with DAB (Sigma D5637-1G). Sections stained GFAP followed an immunofluorescent protocol. Briefly, sections for GFAP were washed in PBS and 0.5% Tween-20 for permeabilization, then blocked with 5% NGS for 1h at RT. Sections were then incubated with primary antibody for GFAP (eBioscience 53-9892-80, 1:400) overnight at 4°C. After washing, sections were mounted, then coverslipped with ProLong Gold Antifade Mountant with 4′,6-diamidino-2-phenylindole (DAPI) (Invitrogen P36935). Axonal injury was histologically evaluated by Neurosilver staining (FD Neurotechnologies) following the manufacturer's instructions.

Entire coronal sections stained for GFAP and Silver were imaged using a Zeiss AxioScan Z1 slide scanner at 20x magnification, while Iba1 sections were imaged using a Zeiss Axio Light Microscope at 10x magnification. For Iba1, GFAP, and silver quantification in grey and white matter regions, images were quantified by manually isolating ROIs, thresholding and reporting the percentage area (% Area) containing signal relative to the grey or white matter total area.

3.2.3 Data analysis and statistics

All statistical analyses were conducted on GraphPad Prism (v6.07).

3.2.3.1 Pilot study

Head kinematic results were normally distributed and were analyzed by student's t-test. Loss of righting reflex latency, plasma biomarkers, and IgG extravasation were analyzed by Mann-Whitney U tests as the data were non-parametric; these data were also transformed to a log scale to improve normality.

3.2.3.2 Behavioral study

NSS, BM acquisition, reverse, and 30d probe trials, as well as electrophysiological data were analyzed by two-way ANOVA followed by Holm-Sidak post-hoc test. 60d probe data were analyzed by student's t-test. Forced swim test data were analyzed by Mann-Whitney U tests. Brain cytokines were analyzed Kruskal-Wallis non-parametric test, followed by Dunn's post-hoc test. Tau, Iba1, GFAP, and silver data were analyzed by one-way ANOVA followed by Holm-Sidak post-hoc test. For correlational analyses, two-tailed parametric Pearson coefficients with a 95% confidence interval were utilized where r values were calculated for X vs every Y in the data set. Data are presented at mean±SEM. For all statistical tests, a p-value of less than 0.05 was considered significant.

The study design is summarized in **Figure 3.1**.

3.3 Results

3.3.1 Pilot results

3.3.1.1 Cadaveric head kinematics with interface-assisted moderate-severe CHIMERA

In Chapter 2, we characterized acute and sub-acute effects of CHIMERA using an upper limit of impact energy of 0.7J, as higher impact energies cause skull fracture in approximately 50% of C57Bl/6 mice and is considered an ethical limit. Below the murine skull fracture threshold, impact energy correlates with phenotypic severity such that a single impact at 0.4J or below causes no detectable behavioral or histopathological change, impact at 0.5J is the threshold of injury and impact at 0.6 or 0.7J causes significant change in both behavioral and neuropathological outcomes. Despite the association of impact energy to phenotype, even impact at 0.7J is still considered to be in the mild TBI range based on full recovery of acute behavioral phenotypes, the presence of and white but not grey matter abnormalities, and the complete absence of traumatic vascular phenotypes. A modified version of the CHIMERA system was recently designed to produce moderate-severe TBI including grey matter damage (Sauerbeck et al., 2018), however, in our hands this method resulted in 100% mortality of experimental animals at 1.7J.

To enable CHIMERA to deliver impacts >0.7J without causing skull fracture or excessive mortality, our team constructed and evaluated a series of physical interfaces that were positioned between the piston tip and the animal's head, which were designed to transmit and distribute impact energy around the skull rather than on the focal area contacted by the impactor tip. We developed eight prototype interfaces that could be used in tandem with the established CHIMERA platform and assessed each for protective and kinematic properties, durability, and

ease of use. After rigorous testing on cadaver mice, an optimal interface, made of a dual layer, 3D-printed PLA frame lined with moldable silicone (**Figure 3.2 A**) was selected for its superior protective performance at 2.5J (interface shown in use in **Figure 3.2 B**). Head kinematic analysis was subsequently performed. Our team decided to glue our constructed head-marker to the animal incisors as the glue ensured that no relative motion between the head and marker would occur. Although the glued system is appropriate for cadaver mice, the strapped version, which was still in its rudimentary stages at the start of this project, will be required for live animal experiments due to ethical and practical limitations with respect to the head-marker fixation and removal procedure. Linear and angular velocity and acceleration were measured following un-interfaced impacts at 0.7J (similar to the impacts used in Chapter 2) and interfaced impacts at 2.5J to determine whether the introduction of the interface slowed down the motion of the head significantly. Linear velocity and acceleration of the mouse head was significantly faster upon impact at 2.5J compared to animals impacted at 0.7J (**Figure 3.2 C,** velocity $p < 0.0001$, **Figure 3.2 D,** acceleration $p < 0.0001$, student's t-test). Angular, or rotational, velocity and acceleration of the head were also faster upon impact at 2.5J compared to impacts at 0.7J (**Figure 3.2 E**, velocity $p < 0.0001$, **Figure 3.2 F**, acceleration $p = 0.003$, student's t-test).

3.3.1.2 Single moderate-severe CHIMERA TBI prolonged loss of righting reflex latency and acutely increased plasma tau and neurofilament-light

Upon completion of head kinematic analyses, a live pilot study of 18 C57Bl/6 animals (10 TBI, 8 sham) impacted at 2.5J in the sagittal plane demonstrated 0% skull fracture, however, the mortality rate for the TBI animals was 20% (2/10). In surviving animals, LRR was measured between impact and when the animal became fully ambulatory within the recovery cage. LRR

was significantly prolonged following single moderate-severe CHIMERA TBI at 2.5J (**Figure 3.3 A**, $p < 0.0001$, Mann-Whitney U). Using the Quanterix Simoa platform, murine tau and NF-L were assayed in plasma collected by cardiac puncture at end-point. Both plasma tau (**Figure 3.3 B**) and NF-L (**Figure 3.3 C**) were significantly elevated by 6h following injury (tau: $p = 0.0379$ and NF-L: $p = 0.0003$, Mann-Whitney U).

3.3.1.3 Acute traumatic vascular injury after single moderate-severe CHIMERA TBI

IgG extravasation was used as an endogenous marker to assess BBB integrity at 6h post-TBI in cortical regions. Coronal sections stained with IgG and DAPI showed evidence of BBB breach within the entorhinal cortex in particular (**Figure 3.3 D-G**). By quantifying fold change in total IgG signal over sham controls, a significant elevation in IgG signal was observed following TBI (**Figure 3.3 G**, $p = 0.0173$, Mann-Whitney U). Prior to electron microscopy, routine osmium tetroxide staining in the entorhinal cortex at 6h illustrated differences in the vasculature following moderate-severe CHIMERA TBI (**Figure 3.3 H**). Electron micrographs were subsequently acquired between 15,000 and 25,000x. In sham animals, EM images showed healthy astrocyte end-feet and vascular endothelium within the entorhinal cortex of sham controls (**Figure 3.3 I, top**). Conversely, vessels showed structural damage, including swollen astrocyte end-feet with edematous cytoplasm, within the entorhinal cortex at 6h post-TBI (**Figure 3.3 I, bottom**).

3.3.2 Behavioral study

3.3.2.1 Single moderate-severe CHIMERA TBI elicits neurological deficits without depressive-like phenotypes

Neurological severity score was performed at 1h and 2d post-TBI. At both time-points, mice that underwent TBI performed significantly worse than their sham counterparts (**Figure 3.4 A**, Interaction $p < 0.0001$, Time $p < 0.0001$, Injury $p < 0.0001$, two-way ANOVA). To assess depressive-like phenotypes, FST was performed at day 45 post-TBI. No differences in latency to immobility from start of test (**Figure 3.4 B**, n.s., student's t-test) or in duration of immobility (measured in the last two minutes for the 5-minute test) were observed (**Figure 3.4 C**, n.s. student's t-test).

3.3.2.2 Single moderate-severe CHIMERA TBI elicits deficits in memory recall

From D14 to D18 post-TBI, acquisition learning trials were performed on 30d animals, and the time to locate and enter into the escape box was reported. The average performance of three trials per day was recorded. No differences between sham and TBI animals were observed across testing days, but shorter test durations over time indicates spatial learning in both sham and TBI groups (**Figure 3.5 A**, Interaction: n.s. Injury: n.s. Day $p < 0.0001$, two-way ANOVA). Probe trials were performed on D19, and D29 post-TBI, during which the escape box was removed. The percentage of time spent inside the north quadrant (the previous escape box location) was reported. Sham animals spend a greater % of time in the north quadrant on both testing days, suggesting better spatial memory recall (**Figure 3.5 B**, Interaction: $p = 0.8634$, Day: $p = 0.0235$, Injury: $p = 0.0133$, two-way ANOVA). Reverse trials were performed on D30 post-TBI, in which the escape box was placed at the opposite location. A shorter test duration over time

indicates spatial unlearning and relearning. No differences between sham and TBI animals were observed across trials (**Figure 3.5 C**, Interaction: n.s., Injury: n.s., Trial: n.s., two-way ANOVA). From D55 to D58 post-TBI, acquisition trials were performed on 60d animals. No differences were observed following TBI (**Figure 3.5 D**, Interaction: n.s., Injury: n.s., Day $p < 0.0001$, two-way ANOVA). A single probe trial was performed on D59. Sham and TBI animals spend equal amounts of time in the north quadrant (**Figure 3.5 E**, Injury: n.s., student's t-test). Reverse trials were performed on D60 post-TBI, and showed no difference between sham and TBI animals (**Figure 3.5 F**, Interaction: n.s., Injury: n.s., Trial: n.s., two-way ANOVA).

3.3.2.3 Single moderate-severe CHIMERA led to decreased hippocampal event amplitudes

Ex vivo electrophysiology was performed at 6h and 14d time-points, which, given the injury-induced deficits observed in memory recall, was focused within the hippocampus. With increasing stimulation intensities, hippocampal event amplitudes at 6h and 14d are significantly lower than sham after TBI (**Figure 3.6 A-C**, Interaction $p < 0.0001$, Injury $p < 0.01$, Amplitude $p < 0.0001$, two-way ANOVA). Hippocampus afferent amplitudes were unchanged following TBI at 6h and 14d (**Figure 3.6 D**, Interaction: n.s., Injury: n.s., Amplitude < $p < 0.0001$).

3.3.2.4 Single moderate-severe CHIMERA TBI acutely increased brain cytokines

Cytokine analysis in hemibrain homogenates revealed that IL-6, TNF-α, and IL-1β showed significant injury effects (**Figure 3.7 A-C**, IL-6: group effect $p < 0.001$, TNF-α: group effect $p < 0.01$, IL-1β: group effect $p < 0.05$). Post-hoc analyses revealed elevations at 6h post-TBI in all cytokines assessed.

3.3.2.5 Single moderate-severe CHIMERA TBI acutely decreased brain tau and increased phosphorylated tau

Analysis of total brain tau and phosphorylated tau (p-tau) were quantified in hemibrain homogenates. Brain total tau was significantly decreased at 6h and 14d post-injury, demonstrating a biphasic response to injury (**Figure 3.8 A,** group effect: $p < 0.0001$). Brain p-tau was significantly elevated at 6h (**Figure 3.8 B,** group effect: $p < 0.05$), and the ratio of p-tau:total tau was significantly elevated at 6h post-TBI (**Figure 3.8 C,** group effect: $p < 0.0001$).

3.3.2.6 Single moderate-severe CHIMERA TBI increased grey and white matter inflammation

To assess evidence of a microglial response following TBI, coronal sections were stained for Iba1 and the percentage of stained area was reported (**Figure 3.9 A-E**). In the optic tract, Iba1 % area was significantly elevated at 14d and 60d post-TBI, while unchanged at the 6h, 2d and 30d time-points (**Figure 3.9 B**, group effect $p < 0.0001$, one-way ANOVA). In the corpus callosum, Iba1% area was unchanged at all time-points assessed (**Figure 3.9 C**, group effect: n.s., one-way ANOVA). In the CA1 region of the anterior hippocampus, % area was significantly elevated at 2d post-TBI, while unchanged at 6h, 14d, 30d and 60d time-points (**Figure 3.9 D**, group effect: n.s., one-way ANOVA). Within the entorhinal cortex, Iba1 % area was significantly elevated at both 6h, and 2d time-points. % area returned to baseline levels by 14d (**Figure 3.9 E**, group effect $p < 0.001$, one-way ANOVA).

GFAP was used to assess the astrocytic response following TBI (**Figure 3.10 A-E**). In the optic tract, GFAP % area was significantly elevated at 60d post-TBI, while unchanged at all acute and sub-acute time-points (**Figure 3.10 B**, group effect $p < 0.01$, one-way ANOVA). In the corpus callosum and CA1 region of the anterior hippocampus, % area was unchanged at all time-points assessed (**Figure 3.10 C, D**, group effect: n.s., one-way ANOVA). Within the entorhinal cortex, % area was significantly different between groups, however post-hoc comparisons were not significant (**Figure 3.10 E**, group effect $p < 0.05$, one-way ANOVA).

3.3.2.7 Single moderate-severe CHIMERA TBI triggered axonal damage at sub-acute and chronic time-points

Silver staining was used to measure the extent of axonal disruption (**Figure 3.11 A-D**), as axons are known to develop an affinity for silver ions when damaged. In the optic tract, silver % area was unchanged at the 6h and 2d time-points, while significantly elevated at 14d, 30d and 60d post-TBI (**Figure 3.11 B**, group effect $p < 0.0001$, one-way ANOVA). In the corpus callosum and the olfactory nerve layer, % area was unchanged at all time-points assessed (**Figure 3.11 C, D**, group effect: n.s., one-way ANOVA).

3.3.2.8 Correlations between loss of consciousness duration and cytokine levels following moderate-severe CHIMERA TBI

We speculated injury-induced inflammation might be positively correlated with loss of consciousness duration immediately following injury, and thus decided to test for correlations between LRR and the cytokine response at 6h (**Table 3.2**). Though the negative correlation between LRR and IL-1β at 6h was trending towards significance ($p = 0.0970$), LRR had no

predictive value for IL-6 (n.s.) and TNFα (n.s.). Cytokines are known to act as pro-inflammatory signaling molecules, therefore correlational analyses were performed between cytokines at 6h and Iba1 in the entorhinal cortex. The positive correlation between Iba1 % area and IL-6 was trending towards significance ($p = 0.0757$), while IL-1β and TNFα appeared to have no relationship with the microglial response at 6h. None of the cytokines assessed were correlated with the astrocytic response within the entorhinal cortex.

3.3.2.9 Correlations between axonal damage and inflammatory outcomes following moderate-severe CHIMERA TBI

Pearson correlations were calculated for TBI animals to determine whether the microglial and astrocytic responses observed after TBI were associated with each other and with silver staining in the optic tract (**Figure 3.12**). GFAP % area was found to positively correlate with silver staining ($r = 0.7522$, $p < 0.0001$, **Figure 3.12 A**) as did Iba1 with silver % area ($r = 0.7577$, $p < 0.0001$, **Figure 3.12 B**). Further, GFAP % area was positively correlated with Iba1in the optic tract ($r = 0.7124$, $p < 0.0001$, **Figure 3.12 C**).

3.4 Discussion

In the current study, we proposed modifications to the CHIMERA platform that can be used to induce more severe injuries, triggering acute vascular damage and grey matter inflammation without fracturing the skull. This is of particular importance as the majority of reported TBIs are not co-morbid with skull fracture. With the application of a carefully designed 3D-printed interface, we were able to significantly increase linear and rotational head kinematics, while maintaining skull fracture at 0%. Other CHIMERA users can add the use of this interface to their

protocols with ease, to enable moderate-severe impacts without necessitating major structural changes to the CHIMERA platform. Previously published work at the mild TBI level demonstrate that CHIMERA can also be used to induce diffuse axonal injury at acute, sub-acute, and chronic time-points (Cheng et al., 2018, 2019; Namjoshi et al., 2014, 2017). Here, axonal injury is slower to develop following CHIMERA injury at 2.5J and is fairly constrained within the optic tract, the contre-coup site of injury. We postulate that corpus callosum inflammation was limited after interface-assisted moderate-severe CHIMERA due to the ability of the interface to prevent substantial skull bending at the site of focal impact. This hypothesis can be tested using high speed x-ray videography to determine the extent to which the skull bends at the site of piston impact at the mild level, and how much the skull bends while the interface is in use. This line of investigation, however, is beyond the scope of this study.

Two key pathological features of TBI that were missing from CHIMERA injuries at the mild level were evidence of BBB damage and changes in phosphorylated tau. At the 2.5J level, BBB damage was evidenced by IgG extravasation in cortical regions and supplemented by electron micrographs depicting decreased lumen diameter and swollen astrocyte end-feet with edematous cytoplasm. Using CHIMERA at 2.5J, we were able to recreate outcomes similar to those described by Rodriguez-Baeza and colleagues (Rodríguez-Baeza et al., 2003). In creating vascular corrosion casts to examine the cerebral microcirculation in patients who died following severe head trauma, Rodríguez-Baeza et al. found that arterioles and capillaries in the middle and deep cortical vascular zones showed extensive injury characterized by sunken endothelial surfaces, longitudinal folds in the vessel wall, decreased lumen diameter, and corrugations, indicating a separation between the endothelium and smooth muscle cells and a disrupted BBB

(Rodríguez-Baeza et al., 2003). Subsequent CHIMERA studies will require functional methods to study vascular injury, such as CBF, as groups have pinpointed dramatic changes in perfusion after clinical TBI (Bonne et al., 2003). Studies using SPECT to measure regional CBF in patients with chronic TBI (Barkai et al., 2004; Bonne et al., 2003; Lewine et al., 2007) have consistently found regions of hypoperfusion in a subset of symptomatic TBI subjects (Raji et al., 2014). Further, SPECT perfusion changes significantly correlated with neuropsychological or neurological deficits. As a pre-clinical platform, it will be necessary that CBF and other clinically-relevant functional outcomes be validated in the CHIMERA model.

As discussed in Chapter 2, we observed that single CHIMERA TBI up to 0.7J did not elicit changes in total or phosphorylated (Thr231) tau. However, in the current study, we were able to detect tau and p-tau changes in half-brain homogenates at acute time-points following TBI, indicating that changes in tau may be dependent on impact energy. Further, the bidirectionality of total tau and p-tau concentrations at the 6h time-point led to a significant increase in the ratio of p-tau:total tau. These findings ware of particular clinical relevance, as hyper-phosphorylated tau deposits within the brain parenchyma are the pathognomonic feature of CTE (Mckee et al., 2016), as described in **Section 1.5.1.1** of Chapter 1.

In addition to neuropathological changes, we also observed immediate and sub-acute neurological changes after moderate-severe CHIMERA TBI. We utilized a number of clinically-relevant behavioral measures, including LRR as a proxy of loss of consciousness, NSS as a proxy of neurological outcomes, BM analyses as proxy for spatial learning and memory, and FST as a proxy of depressive-like states. CHIMERA TBI at 2.5J led to dramatically longer LRR

times, as the average LRR time following 0.7J CHIMERA injury (in Chapter 2) was ~6 minutes, while LRR times following 2.5J injury averaged 20 minutes. We observed significant elevations in NSS, indicating neurological deficits at 1h and 2d time-points following injury. Though no alterations in depressive-like states were observed following 2.5J injury, minor deficits in memory recall were observed at D19 and D29. BM analyses suggest that spatial learning and relearning are unaltered by injury at this level. Of the many clinical features of single and repetitive head trauma, memory impairments can be one of the most disruptive and devastating in the long-term. Many studies have shown that clinical TBI, particularly moderate and severe TBI, may affect memory capabilities, also increasing long-term risk for dementia (Gardner et al., 2014; Wang et al., 2012) and Alzheimer's Disease (Guo et al., 2000; Plassman et al., 2000; Wang et al., 2012).

The deficits in spatial memory that were detected following 2.5J TBI could be related to the electrophysiological changes observed within the hippocampus. With increasing stimulation intensity (from 100 to 600 μA) in the Schaffer collaterals of CA1, healthy neurons responded with a proportionate increase in peak afferent and event amplitudes. In TBI animals, however, we observed a substantial decrease in peak event amplitudes at 6h and 14d, suggesting an altered post-synaptic response. The pre-synapse appears unaltered, as afferent amplitudes are unchanged following TBI. The alteration we detect overlaps with findings in Tagge et al.'s recent study (Tagge et al., 2018). At acute and sub-acute time-points following unilateral closed-head impact injury, bilateral impairments in conduction velocity were observed within the hippocampus. Tagge et al. also carried out long-term potentiation (LTP) experiments in the prefrontal cortex and found bilateral impairments in synaptic transmission of field-excitatory post-synaptic

potentials (fEPSP). Though we did not investigate changes in LTP within this study, future studies may be necessary to determine if the acute and sub-acute alterations in basal release we observed correlate with alterations in plasticity. Exploring electrophysiological changes following mild injuries, where the temporal and spatial pattern of axonal damage is vastly different, will also be crucial. In a recent paper, our group found that two very mild injuries (0.5J) profoundly affected spatial learning and memory, anxiety, and risk-taking behaviors up to 8-month post-TBI, in C57Bl/6 and APP/PS1 mice (Cheng et al., 2019). A biological correlate for these phenotypes remains to be determined, but could lie in long-term electrophysiological deficits following injury.

Due to the cytoskeletal changes that emerge following clinical TBI, axonal filament proteins have emerged as viable fluid biomarker candidates for assessing axonal damage (Shahim et al., 2016; Zetterberg and Blennow, 2016). In our study, we performed preliminary investigations to assess changes in circulating tau and NF-L 6h post-injury. Using our model, we observed significant elevations in both biomarkers after 2.5J injury. Still, how blood biomarkers may reflect brain changes after TBI has not been fully elucidated. Researchers have begun using ultrasensitive assays, like the Quanterix Simoa platform used in this study, to quantify plasma and serum concentrations of tau and NF-L and subsequently correlate biomarker findings with diagnostic and prognostic outcomes (Stukas et al., 2019). With the push towards the use of biomarkers in the clinic, it will be imperative that preclinical TBI research moves in tandem. By pinpointing and validating biomarker endpoints that are elevated following moderate-severe CHIMERA TBI, we propose the use of plasma tau and NF-L as measures of target engagement in future therapeutic studies using CHIMERA.

Further, moderate-severe CHIMERA TBI triggered inflammation that could be detected at the global level. With little-no evidence of gross tissue damage, levels of pro-inflammatory cytokines in half-brain homogenates were elevated at 6h after CHIMERA injury. We initially speculated that injury-induced inflammation may be correlated with duration of loss of consciousness immediately following injury, and thus decided to test for correlations between LRR and the cytokine response at 6h. Though a negative correlation between LRR and IL-1β was trending towards significance, LRR had no predictive value for IL-6 and TNFα. Given the aptly described interplay between cytokine release and the glio-inflammatory response following TBI (Burda et al., 2017; Karve et al., 2016; Kumar and Loane, 2012; Myer et al., 2006), correlational analyses were performed between cytokines at 6h and Iba1 in the entorhinal cortex. The positive correlation between Iba1 % area and IL-6 was trending towards significance, while IL-1β and TNFα appeared to have no relationship with the microglial response at 6h. None of the cytokines assessed were correlated with the astrocytic response within the entorhinal cortex. Interestingly, when we correlate regional inflammatory changes, focusing on the optic tract, we found that GFAP % area correlated positively with Iba1 and silver % area, suggesting that the astrocytic response works in tandem with the microglial response following axonal damage. Future directions for this work include incorporating neuroimaging to detect damage sustained by the optic tract following CHIMERA TBI at 2.5J. As we have already started investigating the pattern of DTI changes associated with mild CHIMERA injuries (Haber et al., 2017), imaging experiments to assess changes in axonal integrity and alterations within the cerebrovasculature after moderate-severe CHIMERA injuries are imminent.

The neurological, biochemical and histological TBI-induced changes presented here lay the foundation for elucidating the temporal response to a moderate-severe insult in a mouse model. Future studies will be required to extend the duration of the study to elucidate the long-term effects (>6 months) of moderate-severe CHIMERA injury on the neurobehavioral and neuroinflammatory sequelae. As we continue to study glial, neuro-axonal and vascular changes induced by mechanical head trauma, we hope to study potential avenues of therapeutics to ameliorate the damage sustained by the brain. Importantly, with the expansion of the CHIMERA platform, it will be of benefit to use CHIMERA's ability to be finetuned to specific TBI endophenotypes (vascular, axonal, etc.) and their associated temporal profiles to study therapeutics. Our data extend the tunability of CHIMERA as a valuable animal model of head injury and establish working parameters to guide future investigations into TBI-induced alterations in behavior, grey and white matter inflammation, cerebrovasculature integrity, and neurotransmission.

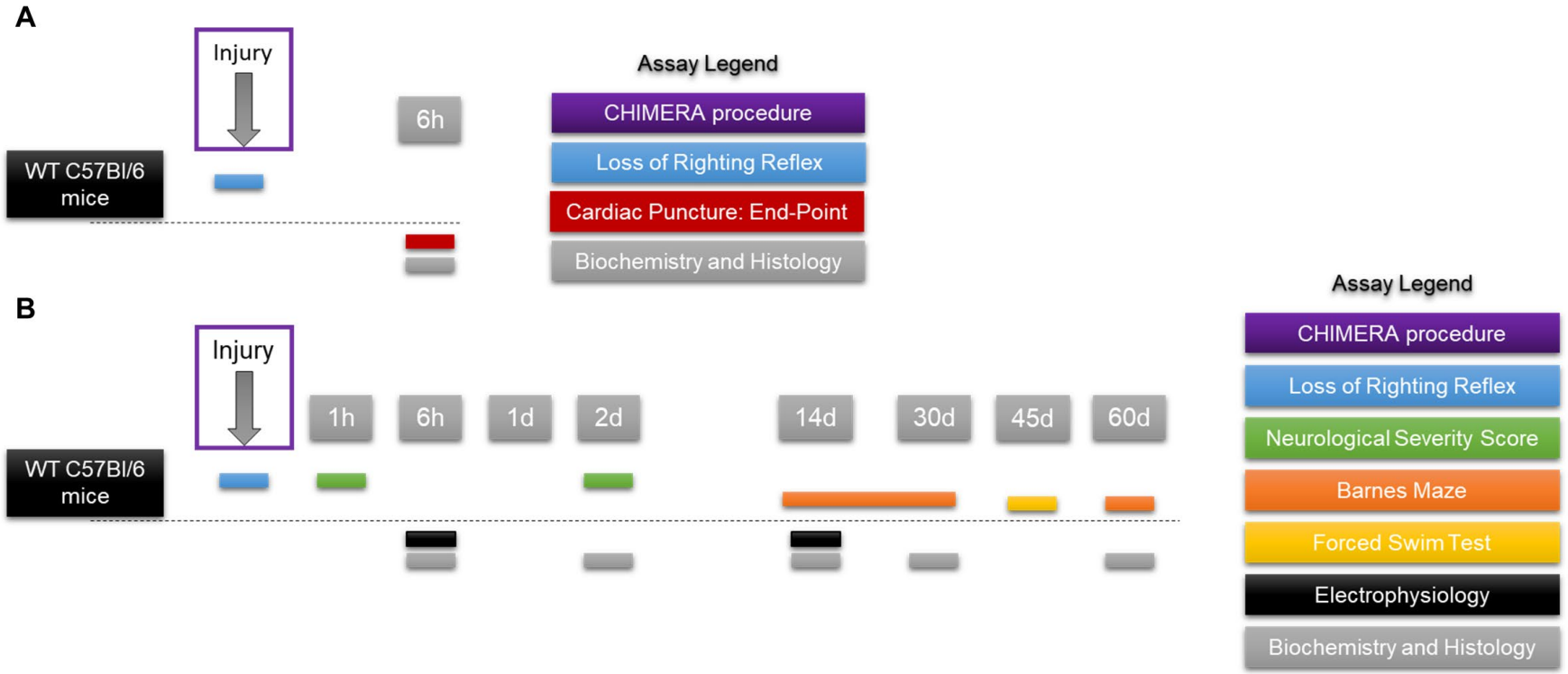

Figure 3.1 Study design.

(A) For the pilot study, 2.5J injury was induced at T=0, immediately after which loss of righting reflex (LRR) latency was recorded. At 6h post-TBI, terminal cardiac puncture was performed followed by brain extraction for biochemical and histological analyses. (B) For the behavioral study, 2.5J injury was induced at T=0, immediately after which LRR latency was recorded. At 1h and 2d, neurological severity score testing occurred. In 30d animals, Barnes maze testing began at D14 and lasted until end-point. In 60d

animals, Barnes maze testing began on D55 and lasted until end-point. Ex vivo electrophysiology was carried out at 6h and 14d post-TBI. Terminal collection procedures for biochemical and histological outcomes for this study occurred at 6h, 2d, 14d, 30d and 60d post-TBI.

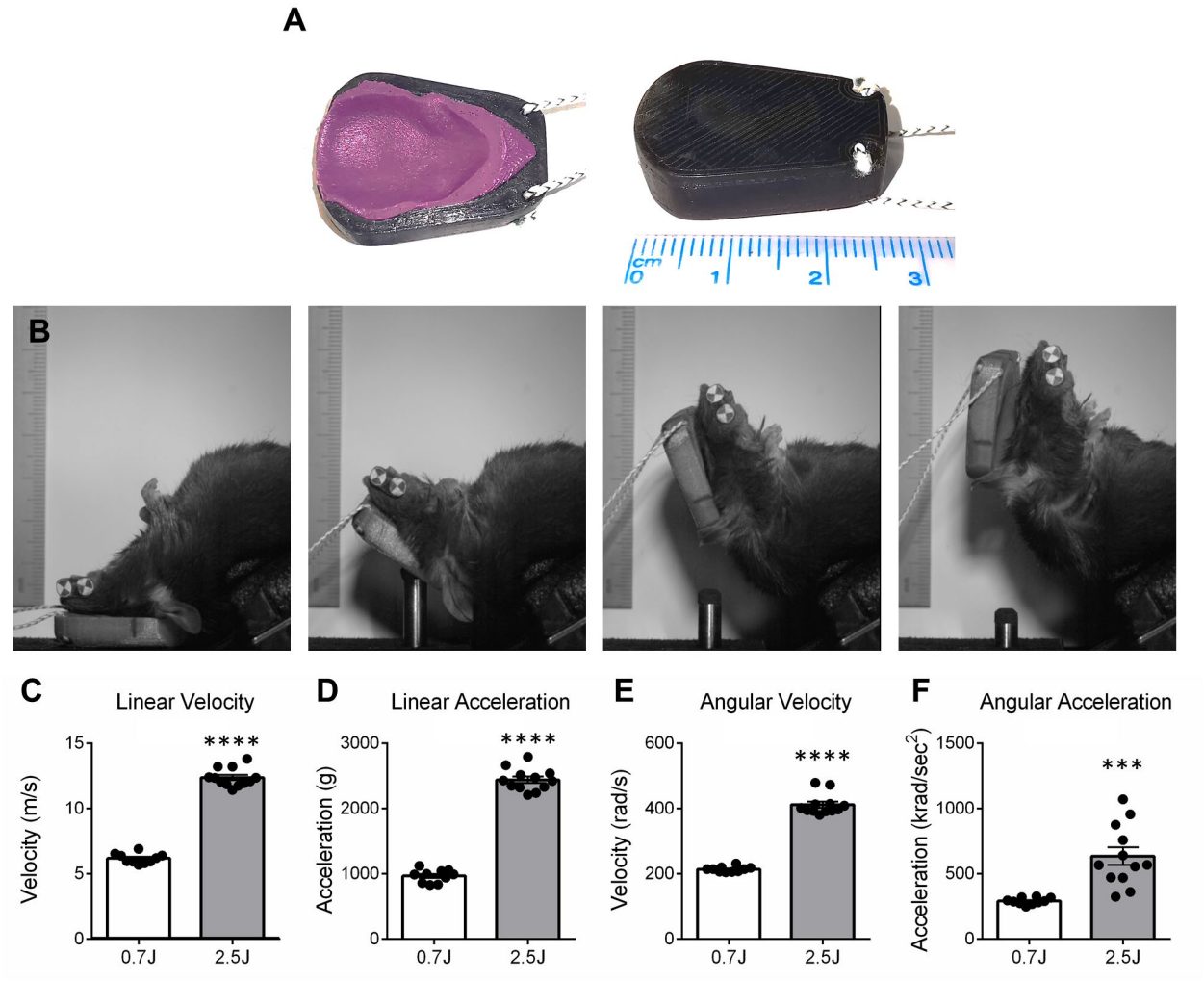

Figure 3.2 3D-printed interface permits CHIMERA impact energies up to 2.5J without skull fracture.

(A) Top (left) and bottom (right) views of the 3D-printed polylactic acid interface, lined with a silicon mold. (B) High-speed videography shows trajectory of the head upon impact at 2.5J. (C) Linear velocity and (D) acceleration of the mouse head was significant faster upon impact at 2.5J compared to animals impacted at 0.7J ($p < 0.0001$). (E) Angular, or rotational, velocity and (F) acceleration of the head was also faster upon impact at 2.5J compared to impacts at 0.7J (E: $p <$

0.0001, F: p = 0.0003). In (C-F), data are presented as mean±SEM and were analyzed by student's t-test; *** $p < 0.001$, **** $p < 0.0001$ relative to sham values.

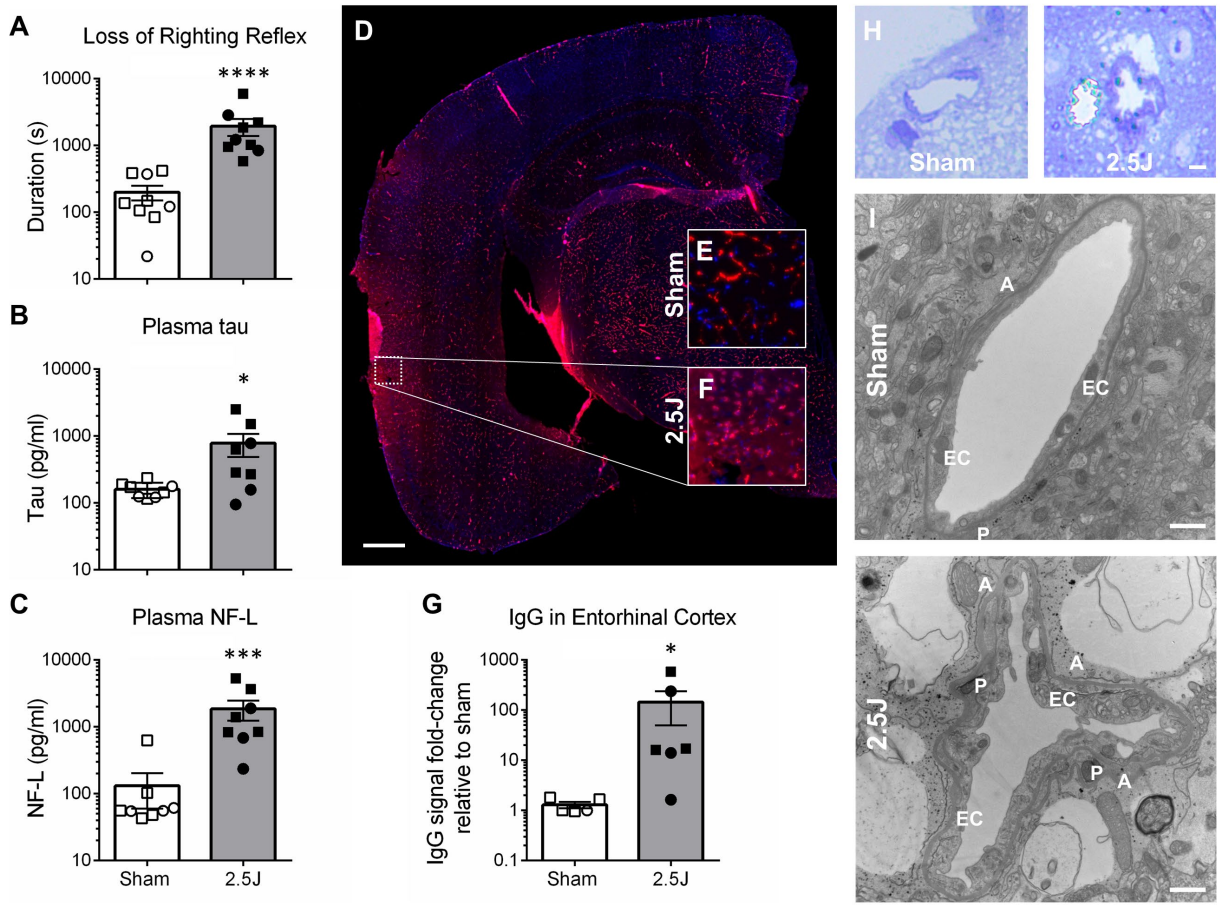

Figure 3.3 Prolonged loss of consciousness, plasma biomarker elevations and blood-brain barrier extravasation following CHIMERA TBI at 2.5J.

(A) Loss of righting reflex latency was significantly prolonged following single moderate-severe CHIMERA TBI at 2.5J ($p < 0.0001$). (B) Plasma tau and (C) neurofilament-light (NF-L) were elevated at the 6h time-point following injury (tau: $p = 0.0379$; NFL: $p = 0.0003$). (D) Coronal sections stained with immunoglobulin G (IgG) and DAPI showed evidence of blood-brain barrier breach within the entorhinal cortex. (E, F) Zoomed-in insets revealed BBB breach within the entorhinal cortex. (G) IgG signal was significantly elevated at the 6h time-point ($p = 0.0173$). (H) Using osmium tetroxide staining at 6h, vessel walls appeared thicker after TBI in the entorhinal cortex at 40x magnification. (I, top) Electron microscopy (EM) acquired at 25,000x

magnification showed healthy pericytes, astrocyte end-feet and vascular endothelium within the entorhinal cortex of sham controls. (I, bottom) Vessels showed structural damage – swollen, edematous astrocyte end-feet, loss of tight junctions, and deformation of pericytes – within the entorhinal cortex at 6h post-TBI. In (A-C, G), data are presented as mean±SEM and were analyzed by Mann-Whitney U test; * $p < 0.05$, *** $p < 0.001$, **** $p < 0.0001$ relative to sham values. Circle icons in scatter plots represent males, whereas square represent females. In (D), scale bar = 100 micrometers. In (H), scale bar = 50 micrometers. In (I), scale bar = 500 nanometers. In (I), abbreviations: A = astrocyte, EC = endothelial cell, P = pericyte.

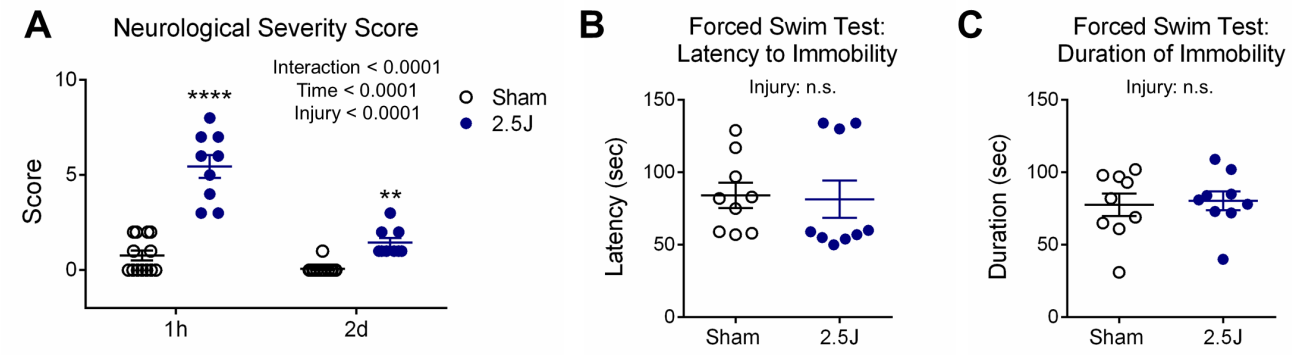

Figure 3.4 Deficits in neurological function following CHIMERA TBI at 2.5J.

(A) Neurological severity score was performed at 1h and 2d post-TBI. At both time-points, mice that underwent TBI performed significantly worse than their sham counterparts. To assess depressive-like phenotypes, forced swim test (FST) was performed at day 45 post-TBI. (B) No differences in latency to immobility from start of test or in (C) duration of immobility (measured in the last two minutes for the 5-minute test) were observed. In (A-C), data are presented as mean±SEM. In (A), data were analyzed by two-way ANOVA followed by Holm-Sidak post-hoc comparisons, where **** $p < 0.0001$ relative to sham values. In (B-C), data were analyzed by Mann-Whitney U test**.**

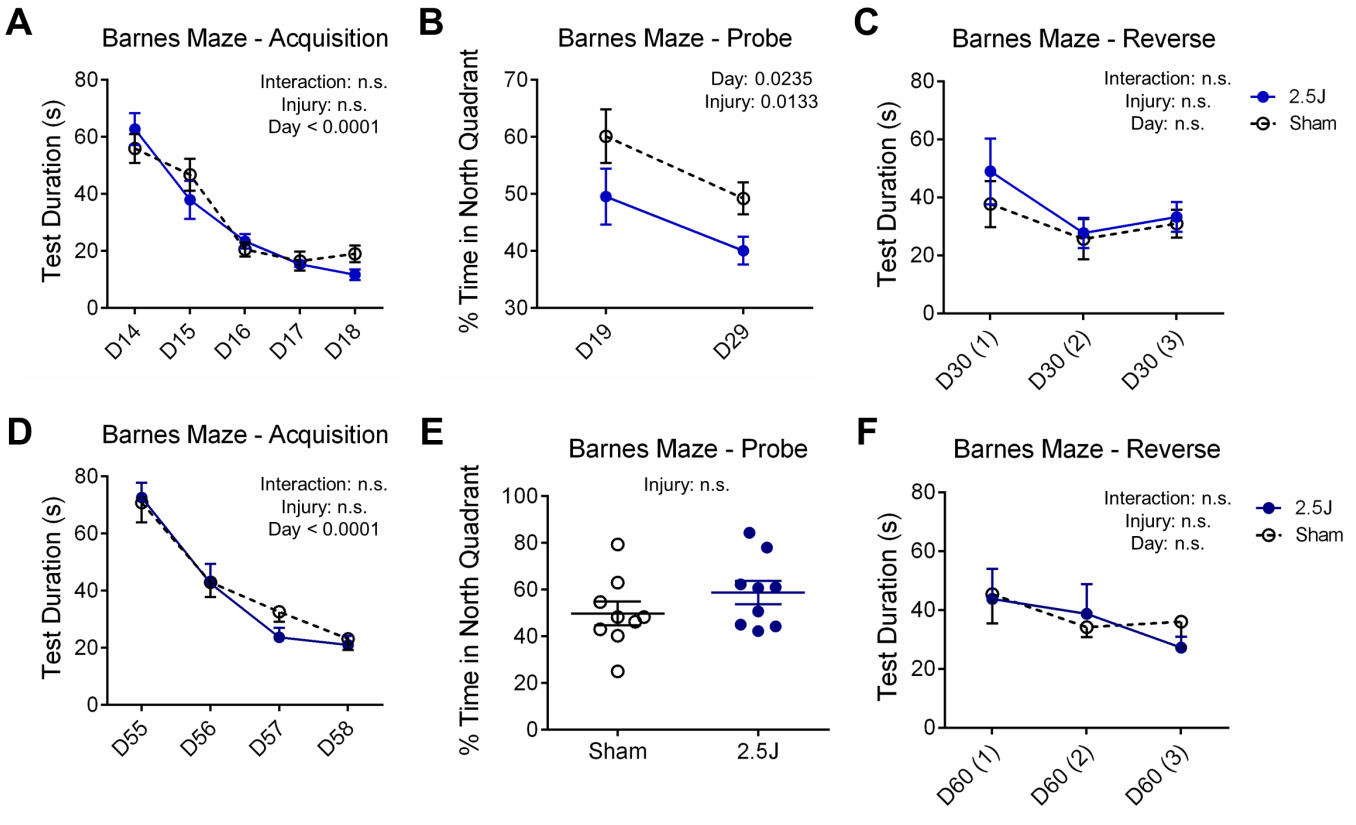

Figure 3.5 Deficits in memory recall using Barnes maze following CHIMERA TBI at 2.5J. (A) From D14 to D18 post-TBI, acquisition learning trials were performed, and the time to locate and enter into the escape box was reported. The average performance of three trials per day was expressed as mean±SEM. A shorter duration over time indicates spatial learning in both sham and TBI groups. (B) Probe trials were performed on D19 and D29 post-TBI, during which the escape box was removed. The % time spent inside the north quadrant (the previous escape box location) is plotted. Sham animals spend a greater % of time in the north quadrant, suggesting better spatial memory recall. (C) Reverse trials were performed on D30 post-TBI, in which the escape box was placed at the opposite location. A shorter test duration over time

indicates spatial unlearning and relearning. (D) From D55 to D58 post-TBI, acquisition trials were performed. (E) A single probe trial was performed on D59. Sham and TBI animals spend equal amounts of time in the north quadrant. (F) Reverse trials were performed on D60 post-TBI, and showed no difference between sham and TBI animals. In (A-F) data are presented as mean±SEM and were analyzed by two-way ANOVA followed by Holm-Sidak post-hoc comparisons**.**

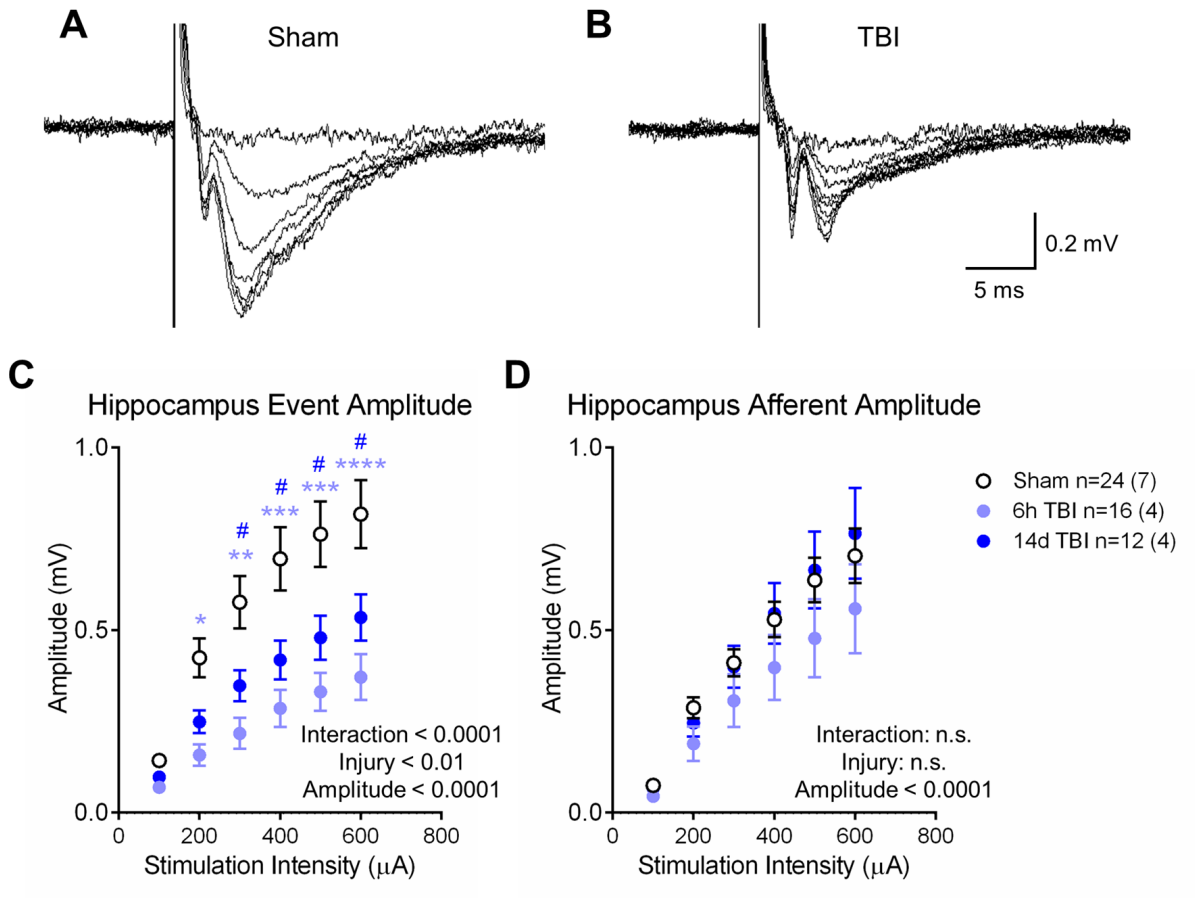

Figure 3.6 Decrease in peak event amplitudes following CHIMERA TBI at 2.5J at 6h and 14d.

(A) Representative traces of hippocampal field recordings at 6h in sham and (B) TBI animals. (C) Hippocampal event amplitudes at 6h (light blue) and 14d (royal blue) are significantly lower than sham (empty circles) after TBI. (D) Hippocampus afferent amplitudes were unchanged following TBI at 6h and 14d. In (C-D) data are presented as mean±SEM and were analyzed by two-way ANOVA followed by Holm-Sidak post-hoc comparisons, where #, * $p<0.05$, ** $p<0.01$, *** $p<0.001$; **** $p<0.0001$ relative to sham values.

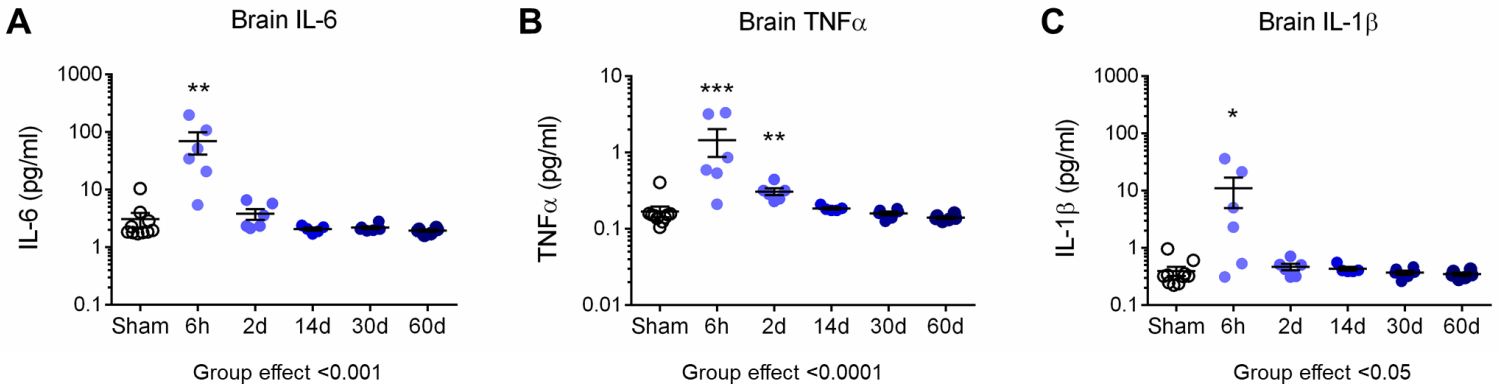

Figure 3.7 Acute increase in pro-inflammatory cytokines after CHIMERA TBI at 2.5J.

(A) IL-6, (B) TNF-α, and (C) IL-1β showed significant injury effects. Post-hoc analyses revealed elevations at 6h post-TBI in all cytokines assessed (** p <0.01, *** p<0.001). In (A-C), data are presented as mean±SEM and were analyzed by Kruskal-Wallis test followed by Dunn's post-hoc test, where * $p < 0.05$, ** $p < 0.01$, *** $p < 0.001$ relative to sham values.

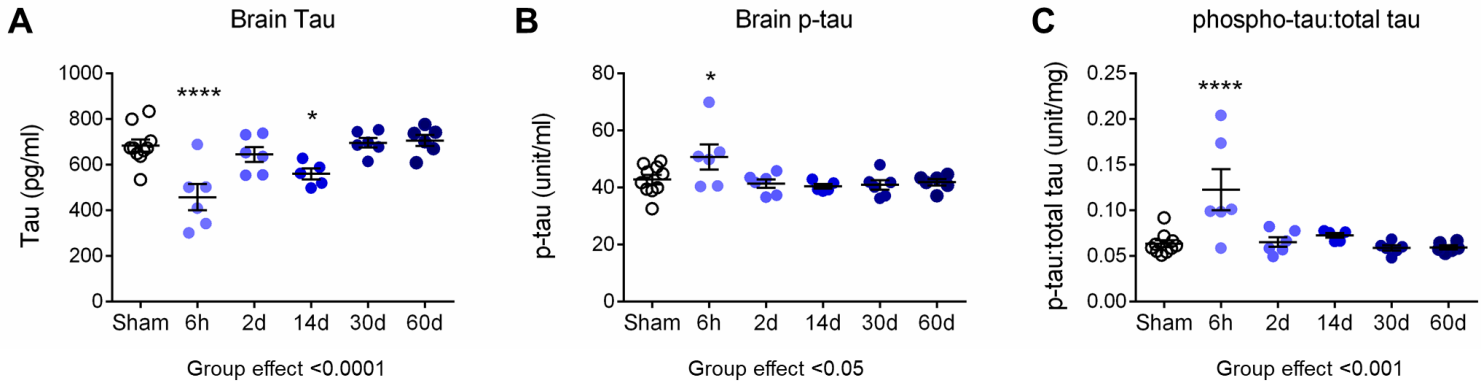

Figure 3.8 Single moderate-severe CHIMERA TBI decreased tau and increased phosphorylated tau at 6h.

(A) Brain tau was significantly decreased at 6h and 14d post-injury, demonstrating a biphasic response to injury. (B) Brain phosphorylated tau (p-tau) was significantly elevated at 6h. (C) The ratio of p-tau:total tau was significantly elevated at 6h post-TBI. In (A-C), data are presented as mean±SEM and were analyzed by one-way ANOVA followed by Holm-Sidak post-hoc test, where * $p<0.05$, and **** $p<0.0001$ relative to sham values.

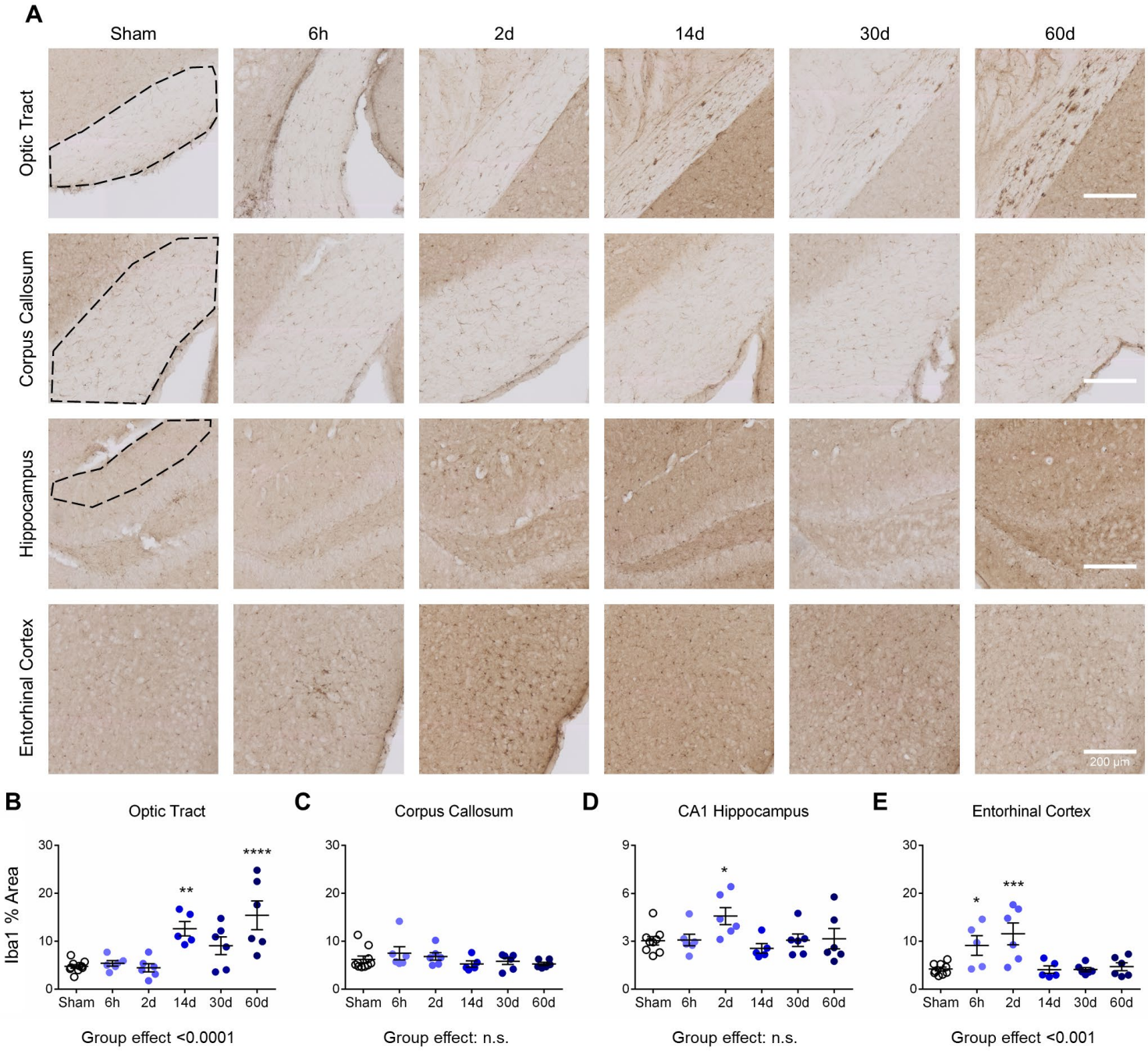

Figure 3.9 Single moderate-severe CHIMERA TBI increased Iba1 immunoreactivity within the optic tract and entorhinal cortex.

(A) Representative images of sham and TBI samples immunohistochemically stained for Iba1, then imaged at 10x magnification. (B) In the optic tract, Iba1 % area was unchanged at the 6h, 2d and 30d time-points, while significantly elevated at 14d and 60d post-TBI. (C) In the corpus callosum, Iba1 % area was unchanged at all time-points assessed. (D) In the CA1 region of the anterior hippocampus, % area was unchanged at 6h, 14d, 30d and 60d time-points, however % area was significantly elevated at 2d post-TBI. (E) Within the entorhinal cortex, Iba1 % area was significantly elevated at both 6h, and 2d time-points. % Area returned to baseline levels by 14d. Data were analyzed by one-way ANOVA followed by Holm-Sidak post-hoc comparisons, where * $p<0.05$, ** $p<0.01$, *** $p<0.001$; **** $p<0.0001$ relative to sham values. In (A), scale bar = 200 microns.

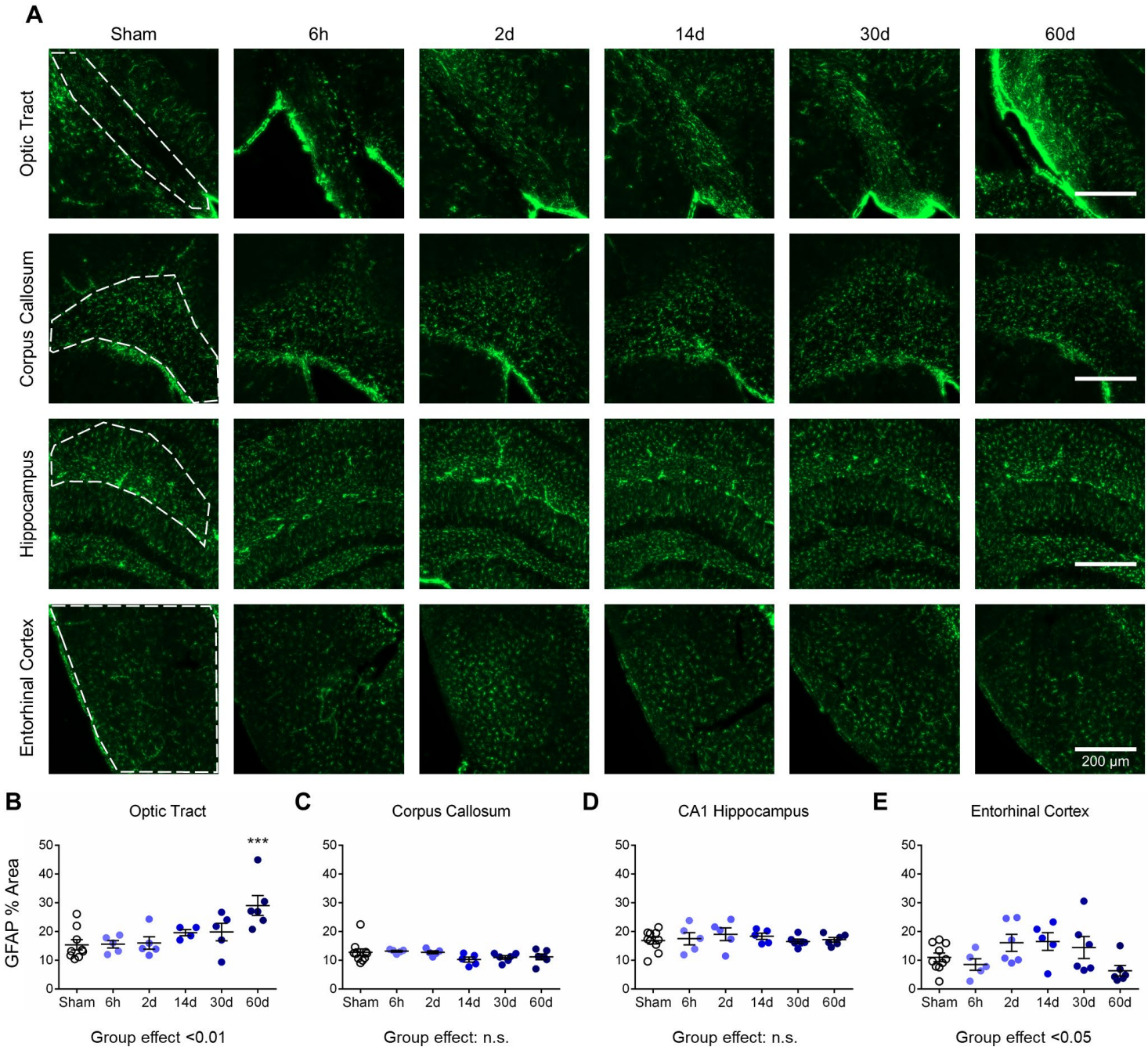

Figure 3.10 Single moderate-severe CHIMERA TBI increased GFAP immunoreactivity within the optic tract.

(A) Representative images of sham and TBI samples immunofluorescently stained for GFAP and imaged at 20x magnification. (B) In the optic tract, GFAP % area was unchanged at the 6h, 2d, 14d, and 30d time-points, while significantly elevated at 60d post-TBI. (C) In the corpus callosum, (D) CA1 region of the anterior hippocampus, and (E) entorhinal cortex, % area was unchanged at all time-points assessed. Data were analyzed by one-way ANOVA followed by Holm-Sidak post-hoc comparisons, where *** $p<0.001$; relative to sham values. In (A), scale bar = 200 microns.

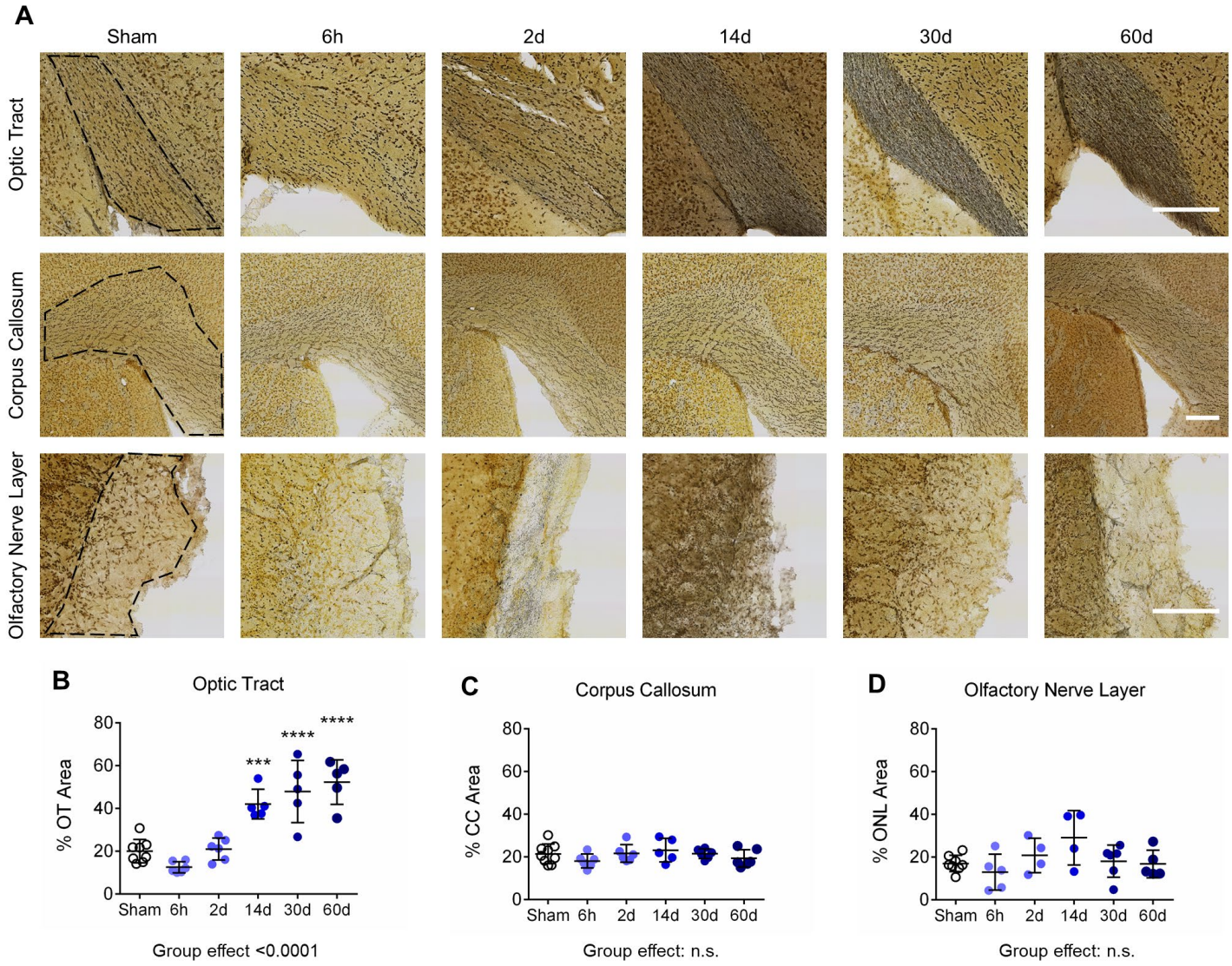

Figure 3.11 Single moderate-severe CHIMERA TBI increased silver uptake within the optic tract.

(A) Representative images of sham and TBI samples stained for silver uptake and imaged at 20x magnification. (B) In the optic tract, silver % area was unchanged at the 6h and 2d time-points, while significantly elevated at 14d, 30d and 60d post-TBI. (C) In the corpus callosum and (D) the olfactory nerve layer, % area was unchanged at all time-points assessed. Data were analyzed

by one-way ANOVA followed by Holm-Sidak post-hoc comparisons, where *** $p<0.001$ and **** $p<0.0001$ relative to sham values. In (A), scale bar = 200 microns.

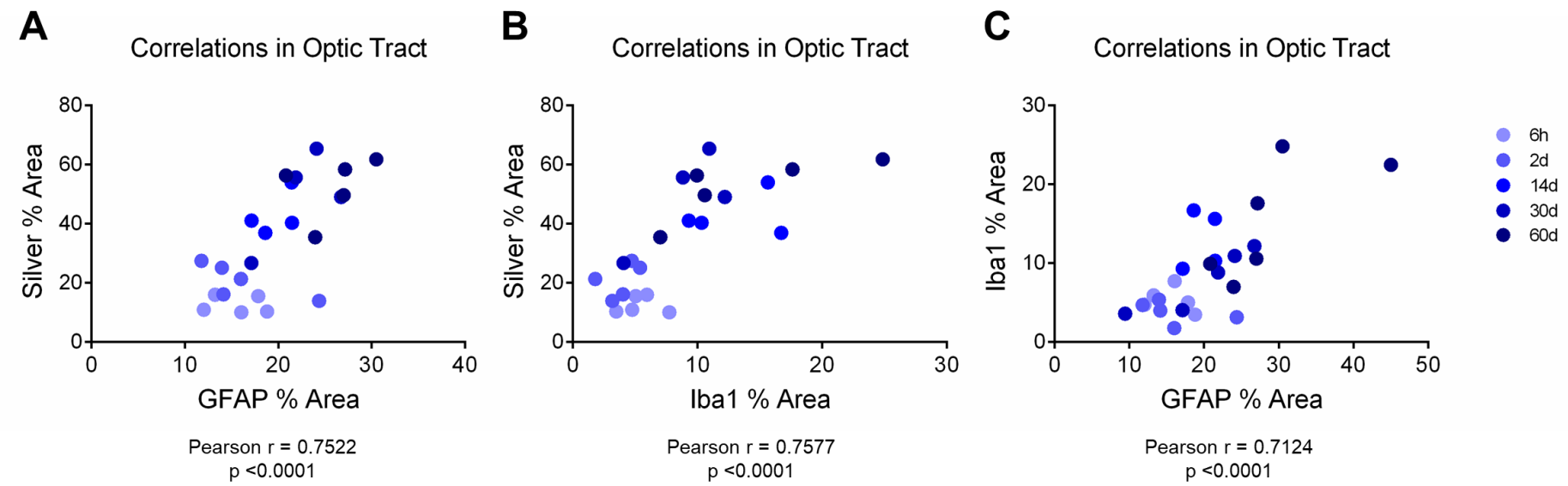

Figure 3.12 Correlations between inflammatory measures and axonal damage in the optic tract.

Pearson correlations were calculated for TBI animals at 6h, 2d, 14d, 30d, and 60d. (A) GFAP % area correlated strongly with silver staining within the optic tract (r = 0.7522, p <0.0001). (B) Iba1 % area was positively correlated with silver staining in the optic tract (r = 0.7577, p<0.0001). (C) GFAP % area was positively correlated with Iba1in the optic tract (r = 0.7124, p<0.0001).

Table 3.1 Sample sizes for outcomes

The table details sample number for each post-TBI parameter at the respective post-TBI time point assessed in this study.

Pilot Parameter	Time Point	Sham	0.7J	2.5J
Head Kinematics	During/immediately following head impact	-	10	12
Loss of Righting Reflex	Immediately following head impact	8	0	8
Plasma tau	6h	8	0	8
Plasma NF-L	6h	8	0	8
IgG IHC	6h	8	0	8
Osmium tetroxide and electron microscopic imaging	6h	2	0	2

Behavioral Study Parameter	Time-point	Sham	2.5J
Neurological Severity Score	1 h	10	9
	2 d	10	9
Barnes Maze	30 d	10	10
	60 d	9	9
Forced swim test	60d	9	9
Electrophysiology*	6 h	4	4
	14d	3	4
Cytokine Quantification*	6 h	2	6
	2 d	2	6
	14 d	2	5
	30 d	2	6
	60 d	2	6
Microglial Quantification*	6 h	2	6
	2 d	2	6
	14 d	2	5
	30 d	2	6
	60 d	2	6

Astrocyte Quantification*	6 h	2	6
	2 d	2	6
	14 d	2	5
	30 d	2	6
	60 d	2	6
Silver Quantification*	6 h	2	6
	2 d	2	6
	14 d	2	5
	30 d	2	6
	60 d	2	6

*for electrophysiology and quantification of cytokines, microglia, astrocytes, and silver, sham animals across time-points were collapsed for statistical analyses.

Table 3.2 Summary of correlation analyses.

The table summarizes the results of correlation analyses testing relationships between the cytokine response at 6h with LRR, and grey matter inflammation. For each correlation pair, the Pearson *r* value is presented in the upper row, while the corresponding *p* value is indicated in lower row. Trending correlations (<0.10) are highlighted in bold and italicized.

Post-TBI Outcome		**Cytokines at 6h**		
		IL-1β	**IL-6**	**TNFα**
LRR	r	-0.7337	-0.05643	-0.1733
	p	***0.0970***	0.9154	0.7427
Iba1 % Area				
Entorhinal Cortex	r	0.02182	0.9243	0.8907
	p	0.9782	***0.0757***	0.1093
GFAP % Area				
Entorhinal Cortex	*r*	-0.7520	0.1234	0.01631
	p	0.2480	0.8766	0.9837

Chapter 4: Repetitive CHIMERA injury in rats increases impulsivity and generates tau pathology

4.1 Introduction

As described in Chapters 2 and 3, CHIMERA is ideal to model the effects of multiple mTBI given the reproducibility and non-surgical nature of the injuries. We chose to expand this platform to rats, given that the behavioral assessments in mice are somewhat limited to the relatively simple tasks of motor, memory and anxiety that mice can readily be trained on. Rats are far more suitable for the study of complex behaviors, including sensitive operant behaviors that measure chronic deficits that can persist for months after surgical TBI induced by the most historical model called open-head controlled cortical impact (CCI) (Vonder Haar et al., 2016, 2017). As this traditional version of CCI is not suitable to investigate repetitive TBI, we adapted the CHIMERA system to rats to enable use of the DDT to explore the relationship between repetitive TBI, impulsive choice, white matter pathology, and dopaminergic signaling. We accomplished this by training rats to perform the DDT, and then subjected them to five consecutive CHIMERA injuries or sham procedures spaced two weeks apart. At end-point, we performed histological and biochemical analyses to elucidate the complex interrelationship between rTBI and impulsivity, allowing mechanisms and potential targets for intervention to be identified.

4.1.1 Behavioral changes following TBI

Behavioral disinhibition, including increased impulsivity, agitation, and poor executive decision-making is common after TBI (Arnould et al., 2016; Kim, 2002; Kocka and Gagnon, 2014) and

can be manifested as substance abuse and aggression (Bjork et al., 2016, 2017; Goswami et al., 2016; Graham and Cardon, 2008). Importantly, loss of impulse control can also be observed in subjects with rmTBI who are subsequently found to have only mild CTE neuropathology (Mahar et al., 2017; Mez et al., 2017), underscoring the important distinctions between the clinical and neuropathological sequelae of rmTBI.

4.1.2 The neuroanatomical basis of impulsive behavior

Choice behavior, and impulsive choice in particular, is strongly regulated by the mesolimbic/mesocortical reward circuit. Dopaminergic neurons in the ventral tegmental area (VTA) project to several brain regions involved in reward processing, including the nucleus accumbens shell (motivation/pleasure), the basolateral amygdala (emotional salience), the orbitofrontal cortex (relative value), the prefrontal cortex (attention/decision), and the hippocampus (memory/context) (Baik, 2013). The mesolimbic circuit facilitates learned associations with motivationally salient events via phasic dopamine release (Brewer and Potenza, 2008). Notably, this is distinct from the nigrostriatal dopaminergic circuit involved in control of motor behavior (Rizzi and Tan, 2017). There is considerable evidence that dopamine physiology is impaired after TBI (Chen et al., 2017b). Although relatively few studies have identified aberrant dopaminergic signaling after human TBI (Donnemiller et al., 2000; Jenkins et al., 2018; Wagner et al., 2014), a number of animal studies have established that the dopamine pathway is altered following TBI, reviewed in (Ozga et al., 2018). The dopaminergic system includes long axonal projections from midbrain structures, namely the substantia nigra and VTA, to the striatum and forebrain, respectively (Chen et al., 2017b). These projections are easily damaged by shearing forces during rapid acceleration and deceleration, leading to acute

hyperdopaminergia followed by chronic hypodopaminergia (Weil and Karelina, 2017) and, in more severe cases, axonal degeneration (Bales et al., 2009; Chen et al., 2017b; Merkel et al., 2017). Chronic white matter inflammation that is nearly universal after TBI may also cause sustained alterations in dopamine signaling (Merkel et al., 2017).

4.1.3 Behavioral outcomes to assess impulsive dysfunction

Understanding how the psychiatric sequelae of TBI potentially relate to dysfunction of reward pathways will require both in-depth characterization of relevant behaviors and accompanying neuropathology in animal models. Task selection is a particularly critical factor when measuring psychiatric-related dysfunction, as most behavioral assays traditionally used in the preclinical neurotrauma field, such as the Morris Water Maze, Barnes Maze, Elevated Plus Maze, or Rotarod, are relatively simple tasks of spatial memory, anxiety, and motor functions, respectively, which cannot assess the more complex aspects of impulsivity that is highly relevant to human repetitive TBI.

4.1.3.1 The delay discounting task

The delay discounting task (DDT) is a well-validated measure of impulsive choice. In this task, the subject chooses between an immediate small reinforcer versus a larger delayed reinforcer. As the delay to the large reinforcer progressively increases across the testing session, subjects tend to switch preference to the smaller reinforcer. Subjects that switch sooner (i.e. can only tolerate small delays) are considered more impulsive. The DDT requires integration of the mesolimbic circuit across the nucleus accumbens shell, basolateral amygdala and orbitofrontal and prefrontal cortices (Bailey et al., 2016; Winstanley, 2010). Importantly, the DDT has high levels of

reliability across many species, including humans, with both intra-subject correlations and Cronbach's alpha near 0.9 (Weafer et al., 2013), and can be performed as early as age four in humans (Hodel et al., 2016). Thus, changes to measured levels of impulsivity in experimental animal models have high clinical relevance.

4.1.4 Study aim

The overall aim of this study was to investigate the relationships between impulsive choice and neuropathology in rats subjected to 5 consecutive CHIMERA impacts at 2.9J (first impact) and 2.4J (subsequent impacts) with a 14d inter-injury interval. These parameters were selected, in part, empirically, to balance the ethical use of animals for the behavioral and neuropathological objectives. Further, we wished to understand how rTBI potentially relate to dysfunction of reward pathways, as emerging evidence suggests that repetitive head injury may play a role in the development of impulsive phenotypes in humans. As assessment of impulsive choice using the DDT requires extensive testing, we selected the 14d interval to allow collection of DDT data for 10 sessions (5 sessions/week) after each injury. We terminated the study after 5 successive TBIs as significant behavioral differences were observed and neuropathological assessment was warranted. For the neuropathological arm of the study, we aimed to identify differences between sham and TBI groups that could explain their different behaviors, as well as to determine whether rat CHIMERA produces diffuse axonal injury similar to mouse CHIMERA.

4.2 Methods

4.2.1 Animals

Subjects were thirty-five male Long-Evans rats (Charles River, Wilmington, MA). Subjects were approximately 3 months of age at the start of training, 4.5 months at the first injury, and 6 months at euthanasia. Rats were food restricted to 85% of free-feeding weight (14-16 g PicoLab Rodent Diet 20 (62.4% carbohydrate, 24.5% protein, 13.1% fat) daily); water was available ad libitum. Rats were triple-housed throughout the duration of the study in trapezoidal Optirat cages (356 x 485 x 218 cm, Animal Care Systems, Centennial, CO) on a reverse light cycle (12h:12h) with a plastic hut and shredded paper towel available as enrichment. All procedures were approved by the University of British Columbia Animal Care Committee (A15-0040) and compliant with guidelines from the Canadian Council on Animal Care.

4.2.2 Delay discounting behavior

4.2.2.1 Apparatus

Training and testing took place in a bank of twelve standard five-hole operant chambers with a stimulus light at the back of each hole, and an infrared beam to measure nose pokes (Med Associates, St. Albans, VT). On the other side were two retractable levers with lights above, a house-light, and a food tray with a sucrose pellet dispenser attached (45 mg pellets, Bio-Serv, Flemington, NJ). Chambers were controlled by custom software written in Med-PC IV.

4.2.2.2 Training

Training on the delay discounting task (DDT) was performed as outlined previously (Vonder Haar et al., 2017). The left, center, and right (1, 3, 5) holes in the five-choice panel and the pellet

dispenser were used in this study. Briefly, rats were habituated to the chamber with sugar pellets placed in the food hopper, and in holes 1, 3, and 5 for one to two sessions. In the first stage of training, rats learned to respond to an illuminated hole 3 to receive one pellet until they successfully completed 30 trials in a single session. In stage two of training, rats responded first to illumination of hole 3, which turned on a light in either hole 1 or 5 (pseudo-randomly) and correct responses were reinforced with a single sugar pellet. Finally, in the last stage, a differential was introduced, with hole 1 delivering four sugar pellets and hole 5 delivering a single pellet. The location of the larger reinforcer hole (hole 1 or 5) was kept constant for each rat throughout training and testing, but was counterbalanced between subjects.

4.2.2.3 Delay Discounting Task

After the above training, the delay discounting task (DDT) began. Sessions lasted forty minutes and consisted of four blocks of twelve trials with a fixed 40 s intertrial interval (ITI). A trial began with the illumination of hole 3, and a nose poke would illuminate both choice holes 1 and 5. Failure to respond within 10 s was scored as an omission and activated the ITI. Rats chose between the large (four pellets) and small (one pellet) option, counterbalanced as above. The small option was always delivered immediately, while the delay to the large option increased in a step-wise fashion across successive blocks of trials, from 0 to 5, 10, and finally 20 s. Every block began with two forced-choice trials to ensure rats were exposed to the current delay contingency. After a choice was made and the reinforcer delivered, there was an ITI equal to the remaining trial time (40 s minus the delay to reinforcement). Rats were tested until a statistically stable choice baseline emerged, which required approximately thirty sessions. A total of N=35 rats successfully learned the DDT were matched for baseline performance and randomly assigned to

sham (N=11) or CHIMERA TBI (N=24) groups. Testing resumed 24 h after each subsequent injury and continued for two weeks (ten sessions at five sessions/week) until the next injury. A total of 5 cycles of injury and recovery were performed in this study.

4.2.3 Rat CHIMERA TBI procedure

Meloxicam (5mg/kg, subcutaneously [s.c.]; Boehringer Ingelheim Vetmedica Inc, Missouri) was administered 1 h prior to injury for analgesia. Rats were anesthetized with 5% isoflurane and placed supine on the rat CHIMERA device. A nose cone delivered 2% isoflurane while rats were strapped to the device with one Velcro strap around the abdomen that was fastened firmly to secure the animal, and another around the thorax that was loosely fastened to prevent hyperflexion of the thoracic spine in the sagittal plane during impact. Once secured, rats received a lactated ringer solution (5 mL, s.c.). Head position was verified as centered on the impact point approximately in front of bregma. The first injury was delivered at 7.6 m/s (2.9 J), but was subsequently reduced to 6.9 m/s (2.4J) for injuries 2-5 due to mortality of 4 rats during the first CHIMERA session (see Results). Piston velocities were obtained using photogate sensors on the rat CHIMERA device. Immediately after impact, animals were placed in a heated recovery cage and the time to right was recorded. Total procedure time, including anesthetic induction, took approximately 3 minutes. Sham animals received anesthesia yoked to the duration of injured animals, analgesic, hydration, and positioning on the CHIMERA device, but no impact.

4.2.4 Euthanasia and Tissue Collection

Rats were euthanized at the conclusion of the final testing period, eleven weeks after initial injury and three weeks after the fifth and final injury. Briefly, rats were anesthetized with a

combination of ketamine (100 mg/kg, intraperitoneal [i.p.]; Zoetis, New Jersey) and xylazine (7 mg/kg, i.p.; Bayer, Pennsylvania) and transcardially perfused with ice-cold heparinized phosphate-buffered saline (PBS). Brains were rapidly removed and one hemisphere was post-fixed in a 4% paraformaldehyde (PFA) solution for histology, while the other was sectioned into forebrain (7.56 to ~0 mm from bregma), midbrain (~0 to -3 mm from bregma) and hindbrain with a razor blade and immediately frozen on dry ice for biochemistry.

4.2.5 Immunohistochemistry

Hemibrains were post-fixed in 4% PFA for 2 d, then cryoprotected with 30% sucrose in PBS and 0.01% sodium azide for 3-4 d, after which 40 μm-thick coronal sections were cut using a cryotome (Leica Biosystems, Concord, ON). Immunohistochemistry was performed largely as described (Namjoshi et al., 2013) and included staining for tyrosine hydroxylase (TH) and dopamine active transporter (DAT) to detect dopaminergic neurons, Iba-1 to detect microglia, glial fibrillary acidic protein (GFAP) to detect astrocytes, SMI312 to detect neurofilament-light, CP13 to detect S202 phosphorylated tau, and silver staining to detect degenerating, argyrophilic axons. Sections stained for dopaminergic neurons (TH, DAT) followed an immunofluorescent protocol. Briefly, sections were washed in PBS and 0.5% Tween-20 for permeabilization, then blocked with 5% normal goat serum (NGS; Millipore Sigma S26-100ML) for 1h at room temperature (RT). Sections were incubated with primary antibodies for TH and DAT overnight at 4°C. Sections were then incubated with Alexa-Fluor secondary antibodies (Invitrogen, 1:1000) for visualization using fluorescence microscopy. For nuclear co-stain, mounted sections were coverslipped with ProLong Gold Antifade Mountant with 4′,6-diamidino-2-phenylindole (DAPI) (Invitrogen P36935). Sections stained for FluoroJade-C were co-stained with TH for

degenerating dopaminergic neurons. Sections were washed in PBS and 0.5% Tween-20 for permeabilization, then blocked with 5% NGS for 1h at RT. Sections were incubated with primary antibody for TH overnight at 4°C. Sections were then incubated with Alexa-Fluor 594 secondary for 4h at RT. After washing, sectioned were mounted on charged slides and dried. An abridged FluoroJade protocol was utilized to preserve the fluorescent TH signal. Slides were immersed on basic ethanol for 4 minutes, followed by a 2-minute rinse in 70% ethanol, then 1-minute rinse in distilled water. Slides were incubated in 0.06% potassium permanganate for 2 minutes, rinsed in distilled water for 1 minute, then incubated in 0.0001% FluoroJade in 0.01% acetic acid for 10 minutes. After washes and drying, sections were coverslipped with ProLong Gold Antifade Mountant with DAPI.

Sections stained for Iba-1, CP-13, NFL and GFAP followed a 3,3' Diaminobenzidine (DAB) staining protocol. Briefly, sections were quenched with hydrogen peroxide for 10 min and blocked with 5% NGS or 5% skim milk in PBS for 1h at RT. Sections were incubated with primary antibodies overnight at 4°C. Sections were then incubated with biotin-conjugated secondary antibodies (1:1000) and detected using a colorimetric procedure by incubating with ABC reagent (Vector Labs PK-6100, 1:400) before color development with DAB (Sigma D5637-1G).

Antibodies and dilutions were: TH (Millipore 657012, 1:500), DAT (Millipore MAB369, 1:500), Iba-1 (Wako 019-19741, 1:1000), CP-13 (Gift from Peter Davies, 1:500), NF-L (Abcam SMI-312 1:1000), and GFAP (Abcam ab7260, 1:500). Axonal injury was histologically evaluated by

Neurosilver staining (FD Neurotechnologies) following the manufacturer's instructions as described (Namjoshi et al., 2013).

4.2.6 Imaging of histological sections

Entire coronal sections were imaged using a Zeiss AxioScan Z1 slide scanner at 20x magnification. DAT and TH images of the VTA, basolateral amygdala, nucleus accumbens shell, olfactory tubercle, and orbitofrontal cortex were acquired as 0.5 μm z-stacks with a 40x oil objective on a Zeiss confocal laser scanning microscope (LSM880). FluoroJade-C and TH images of the VTA and olfactory tubercle were acquired as 1 μm z-stacks at 20x a Zeiss confocal laser scanning microscope. Images were flattened using the max projection function of Zen Black Pro software (v.14.0.12.201). Excitation and acquisition parameters were constrained across all images. The anterior commissure size and position relative to the corpus callosum and dorsal/anterior hippocampus were used as anatomical landmarks for consistent coronal section selection. Image quantification was performed using Image J (NIH), unless otherwise specified, on sections from N=7-10 rats in the Sham group and N=12-16 from the 5x TBI group.

4.2.7 Quantification of histological images

For TH and DAT quantification, images were manually thresholded and binarized. For puncta count and colocalization, binarized images were masked and analyzed using CellProfiler cell image analysis software (http://www.cellprofiler.org). Puncta size was set between 1- and 50-pixel units. A quantitative average of two acquired images per ROI was calculated and statistical analyses were performed on averaged values. CellProfiler pipelines can be made available upon request. For FluoroJade-C quantification, an ImageJ macro script was written to binarize,

threshold, and convert the images to masks. To measure the colocalization of FluoroJade to TH-positive signal, the FluoroJade signal was measured within the TH mask and reported as percent colocalization. Total FluoroJade signal, expressed as a percentage of the region, was also reported. For Iba-1 and GFAP quantification in grey and white matter regions, ROIs were manually isolated and thresholded; subsequently, count per area was used to determine differences between sham and 5x TBI groups after filtering background noise of particles less than 250-pixel units. For NF-L quantification, images were manually isolated, converted to 8 bit and thresholded using the ImageJ Auto-Thresholding function "Max Entropy". Background noise of particle size $<17\mu m^2$ or with circularity <0.2 were filtered. The number of axonal swellings per area of optic tract was then reported. For CP13 quantification, white matter areas, including corpus callosum and optic tract, were cropped and converted to 8 bit and thresholded. Background noise of particle size $<3.5\mu m^2$ were filtered. The number of stained particles per area of the white matter area was then reported. For grey matter areas, including prefrontal cortex (prelimbic and infralimbic area), layer 2-5 was aligned and cropped. Quantification was not possible due to strong variations in background stain intensity. However, CP13-positive neurons were manually identified based on shape (neuronal cell body and neurite). Representative images of the injury group were then reported. Silver staining images were quantified by manually isolating ROIs, thresholding and reporting the percentage area containing signal relative to the white matter area, as described (Namjoshi et al., 2013). Corpus callosum thickness was measured using Iba1-stained sections at bregma. The corpus callosum was isolated and measured using the 'polygon selections' tool in ImageJ. The area was then measured and reported.

4.2.8 Biochemistry in fore- and midbrain homogenates

Midbrain and forebrain sections were homogenized in 8-volumes of ice-cold radioimmunoprecipitation assay (RIPA) lysis buffer containing protease and phosphatase inhibitor cocktails (Roche, Branford, CT) and centrifuged at 9,000 rpm for 10min at 4°C. The supernatant was extracted and frozen at -80°C until analyzed. Total protein concentration was measured by bicinchoninic acid (BCA) assay (Biorad, Redmond, WA). Forebrain and midbrain regions were analyzed separately given the frontal-sensitive nature of impulsivity (Clark et al., 2004; Winstanley, 2007). Forebrain and midbrain homogenates were diluted 1:2 in dilution buffer provided in the assay kit, and incubated overnight (4°C) in a multiplex ELISA to measure IL-1β, IL-6, and TNF-α (V-plex K15059D, Mesoscale Diagnostics). Samples were read on a microplate reader (Mesoscale Sector Imager). For analysis of total and phosphorylated tau (threonine 231), brain homogenates were diluted 1:50 in 10% blocker A in the provided Tris wash buffer, and assayed for tau and phosphorylated tau (p-tau; thr231) levels in a duplex ELISA (Mesoscale Diagnostics, K15121D), following the manufacturer's protocol. All analyte concentrations were normalized to the total protein concentration in the lysate.

4.2.9 Data analysis and statistics

In previous work, we used the fit of a hyperbolic discounting function to analyze choice behavior (Vonder Haar et al., 2017). This formula works best when multiple data points are available (e.g. one week of data). In the current study, this was not feasible because a measure of daily change as a result of the injury was a planned part of the study. We therefore elected to use the measure of Area Under the Curve (AUC) (Myerson et al., 2001), which is calculated by drawing straight lines between data points and calculating the percent or proportion of total area that falls beneath

those lines. This measure correlates with the fitted discounting function and allows for more reliable daily measurement of choice. Curve fits (using the hyperbolic function) for an entire week of data are still provided alongside the raw data for context.

Statistical tests for behavioral and biochemical outcomes were conducted using R statistical software (http://www.r-project.org/), using the *stats*, *lme4* and *lmerTest* libraries. Repeated measures data (delay discounting, loss of righting, impulsive choice impairment status) were analyzed using mixed effects regression, with individual rat intercepts as the random effect. Linear regressions were used for group comparisons, while piecewise regression (on AUC) and logistic mixed effects regression (on impairment status) evaluated within-subjects effects. P-values were estimated using the *lmerTest* library. Cytokine and tau protein levels were compared in one-way ANOVAs. Any main effects of group were followed by a Dunnett's post-hoc test to compare to the sham group. Statistical analyses for histological quantification were conducted on GraphPad Prism (v6.07). Unless otherwise specified, Welch's t-test was utilized as the groups were normally distributed, but had unequal variances and unequal sample sizes. Ratio data was log transformed to improve normality assumptions. Two-tailed parametric Pearson coefficients with a 95% confidence interval were utilized where r values were calculated for X vs every Y in the data set. For all statistical tests, a p-value of less than 0.05 was considered significant.

The study design is summarized in (**Figure 4.1**)

4.3 Results

4.3.1 Rat CHIMERA design

A new CHIMERA device was engineered to produce TBI in rats (**Figure 4.2 A-C**). To produce the desired impact characteristics, a 100 g stainless-steel piston body with a diameter of 0.75 and a 0.394 (10 mm) tip was made. It was also necessary to increase the impact energy (piston velocity) substantially to obtain the desired head kinematics. Larger air pressures were required to provide the necessary impact energies, which required using higher capacity pneumatic components specifically for the pressure regulator and pressure gauge. With higher impact energies, additional venting was also required to prevent the piston from rebounding off of the compressed air and striking the head a second time. Venting was accomplished by installing a second solenoid valve with a pipe tee at the bottom of the barrel that would open after the piston had finished accelerating.

To accommodate the larger size of the rat, the length of the body platform was increased from 6 to 9 in. Animal body restraints were adjusted by using a rice-filled bag instead of a carved closed cell foam bed, and by adapting the locations of the Velcro straps. The head plate was modified to accommodate the larger impactor tip and to align the head properly with the impact location. A 30° body-plate inclination angle allowed the frontal and parietal bones to lie flat over the hole in the head plate. To prevent rats from sliding down the body platform at this angle, the device frame was inclined to match the angle of the body platform such that the body was horizontal and the head was inclined relative to the ground.

In addition to these structural changes, the rat CHIMERA device also included the first implementation of an electronic controller. This controller offers two major functional improvements: direct measurement of piston impact velocity and improved impact energy repeatability. The controller utilizes a pair of infrared photo-interrupters located at the end of the piston barrel (nearest the head), which send a signal to the controller when the piston passes by each of them. With a constant distance between the photo-interrupter pair, the piston velocity can be determined by dividing this distance by the time between the signals. Photogate velocity readings are calibrated using velocity measurements obtained from analysis of high-speed video of the piston tip as it protrudes beyond the head plate.

4.3.2 Injury-related morbidity and mortality

The total number of animals that were removed over the course of the study due to death, humane endpoint, or morbidity was eight of twenty-four injured animals (33%) and 0 of 11 sham animals (0%) (**Figure 4.2 D**). During first injury at 7.5 m/s (2.9 J), three of twenty-four rats in the CHIMERA TBI group died and one reached humane endpoint and required euthanasia during acute recovery. Specifically, two animals died as a result of intracranial hemorrhage, one died as a result of nasal hemorrhage, and one was humanely euthanized after poor recovery and showed signs of intracranial hemorrhage on necropsy. The high levels of morbidity and mortality were unexpected, as results from pilot experiments on cadaveric animals suggested that impacts <3.0 J would not cause hemorrhage (data not shown). Impacts at 4.4 and 6 J led to skull fracture around the site of impact, while impacts at 3.2 and 3.4 J caused severe hemorrhaging within the nasal cavity. Upon extraction of the brain, subdural hemorrhages were also observed in animals subjected to 3.2 and 3.4 J. In a live pilot, impacts <3.0 J (2.7 – 2.9 J) did not lead to skull

fracture, nasal bleeds, or subdural hemorrhage (N = 24). In the present study, we observed significantly higher levels of morbidity and mortality following a single impact at 2.9 J, which led us to consult our veterinary staff. We subsequently reduced injury severity to 6.9 m/s (2.4 J) for subsequent injuries to limit mortality. The recorded average impact velocity for injury 1 was 7.56 m/s (2.86 J energy), while injuries 2-5 averaged 6.95 m/s (2.42 J energy). After injury 2, one rat was humanely euthanized after poor recovery and showed intracranial hemorrhage on necropsy, one was removed from the study due to blindness, and one displayed transient seizure activity but recovered, leaving N=18 rats in the CHIMERA TBI group that progressed to injury 3. After injury 3, one rat displayed seizures and died due to intracranial hemorrhage, leaving N=17 rats in the TBI group that progressed to injury 4. There was no morbidity or mortality for injury 4, and one rat died after injury 5, leaving a total of N=16 rats that completed the CHIMERA TBI arm of the study. No morbidity or mortality was observed for the N=11 rats in sham group and all sham animals completed the study. Because mixed-effects regression does not require list-wise deletion (i.e., removal of a rat's data from the study), all available data were used, even for rats with early mortality. The only behavioral exclusion was the rat that developed blindness. Histological analyses only included data from rats that completed the study as it was not feasible to collect tissue in the cases of early mortality.

4.3.3 Loss of righting reflex

Loss of righting reflex (LRR) was recorded for all animals (**Figure 4.2 E**), however, data from injury 3 was lost due to a computer malfunction. To control for anesthesia effects, the anesthesia time for each sham procedure was yoked to an injured animal. A mixed effects linear regression (LRR~Group*Injury#) revealed that CHIMERA injury tended to increase LRR duration that

approached but did not reach statistical significance across the entire study (β=0.69, t=2.06, p=0.057), likely driven by considerable LRR durations in injuries 1 and 2 for CHIMERA rats. LRR duration tended to decrease across subsequent CHIMERA injuries, however this decrease did not reach significance.

4.3.4 Impulsive decision-making increases as a function of CHIMERA injury exposure

CHIMERA TBI and sham groups were evaluated for impulsivity on the DDT by measuring their area under the discounting curve (AUC) followed by linear mixed effects regression analysis (AUC~Group*Injury #). Raw data and curve fitting using a hyperbolic function for an entire week of data are provided for context **(Figure 4.3)**.

As the interaction of Group and Injury number was significant (p<0.001), follow-up linear mixed effects regression analyses were performed for the ten sessions after each injury (AUC~Group*Session). The CHIMERA TBI group displayed significantly increased impulsivity (reduced AUC) after injuries 4 and 5 (p's<0.016, **Figure 4.4 A**). However, a significant Group x Session interaction on Injury 1 (p=0.013), showed a significant, but transient decline in performance, and the interaction on Injury 2 also approached significance (p=0.087; **Figure 4.4 A**).

The lack of early group differences can largely be attributed to considerable heterogeneity in individual rats' responses to injuries. To examine the effects of injury within subjects, a piecewise linear mixed effects regression was then performed on impulsivity as a function of injury number and post-injury slope (AUC~Injury1 + Injury1 Slope … + Injury5 + Injury5 Slope + Overall Time) separately for each group **(Figure 4.4 B).** Sham animals displayed one

significant *decrease* in impulsive decision-making from injury 2 to injury 3 (p= 0.039). By contrast, the CHIMERA TBI group showed significant increases in impulsivity from baseline to Injury 1 (p=0.006), from Injury 1 to Injury 2 (p=0.023), and from Injury 3 to Injury 4 (p=0.010; see **Table 4.1** for a summary of statistics), suggesting that substantial effects still occur at earlier injuries.

An additional means of considering the cumulative effects of injury is to determine the likelihood of impairment as a result of successive TBIs. To analyze this, we performed linear mixed effects logistic regression on the percent of animals that showed mild, moderate, or severe impairments in impulsive decision-making (defined as greater than 1, 2, or 3 standard deviations below their own individual baseline; Impaired~Group*Injury#) **(Figure 4.4 C-E)**. A 1 standard deviation increase in impulsivity occurs in slightly under 20% of sessions (baseline), whereas a 2 standard deviation or greater change occurs extremely rarely under uninjured conditions. Successive CHIMERA injuries produced a significant shift in the percent of animals displaying greater than 1 or 2 standard deviations in impairment (1 SD: b=0.44, z=4.87, p<0.001; 2 SD: b=0.29, z=1.98, p=0.047). When measured at 3 standard deviations, there was no interaction, but main effects of group and cumulative injuries remained (Group: b=3.72, z=2.19, p=0.029; Injury: b=0.60, z=2.13, p=0.033*;*). Because injured animals were significantly different from sham when measured at 1, 2, or 3 standard deviations below baseline, a separate logistic function was calculated with only injured animals (Impaired~Injury) to evaluate the predicted impairment functions as a result of successive injuries **(Figure 4.4 F)**. Extrapolated from these data, the ED50 for mild impairment is 3.32 CHIMERA injuries, for moderate impairment is 5.44 CHIMERA injuries, and for severe impairment is 7.62 CHIMERA injuries **(Figure 4.4 F)**.

4.3.5 5xTBI induces neuropathological changes consistent with disruption of the mesolimbic reward circuit

The alteration of impulsive choice prompted us to test for neuropathological changes in the mesolimbic reward pathway. Intriguingly, quantitation of tyrosine hydroxylase (TH)-positive puncta showed that the reduction of dopaminergic innervation trended towards significance in the olfactory tubercle in the 5xTBI group (p=0.0545), with no significant changes compared to sham animals in the VTA, basolateral amygdala, nucleus accumbens (shell) or orbitofrontal cortex **(Figure 4.5 A).** As it is important to assess the synaptic lifetime of dopamine through probing of its reuptake machinery, we also quantified dopamine transporter (DAT) in the aforementioned regions and observed no significant changes **(Figure 4.5 B)**. However, when DAT:TH colocalization were assessed, we found that colocalization within the olfactory tubercle was significantly reduced (p=0.0308), whereas the VTA, basolateral amygdala, nucleus accumbens (shell) and orbitofrontal cortex showed no differences following repetitive injury **(**Figure 4.6**Figure 4.6 B-E)**.

Analysis of the nigrostriatal dopaminergic pathway showed that 5xTBI has no significant effect on TH, DAT or their colocalization within the substantia nigra and dorsolateral striatum **(Figure 4.7)**. These observations support a selective effect of repetitive CHIMERA TBI on the dopaminergic mesolimbic reward pathway consistent with our behavioral observations of increased impulsivity without alterations in overall motor behavior. As the olfactory tubercle is located almost exactly opposite to the injury site, and may be vulnerable to contrecoup injury, we postulated that the region might be undergoing neuronal degeneration. However, quantification

of FluoroJade-C signal colocalized with TH-positive neurons and puncta showed no significant changes in the VTA and olfactory tubercle following 5xTBI **(Figure 4.8 A).** Furthermore, no significant differences in total FluoroJade signal, expressed as a percentage of the entire region of interest, were observed in the ventral tegmental area and the olfactory tubercle **(Figure 4.8 B)**.

4.3.6 5xTBI induces white matter inflammation and degeneration

We investigated injury-related inflammatory and degenerative changes in two white matter tracts sensitive to murine CHIMERA injury, namely the corpus callosum and optic tract, using silver staining, and immunohistochemistry for microglia (Iba-1), glial fibrillary acidic protein (GFAP), neurofilament-light (NF-L) and phosphorylated (p-) tau **(Figure 4.9 A-G, Figure 4.10 A-G).**

In the corpus callosum, no changes were observed by silver staining **(Figure 4.9 C),** however a significant increase in Iba-1 and GFAP immunoreactivity was evident **(Figure 4.9D,** Iba-1: p=0.0080; **Figure 4.9**Figure 4.9 **E,** GFAP: p=0.0007), indicating increases in microglial and astrocytic recruitment and/or proliferation. While there were no changes in NF-L immunoreactivity following 5xTBI, we saw an interesting decrease in corpus callosum thickness **(Figure 4.9 G,** p=0.0248). Within the optic tract, we observed significant increases in silver staining **(Figure 4.10 C;** p<0.0001**)** and Iba-1 immunoreactivity **(Figure 4.10 D;** p<0.0001**).** However, we did not see changes in GFAP and NF-L immunoreactivity in the optic tract **(Figure 4.10 E, F)**. We also observed increased p-tau within the optic tract following 5xTBI associated with distinct dystrophic axonal punctae **(Figure 4.10 G**; p<0.0001**).**

4.3.7 5xTBI induces selective changes in p-tau and microglia within the mesolimbic pathway

We examined gray matter regions involved in the mesolimbic pathway for the presence of pre-tangle-like aggregates and dystrophic neurites using p-tau immunohistochemistry. Increased p-tau S202 was qualitatively observed within the nucleus accumbens (shell) and orbitofrontal cortex, but not in the VTA, basolateral amygdala and olfactory tubercle **(Figure 4.11)**. Quantification was not possible due to strong individual variations in background stain intensity.

Upon examination of the mesolimbic pathway using Iba-1 immunohistochemistry **(Figure 4.12)**, we saw increased Iba-1 within the olfactory tubercle, but not in the VTA, basolateral amygdala, nucleus accumbens (shell), or orbitofrontal cortex **(Figure 4.12 C-G)**. This inflammatory profile may be related to decreased dopaminergic innervation into the olfactory tubercle.

4.3.8 Correlations between DDT performance and neuropathology

We calculated Pearson correlations using sham and 5xTBI data extracted from final performance on DDT performance with the neuropathological observations of p-tau deposition and corpus callosum thinning. We observed a significant negative correlation between degree of behavioral impairment and quantified p-tau in the optic tract (r=-0.5496, p=0.0036; **Figure 4.13 A**). Conversely, corpus callosum thickness was positively correlated with lesser impairments, suggesting that subjects with callosal thinning exhibited increased impulsivity (r=0.4647, p=0.0450; **Figure 4.13 B**). We also assessed correlations between DDT performance and all significant neuropathological outcomes, presented in **Table 4.2**. None of the other significant neuropathological findings were found to correlate with DDT performance.

4.3.9 No changes in tau or inflammatory biochemical markers in fore- and midbrain homogenates are observed after 5xTBI

ELISA was used to test for altered biochemical profiles of total tau, p-tau, IL-1β, Il-6 and TNF-α in forebrain and midbrain segments at endpoint. No significant differences were observed for any analyte tested, nor of the p-tau:t-tau ratio, between sham and 5xTBI groups for either forebrain or midbrain segments **(Table 4.3)**, highlighting the importance of the regional specificity shown above.

4.4 Discussion

A variety of neurological problems and increased risk for psychiatric disease are associated with both single and repetitive TBI (Broshek et al., 2015; Donnell et al., 2012; Wilk et al., 2012). The current study was designed to explore the relationship between repetitive TBI, impulsive choice, white matter pathology and dopaminergic signaling in rats. We adapted CHIMERA, an established model of diffuse axonal injury in mice, to rats, and demonstrated that repeated TBIs caused progressively increased impulsive choice, reduced dopaminergic terminals in the olfactory tubercle of the ventral striatum, and caused white matter pathology including neuroinflammation, tau pathology and atrophy. Thus, repetitive rat CHIMERA produces a constellation of behavioral and neuropathological outcomes and may serve as useful model to investigate the sequelae of rTBI. Impulsivity, broadly defined as action without forethought (Winstanley et al., 2006), is a relatively common psychiatric-like complication as a result of moderate-to-severe TBI (Bjork et al., 2016; Goswami et al., 2016). Choice impulsivity, or decisions that result in short-term gains to the detriment of long-term outcomes, is specifically

increased following severe, focal TBI (Dixon et al., 2005; Rochat et al., 2010). Reports of specific impulsivity measurements following human concussion are somewhat limited; however, many studies indicate that impulsive phenotypes or impulsive-related disorders are associated with mild brain injury (Bjork et al., 2016; Goswami et al., 2016; Graham and Cardon, 2008). Studies in athletes may provide a better quantification of mTBI incidence, and indeed, such research demonstrates a relationship between items such as total fight exposure (in boxers and mixed martial arts fighters), reduced subcortical structure volume, and trait impulsivity as measured by questionnaires (Banks et al., 2014).

The underlying etiology of impulsivity and other psychiatric-like dysfunction in TBI are still relatively unknown, although monoaminergic dysfunction may be a major contributor to impulsive symptoms (Ozga et al., 2018). Data in patients demonstrate enduring dopamine dysfunction, including reduced DAT densities, even when measured many months after injury (Donnemiller et al., 2000; Jenkins et al., 2018). However, in the case of TBI, this dysfunction does not happen in isolation. Notably, the disruption of dopamine pathways may be directly mediated by other pathological factors such as lesion formation and neuroinflammation, and ultimately lead to the emergence of psychiatric symptoms, as well as Parkinsonian-like neurodegeneration (Najjar et al., 2013; Zgaljardic et al., 2015). Given the importance of the mesolimbic circuit in mediating reinforcement-driven behaviors, these dopamine disruptions may reduce capacity for carrying out decisions involving risk and reward, resulting in cognitive impairments.

Despite high clinical relevance, relatively little animal work has focused on the psychiatric aspects of brain injury. In the current study, we measured the effects of repetitive CHIMERA injuries in rats on the DDT, an assessment of trait impulsivity with established translational relevance. While transient changes were observed after a single injury, significant group differences in impulsivity did not emerge until rats were exposed to four or more injuries **(Figure 4.3 A)**. Studies of human concussion show large individual variability as some patients develop marked deficits (Carroll et al., 2014) while others display relatively minor impairment (Shultz et al., 2017; Williams et al., 2015). Here, we also observed considerable heterogeneity in how individual rats responded to injuries, both behaviorally and neuropathologically. Importantly, measurement of impairment as a function of individual baseline performance across 5 injury cycles allowed us predict the likelihood of mild, moderate, or severe impairment in impulsive decision-making after a given number of TBIs. We determined that 3-4 injuries would be necessary to produce mild impairment in half of our population, whereas 5-6 injuries would be needed for moderate impairment, and 7-8 injuries would be required for severe impairment.

Importantly, the current study is the first to demonstrate the effects of successive TBI on impulsive choice in either human or animal settings. However, we have previously reported similar increases in impulsive choice in the CCI model of TBI, a focal means of inducing injury, where impulsivity was increased even with relatively mild focal injury. In contrast to the current data, and possibly due to the open-skull nature of the injury, we also observed cortical inflammation as measured by cytokine elevation in brain homogenate (Vonder Haar et al., 2017). The current study with rat CHIMERA injury suggests a more muted pathological phenotype, with no overt loss of tissue as occurs in focal open-skull models, and selective

inflammation as measured by microglia activity in the mesolimbic pathway, potentially owing to the repeat stress of rotational forces. While the pathophysiology of mild TBI is, not surprisingly, subtle, multiple studies are beginning to converge upon similar findings. For instance, one recent study examined the ability to inhibit actions (motor impulsivity) after concussive TBI in juvenile rats and found that behavioral disinhibition was increased (albeit, selectively in males) (Hehar et al., 2015). Further, the researchers found pathological features similar to what we report here: alteration of dopamine-related genes (*Comt*, *Drd2*, *Drd3*, *Drd4*, *Maoa*) in the nucleus accumbens and prefrontal cortex as well as changes in dendritic complexity, suggesting alterations to these pathways.

Of particular interest in the current study are the selective alterations to the mesolimbic circuit while sparing the nigrostriatal pathway. Additional studies will be needed to determine the mechanisms that underlie loss of DAT, including loss of the transporter itself, synaptic changes, and axonal damage. Further, the CHIMERA injury settings used here appear to restrict dopaminergic changes to the mesolimibic circuit, which differs from studies using more severe injury models of CCI or fluid percussion injury where significantly decreased TH and DAT in the substantia nigra have been observed (Impellizzeri et al., 2016; Liu et al., 2017). These differences suggest the more subtle nature of the pathology associated with repeated CHIMERA TBI. While dopamine dysfunction may be a proximal cause of impulsive symptoms, our neuropathological analysis showed that repeated CHIMERA TBI resulted in diffuse white matter pathology including axonal damage, microgliosis, astrogliosis, corpus callosum thinning and elevated p-tau immunoreactivity. These observations are consistent with a growing number of rat TBI studies across a wide variety of models. For example, Thomsen et. al. observed persistent

motor dysfunction, corpus callosum thinning and tauopathy in rats subjected to 5X CCI (Thomsen et al., 2016), which persisted at chronic time points ~8 months post-injury (Thomsen et al., 2017). Using 4X mild lateral fluid percussion injury in rats, Brooks et. al. observed inflammation in the ipsilateral corpus callosum, cortex, internal capsule and thalamus that was accompanied by corpus callosum thinning and reduced performance in MWM probe trials (Brooks et al., 2017). Mountey et. al. observed sensorimotor dysfunction, prolonged gait abnormalities, inflammation, GFAP, tau, and white matter thinning in rats subjected to repeated noninvasive closed head mTBI (Mountney et al., 2017), whereas Gao et. al. observed behavioral dysfunction and activated microglia and GFAP without changes in total or p-tau (ser 202) levels after repetitive mTBI in rats (Gao et al., 2017). Using a modified focal weight drop model with up to 3X TBI spaced 5 days apart, McAteer et. al. observed increased tau phosphorylation and microglial activation in the cortex, amyloid precursor protein immunoreactivity, increased escape latency in the Barnes maze and increased anxiety-like behavior (McAteer et al., 2016). Much remains to be learned about how histological changes induced by CHIMERA compare to those of other models, and which of these reflect pathological compared to repair processes.

The approach reported here has several clear advantages over prior research. The first is the use of CHIMERA to deliver well-controlled repeat injuries. The current iteration of this device includes a two-solenoid design for the release of air pressure to drive the piston, and the venting of air pressure to stabilize the piston after impact. This minimizes inter-operator variability, and provides a reliable (± 2%) impact velocity. Second, the reliability of the injury model is combined with sensitive behavioral testing which can be directly translated into neuropsychological and clinical settings. The DDT in particular has high levels of retest validity,

meaning that changes to measured levels of impulsivity are likely to be clinically relevant. Finally, repeated testing with a behavioral assay that is stable across time allowed us to detect relatively subtle effects. One of the largest challenges of studying mild TBI is how to measure what is, by definition, a condition that exerts very minor effects or only affects a subset of individuals (Cassidy et al., 2004). This consideration empowered the generation of predictive models to estimate the likelihood of impairment after a given number of TBIs. Models such as this could be useful, especially when considering questions such as return to play for athletes, return to work for military personnel, or for the inclusion of biomarker data.

As CHIMERA is a relatively new platform to model TBI in multiple animal species, there is as yet no consensus on which criteria should be used to assign injury severity. In mice, we have found that impact energies up to the skull fracture threshold produce surprisingly mild behavioral and neuropathological phenotypes characterized primarily by white matter inflammation (Namjoshi et al., 2014, 2017). In this inaugural rat CHIMERA study, we observed significant mortality and instances of intracranial hemorrhage suggestive of moderate-severe injury even though the LRR data, akin to GCS, did not differ significantly between sham and TBI groups, which is more suggestive of a mild injury. Consistent with the expected phenotype of mild injury, our neuropathological assessment revealed no evidence of gross structural damage or neuronal death, as shown by a lack of significant FluoroJade-C staining, but indicated consistent diffuse axonal injury and some regions with grey matter inflammation and p-tau deposition. We have therefore refrained from assigning an injury severity to the 5xTBI group.

The study of mTBI is one of the more difficult topics in the field of neurotrauma, with multiple research challenges including selection of injury models, biomarkers, and relevant behavioral assessments. Therefore, it may be beneficial to shift the core question of mTBI from "what are the effects of *X* concussions?" to "how many concussions are necessary for *X* level of dysfunction?" as described herein. This approach may facilitate the identification of biological markers that help identify and predict when an individual is on the cusp of transitioning to impairment as a result of successive injuries. In the current study, we suggest that altered dopamine signaling, combined with white matter neuroinflammation, may be one such marker. Future studies, ideally using a drop-out design including gene expression changes and analyses of neuronal architecture, will be required to fully delineate how altered dopaminergic signaling after repetitive CHIMERA TBI in rats relates to behavioral changes. It will also be important to determine if additional repeated TBIs lead to dysfunction in the nigrostriatal pathway or alter responses to dopaminergic drugs which may be prescribed for both impulsive and motoric dysfunction. As this area is further developed, we may better understand the relationships among head injury exposure, alterations to both neuroinflammatory and dopamine signaling, emergence of psychiatric-like complications, and development of neuropathology including but not limited to findings associated with CTE.

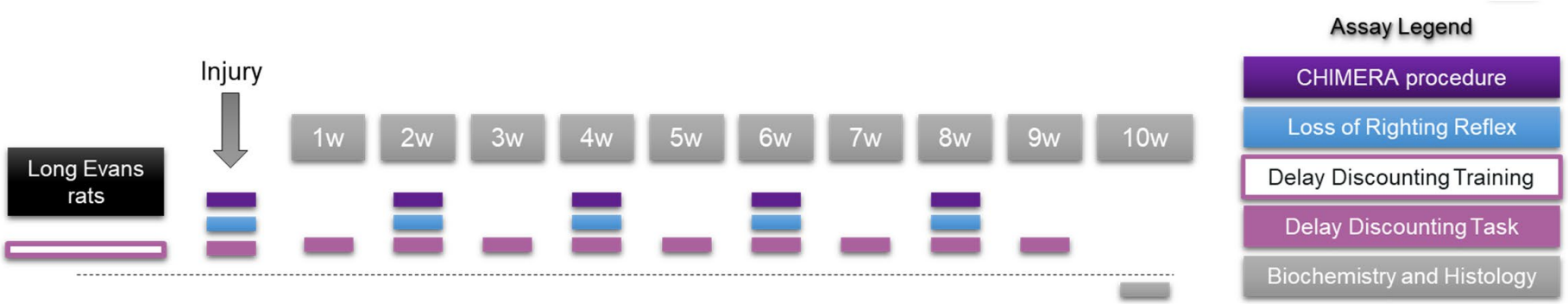

Figure 4.1 Study design.

Prior to first TBI, rats were trained on the delay discounting task. At T=0, injury was induced at 2.9J, after which LRR latency was recorded. Subsequent injuries were induced two weeks apart, at 2.4J. In the two weeks between injuries, the delay discounting task was carried out in sham and TBI animals. Animals were euthanized 10 weeks after the initial injury, 3 weeks after the final injury.

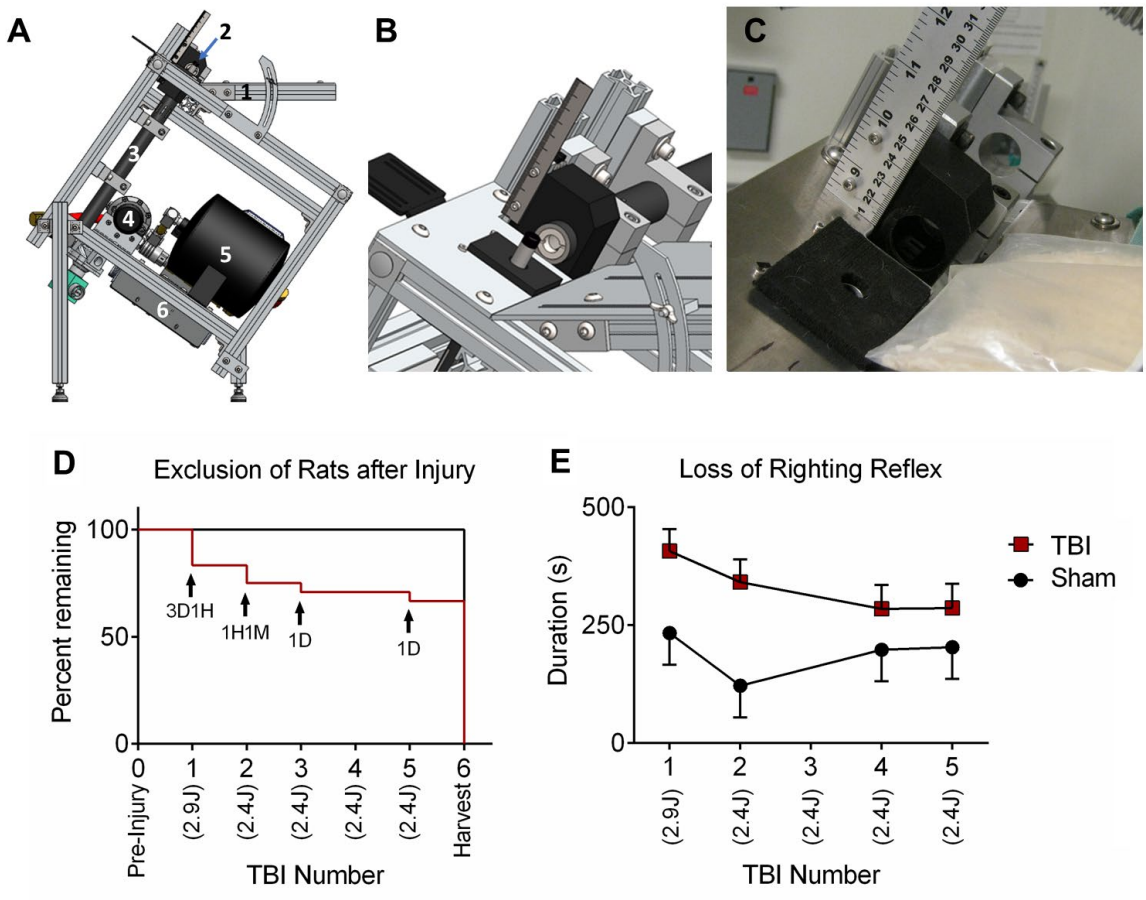

Figure 4.2 Schematics of the rat CHIMERA, mortality rates and loss of righting reflex latency following CHIMERA TBI.

(A) Rat CHIMERA digital schematic is shown from frontal view. Parts are labelled with numbers as follows: 1) body plate, 2) impact piston, 3) vertical-impact piston barrel, 4) air pressure regulator, 5) air tank, 6) CHIMERA motherboard. (B) Zoomed in head plate shown for clarity. (C) Photo of rat CHIMERA animal platform. (D) Cumulative exposure to TBI at 2.9J (1st week) or 2.4J (2nd to 5th week) resulted in a final exclusion rate of 33%. The abbreviations under the exclusion curve indicate the number of animals excluded after each TBI. D: pre-mature death, H: humane endpoint, M: morbidity, including blindness. (E) Repetitive CHIMERA TBI in

resulted in an increase that trended toward significance for the duration of loss of righting reflex (LRR) (p=0.057). LRR at week 3 was not recorded due to computer failure.

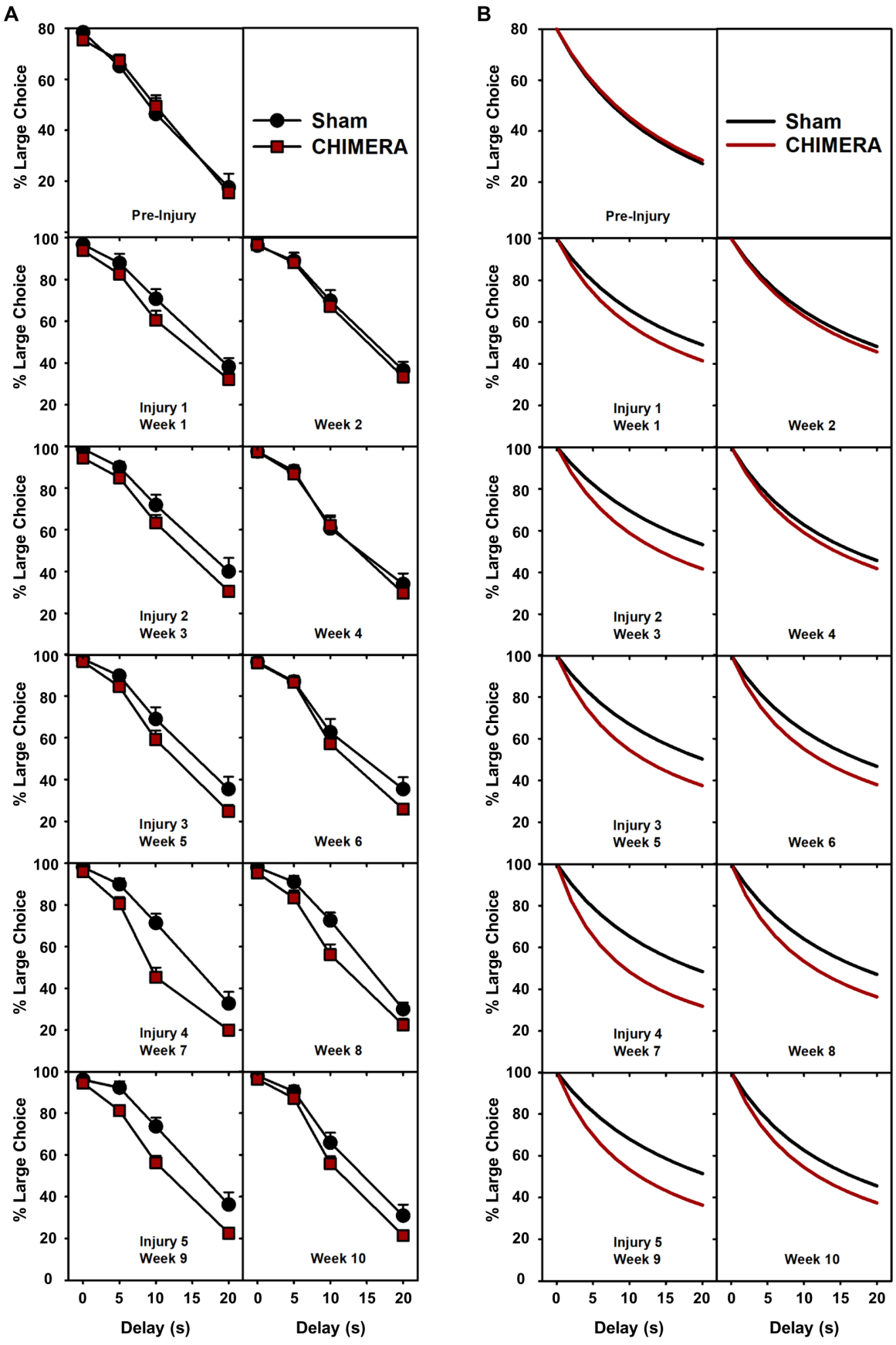
A
B
Sham
CHIMERA
% Large Choice
Pre-Injury
Injury 1
Week 1
Week 2
Injury 2
Week 3
Week 4
Injury 3
Week 5
Week 6
Injury 4
Week 7
Week 8
Injury 5
Week 9
Week 10
Delay (s)
0
5
10
15
20
0
20
40
60
80
100

Figure 4.3 Raw behavioral findings following delay discounting task.

(A) Raw data from the delay discounting task (mean + SEM) and (B) curve fits from the hyperbolic discounting function. Over several weeks of testing, the CHIMERA animals shifted downward, demonstrating less tolerance for delays, or increased impulsivity. These data were used to calculate the area under the curve for subsequent analyses.

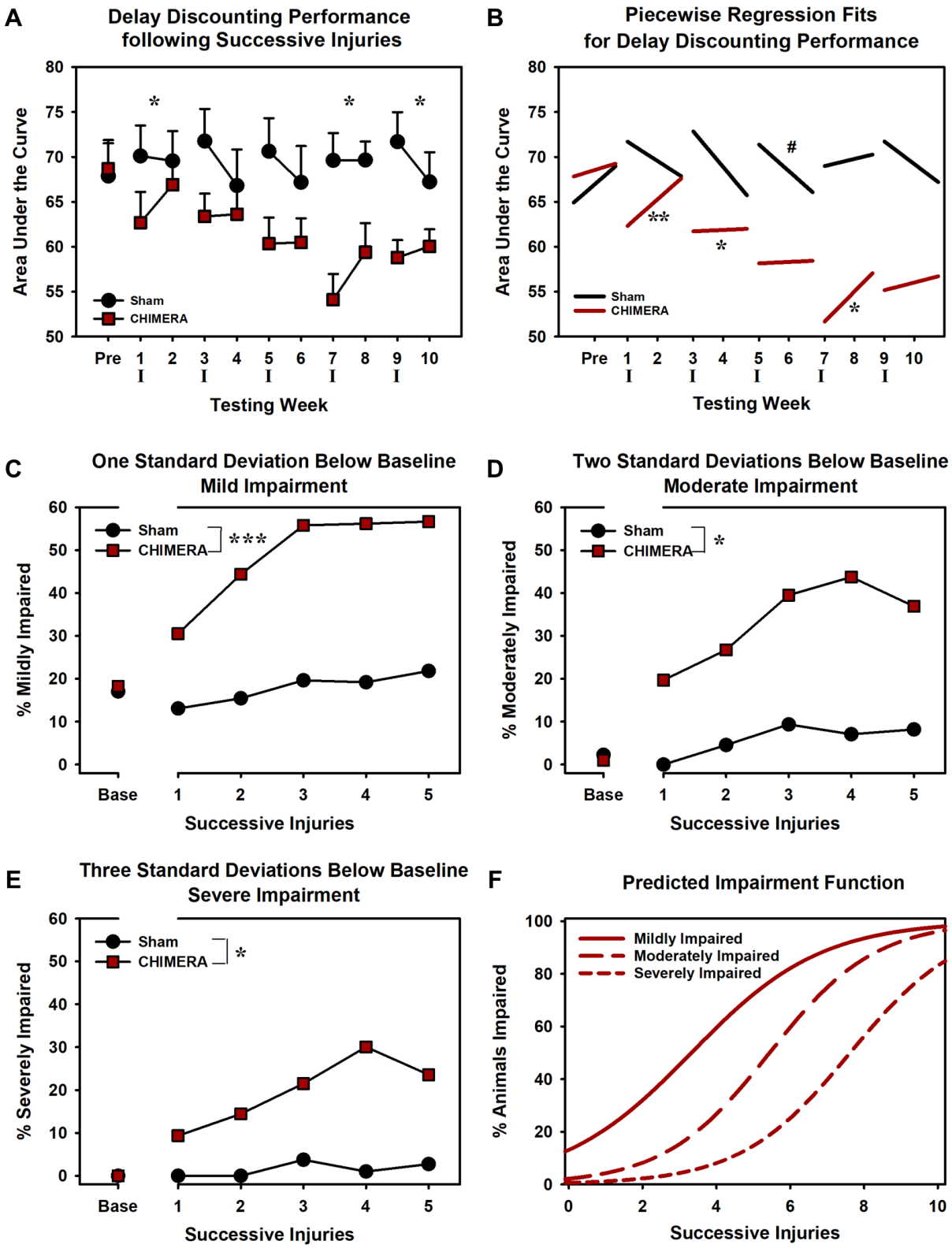
A
Delay Discounting Performance
following Successive Injuries
Area Under the Curve
Testing Week
Sham
CHIMERA
B
Piecewise Regression Fits
for Delay Discounting Performance
Area Under the Curve
Testing Week
Sham
CHIMERA
C
One Standard Deviation Below Baseline
Mild Impairment
% Mildly Impaired
Successive Injuries
Sham
CHIMERA
D
Two Standard Deviations Below Baseline
Moderate Impairment
% Moderately Impaired
Successive Injuries
Sham
CHIMERA
E
Three Standard Deviations Below Baseline
Severe Impairment
% Severely Impaired
Successive Injuries
Sham
CHIMERA
F
Predicted Impairment Function
% Animals Impaired
Successive Injuries
Mildly Impaired
Moderately Impaired
Severely Impaired

Figure 4.4 Impulsive decision-making increases as a function of CHIMERA injury exposure.

(A) Averaged area under the curve (AUC) for each group across time (mean + SEM); smaller AUC values are representative of increased impulsivity. Overall, there was a significant effect of group on impulsivity (p=0.041). Individual analyses revealed that CHIMERA animals were significantly different from sham after the first (Group X Session interaction: p=0.013), fourth, and fifth injuries (main effect of Group: p's < 0.016). (B) Piecewise regression fits to compare the effects of each injury within subjects. Sham animals significantly improved impulsivity from injury 2 to injury 3 (p=0.039). CHIMERA animals got significantly worse after injuries, 1, 2, and 4 (p's < 0.024). (C) Mild impairment, defined as one standard deviation below individual baseline increased over time in the CHIMERA group (p<0.001). (D) Moderate impairment also increased across time for CHIMERA animals (p=0.047). (E) Severe impairment levels were significantly increased overall in the CHIMERA group (p=0.029). (F) Prediction function showing that the likelihood of impairment increases as a function of successive injuries for CHIMERA animals. Symbols: * = p<0.05; ** = p<0.01; *** = p<0.001 relative to sham. # = p<0.05 for Sham animals. Data are mean±SEM for (A), regression predictions for (B, F), and means for (C-E).

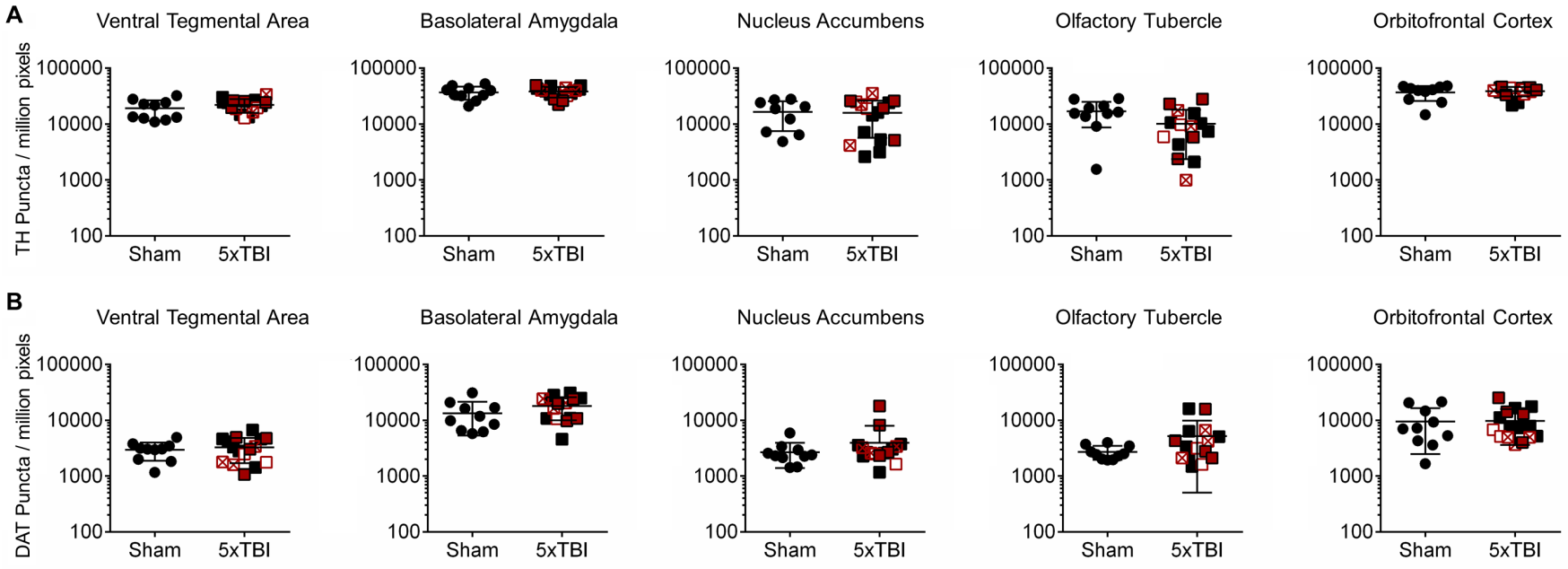

Figure 4.5 Raw quantification of TH and DAT immunohistochemistry in the mesolimbic pathway showed no changes in puncta count following 5xTBI.

(A) After 5xTBI, no differences in TH puncta count were observed in the ventral tegmental area, basolateral amygdala, nucleus accumbens, olfactory tubercle and orbitofrontal cortex, although the decrease is trending towards significance in the olfactory tubercle (p=0.0545). (B) After 5xTBI, no differences in DAT puncta count were observed in the aforementioned structures. In (a-b) TBI samples are color coded based on performance on the DDT relative to individual baseline: solid black = within baseline; red border, white fill = 1 SD below baseline; red cross = 2 SD below baseline; solid red = 3 SD below baseline. Data are presented as mean±SD.

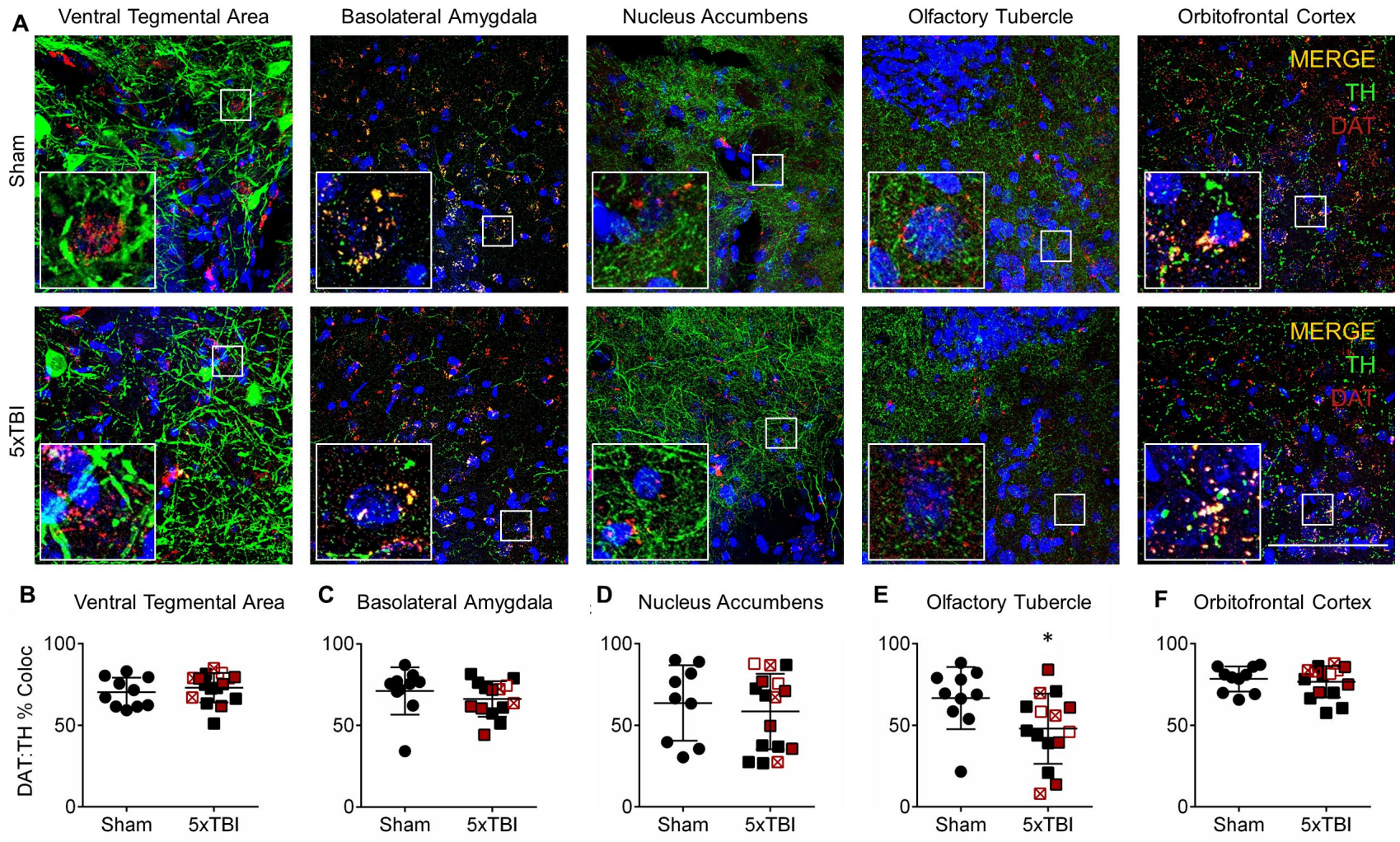

Figure 4.6 5xTBI induces neuropathological changes consistent with disruption of the mesolimbic reward circuit.

(A) A panel displaying 40x TH and DAT images within the mesolimbic system with high magnification insets; scale bar = 100 μm. (B) After 5xTBI, no differences in DAT to TH colocalization were observed in the ventral tegmental area, (C) basolateral amygdala, and (D) nucleus accumbens shell. Interestingly, there was a significant decrease in DAT:TH colocalization within the (E) olfactory tubercle of the ventral striatum (p=0.0330), due to a trending decrease in the presence of TH+ neurons. (F) No differences were observed in the orbitofrontal cortex. In (B-F), TBI samples are color coded based on performance on the delay discounting task relative to individual baseline: solid black = within baseline; red border, white fill = 1 SD below baseline; red cross = 2 SD below baseline; solid red = 3 SD below baseline. Data are presented as mean±SD. Symbols: * = p<0.05.

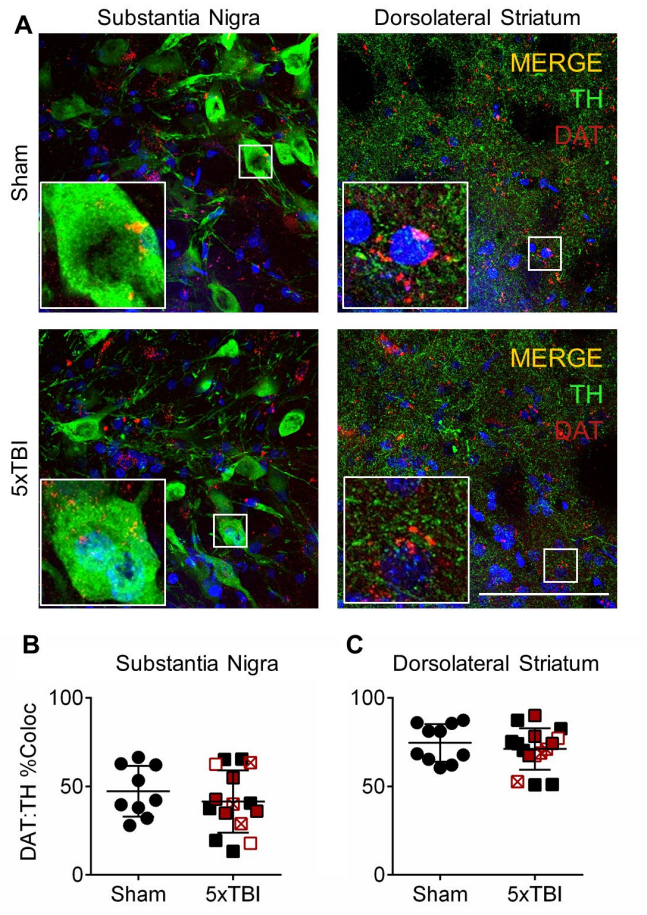

Figure 4.7 The dopaminergic nigrostriatal pathway showed no changes in DAT:TH colocalization following 5xTBI.

(A) A panel displaying 40x TH and DAT images within the nigrostriatal system with high magnification insets; scale bar = 100 μm. (B) After 5xTBI, no differences in DAT to TH colocalization were observed in the substantia nigra and (C) dorsolateral striatum, indicating that the motor pathway of the dopaminergic system remained intact after injury. In (B-C) TBI samples are color coded based on performance on the DDT relative to individual baseline: solid black = within baseline; red border, white fill = 1 SD below baseline; red cross = 2 SD below baseline; solid red = 3 SD below baseline. Data are presented as mean±SD.

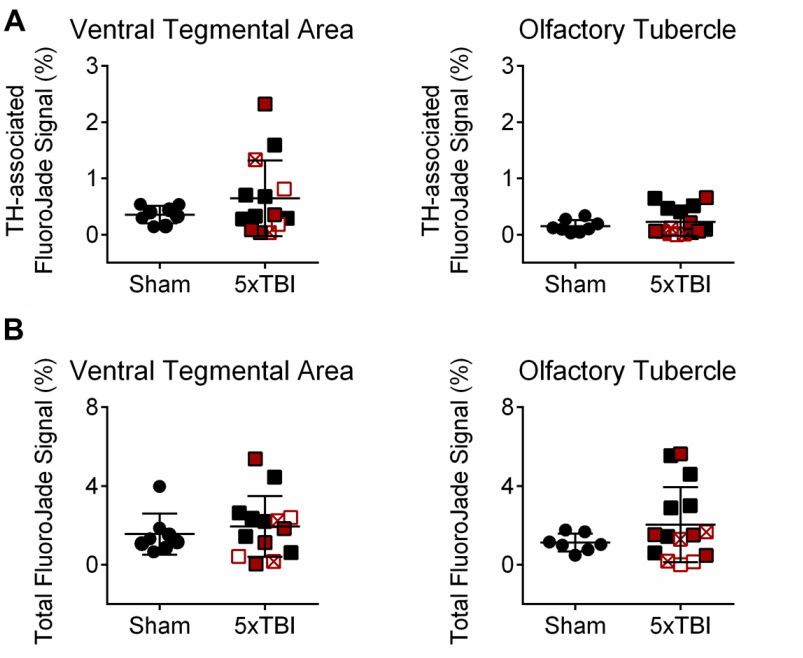

Figure 4.8 FluoroJade-C signal in the VTA and olfactory tubercle showed no changes following 5xTBI.

(A) After 5xTBI, no significant differences in FluoroJade colocalization with TH were observed in the VTA and the olfactory tubercle, suggesting a lack of dopaminergic neuronal death in these regions. (B) After 5xTBI, no significant differences in total FluoroJade signal, expressed as a percentage of the entire region of interest, were observed in the VTA and the olfactory tubercle. However, FluoroJade signal is trending towards significance in the olfactory tubercle ($p=0.0993$). In (A-B), TBI samples are color coded based on performance on the DDT relative to individual baseline: solid black = within baseline; red border, white fill = 1 SD below baseline; red cross = 2 SD below baseline; solid red = 3 SD below baseline. Data are presented as mean±SD.

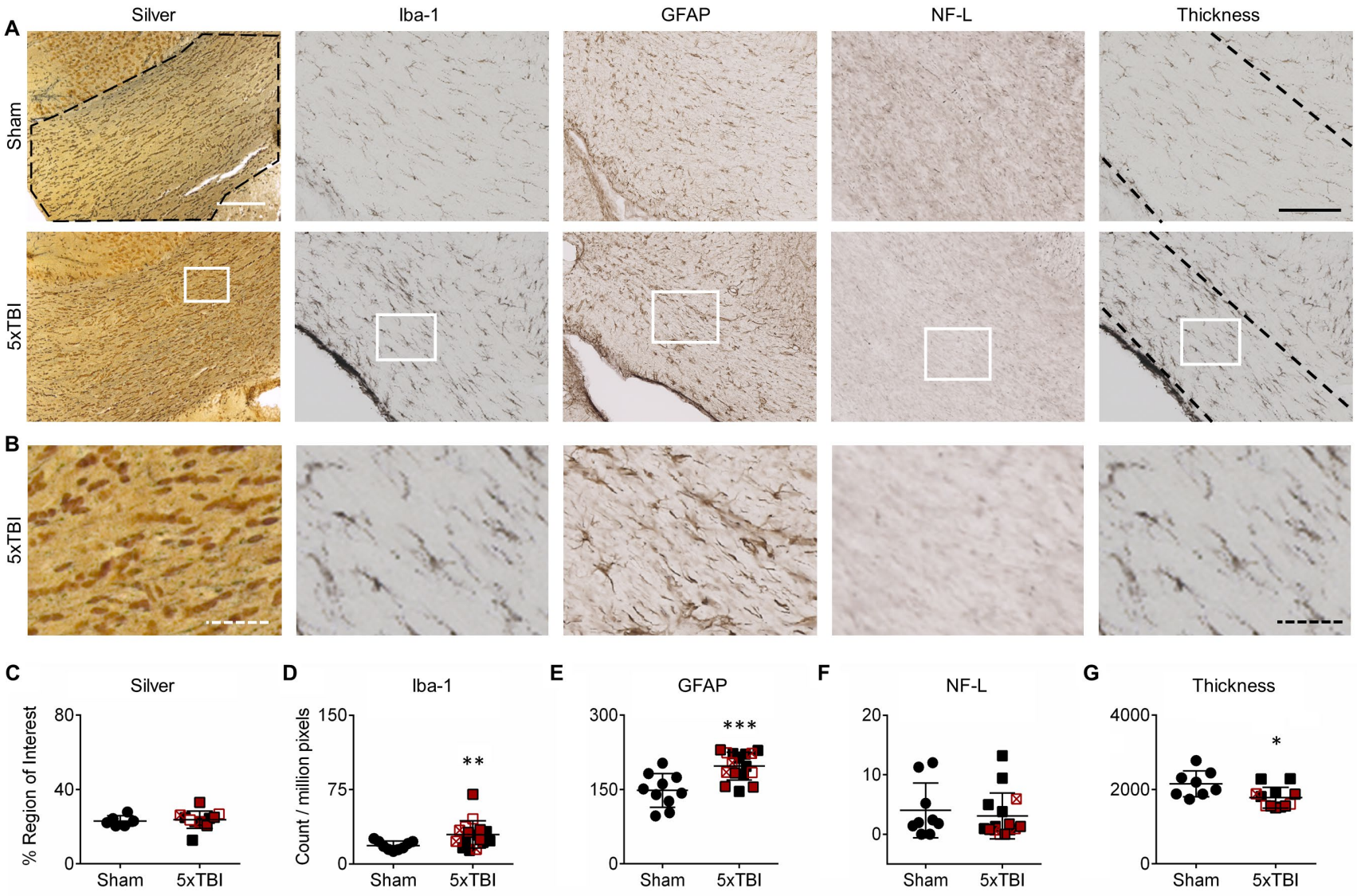

Figure 4.9 5xTBI induces white matter inflammation and degeneration in the corpus callosum.

(A) A panel displaying silver, Iba-1, GFAP, and NF-L staining within the corpus callosum at 20x magnification; scale bar = 100 μm. (B) Higher magnification images showing silver, Iba-1, GFAP, and NF-L staining within the corpus callosum following 5xTBI using digital zoom; scale bar = 25 μm. (C) After 5xTBI, the corpus callosum showed no changes in argyrophilic axons. However, (D) activated microglia (Iba-1) were increased following 5xTBI. p=0.0080. (E) Increased astrogliosis was observed in the corpus callosum following 5xTBI (p=0.0007) whereas (F) no differences were observed for NF-L positive axonal bulbs (SMI312). (G) There was a significant decrease in thickness of the corpus callosum after 5xTBI (p=0.0248). In (C-G), TBI samples are color coded based on performance on the DDT relative to individual baseline: solid black = within baseline; red border, white fill = 1 SD below baseline; red cross = 2 SD below baseline; solid red = 3 SD below baseline. Data are presented as mean±SD. Symbols: * = p<0.05, ** = p<0.01, *** = p<0.001.

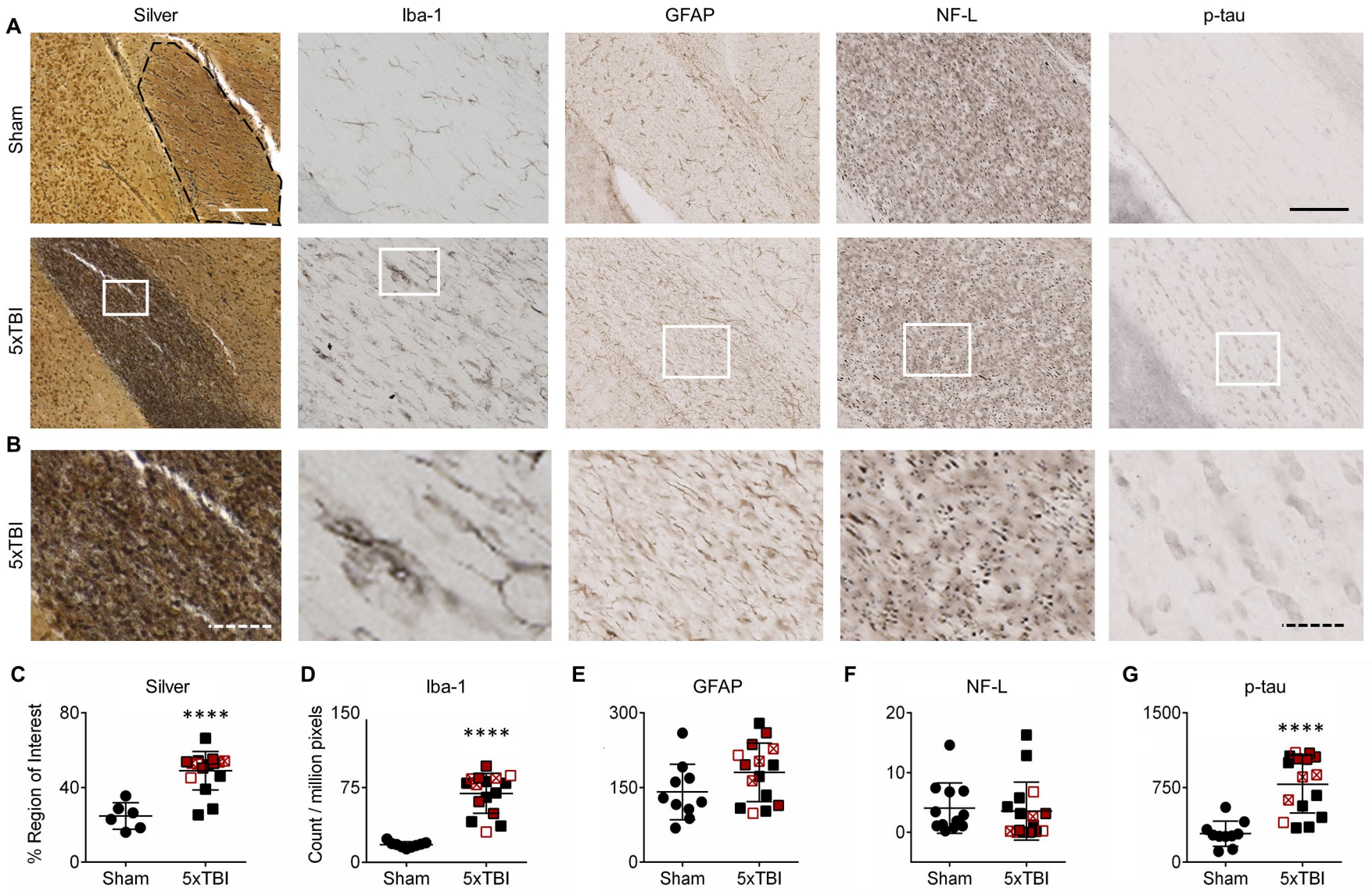
A
Silver
Iba-1
GFAP
NF-L
p-tau
Sham
5xTBI
B
5xTBI
C
Silver
% Region of Interest
80
40
0
****
Sham
5xTBI
D
Iba-1
Count / million pixels
150
75
0
****
Sham
5xTBI
E
GFAP
300
150
0
Sham
5xTBI
F
NF-L
20
10
0
Sham
5xTBI
G
p-tau
1500
750
0
****
Sham
5xTBI

Figure 4.10 5xTBI induces white matter inflammation and degeneration in the optic tract.

(A) A panel displaying silver, Iba-1, GFAP, NF-L and p-tau staining within the optic tract imaged at 20x magnification; scale bar = 100 μm. (B) Higher magnification images showing silver, Iba-1, GFAP, NF-L and p-tau staining within the optic tract following 5xTBI using digital zoom; scale bar = 25 μm. (C) After 5xTBI, the optic tract showed increased number of argyrophilic axons (silver; $p<0.0001$) and (D) activated microglia (Iba-1; $p<0.0001$). (E, F) No differences were observed for GFAP and NF-L positive axonal bulbs (SMI312) in the optic tract. (G) The optic tract showed increased number of p-tau-positive dystrophic axonal punctae (CP13; $p<0.0001$). In (C-G), TBI samples are color coded based on performance on the DDT relative to individual baseline: solid black = within baseline; red border, white fill = 1 SD below baseline; red cross = 2 SD below baseline; solid red = 3 SD below baseline. Data are presented as mean±SD. Symbols: **** = $p<0.0001$.

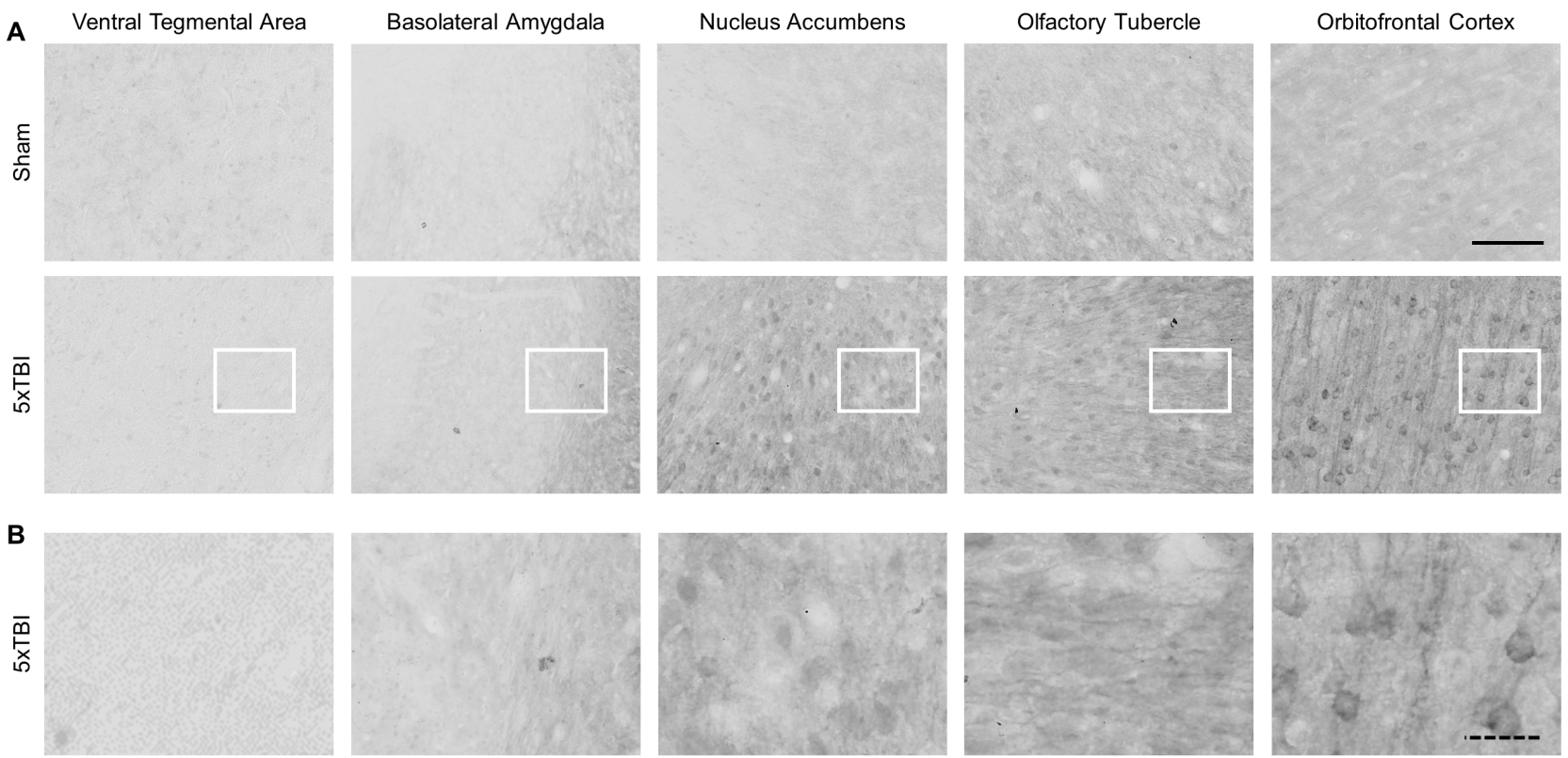

Figure 4.11 5xTBI induces selective changes in p-tau within the mesolimbic pathway.

(A) A panel displaying p-tau staining within the mesolimbic system at 20x magnification; scale bar = 100 μm. (B) Higher magnification images showing p-tau staining within the mesolimbic system following 5xTBI using digital zoom; scale bar = 25 μm. After 5xTBI, no qualitative differences in p-tau staining were observed in the ventral tegmental area, basolateral amygdala, and

olfactory tubercle. Interestingly, there was a qualitative increase in p-tau staining within the nucleus accumbens shell and orbitofrontal cortex. Quantification was not possible due to strong variations in background stain intensity.

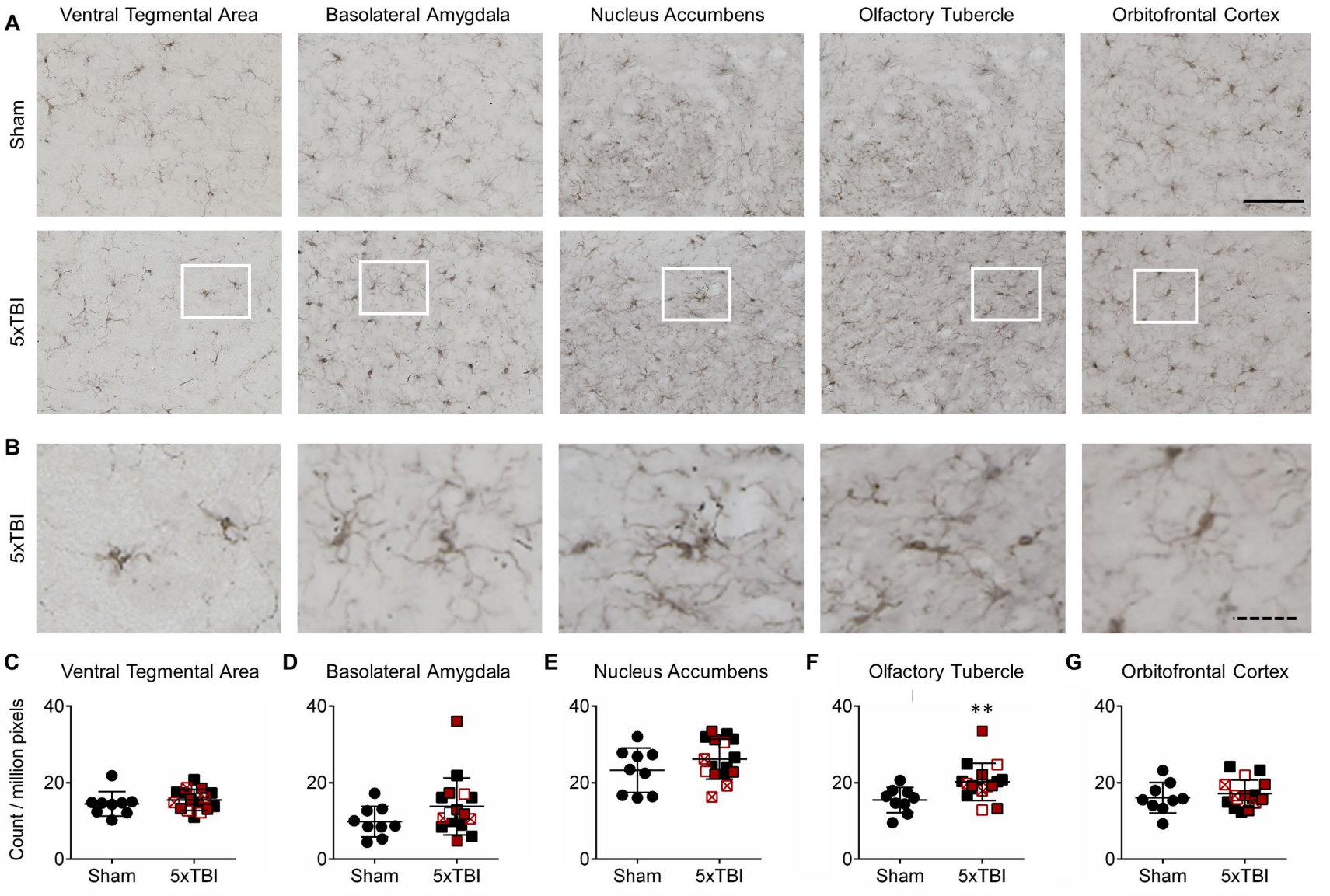
A
Ventral Tegmental Area
Basolateral Amygdala
Nucleus Accumbens
Olfactory Tubercle
Orbitofrontal Cortex
Sham
5xTBI
B
5xTBI
C
Ventral Tegmental Area
D
Basolateral Amygdala
E
Nucleus Accumbens
F
Olfactory Tubercle
G
Orbitofrontal Cortex
Count / million pixels
40
20
0
Sham
5xTBI
**

Figure 4.12 5xTBI induces selective changes in microglia within the mesolimbic pathway.

(A) A panel displaying Iba-1 staining within the mesolimbic system at 20x magnification; scale bar = 100 μm. (B) Higher magnification images showing Iba-1 staining within the mesolimbic system following 5xTBI using digital zoom; scale bar = 25 μm. (C) After 5xTBI, no differences in Iba-1 staining were observed in the ventral tegmental area, (D) basolateral amygdala, (E) nucleus accumbens shell. (F) Interestingly, there was a significant increase in Iba-1 staining within the olfactory tubercle of the ventral striatum (p=0.0088). (G) No differences were observed in the orbitofrontal cortex. In (C-G), TBI samples are color coded based on performance on the DDT relative to individual baseline: solid black = within baseline; red border, white fill = 1 SD below baseline; red cross = 2 SD below baseline; solid red = 3 SD below baseline. Data are presented as mean±SD. Symbols: ** = p<0.01.

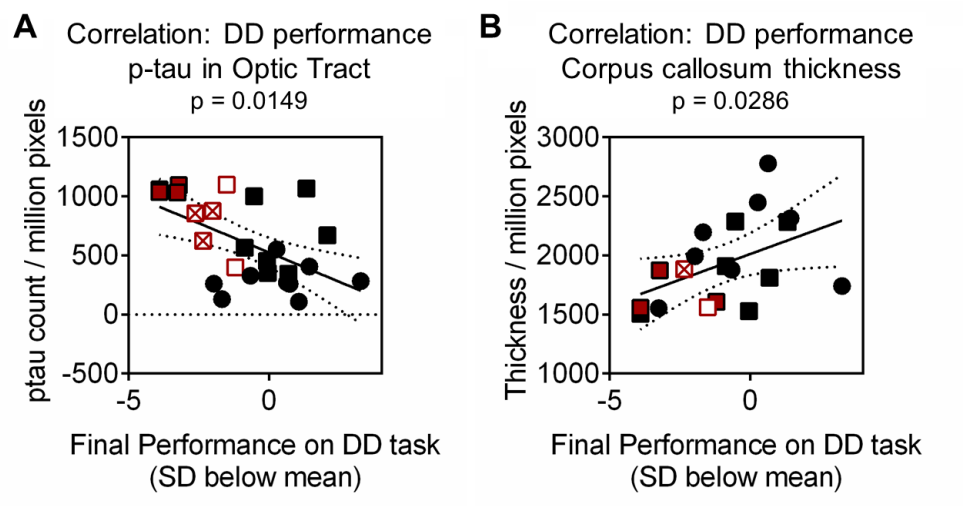

Figure 4.13 Correlations between DDT performance and neuropathology.

(A) Pearson correlations were calculated for sham and 5xTBI data extracted from final performance on delay discounting task and p-tau quantification in optic tract. The negative correlation reached significance (r=-0.5496, p=0.0036). (B) The positive correlation between sham and 5xTBI data extracted from final performance on delay discounting task and corpus callosum thickness was also significant (r=0.4647, p=0.0450). In (A-B) TBI samples are color coded based on performance on the DDT relative to individual baseline: solid black square = within baseline; red border, white fill = 1 SD below baseline; red cross = 2 SD below baseline; solid red = 3 SD below baseline. Sham samples: solid black circle.

Table 4.1 Linear regression results for group differences across injuries.

		β	*t*	*p*
Overall	Group	-0.50	-2.14	***0.041***
	Injury #	0.03	1.02	*0.307*
	Group*Injury #	-0.33	-8.37	***<0.001***
Injury1	Group	-0.31	-1.03	*0.312*
	Session	-0.08	-1.30	*0.196*
	Group*Session	0.18	2.49	***0.013***
Injury2	Group	-0.53	-1.47	*0.154*
	Session	-0.14	-2.36	***0.019***
	Group*Session	0.13	1.72	*0.087*
Injury3	Group	-0.52	-1.68	*0.105*
	Session	-0.09	-1.60	*0.111*
	Group*Session	0.10	1.34	*0.183*
Injury4	Group	-0.79	-2.77	***0.010***
	Session	0.03	0.41	*0.685*
	Group*Session	0.08	1.01	*0.315*
Injury5	Group	-0.69	-2.61	***0.015***
	Session	-0.10	-1.45	*0.148*
	Group*Session	0.14	1.54	*0.126*

Table 4.2 Correlations between DDT performance and neuropathology

	Pearson's coefficients: DDT performance and neuropathological outcomes
DAT:TH Olfactory Tubercle	r = 0.08428 *p = 0.7652*
Iba1 Corpus Callosum	r = -0.4751 *p = 0.0629*
Iba1 Optic Tract	r = -0.2969 *p = 0.2641*
Iba1 Olfactory Tubercle	r = 0.3165 *p = 0.2323*
GFAP Corpus Callosum	r = 0.1975 *p = 0.4635*
Silver Optic Tract	r = -0.4859 *p = 0.0563*

Table 4.3 Biochemical measurement of tau and inflammatory cytokines following repetitive CHIMERA injury.

	Forebrain			Midbrain		
Analyte	**Sham (n=11)**	**TBI (n=16)**	***p-value***	**Sham (n=11)**	**TBI (n=16)**	***p-value***
Total tau (ng/mg)	4297 ± 190	4843 ± 190	*0.0613*	4740 ± 248	5155 ± 139	*0.1298*
P-tau (unit/mg)	242.3 ± 12.2	258.2 ± 10.5	*0.3357*	304.6 ± 17.2	335.8 ± 11.6	*0.1299*
Ratio p:total tau (unit/ng)	0.0563 ± 0.00147	0.0535 ± 0.00140	*0.1892*	0.0646 ± 0.00233	0.0653 ± 0.00175	*0.8174*
IL-1β (pg/mg)	11.0 ± 0.566	10.8 ± 0.492	*0.7453*	6.49 ± 0.300	7.15 ± 0.314	*0.1588*
IL-6 (pg/mg)	53.4 ± 1.94	54.9 ± 1.86	*0.5983*	45.0 ± 1.38	45.7 ± 1.34	*0.7108*
TNFα (pg/mg)	0.130 ± 0.0133	0.152 ± 0.0179	*0.3695*	0.0677 ± 0.00481	0.0748 ± 0.00387	*0.2586*

Chapter 5: Conclusions

5.1 Summary of findings

The social burden of head injury is undeniable, with TBI affecting almost 3 million individuals in the US (Faul et al., 2010) and about 155,000 in Canada (Rao et al., 2017) on an annual basis. Our neuropathological understanding of TBI is largely derived from post-mortem human samples, which are not only scarce, but are also skewed to the most severe injuries. To help fill the gaps in our understanding of the neuropathological sequelae following TBI, we developed CHIMERA, a scalable, non-surgical, impact-acceleration model of rodent TBI that reliably produces DAI characterized by white matter inflammation and axonal damage.

We began by investigating the behavioral and neuropathological phenotypes induced by single CHIMERA TBI up to 0.7J. We demonstrated the capability of CHIMERA to induce scalable outcomes based on biomechanical inputs, as single CHIMERA TBI at 0.6 and 0.7J in wild-type mice induced acute neurological and motor deficits, increased proinflammatory cytokines in brain, and triggered white matter damage and inflammation, in the absence of blood-brain barrier leakage and grey matter microgliosis.

Subsequently, we used a 3D-printed interface to induce more severe injuries with evidence of vascular damage and grey matter inflammation. Interface-assisted single CHIMERA TBI at 2.5J in wild-type mice induced acute neurological deficits, elevated plasma total tau and NF-L levels, transiently increased proinflammatory cytokines in brain, and induced blood-brain barrier leakage and microstructural vascular abnormalities, as well as grey matter microgliosis. Memory

deficits emerged at sub-acute time-points. Though the memory deficits we observed are largely resolved by chronic time-points, white matter inflammation was most extensive at our chronic time-point.

Lastly, we expanded the CHIMERA platform to rats, to better understand the relationship between rTBI, impulsivity and neuropathology. Compared to sham controls, rats with rTBI displayed progressive impairment in impulsive choice. In addition to histological changes sustained by the mesolimbic dopaminergic system, grey and white matter inflammation along with tau immunoreactivity were observed.

5.2 Significance of findings

Prior to CHIMERA, there existed a void in the pre-clinical space for a reproducible rodent model of TBI that uses impact-acceleration to generate the behavior and neuropathology associated with human TBI. The CHIMERA model produces an impact-acceleration injury by allowing unrestricted head motion post-impact, with the intent to mimic the pathophysiology following mild and moderate-severe TBI in humans. Ultimately, we hope that, by mimicking the outcomes associated with human TBI, we will be able to create a platform that can be used to test therapeutics. Animal studies have been widely used to provide target validation and proof-of-concept efficacy data for TBI therapeutics. Thus far, however, all of the tested therapies for TBI have not translated into effective intervention for the human condition (Stein, 2015). Though no single animal model has been able to capture the entire spectrum of pathological outcomes of human TBI, rotational platforms are showing promise (Clevenger et al., 2015; Johnson et al., 2018). From a biomechanical perspective, few models are able to capture the head kinematics

that contribute to TBI-induced tissue deformation. We speculate that impact-acceleration and rotation are key biomechanical features that would increase the likelihood of a pre-clinical model being sufficient to reproduce the complex pathophysiology following TBI.

The mouse CHIMERA was specifically developed to fill the void of a non-surgical rodent model of impact-acceleration injury, maintaining the reproducibility associated with FP and CCI, while incorporating the linear and rotational head movement that is associated with clinical TBI. The CHIMERA platform, which has been distributed to fifteen international sites since its conception, is now yielding data sets that are encouragingly consistent across sites. Chen et al., who delivered three CHIMERA impacts at 0.6J in young C57Bl/6, observed acute behavioral and inflammatory changes that were congruent with previously published results using CHIMERA, including LRR changes, motor deficits, and acute gliosis in major white matter structures (optic tract and corpus callosum). Chen et al also found that CHIMERA rTBI produced chronic gliosis in both white matter and grey matter (hippocampus and cortex) and cognitive learning and memory impairments that lasted up to 6.5 months after the initial injuries. In particular, injured mice required more time to travel to the visible platform during the Morris Water Maze, also spending less time in the platform quadrant during probe trials when the platform had been removed. Their findings overlap significantly with the findings discussed in this thesis, and also demonstrate the capacity for CHIMERA to model long-lasting effects following CHI events.

In addition to the mouse CHIMERA, we adapted the CHIMERA system to rats, to first understand the relationship between rTBI, impulsivity, and neuropathology. The results from our

inaugural study have begun to elucidate some of the neurobiological underpinning of impulsivity following rTBI, which is of particular clinical relevance. There has been much lay media attention on the clinical features of CTE as a consequence of repetitive head trauma, which can include impulsivity-related neuropsychiatric disturbances, however, much remains to be learned about how rTBI precedes behavioral changes and neurodegeneration. The rat CHIMERA platform will be of particular benefit to help answer these research questions.

5.3 Limitations of studies

5.3.1 Use of rodents

The major limitation of the experiments presented within this thesis lies in the use of rodents to help elucidate a human condition. In general, animal models of disease have inherent biological characteristics that make the move from bench to bedside increasingly difficult. In addition to possessing lissencephalic (smooth) brains instead of gyrencephalic (folded) brains, rodents have a lipid profile that differs substantially from that of the human; they possess vastly higher levels of the vasoprotective high density lipoproteins (HDL), and are therefore more resistant to atherosclerosis. It is speculated that this evolutionary difference endows rodents with inherent vascular resilience and thus may make both mice and rats a less than optimal choice for modelling cerebrovascular damage sustained following TBI. We speculate that animals with a lipid profile that is more akin to humans (e.g. hamsters, mini-pigs, etc.) may be better suited for studying injury-induced cerebrovascular damage in particular, but there are a number of limitations to their use. However, genetic manipulation of rodents, and mice in particular, has been very well elucidated, which makes studying the combination of brain injury and neurodegeneration feasible.

5.3.2 Use of males

Though we incorporated females into the pilot study described in Chapter 3, we were not sufficiently powered to assess sex differences appropriately. The lack of females in our studies is a limitation, as numerous sex-specific alterations have been reported in outcomes of neuronal morphology and connectivity (McGlade et al., 2015; Semple et al., 2017), behavior (Scott et al., 2015), in-hospital complications (Adediran et al., 2019), and mortality (Adediran et al., 2019; Albrecht et al., 2016) following TBI across the age spectrum. It is worth noting that contrary to popular belief, the rates of TBI in girls' sports are much higher than in boys' sports (Arambula et al., 2019; Marar et al., 2012; Rosenthal et al., 2014), with girls soccer having the highest rates of sports-related mTBI than any other sport, regardless of gender. In addition to high incidence rates, intriguing psychosocial sex-differences emerge in adulthood following a history of pediatric TBI. While males are more likely to report externalizing problems (e.g. substance abuse), females are more likely to report internalizing problems (e.g. mood disorders) even years after injury (Scott et al., 2015). In a recent study assessing pediatric brain injury in mice, males were significantly more affected by the reduction of dendritic complexity in hippocampal dentate gyrus neurons as compared to females (Semple et al., 2017). These neuronal deficits were thought to precede deficits in sociability and social recognition, as the males subjected to TBI showed deficits in both domains. The females only showed deficits in sociability after injury, but not in social recognition (Semple et al., 2017). The neuroinflammatory sequelae following TBI is also thought to be influenced by sex. At acute time-points (up to 7d post-injury), experimental TBI in male adolescent/young adult mice led to a more 'aggressive' neuroinflammatory profile, characterized by a rapid increase in pro-inflammatory cytokines and cortical microgliosis that

peaks at 1d post-TBI (Villapol et al., 2017). In the females, cortical microgliosis peaks at 7d post-TBI.

In adulthood, the causes of TBI in humans differ across gender, as men are more likely to sustain a TBI from falls or motor vehicle accidents, and women are more like to sustain a TBI from an intimate partner (Gupte et al., 2019). Further, men and women tend to report different symptoms after injury, with men reported amnesia and confusion more often, while women tend to report headaches and dizziness (Colantonio et al., 2010). Future studies using CHIMERA will require the incorporation of female mice, as sex differences are a crucial and often over-looked aspect of translational research. The sex differences outlined here cannot be ignored when designing exploratory and therapeutic TBI studies.

5.4 Future directions

5.4.1 Neuroimaging

As alluded to throughout this thesis, it will be important to move towards more clinically relevant outcomes to assess changes after TBI. In particular, we will need to further evaluate the ability of CHIMERA to elicit structural changes that can be detected using MR imaging, including diffusion tensor imaging (DTI) and susceptibility weighted imaging (SWI). As we have already started investigating the pattern of DTI changes associated with mild CHIMERA injuries (Haber et al., 2017), imaging experiments to assess changes in axonal integrity after moderate-severe CHIMERA injuries are imminent. It is worth noting that there are a number of challenges of using DTI in the clinic, reviewed in (Douglas et al., 2015, 2019). Multiple TBI studies have consistently reported decreased fractional anisotropy (FA; reviewed in (Douglas et

al., 2015)), which is thought to be a product of disturbances within the axonal microstructure. However, there is an undoubted variability in the reported anatomical locations of FA, likely due to the heterogeneity of cohorts used in large clinical studies (Hulkower et al., 2013). Currently, DTI is a sensitive measure at the group level (injured versus uninjured), but seldom plays a diagnostic or prognostic role at the individual level to determine the extent of white matter injury (Douglas et al., 2015; Shenton et al., 2012). The generation of normative DTI databases will be necessary before DTI has any diagnostic or prognostic value.

Given the clinical limitations of DTI, we also wish to incorporate SWI after CHIMERA TBI, which has emerged as a sensitive tool for detecting microbleeds after clinical TBI (Huang et al., 2015; Lawrence et al., 2017). In a small SWI pilot study (n=2/injury condition) focusing on the acute response (6h after 2.5J CHIMERA TBI), we observed parenchymal bleeds (**Figure 5.1**) which were localized to the entorhinal and perirhinal cortices. As described in Chapter 3, the entorhinal cortex is particularly sensitive to interfaced CHIMERA injuries at 2.5J, demonstrated by IgG extravasation and gliosis at the 6h time-point. Sufficiently powered imaging studies are a logical next step and assessments of the sub-acute and chronic cerebrovascular responses following CHIMERA TBI are also worth pursuing. Incorporating assessments of CBF is also extremely clinically relevant as there is a consistent body of literature in humans indicating that alterations in CBF are common after TBI (Bonne et al., 2003). As discussed in the introduction, SPECT studies have been used to measure regional CBF in patients with chronic TBI (Barkai et al., 2004; Bonne et al., 2003; Lewine et al., 2007), and changes in CBF perfusion rates have been found to correlate with neuropsychological and neurological deficits (Raji et al., 2014). The exact causes of these alterations in CBF following TBI are unclear, however we can begin to

answer questions surrounding the temporal response of the cerebrovasculature following injury using the CHIMERA platform. CVR can also be altered after TBI, and is reported to be more sensitive than CBF at discriminating between injured and uninjured participants (Amyot et al., 2018; Haber et al., 2018). The hypercapnic challenge (Amyot et al., 2018; Mutch et al., 2016a, 2016b) is one way by which we could quantify the ability of the cerebrovasculature to react to a vasodilatory stimulus following CHIMERA injury. Pilot studies combining MRI and the hypercapnic challenge are currently underway to elucidate CVR changes following CHIMERA TBI in mice.

5.4.2 Chronic time-points

The longest time-points we assessed after TBI were 14d, 60d, and 70d (10 weeks), respectively. Future studies will be required to extend the duration of our studies to elucidate the long-term effects (up to 12+ months) of impact-acceleration head injury on the neuroinflammatory and behavioral sequelae. There exists mounting evidence that history of TBI is associated with neurodegeneration. In particular, moderate and severe TBI in early and mid-life is associated with an increased risk of late-life dementia (Fleminger et al., 2003; Guo et al., 2000; Plassman et al., 2000). Despite these findings, most experimental TBI studies rarely extend beyond a few months following impact. Recent work by Mouzon et al. was the first to describe the effects of single and repetitive mTBI up to 24 months after the initial insult (Mouzon et al., 2018). At end-point, mice subjected to rmTBI displayed learning deficits, increased risky behavior, DAI, white matter inflammation in the absence of p-tau. Future work using CHIMERA should continue to elaborate on findings from Mouzon et al.'s study, investigating chronic behavioral and

neuropathological outcomes following single and repetitive CHIMERA TBI across the injury spectrum.

5.4.3 Electrophysiology

Future studies are necessary to determine if the acute and sub-acute alterations in basal release discussed in Chapter 3 correlate with alterations in neuronal plasticity. In a recent paper, our group found that two very mild injuries (0.5J) profoundly affected spatial learning and memory, anxiety, and risk-taking behaviors up to 8-month post-TBI, in C57Bl/6 and APP/PS1 mice (Cheng et al., 2019). A biological correlate for these phenotypes remains to be determined, but could lie in long-term electrophysiological deficits following injury.

Post-traumatic epilepsy (PTE) is also an intriguing line of investigation that can be pursued using CHIMERA. Defined as a "recurrent seizure disorder due to injury to the brain following trauma" (Pitkänen and Bolkvadze, 2010), PTE is thought to affect anywhere between 1.9% to 30% of TBI patients (Herman, 2002; Lamar et al., 2014). Risk factors for PTE include intracerebral hemorrhage, diffuse cerebral contusions, and post-traumatic seizure soon after TBI (Herman, 2002; Lamar et al., 2014; Lucke-Wold et al., 2015; Tomkins et al., 2011; Verellen and Cavazos, 2010). The latter is of particular interest as we observed two occurrences of post-traumatic seizures in the form of barrel-rolling activity immediately after CHIMERA TBI at 2.5J in unconscious C57Bl/6 mice. Experimentally, we hope to use implanted EEG electrodes to measure epileptiform activity in a quantitative manner through spike-wave discharges following TBI. Epileptiform activity can also be used as a measure of target engagement in future

CHIMERA studies assessing therapeutics, potentially using anti-epileptic drugs to ameliorate some of the chronic outcomes of head injury.

5.4.4 Impact direction

As studies described in this thesis used impacts delivered in the sagittal plane, future studies will be necessary to address how injury tolerance and subsequent pathology may vary by anatomical plane of movement. At this stage, CHIMERA can generate precise impacts in either the sagittal and lateral plane of motion, however, studies focusing on lateral CHIMERA impacts have not been adequately explored. Pilot studies have been carried out to develop impactor interfaces for lateral CHIMERA injuries, which elicit different patterns of rotational displacement (**Figure 5.2 A-C**). With our first interface iteration (**Figure 5.2 A**), we pinpointed an *in vivo* threshold for impacts in the lateral plane, approximately 7 m/s piston velocity (**Figure 5.2 D**). In a pilot study using eight C57Bl/6 male mice aged 5-7 months, TBI animals were subjected to a single 1.1J (6.6 m/s) CHIMERA injury (n=4). Sham animals (n=4) were subjected to isoflurane exposure. We observed a significant elevation in LRR latency following injury ($p = 0.0286$, Mann Whitney-U, **Figure 5.2 E**) and an increase in NSS that trended towards significance at 1h post-injury ($p = 0.0857$, Mann Whitney-U, **Figure 5.2 F**). We also observed a positive linear correlation between LRR and NSS (Spearman $r = 0.7259$, $p = 0.05$, **Figure 5.2 G)**. Upon close examination of perfused brain tissue upon sacrifice at 2d post-TBI, 50% (2/4) of animals showed evidence of BBB breach ipsilateral to injury. Burst blood vessels and hemorrhages were identified in motor, somatosensory and piriform cortices (**Figure 5.2 I, J**). The pattern of histopathology following lateral CHIMERA TBI remains to be explored. We speculate that the phenotypes of lateral impact CHIMERA may overlap with findings from Tagge et al.'s recent

work (Tagge et al., 2018). Their lateral impact-acceleration platform also induces tissue strains concentrated on the ipsilateral side. Neuronal loss, gliosis, and breach of the BBB were reported in the ipsilateral perirhinal cortex, suggesting that though the injury itself triggers rotational displacement, the neuropathology generated by this platform is largely contained around the site of direct impact (Tagge et al., 2018). Nonetheless, diffuse p-tau was reported months after injury (Tagge et al., 2018).

Recent studies in porcine TBI models have begun to elucidate the correlations between impact direction and neuropathology (Cullen et al., 2016; Eucker et al., 2011; Johnson et al., 2018). Compared to coronal TBIs, injuries in the sagittal and axial planes produced the most significant neuropathology, including bleeding and inflammation at the sulcal depths, subdural hematomas, and accumulation of blood within the ventricles at acute time-points (Cullen et al., 2016). Quantitative biomechanical assessments in experimental models have shown that rotational displacement, velocity and acceleration play a tremendous role in shear strains of brain tissue (Cullen et al., 2016; Ommaya et al., 1968). Thus, impact direction is an increasingly clinically relevant line of investigation.

In future CHIMERA studies, particular focus should be directed at more accurately quantifying rotational displacement, velocity, and acceleration in sagittal and lateral planes of movement, which would require the addition of a second, perpendicularly-placed, high-speed camera to capture three-dimensional head movement. Subsequently, the temporal and spatial patterns of acute and chronic pathology can be correlated head kinematics following sagittal or lateral CHIMERA injury.

5.4.5 Impact number

Impact number, especially using mouse CHIMERA, is yet to be sufficiently explored. In a pilot study using thirteen C57Bl/6 female mice aged 5-6 months, TBI animals were subjected to twenty (n=4) or thirty-one 0.5J CHIMERA injuries (n=4) spaced 24h apart. Sham animals (n=5) underwent repetitive isoflurane exposure (20x or 31x) at identical intervals. Animals were euthanized 24h after the last TBI or sham procedure. Body weight, loss of righting reflex, and neurological severity score were surprisingly unaltered by 20x TBI (n.s., paired t-test, **Figure 5.3 A-C**). Further, cytokines and tau biochemistry measured in half-brain homogenates were unchanged after 20x and 31x TBI (n.s., one-way ANOVA, **Figure 5.3 D-I**). Interestingly, qualitative histological changes were observed within the optic tract following 20x and 31x TBI (**Figure 5.3 J**). At both time-points, microgliosis was observed (**Figure 5.3 J, left**), along with axonal damage, demonstrated by silver uptake (**Figure 5.3 J, right**).

Using 0.5J injuries, we have begun our investigation into the cumulative effect of subconcussive injury, as emerging evidence suggests that cumulative exposure to head impacts may predict clinical deficits later in life (Montenigro et al., 2017). By definition, a subconcussive event "involves a transfer of mechanical energy to the brain at enough force to injure axonal integrity, but does not result in behavioral symptoms" (Montenigro et al., 2017; Namjoshi et al., 2017). At the 0.5J level, even up to thirty-one cumulative injuries, we did not observe any neurological deficits by LRR or NSS. However, we did find histopathological evidence of DAI and white matter inflammation. Conversely, results from Gangolli et al.'s recent repetitive CHIMERA TBI study showed no significant changes in glial histology (Gangolli et al., 2018). Gangolli et al.

subjected mice to twenty CHIMERA impacts (0.13J or 0.24J) spaced 24h apart. Given the chosen impact energies, both of which we have characterized in this thesis as sub-threshold, it is not surprising that significant inflammatory changes were absent. Interestingly, spatial memory deficits, measured using Morris Water Maze were found to persist up to 1 year after the final injury (Gangolli et al., 2018). Like the Gangolli et al. study, future in-house CHIMERA studies should include long-term time-points following a period of sub-concussive and concussive injury, in an attempt to mimic seasonal injuries sustained primarily in contact sports, but also in the military.

5.4.6 Rat CHIMERA

Although we focused on repetitive TBI using the rat CHIMERA platform in this thesis, we were also interested in the pathology associated with single mild, and moderate-severe TBI in rats. Immediately preceding our repetitive TBI study, we carried out an acute study using single-impact CHIMERA TBI in rats up to 2.9J, but did not observe any evidence of DAI or white matter inflammation up to 7d post-injury. Impacts greater than 2.9J in rats elicited skull fracture and nose bleeds (see **Section 4.3.2**). These results speak to the narrowness of the safety window for CHIMERA injuries in rats using the current first-generation rat piston design, where no detectable changes are observed following a single impact at or below 2.9J, while impacts >2.9J regularly lead to mortality or humane end-point. Before developing impactor interfaces for the rat platform, we attempted to change the cap on the piston tip from a soft, synthetic-rubber tip (1/4”) to a hard, natural-rubber tip (3/32”), to trigger more extensive skull deformation for impacts <2.9J. Using cadaveric rats, we performed projectional radiography (static x-ray) immediately following CHIMERA TBI, and found that impactor tip played a significant role in

skull integrity following TBI. Skull fracture was observed at 2.65J following impacts using a hard-tipped piston, whereas impacts using the soft-tipped piston did not elicit overt skull fracture (**Figure 5.4 A-C**).

We then designed and printed impactor interfaces to be used on the rat CHIMERA and proceeded to a live pilot study, comparing rats impacted at 8J (n=3) and 5.1J (n=3) with rats subjected to sham procedures (n=2). As we were not powered to perform quantitative analyses, we performed qualitative assessments of Iba1 immunoreactivity and silver staining, and primarily observed regional inflammatory changes at 7d post-injury. Within the assessed grey matter regions, the basolateral amygdala and orbitofrontal cortex showed increases in Iba1 immunoreactivity following high energy impacts (8J) compared to animals subjected to sham procedures and lower energy impacts (5.1J) (**Figure 5.5**). In white matter regions, we observed a dramatic increase in Iba1 reactivity in the olfactory nerve layer, while the optic tract was unchanged following interfaced low and high energy CHIMERA TBI (**Figure 5.5**). No changes in silver uptake were observed within the olfactory nerve layer at 7d post-injury, while minimal evidence of silver uptake was observed within the optic tract of samples subjected to high energy TBI (**Figure 5.6**). As impacts greater than 8J led to high levels of mortality, future directions of this work do not include more severe impacts, but we hope to extend the time-point beyond 7d post-TBI. We also wish to incorporate behavioral assessments, including the delay discounting task, to determine whether single, more severe impacts induce a similar behavioral phenotype as repetitive CHIMERA TBI at lower energies. Subsequent experiments will be required to properly titrate impact energies using the rat CHIMERA. Assessments of cerebrovascular

damage are also worth investigating, as BBB changes are thought to trigger many long-term inflammatory cascades (Shlosberg et al., 2010; Zlokovic, 2011).

5.4.7 Ferret CHIMERA

Ferrets possess gyrencephalic brains (i.e. with convolutions). The development of the ferret CHIMERA was important for this reason, and for the similarity of grey:white matter ratios between ferrets and humans. Pilot investigations using the ferret CHIMERA suggest a susceptibility for inflammation within the sulcal depths, much like humans after TBI (Cherry et al., 2016). When staining for astrocytes, we qualitatively observed an increase in GFAP signal within several regions of interest: the lateral sulcus, hippocampus, and white matter structures (**Figure 5.7**). Nonetheless, a full study is required before we draw any concrete conclusions.

Our collaborators recently published pilot investigations assessing *in vivo* brain motion during CHIMERA TBI in ferrets (Whyte et al., 2019). For this study, animals were placed in a stereotaxic frame, after which three or four small burr-holes were made in the superior skull, within the lateral parietal bones. Radio-opaque tantalum beads were implanted within brain tissue, with additional beads affixed to the skull as reference points to track skull motion. During subsequent CHIMERA TBI, Whyte et al. observed that brain motion significantly lagged behind that of the skull, suggesting that the material properties of the brain and skull lead to differential tissue motion following impact. These data also suggest that head motion extrapolated from the skull or an apparatus affixed to the skull (as described in Chapter 3) does not quantify brain motion upon impact (Whyte et al., 2019). This work is of particular importance for computational modeling of brain injury, as current computational models of the human brain are

primarily based on data from cadaveric tissue (Giordano and Kleiven, 2016). The biological fidelity of *ex vivo* tissue relative to *in vivo* tissue remains to be elucidated, and this line of investigation would be most aptly demonstrated using the ferret CHIMERA platform. We predict understanding ferret tissue mechanics and deformation will lay the groundwork for clinically relevant investigations into the sequelae of sulcal and perivascular damage, as well as white matter pathology, following TBI.

5.5 Conclusion

We have begun to establish working parameters to guide future investigations of head injury using CHIMERA by assessing alterations in behavior, grey and white matter inflammation, cerebrovasculature integrity, and neurotransmission. In doing so, we are beginning to describe the neuropathological time-course of head injury. In the near future, we hope to pinpoint possible preventative strategies and evaluate therapies using CHIMERA. Given the ability of the CHIMERA model to recapitulate many of the hallmarks of human TBI, we hypothesize that therapeutic candidates that have shown promise following CHIMERA injury may have a better chance at ameliorating the clinical and neuropathological sequelae after head injury in humans.

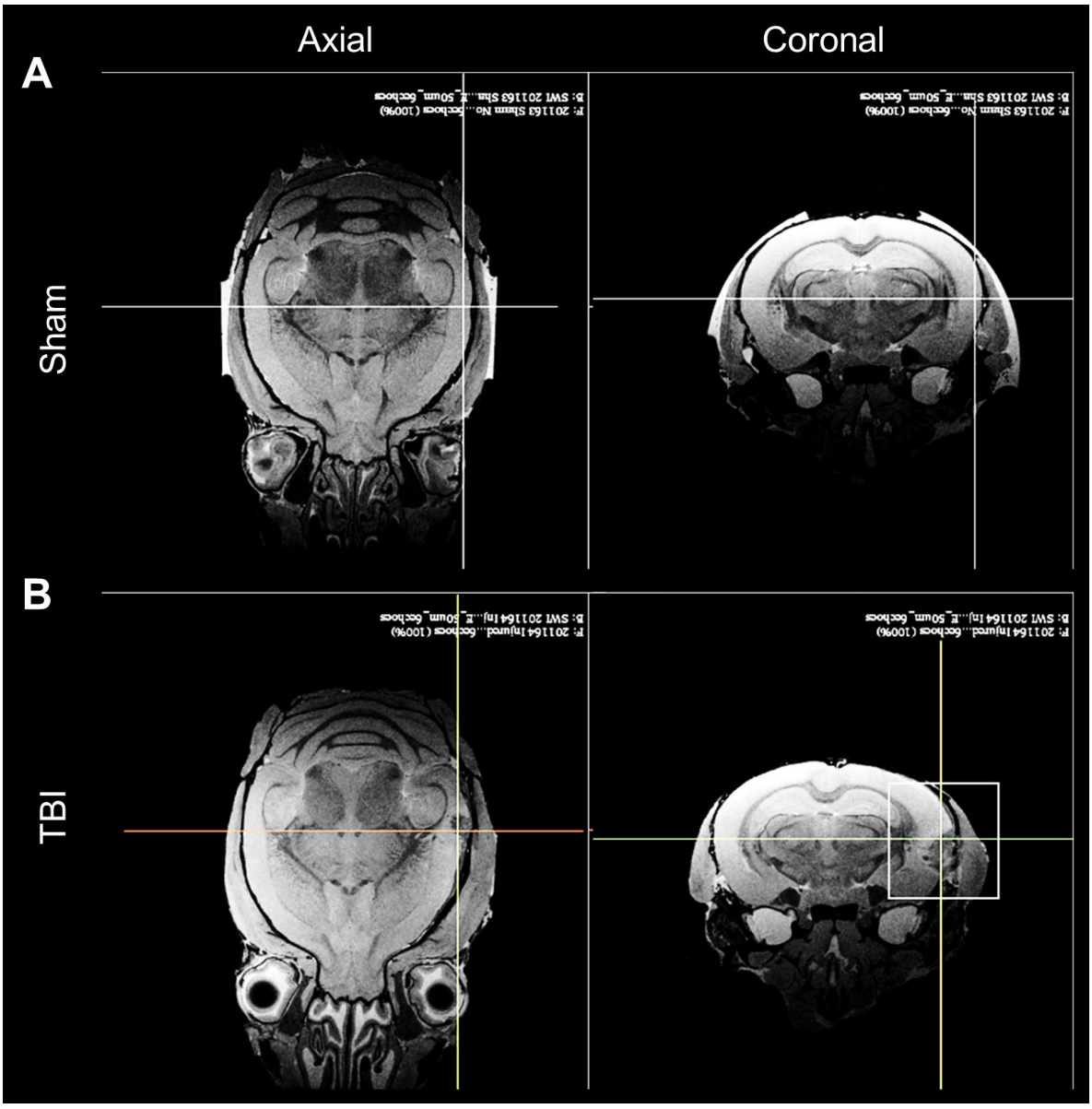

Figure 5.1 Ex vivo susceptibility weighted imaging after CHIMERA TBI in mice.

(A) In sham animals, cerebrovascular abnormalities were absent. (B) After CHIMERA TBI (2.5J) we saw evidence of a lateral hemorrhage in the entorhinal/perirhinal cortex, indicated by crosshairs and outlined by white box in the coronal plane.

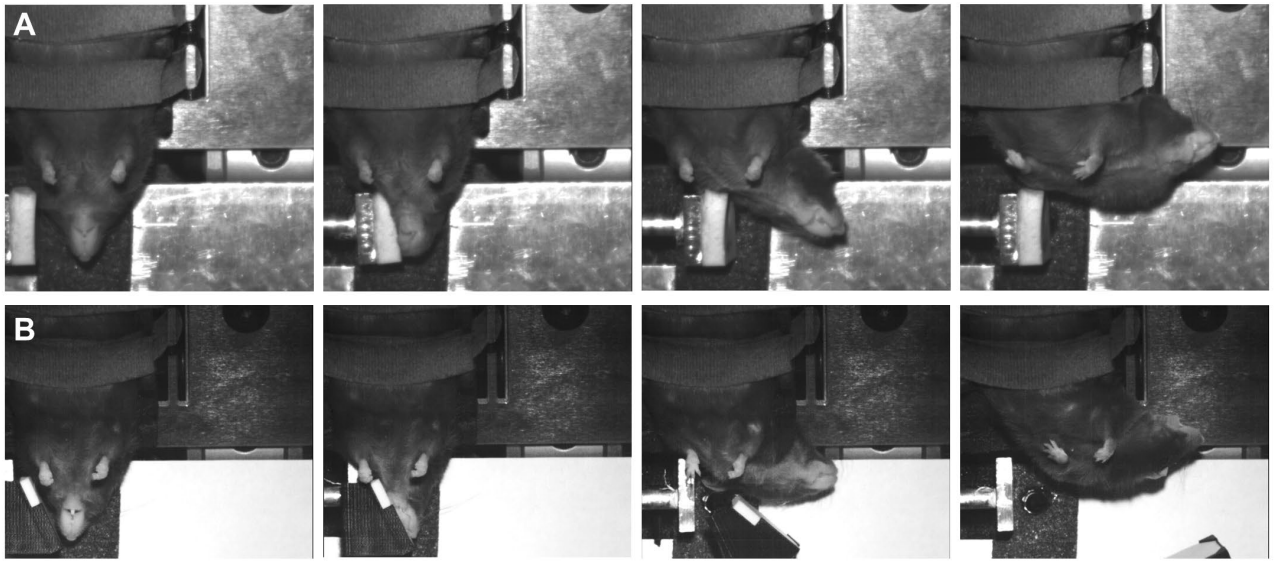
A
B

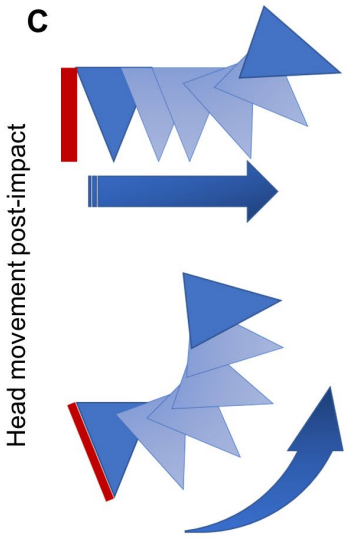
C
Head movement post-impact

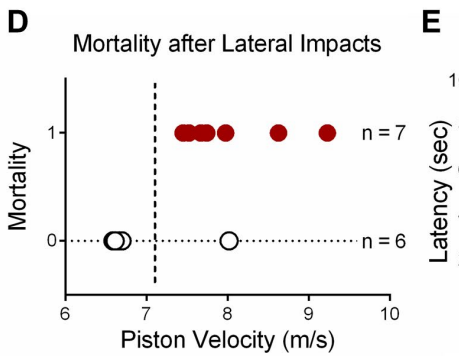
D
Mortality after Lateral Impacts
Mortality
1
0
n = 7
n = 6
6
7
8
9
10
Piston Velocity (m/s)

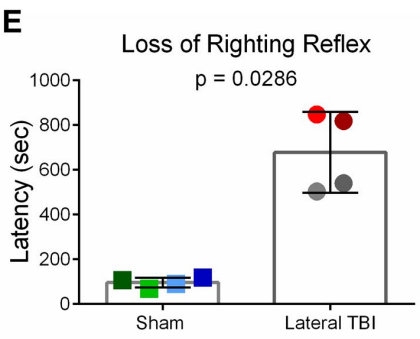
E
Loss of Righting Reflex
p = 0.0286
Latency (sec)
1000
800
600
400
200
0
Sham
Lateral TBI

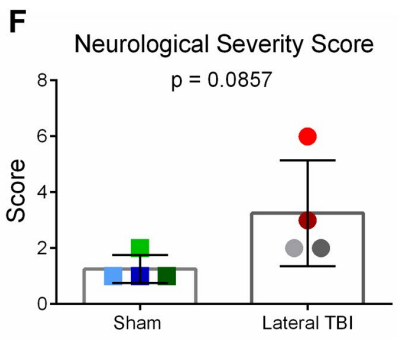
F
Neurological Severity Score
p = 0.0857
Score
8
6
4
2
0
Sham
Lateral TBI

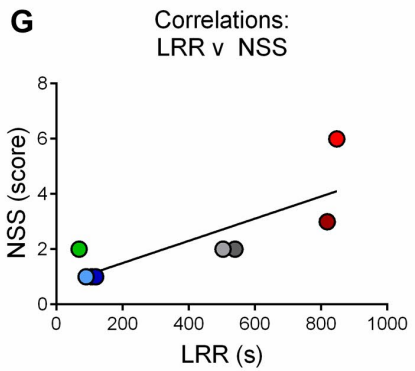
G
Correlations:
LRR v NSS
NSS (score)
8
6
4
2
0
0
200
400
600
800
1000
LRR (s)
Spearman's coefficient: 0.7259
p-value: 0.05

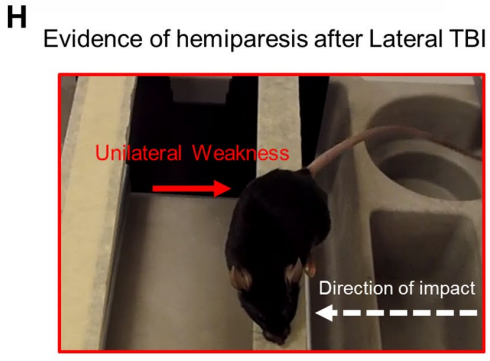
H
Evidence of hemiparesis after Lateral TBI
Unilateral Weakness
Direction of impact

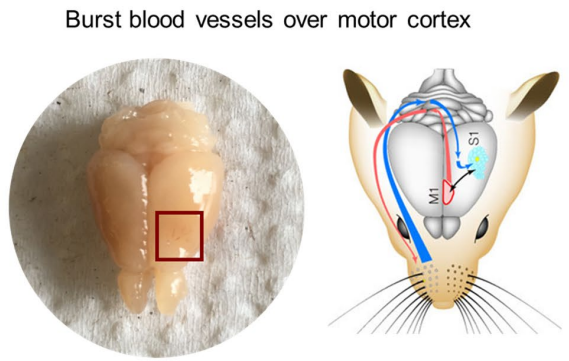
I
Burst blood vessels over motor cortex
M1
S1

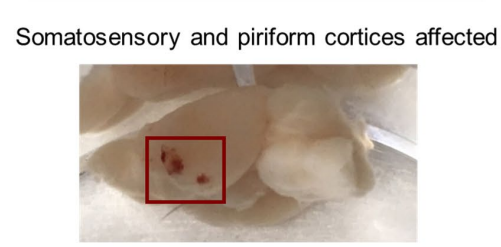
J
Somatosensory and piriform cortices affected

Figure 5.2 Lateral-impact CHIMERA TBI in mice.

(A, B) High-speed videography shows trajectory of the mouse head upon impact at using (A) a poron foam-pad oriented perpendicular to in the impactor axis and (B) an angled interface also lined with poron foam. The foam-pad of the angled interface contacts the entire face, in the hopes of decreasing the amount of shearing force at the cervical spine. (C) Schematic shows animated trajectory of the mouse head following impact. Blue triangles represent the mouse head and red rectangles represent the lateral impactor interface. (D) Mortality following TBI. Impacts greater than 7 m/s piston velocity led to 87.5% mortality (7/8). Impact less than 7 m/s piston velocity led to 100% survival. (E) Loss of righting reflex latency was prolonged following lateral CHIMERA TBI (6.6 m/s, 1.1J, $p = 0.0286$). (F) The increase in NSS 1h post-TBI was trending towards significance ($p = 0.0857$). (G) LRR and NSS were positively correlated with each other ($r = 0.7259$, $p = 0.05$). (H) Evidence of hemiparesis was observed during the NSS task at 1h post-injury. (I) Upon close examination of perfused brain tissue following sacrifice, burst blood vessels and hemorrhages were identified in motor, (J) somatosensory and piriform cortices, respectively. In (E, F), data were analyzed by Mann Whitney-U test. In (G), correlations were calculated using Spearman's coefficients.

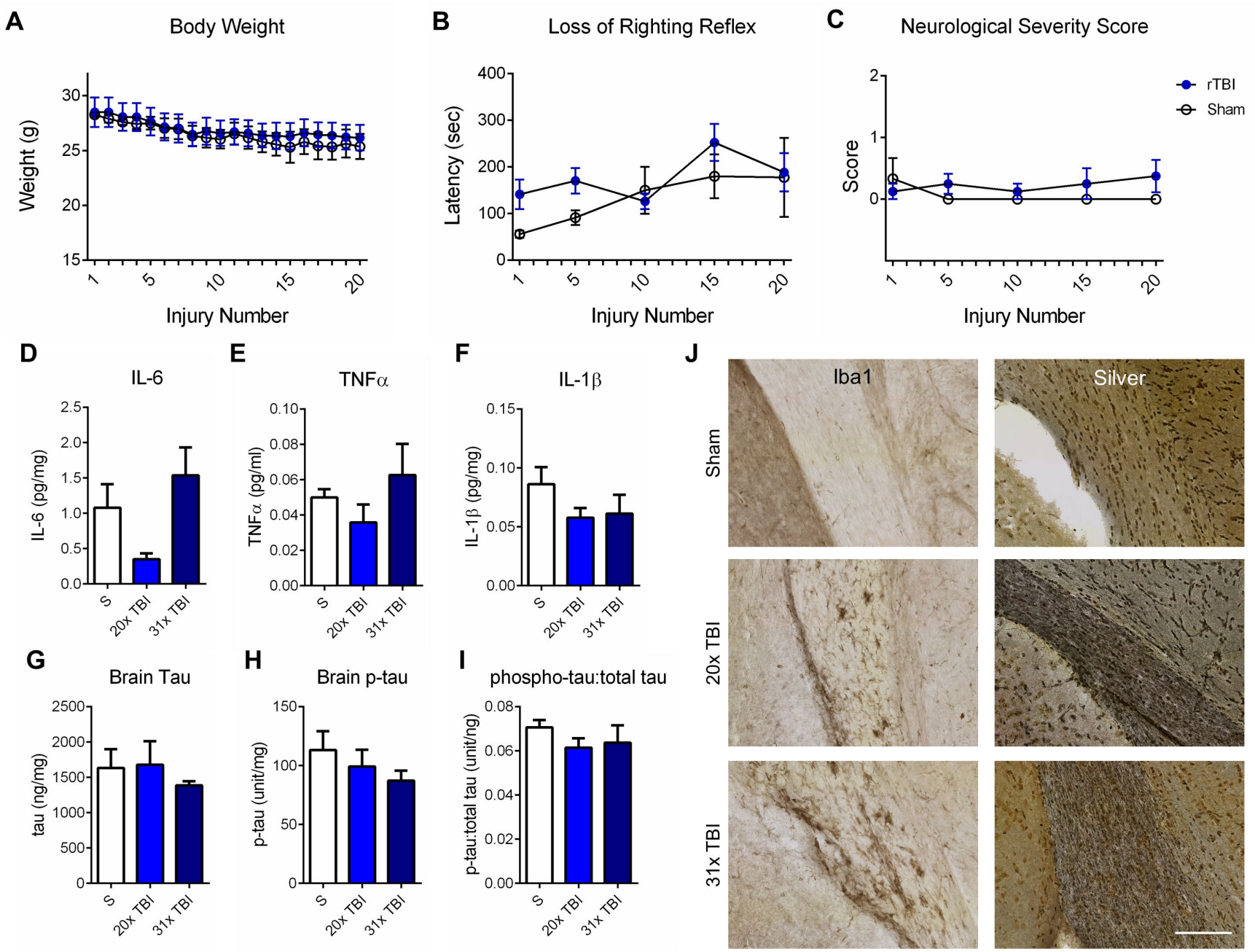
A
Body Weight
Weight (g)
30
25
20
15
1
5
10
15
20
Injury Number
B
Loss of Righting Reflex
Latency (sec)
400
300
200
100
0
1
5
10
15
20
Injury Number
C
Neurological Severity Score
Score
2
1
0
rTBI
Sham
1
5
10
15
20
Injury Number
D
IL-6
IL-6 (pg/mg)
2.5
2.0
1.5
1.0
0.5
0.0
S
20x TBI
31x TBI
E
TNFα
TNFα (pg/ml)
0.10
0.08
0.06
0.04
0.02
0.00
S
20x TBI
31x TBI
F
IL-1β
IL-1β (pg/mg)
0.15
0.10
0.05
0.00
S
20x TBI
31x TBI
G
Brain Tau
tau (ng/mg)
2500
2000
1500
1000
500
0
S
20x TBI
31x TBI
H
Brain p-tau
p-tau (unit/mg)
150
100
50
0
S
20x TBI
31x TBI
I
phospho-tau:total tau
p-tau:total tau (unit/ng)
0.08
0.06
0.04
0.02
0.00
S
20x TBI
31x TBI
J
Iba1
Silver
Sham
20x TBI
31x TBI

Figure 5.3 Repetitive CHIMERA TBI in mice.

(A) Body weight, (B) loss of righting reflex, and (C) neurological severity score were unaffected by 20x TBI at 0.5J. (D) IL-6, (E) TNFα and (F) IL-1β were not affected by 20x and 31x TBI at 0.5J, however the group differences in IL-6 were trending towards significance ($p = 0.0948$). (G) Brain tau and (H) phosphorylated (p-) tau were unchanged after TBI. (I) The ratio of p-tau to total tau was also unaltered after injury. (J, left) Iba1 within the optic tract showed qualitative increases in microglial count and changes in morphology after 20x and 31x TBI. (J, right) Silver staining in the optic tract showed increases in silver uptake following 20x and 31x TBI. In (A-C) data were analyzed by paired t-test. In (D-I), data were analyzed by one-way ANOVA followed by Dunnett's post hoc comparisons.

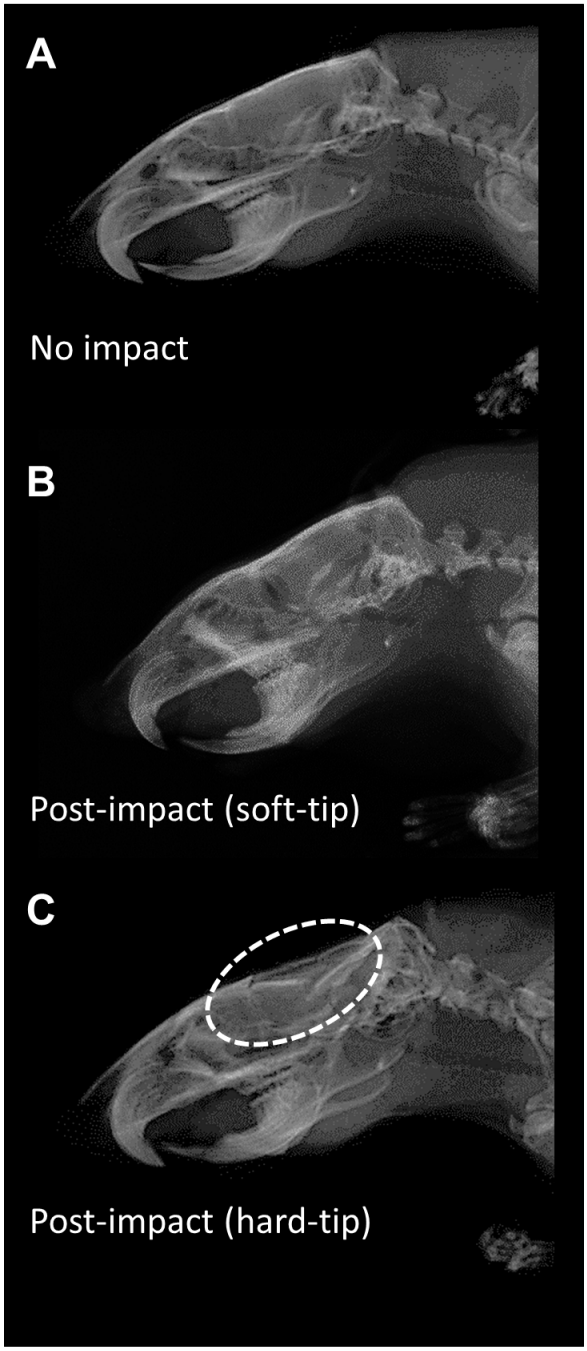

Figure 5.4 Projectional radiography demonstrates that CHIMERA impactor tip plays a significant role in skull integrity following TBI in cadaveric rats.

(A) No evidence of skull fracture was observed prior to impact. (B) Following impact at 2.9J using a soft-tipped piston, no evidence of skull fracture was observed, but a slight skull indentation was visible. (C) Impact at 2.65J using a hard-tipped piston led to skull fracture (dashed circle) immediately following CHIMERA TBI.

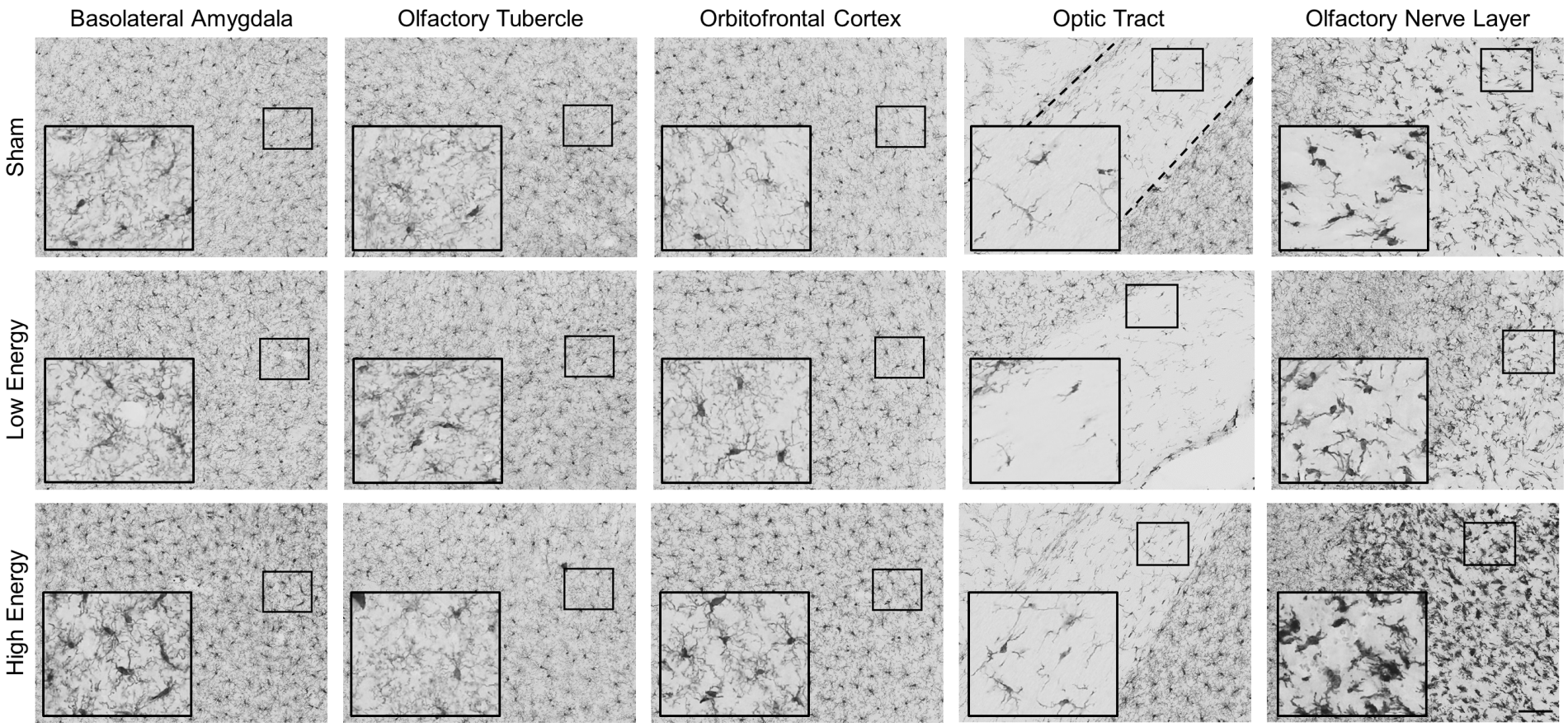

Figure 5.5 Iba1 immunohistochemistry in the basolateral amygdala, olfactory tubercle, orbitofrontal cortex, optic tract, and olfactory nerve layer 7d after single CHIMERA TBI in rats.

The basolateral amygdala and orbitofrontal cortex showed increased Iba1 immunoreactivity following high energy (8J) TBI, indicating a microglial response. The olfactory tubercle and optic tract did not show obvious differences in Iba1 post-TBI. The olfactory nerve layer showed a dramatic increase in Iba1 immunoreactivity following high energy TBI. Scale bar = 100μm.

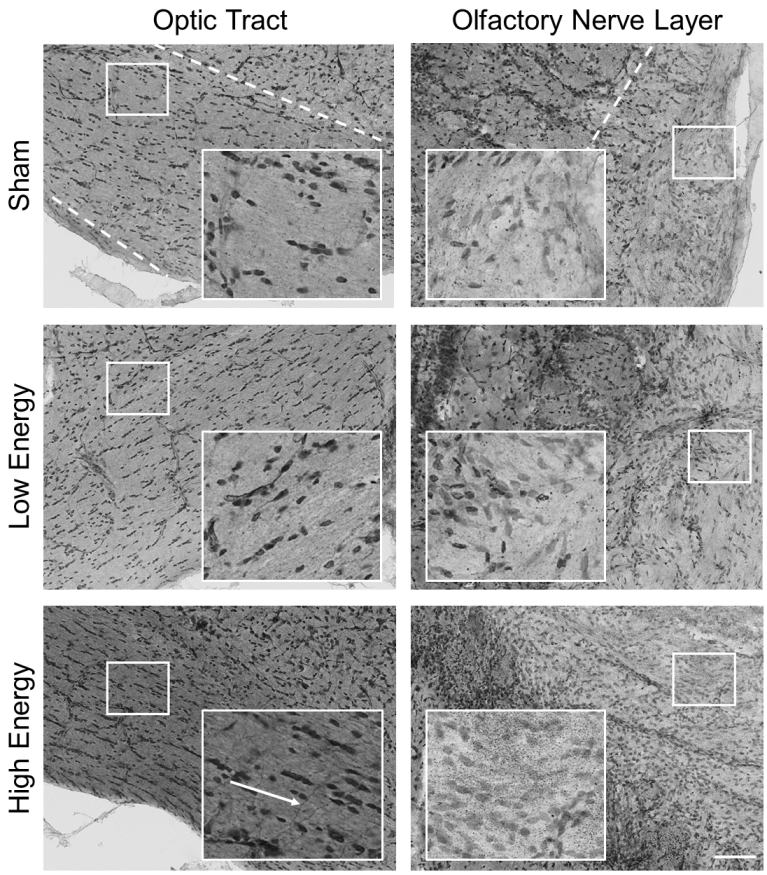

Figure 5.6 Silver staining in the optic tract and olfactory nerve layer 7d after single CHIMERA TBI in rats.

No changes in silver staining following low (5.1J) or high energy (8J) TBI within the olfactory nerve layer. However, silver fibers (arrow) were present within the optic tract of samples subjected to high energy TBI. Scale bar = 100μm.

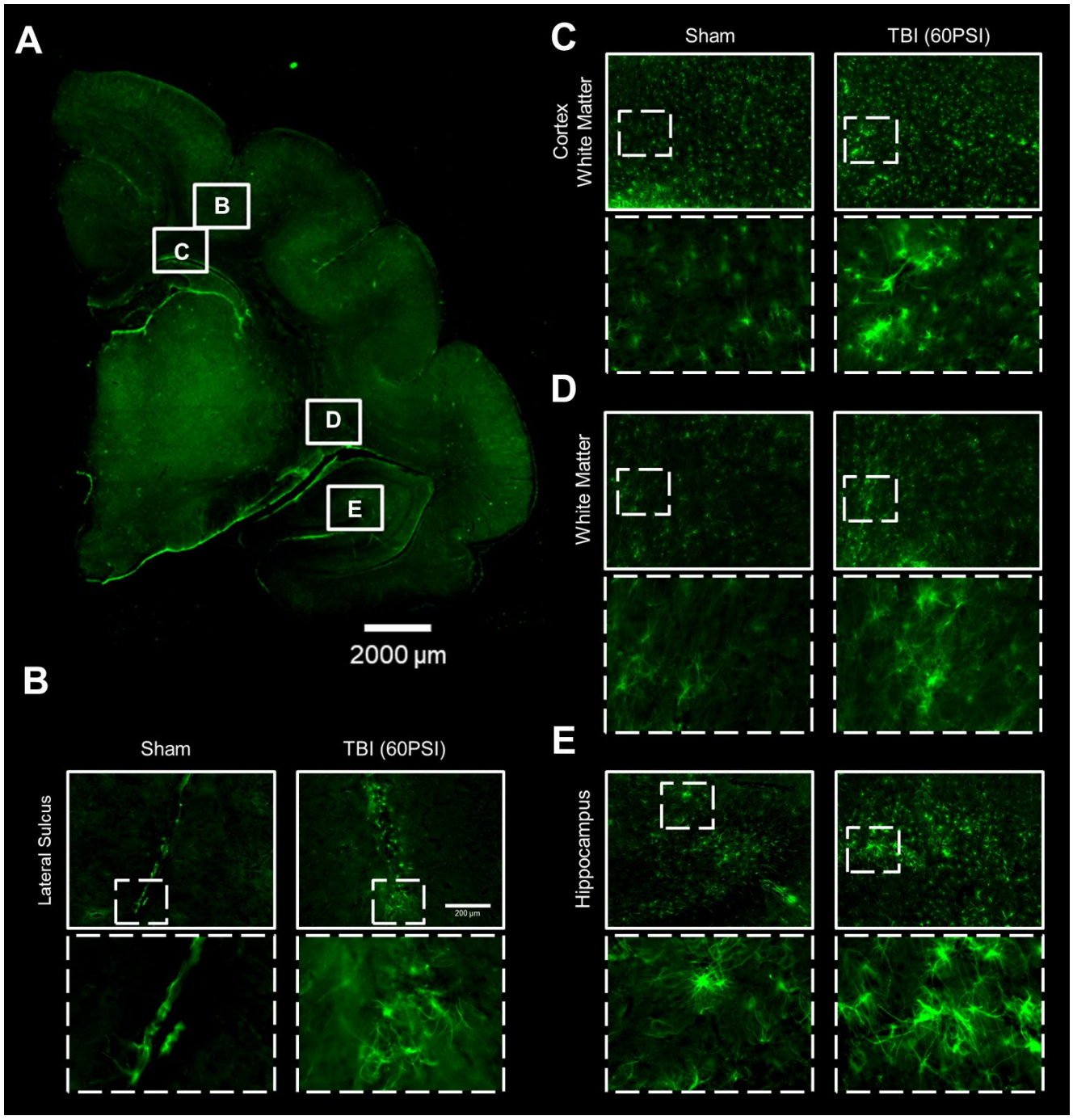

Figure 5.7 GFAP immunofluorescent staining following CHIMERA TBI in ferrets.

(A) Qualitative assessments of GFAP immunofluorescence within ferret brain tissue suggest proliferation of astrocytes in (B) the lateral sulcus, (C) the cortex white matter, (D) the general white matter, and (E) the hippocampus at 2d post-CHIMERA TBI. Scale bar = 2000 microns.

Bibliography

Adediran, T., Drumheller, B.C., McCunn, M., Stein, D.M., and Albrecht, J.S. (2019). Sex Differences in In-hospital Complications Among Older Adults After Traumatic Brain Injury. J. Surg. Res. *243*, 427–433.

Albrecht, J.S., McCunn, M., Stein, D.M., Simoni-Wastila, L., and Smith, G.S. (2016). Sex differences in mortality following isolated traumatic brain injury among older adults. J. Trauma Acute Care Surg. *81*, 486–492.

Allsop, D.L., Perl, T.R., and Warner, C.Y. (1991). Force/Deflection and Fracture Characteristics of the Temporo-parietal Region of the Human Head. SAE Trans. *100*, 2009–2018.

Amyot, F., Kenney, K., Moore, C., Harber, M., Turtzo, L.C., Shenouda, C.N., Silverman, E., Gong, Y., Qu, B.-X., Harburg, L., et al. (2018). Imaging of Cerebrovascular Function in Chronic Traumatic Brain Injury. J. Neurotrauma *35*, 1116–1123.

Te Ao, B., Brown, P., Tobias, M., Ameratunga, S., Barker-Collo, S., Theadom, A., McPherson, K., Starkey, N., Dowell, A., Jones, K., et al. (2014). Cost of traumatic brain injury in New Zealand. Neurology *83*, 1645–1652.

Arambula, S.E., Reinl, E.L., El Demerdash, N., McCarthy, M.M., and Robertson, C.L. (2019). Sex differences in pediatric traumatic brain injury. Exp. Neurol. *317*, 168–179.

Arnould, A., Dromer, E., Rochat, L., Linden, M. Van Der, and Azouvi, P. (2016). Neurobehavioral and self-awareness changes after traumatic brain injury : Towards new multidimensional approaches. Ann. Phys. Rehabil. Med. *59*, 18–22.

Baik, J.-H. (2013). Dopamine signaling in reward-related behaviors. Front. Neural Circuits *7*, 1–16.

Bailey, D.M., Jones, D.W., Sinnott, A., Brugniaux, J.V., New, K.J., Hodson, D., Marley, C.J.,

Smirl, J.D., Ogoh, S., and Ainslie, P.N. (2013). Impaired cerebral haemodynamic function associated with chronic traumatic brain injury in professional boxers. Clin. Sci. *124*, 177–189.

Bailey, M.R., Simpson, E.H., and Balsam, P.D. (2016). Neural substrates underlying effort, time, and risk-based decision making in motivated behavior. Neurobiol. Learn. Mem. *133*, 233–256.

Bales, J.W., Wagner, A.K., Kline, A.E., and Dixon, C.E. (2009). Persistent cognitive dysfunction after traumatic brain injury: A dopamine hypothesis. Neurosci. Biobehav. Rev. *33*, 981–1003.

Banks, S.J., Mayer, B., Obuchowski, N., Shin, W., Lowe, M., Phillips, M., Modic, M., and Bernick, C. (2014). Impulsiveness in Professional Fighters. J. Neuropsychiatry Clin. Neurosci. *26*, 44–50.

Barkai, G., Goshen, E., Tzila Zwas, S., Dolberg, O.T., Pick, C.G., Bonne, O., and Schreiber, S. (2004). Acetazolamide-enhanced neuroSPECT scan reveals functional impairment after minimal traumatic brain injury not otherwise discernible. Psychiatry Res. *132*, 279–283.

Barnes, D.E., Byers, A.L., Gardner, R.C., Seal, K.H., Boscardin, W.J., and Yaffe, K. (2018). Association of mild traumatic brain injury with and without loss of consciousness with dementia in US military veterans. JAMA Neurol. *75*, 1055–1061.

Bartnik-Olson, B.L., Holshouser, B., Wang, H., Grube, M., Tong, K., Wong, V., and Ashwal, S. (2014). Impaired neurovascular unit function contributes to persistent symptoms after concussion: a pilot study. J. Neurotrauma *31*, 1497–1506.

Bhowmick, S., D'Mello, V., Caruso, D., Wallerstein, A., and Abdul-Muneer, P.M. (2019). Impairment of pericyte-endothelium crosstalk leads to blood-brain barrier dysfunction

following traumatic brain injury. Exp. Neurol. *317*, 260–270.

Bjork, J.M., Burroughs, T.K., Franke, L.M., Pickett, T.C., Johns, S.E., Moeller, F.G., and Walker, W.C. (2016). Laboratory impulsivity and depression in blast-exposed military personnel with post-concussion syndrome. Psychiatry Res. *246*, 321–325.

Bjork, J.M., Burroughs, T.K., Franke, L.M., Pickett, T.C., Johns, S.E., Moeller, F.G., and Walker, W.C. (2017). Rapid-Response Impulsivity Predicts Depression and Posttraumatic Stress Disorder Symptomatology at 1-Year Follow-Up in Blast-Exposed Service Members. Arch. Phys. Med. Rehabil. *98*, 1646–1651.

Bonne, O., Gilboa, A., Louzoun, Y., Kempf-Sherf, O., Katz, M., Fishman, Y., Ben-Nahum, Z., Krausz, Y., Bocher, M., Lester, H., et al. (2003). Cerebral blood flow in chronic symptomatic mild traumatic brain injury. Psychiatry Res. *124*, 141–152.

Bowman, C., Ding, J.-P., Sachs, F., and Sokabe, M. (1992). Mechanotransducing ion channels in astrocytes. Brain Res. *584*, 272–286.

Bramlett, H.M., Kraydieh, S., Green, E.J., and Dietrich, W.D. (1997). Temporal and regional patterns of axonal damage following traumatic brain injury: A beta-amyloid precursor protein immunocytochemical study in rats. J. Neuropathol. Exp. Neurol. *56*, 1132–1141.

Brewer, J.A., and Potenza, M.N. (2008). The neurobiology and genetics of impulse control disorders: Relationships to drug addictions. Biochem. Pharmacol. *75*, 63–75.

Brooks, D.M., Patel, S.A., Wohlgehagen, E.D., Semmens, E.O., Pearce, A., Sorich, E.A., and Rau, T.F. (2017). Multiple mild traumatic brain injury in the rat produces persistent pathological alterations in the brain. Exp. Neurol. *297*, 62–72.

Broshek, D.K., De Marco, A.P., and Freeman, J.R. (2015). A review of post-concussion syndrome and psychological factors associated with concussion. Brain Inj. *29*, 228–237.

Burda, J.E., Bernstein, A.M., Sofroniew, M. V, and Angeles, L. (2017). Astrocyte roles in traumatic brain injury. Exp Neurol. *275*, 305–315.

Bylicky, M.A., Mueller, G.P., and Day, R.M. (2018). Mechanisms of Endogenous Neuroprotective Effects of Astrocytes in Brain Injury. Oxid. Med. Cell. Longev. *2018*, 1–17.

Carroll, L.J., Cassidy, J.D., Cancelliere, C., Côté, P., Hincapié, C.A., Kristman, V.L., Holm, L.W., Borg, J., Nygren-De Boussard, C., and Hartvigsen, J. (2014). Systematic review of the prognosis after mild traumatic brain injury in adults: Cognitive, psychiatric, and mortality outcomes: Results of the international collaboration on mild traumatic brain injury prognosis. Arch. Phys. Med. Rehabil. *95*, S152–S173.

Cassidy, J.D., Carroll, L.J., Peloso, P.M., Borg, J., von Holst, H., Holm, L., Kraus, J., Coronado, V.G., and WHO Collaborating Centre Task Force on Mild Traumatic Brain, I. (2004). Incidence, risk factors and prevention of mild traumatic brain injury: results of the WHO Collaborating Centre Task Force on Mild Traumatic Brain Injury. J. Rehabil. Med. *43*, 28–60.

Changa, A.R., Vietrogoski, R.A., and Carmel, P.W. (2018). Dr Harrison Martland and the history of punch drunk syndrome. Brain *141*, 318–321.

Chen, H., Desai, A., and Kim, H.-Y. (2017a). Repetitive Closed-Head Impact Model of Engineered Rotational Acceleration Induces Long-Term Cognitive Impairments with Persistent Astrogliosis and Microgliosis in Mice. J. Neurotrauma *34*, 2291–2302.

Chen, Y.-H., Huang, E.Y.-K., Kuo, T.-T., Miller, J., Chiang, Y.-H., and Hoffer, B.J. (2017b). Impact of Traumatic Brain Injury on Dopaminergic Transmission. Cell Transplant. *26*, 1156–1168.

Cheng, W.H., Stukas, S., Martens, K.M., Namjoshi, D.R., Button, E.B., Wilkinson, A., Bashir, A., Robert, J., Cripton, P.A., and Wellington, C.L. (2018). Age at injury and genotype modify acute inflammatory and neurofilament-light responses to mild CHIMERA traumatic brain injury in wild-type and APP/PS1 mice. Exp. Neurol. *301*, 26–38.

Cheng, W.H., Martens, K.M., Bashir, A., Cheung, H., Stukas, S., Gibbs, E., Namjoshi, D.R., Button, E.B., Wilkinson, A., Barron, C.J., et al. (2019). CHIMERA repetitive mild traumatic brain injury induces chronic behavioural and neuropathological phenotypes in wild-type and APP/PS1 mice. Alzheimers. Res. Ther. *11*, 6.

Cherry, J.D., Tripodis, Y., Alvarez, V.E., Huber, B., Kiernan, P.T., Daneshvar, D.H., Mez, J., Montenigro, P.H., Solomon, T.M., Alosco, M.L., et al. (2016). Microglial neuroinflammation contributes to tau accumulation in chronic traumatic encephalopathy. Acta Neuropathol. Commun. Commun. *4*, 1–9.

Clark, L., Cools, R., and Robbins, T.W. (2004). The neuropsychology of ventral prefrontal cortex: Decision-making and reversal learning. Brain Cogn. *55*, 41–53.

Clevenger, A.C., Kilbaugh, T., and Margulies, S. (2015). Carotid Artery Blood Flow Decreases after Rapid Head Rotation in Piglets. J. Neurotrauma *32*, 120–126.

Colantonio, A., Harris, J.E., Ratcliff, G., Chase, S., and Ellis, K. (2010). Gender differences in self reported long term outcomes following moderate to severe traumatic brain injury. BMC Neurol. *10*.

Corrigan, J.D., and Hammond, F.M. (2013). Traumatic brain injury as a chronic health condition. Arch. Phys. Med. Rehabil. *94*, 1199–1201.

Corso, P., Finkelstein, E., Miller, T., Fielbelkorn, I., and Zaloshnja, E. (2006). Incidence and lifetime costs of injuries in the United States. Inj. Prev. *21*, 212–218.

Cortez, S.C., McIntosh, T.K., and Noble, L.J. (1989). Experimental fluid percussion brain injury: vascular disruption and neuronal and glial alterations. Brain Res. *482*, 271–282.

Crane, P.K., Gibbons, L.E., Dams-O'Connor, K., Trittschuh, E., Leverenz, J.B., Dirk Keene, C., Sonnen, J., Montine, T.J., Bennett, D.A., Leurgans, S., et al. (2016). Association of traumatic brain injury with late-life neurodegenerative conditions and Neuropathologic findings. JAMA Neurol. *73*, 1062–1069.

Cullen, D.K., Harris, J.P., Browne, K.D., Wolf, J.A., Duda, J.E., David, F., Margulies, S.S., and Smith, D.H. (2016). A Porcine Model of Traumatic Brain Injury via Head Rotational Acceleration. Methods Mol Biol *1462*, 289–324.

Dams-O'Connor, K., Gibbons, L.E., Bowen, J.D., McCurry, S.M., Larson, E.B., and Crane, P.K. (2013). Risk for late-life re-injury, dementia and death among individuals with traumatic brain injury: a population-based study. J. Neurol. Neurosurg. Psychiatry *84*, 177–182.

Diaz-Arrastia, R., Kochanek, P.M., Bergold, P., Kenney, K., Marx, C.E., Grimes, C.J.B., Loh, L.Y., Adam, L.G.E., Oskvig, D., Curley, K.C., et al. (2014). Pharmacotherapy of Traumatic Brain Injury: State of the Science and the Road Forward: Report of the Department of Defense Neurotrauma Pharmacology Workgroup. J. Neurotrauma *31*, 135–158.

Diedler, J., Zweifel, C., Budohoski, K.P., Kasprowicz, M., Sorrentino, E., Haubrich, C., Brady, K.M., Czosnyka, M., Pickard, J.D., and Smielewski, P. (2011). The limitations of near-infrared spectroscopy to assess cerebrovascular reactivity. Anesth. Analg. *113*, 849–857.

Dixon, M.R., Jacobs, E.A., Sanders, S., Guercio, J.M., Soldner, J., Parker-Singler, S., Robinson, A., Small, S., and Dillen, J.E. (2005). Impulsivity, self-control, and delay discounting in persons with acquired brain injury. Behav. Interv. *20*, 101–120.

Donat, C.K., Scott, G., Gentleman, S.M., and Sastre, M. (2017). Microglial activation in traumatic brain injury. Front. Aging Neurosci. *9*, 1–20.

Donnell, A.J., Kim, M.S., Silva, M.A., and Vanderploeg, R.D. (2012). Incidence of postconcussion symptoms in psychiatric diagnostic groups, mild traumatic brain injury, and comorbid conditions. Clin. Neuropsychol. *26*, 1092–1101.

Donnemiller, E., Brenneis, C., Wissel, J., Scherfler, C., Poewe, W., Riccabona, G., and Wenning, G. (2000). Impaired dopaminergic neurotransmission in patients with traumatic brain injury: A SPET study using 123I-beta-CIT and 123I-IBZM. Eur. J. Nucl. Med. *27*, 1410–1414.

Douglas, D.B., Iv, M., Douglas, P.K., Anderson, A., Vos, S.B., Bammer, R., Zeineh, M., and Wintermark, M. (2015). Diffusion tensor imaging of TBI: Potentials and challenges. Top. Magn. Reson. Imaging *24*, 241–251.

Douglas, D.B., Iv, M., Douglas, P.K., Ariana, A., Vos, S.B., Bammer, R., Zeineh, M., and Wintermark, M. (2019). Neuroimaging of traumatic brain injury. Med Sci *7*, 1–19.

Eikelenboom, P., van Exel, E., Hoozemans, J.J.M., Veerhuis, R., Rozemuller, A.J.M., and van Gool, W.A. (2010). Neuroinflammation – An Early Event in Both the History and Pathogenesis of Alzheimer's Disease. Neurodegener. Dis. *7*, 38–41.

Eucker, S., Smith, C., Ralston, J., Friess, S., and Margulies, S. (2011). Physiological and histopathological responses following closed rotational head injury depend on direction of head motion. Exp Neurol. *227*, 79–88.

Faden, A.I., and Loane, D.J. (2015). Chronic Neurodegeneration After Traumatic Brain Injury: Alzheimer Disease, Chronic Traumatic Encephalopathy, or Persistent Neuroinflammation? Neurotherapeutics *12*, 143–150.

Faul, M., Xu, L., Wald, M.M., Coronado, V., and Dellinger, A.M. (2010). Traumatic Brain Injury in the United States: National estimates of prevalence and incidence, 2002-2006. Inj. Prev. *16*, A1–A289.

Fleminger, S., Oliver, D.L., Lovestone, S., Rabe-Hesketh, S., and Giora, A. (2003). Head injury as a risk factor for Alzheimer's disease: the evidence 10 years on; a partial replication. J. Neurol. Neurosurg. Psychiatry *74*, 857–862.

Flierl, M.A., Stahel, P.F., Beauchamp, K.M., Morgan, S.J., Smith, W.R., and Shohami, E. (2009). Mouse closed head injury model induced by a weight-drop device. Nat. Protoc. *4*, 1328–1337.

Furuya, Y., Hlatky, R., Valadka, A.B., Diaz, P., and Robertson, C.S. (2003). Comparison of cerebral blood flow in computed tomographic hypodense areas of the brain in head-injured patients. Neurosurgery *52*, 340–346.

Gangolli, M., Benetatos, J., Esparza, T.J., Fountain, E.M., Seneviratne, S., and Brody, D. (2018). Repetitive concussive and subconcussive injury in a human tau mouse model results in chronic cognitive dysfunction and disruption of white matter tracts, but not tau pathology. J. Neurotrauma *21*, neu.2018.5700.

Gao, H., Han, Z., Bai, R., Huang, S., Ge, X., Chen, F., and Lei, P. (2017). The accumulation of brain injury leads to severe neuropathological and neurobehavioral changes after repetitive mild traumatic brain injury. Brain Res. *1657*, 1–8.

Gardner, A.J., Tan, C.O., Ainslie, P.N., van Donkelaar, P., Stanwell, P., Levi, C.R., and Iverson, G.L. (2015). Cerebrovascular reactivity assessed by transcranial Doppler ultrasound in sport-related concussion: a systematic review. Br. J. Sports Med. *49*, 1050–1055.

Gardner, R.C., Burke, J.F., Nettiksimmons, J., Kaup, A., Barnes, D.E., and Yaffe, K. (2014).

Dementia risk after traumatic brain injury vs nonbrain trauma: The role of age and severity. JAMA Neurol. *71*, 1490–1497.

Gardner, R.C., Byers, A.L., Barnes, D.E., Li, Y., Boscardin, J., and Yaffe, K. (2018). Mild TBI and risk of Parkinson disease. Neurology *90*, e1771–e1779.

Geets, W., and Louette, N. (1985). The EEG of three hundred recent concussions. Rev E.E.G. Neurophysiol *14*, 333–338.

Gentleman, S.M., Greenberg, B.D., Savage, M.J., Noori, M., Newman, S.J., Roberts, G.W., Griffin, W.S., and Graham, D.I. (1997). A beta 42 is the predominant form of amyloid beta-protein in the brains of short-term survivors of head injury. Neuroreport *8*, 1519–1522.

Giordano, C., and Kleiven, S. (2016). Development of an Unbiased Validation Protocol to Assess the Biofidelity of Finite Element Head Models used in Prediction of Traumatic Brain Injury. Stapp Car Crash J. *60*, 363–471.

Goldstein, L.E., Fisher, A.M., Tagge, C.A., Zhang, X.-L., Velisek, L., Sullivan, J.A., Upreti, C., Kracht, J.M., Ericsson, M., Wojnarowicz, M.W., et al. (2012). Chronic Traumatic Encephalopathy in Blast-Exposed Military Veterans and a Blast Neurotrauma Mouse Model. Sci. Transl. Med. *4*, 134ra60.

Gosselin, N., Bottari, C., Chen, J.-K., Huntgeburth, S.C., De Beaumont, L., Petrides, M., Cheung, B., and Ptito, A. (2012). Evaluating the cognitive consequences of mild traumatic brain injury and concussion by using electrophysiology. Neurosurg. Focus *33*, E7.

Goswami, R., Dufort, P., Tartaglia, M.C., Green, R.E., Crawley, A., Tator, C.H., Wennberg, R., Mikulis, D.J., Keightley, M., and Davis, K.D. (2016). Frontotemporal correlates of

impulsivity and machine learning in retired professional athletes with a history of multiple concussions. Brain Struct. Funct. *221*, 1911–1925.

Graham, D.P., and Cardon, A.L. (2008). An update on substance use and treatment following traumatic brain injury. Ann. N. Y. Acad. Sci. *1141*, 148–162.

Graham, D.I., Gentleman, S.M., Lynch, A., and Roberts, G.W. (1995). Distribution of beta-amyloid protein in the brain following severe head injury. Neuropathol. Appl. Neurobiol. *21*, 27–34.

Graham, D.I., Raghupathi, R., Saatman, K.E., Meaney, D., and McIntosh, T.K. (2000). Tissue tears in the white matter after lateral fluid percussion brain injury in the rat: Relevance to human brain injury. Acta Neuropathol. *99*, 117–124.

Guo, Z., Cupples, L.A., Kurz, A., Auerbach, S.H., Volicer, L., Chui, H., Green, R.C., Sadovnick, A.D., Duara, R., DeCarli, C., et al. (2000). Head injury and the risk of AD in the MIRAGE study. Neurology *54*, 1316–1323.

Gupte, R., Brooks, W.M., Vukas, R.R., Pierce, J.D., and Harris, J.L. (2019). Sex differences in traumatic brain injury: What we know and what we should know. J. Neurotrauma *29*, 1–29.

Guskiewicz, K.M., Ph, D., and Marshall, S.W. (2007). Measurement of Head Impacts in Collegiate Impact Biomechanics and acute Clinical Outcome after Concussion. Neurosurgery *61*, 1244–1253.

Haber, M., Hutchinson, E.B., Sadeghi, N., Cheng, W.H., Namjoshi, D., Cripton, P., Irfanoglu, M.O., Wellington, C., Diaz-Arrastia, R., and Pierpaoli, C. (2017). Defining an Analytic Framework to Evaluate Quantitative MRI Markers of Traumatic Axonal Injury: Preliminary Results in a Mouse Closed Head Injury Model. Eneuro *4*, ENEURO.0164-

17.2017.

Haber, M., Amyot, F., Kenney, K., Meredith-Duliba, T., Moore, C., Silverman, E., Podell, J., Chou, Y.-Y., Pham, D.L., Butman, J., et al. (2018). Vascular Abnormalities within Normal Appearing Tissue in Chronic Traumatic Brain Injury. J. Neurotrauma *35*, 2250–2258.

Haydel, M., Preston, C., Mills, T., Luber, S., Blaudeau, A., and DeBlieux, P. (2000). Indications for computed tomography in patients. N. Engl. J. Med. *343*, 100–195.

Hehar, H., Yeates, K., Kolb, B., Esser, M.J., and Mychasiuk, R. (2015). Impulsivity and concussion in juvenile rats: Examining molecular and structural aspects of the frontostriatal pathway. PLoS One *10*, 1–24.

Herman, S.T. (2002). Epilepsy after brain insult: Targeting epileptogenesis. Neurology *59*, S21–S26.

Hodel, A.S., Brumbaugh, J.E., Morris, A.R., and Thomas, K.M. (2016). Hot executive function following moderate-to-late preterm birth: Altered delay discounting at 4 years of age. Dev. Sci. *19*, 221–234.

Huang, Y.L., Kuo, Y.S., Tseng, Y.C., Chen, D.Y.T., Chiu, W.T., and Chen, C.J. (2015). Susceptibility-weighted MRI in mild traumatic brain injury. Neurology *84*, 580–585.

Hulkower, M.B., Poliak, D.B., Rosenbaum, S.B., Zimmerman, M.E., and Lipton, M.L. (2013). A decade of DTI in traumatic brain injury: 10 years and 100 articles later. Am. J. Neuroradiol. *34*, 2064–2074.

Impellizzeri, D., Campolo, M., Bruschetta, G., Crupi, R., Cordaro, M., Paterniti, I., Cuzzocrea, S., and Esposito, E. (2016). Traumatic brain injury leads to development of Parkinson's disease related pathology in mice. Front. Neurosci. *10*, 1–13.

Ito, K., Asano, Y., Ikegame, Y., and Shinoda, J. (2016). Differences in brain metabolic impairment between chronic mild/moderate TBI patients with and without visible brain lesions based on MRI. Biomed Res. Int. *2016*, 1–8.

Jack, C.R., Vemuri, P., Wiste, H.J., Weigand, S.D., Aisen, P.S., Trojanowski, J.Q., Shaw, L.M., Bernstein, M.A., Petersen, R.C., Weiner, M.W., et al. (2011). Evidence for ordering of Alzheimer Disease biomarkers. Arch. Neurol. *68*, 1526.

Jack, C.R., Bennett, D.A., Blennow, K., Carrillo, M.C., Dunn, B., Haeberlein, S.B., Holtzman, D.M., Jagust, W., Jessen, F., Karlawish, J., et al. (2018). NIA-AA Research Framework: Toward a biological definition of Alzheimer's disease. Alzheimer's Dement. *14*, 535–562.

Jenkins, P.O., De Simoni, S., Bourke, N.J., Fleminger, J., Scott, G., Towey, D.J., Svensson, W., Khan, S., Patel, M., Greenwood, R., et al. (2018). Dopaminergic abnormalities following traumatic brain injury. Brain *141*, 797–810.

Johnson, V.E., Stewart, W., and Smith, D.H. (2012). Widespread Tau and Amyloid-Beta Pathology Many Years After a Single Traumatic Brain Injury in Humans. Brain Pathol. *22*, 142–149.

Johnson, V.E., Stewart, J.E., Begbie, F.D., Trojanowski, J.Q., Smith, D.H., and Stewart, W. (2013). Inflammation and white matter degeneration persist for years after a single traumatic brain injury. Brain *136*, 28–42.

Johnson, V.E., Weber, M.T., Xiao, R., Cullen, D.K., Meaney, D.F., Stewart, W., and Smith, D.H. (2018). Mechanical disruption of the blood – brain barrier following experimental concussion. Acta Neuropathol. *135*, 711–726.

Juengst, S.B., Kumar, R.G., Arenth, P.M., and Wagner, A.K. (2014). Exploratory associations

with Tumor Necrosis Factor- a , disinhibition and suicidal endorsement after traumatic brain injury. Brain Behav. Immun. *41*, 134–143.

Kainerstorfer, J.M., Sassaroli, A., Tgavalekos, K.T., and Fantini, S. (2015). Cerebral autoregulation in the microvasculature measured with near-infrared spectroscopy. J. Cereb. Blood Flow Metab. *35*, 959–966.

Kallakuri, S., Bandaru, S., Zakaria, N., Shen, Y., Kou, Z., Zhang, L., Haacke, E., and Cavanaugh, J. (2015). Traumatic Brain Injury by a Closed Head Injury Device Induces Cerebral Blood Flow Changes and Microhemorrhages. J. Clin. Imaging Sci. *5*.

Kane, M.J., Angoa-Pérez, M., Briggs, D.I., Viano, D.C., Kreipke, C.W., and Kuhn, D.M. (2012). A mouse model of human repetitive mild traumatic brain injury. J. Neurosci. Methods *203*, 41–49.

Karve, I.P., Taylor, J.M., and Crack, P.J. (2016). The contribution of astrocytes and microglia to traumatic brain injury. Br. J. Pharmacol. *173*, 692–702.

Kassner, A., and Roberts, T.P.L. (2004). Beyond perfusion: cerebral vascular reactivity and assessment of microvascular permeability. Top. Magn. Reson. Imaging *15*, 58–65.

Kim, E. (2002). Agitation , aggression , and disinhibition syndromes after traumatic brain injury. NeuroRehabilitation *17*, 297–310.

Kim, J., Whyte, J., Patel, S., Avants, B., Europa, E., Wang, J., Slattery, J., Gee, J.C., Coslett, H.B., and Detre, J.A. (2010). Resting Cerebral Blood Flow Alterations in Chronic Traumatic Brain Injury: An Arterial Spin Labeling Perfusion fMRI Study. J. Neurotrauma *27*, 1399–1411.

Kocka, A., and Gagnon, J. (2014). Definition of Impulsivity and Related Terms Following Traumatic Brain Injury: A Review of the Different Concepts and Measures Used to

Assess Impulsivity, Disinhibition and other Related Concepts. Behav. Sci. *4*, 352–370.

Koliatsos, V.E., Cernak, I., Xu, L., Song, Y., Savonenko, A., Crain, B.J., Eberhart, C.G., Frangakis, C.E., Melnikova, T., Kim, H., et al. (2011). A mouse model of blast injury to brain: Initial pathological, neuropathological, and behavioral characterization. J. Neuropathol. Exp. Neurol. *70*, 399–416.

Kukull, W.A., Larson, E.B., Reifler, B. V, Lampe, T.H., Yerby, M.S., and Hughes, J.P. (1990). The validity of 3 clinical diagnostic criteria for Alzheimer's disease. Neurology *40*, 1364–1369.

Kumar, A., and Loane, D.J. (2012). Neuroinflammation after traumatic brain injury: Opportunities for therapeutic intervention. Brain. Behav. Immun. *26*, 1191–1201.

Lamar, C.D., Hurley, R.A., Rowland, J.A., and Taber, K.H. (2014). Post-Traumatic Epilepsy: Review of Risks, Pathophysiology, and Potential Biomarkers. J. Neuropsychiatry Clin. Neurosci. *26*, iv–113.

Lawrence, T.P., Pretorius, P.M., Ezra, M., Cadoux-Hudson, T., and Voets, N.L. (2017). Early detection of cerebral microbleeds following traumatic brain injury using MRI in the hyper-acute phase. Neurosci. Lett. *655*, 143–150.

Lee, J.K., Kibler, K.K., Benni, P.B., Easley, R.B., Czosnyka, M., Smielewski, P., Koehler, R.C., Shaffner, D.H., and Brady, K.M. (2009). Cerebrovascular reactivity measured by near-infrared spectroscopy. Stroke *40*, 1820–1826.

Lewine, J.D., Davis, J.T., Bigler, E.D., Thoma, R., Hill, D., Funke, M., Sloan, J.H., Hall, S., and Orrison, W.W. (2007). Objective documentation of traumatic brain injury subsequent to mild head trauma: multimodal brain imaging with MEG, SPECT, and MRI. J. Head Trauma Rehabil. *22*, 141–155.

Liu, M., Bachstetter, A.D., Cass, W.A., Lifshitz, J., and Bing, G. (2017). Pioglitazone Attenuates Neuroinflammation and Promotes Dopaminergic Neuronal Survival in the Nigrostriatal System of Rats after Diffuse Brain Injury. J. Neurotrauma *34*, 414–422.

Lucke-Wold, B.P., Nguyen, L., Turner, R.C., Logsdon, A.F., Chen, Y.W., Smith, K.E., Huber, J.D., Matsumoto, R., Rosen, C.L., Tucker, E.S., et al. (2015). Traumatic brain injury and epilepsy: Underlying mechanisms leading to seizure. Seizure *33*, 13–23.

Lucke-Wold, B.P., Logsdon, A.F., Smith, K.E., Turner, R.C., Alkon, D.L., Tan, Z., Naser, Z.J., Knotts, C.M., Huber, J.D., and Rosen, C.L. (2016). Bryostatin-1 Restores Blood Brain Barrier Integrity following Blast-Induced Traumatic Brain Injury. Mol. Neurobiol. *52*, 1119–1134.

Luo, J., Nguyen, A., Villeda, S., Zhang, H., Ding, Z., Lindsey, D., Bieri, G., Castellano, J.M., Beaupre, G.S., and Wyss-Coray, T. (2014). Long-term cognitive impairments and pathological alterations in a mouse model of repetitive mild traumatic brain injury. Front. Neurol. *5 FEB*, 1–13.

Lyeth, B.G. (2016). Historical review of the fluid-percussion TBI model. Front. Neurol. *7*, 1–7.

Maas, A.I.R., Menon, D.K., Adelson, P.D., Andelic, N., Bell, M.J., Belli, A., Bragge, P., Brazinova, A., Büki, A., Chesnut, R.M., et al. (2017). Traumatic brain injury: integrated approaches to improve prevention, clinical care, and research. Lancet Neurol. *16*, 987–1048.

Mahar, I., Alosco, M.L., and McKee, A.C. (2017). Psychiatric phenotypes in chronic traumatic encephalopathy. Neurosci. Biobehav. Rev. *83*, 622–630.

Marar, M., McIlvain, N.M., Fields, S.K., and Comstock, R.D. (2012). Epidemiology of concussions among united states high school athletes in 20 sports. Am. J. Sports Med. *40*,

747–755.

Marotti, K.R., Castle, C.K., Boyle, T.P., Lin, A.H., Murray, R.W., and Melchior, G.W. (1993). Severe atherosclerosis in transgenic mice expressing simian cholesteryl ester transfer protein. Nature *364*, 73–75.

Martland, H.S. (1928). Punch Drunk. J. Am. Med. Assoc. *91*, 1103.

Masel, B.E., and DeWitt, D.S. (2010). Traumatic brain injury: a disease process, not an event. J. Neurotrauma *27*, 1529–1540.

Max, W., MacKenzie, E.J., and Rice, D.P. (1991). Head injuries: costs and consequences. J Head Inj Rehab *6*, 76–91.

McAteer, K.M., Corrigan, F., Thornton, E., Turner, R.J., and Vink, R. (2016). Short and long term behavioral and pathological changes in a novel rodent model of repetitive mild traumatic brain injury. PLoS One *11*, 1–18.

McGlade, E., Rogowska, J., and Yurgelun-Todd, D. (2015). Sex differences in orbitofrontal connectivity in male and female veterans with TBI. Brain Imaging Behav. *9*, 535–549.

McIntosh, A.S., Patton, D.A., Fréchède, B., Pierré, P.A., Ferry, E., and Barthels, T. (2014). The biomechanics of concussion in unhelmeted football players in Australia: A case-control study. BMJ Open *4*, 1–9.

McIntosh, T.K., Juhler, M., and Wieloch, T. (1998). Novel pharmacologic strategies in the treatment of experimental traumatic brain injury: 1998. J. Neurotrauma *15*, 731–769.

Mckee, A.C., Stein, T.D., Kiernan, P.T., and Alvarez, V.E. (2016). The Neuropathology of Chronic Traumatic Encephalopathy. Brain Pathol. *25*, 350–364.

McKee, A.C., and Daneshvar, D.H. (2015). The neuropathology of traumatic brain injury. Handb. Clin. Neurol. *127*, 45–66.

McKee, A.C., Cairns, N.J., Dickson, D.W., Folkerth, R.D., Dirk Keene, C., Litvan, I., Perl, D.P., Stein, T.D., Vonsattel, J.P., Stewart, W., et al. (2016). The first NINDS/NIBIB consensus meeting to define neuropathological criteria for the diagnosis of chronic traumatic encephalopathy. Acta Neuropathol. *131*, 75–86.

Meabon, J.S., Huber, B.R., Cross, D.J., Richards, T.L., Minoshima, S., Pagulayan, K.F., Li, G., Meeker, K.D., Kraemer, B.C., Petrie, E.C., et al. (2016). Repetitive blast exposure in mice and combat veterans causes persistent cerebellar dysfunction. Sci. Transl. Med. *8*, 1–16.

Mehta, K.M., Ott, A., Kalmijn, S., Slooter, A.J., van Duijn, C.M., Hofman, A., and Breteler, M.M. (1999). Head trauma and risk of dementia and Alzheimer's disease: The Rotterdam Study. Neurology *53*, 1959–1962.

Menon, D.K. (2006). Brain ischaemia after traumatic brain injury: Lessons from 15O2 positron emission tomography. Curr. Opin. Crit. Care *12*, 85–89.

Menon, D.K., and Maas, A.I.R. (2015). Traumatic brain injury in 2014 : Progress, failures and new approaches for TBI research. Nat. Rev. Gastroenterol. Hepatol. *12*, 57–58.

Menon, D.K., Schwab, K., Wright, D.W., and Maas, A.I. (2010). Position statement: Definition of traumatic brain injury. Arch. Phys. Med. Rehabil. *91*, 1637–1640.

Merkel, S.F., Cannella, L.A., Razmpour, R., Lutton, E., Raghupathi, R., Rawls, S.M., and Ramirez, S.H. (2017). Factors affecting increased risk for substance use disorders following traumatic brain injury: What we can learn from animal models. Neurosci. Biobehav. Rev. *77*, 209–218.

Mez, J., Daneshvar, D.H., Kiernan, P.T., Abdolmohammadi, B., Alvarez, V.E., Huber, B.R., Alosco, M.L., Solomon, T.M., Nowinski, C.J., McHale, L., et al. (2017).

Clinicopathological evaluation of chronic traumatic encephalopathy in players of American football. JAMA - J. Am. Med. Assoc. *318*, 360–370.

Modarres, M.H., Kuzma, N.N., Kretzmer, T., Pack, A.I., and Lim, M.M. (2017). EEG slow waves in traumatic brain injury: Convergent findings in mouse and man. Neurobiol. Sleep Circadian Rhythm. *2*, 59–70.

Montenigro, P.H., Alosco, M.L., Martin, B.M., Daneshvar, D.H., Mez, J., Chaisson, C.E., Nowinski, C.J., Au, R., McKee, A.C., Cantu, R.C., et al. (2017). Cumulative Head Impact Exposure Predicts Later-Life Depression, Apathy, Executive Dysfunction, and Cognitive Impairment in Former High School and College Football Players. J. Neurotrauma *34*, 328–340.

Mountney, A., Boutté, A.M., Cartagena, C.M., Flerlage, W.F., Johnson, W.D., Rho, C., Lu, X.-C., Yarnell, A., Marcsisin, S., Sousa, J., et al. (2017). Functional and Molecular Correlates After Single and Repeated Rat Closed-Head Concussion: Indices of Vulnerability After Brain Injury. J. Neurotrauma *34*, 2768–2789.

Mouzon, B.C., Bachmeier, C., Ojo, J.O., Acker, C.M., Ferguson, S., Paris, D., Ait-Ghezala, G., Crynen, G., Davies, P., Mullan, M., et al. (2018). Lifelong behavioral and neuropathological consequences of repetitive mild traumatic brain injury. Ann. Clin. Transl. Neurol. *5*, 64–80.

Mutch, W.A.C., Ellis, M.J., Ryner, L.N., Ruth Graham, M., Dufault, B., Gregson, B., Hall, T., Bunge, M., Essig, M., Fisher, J.A., et al. (2016a). Brain magnetic resonance imaging CO 2 stress testing in adolescent postconcussion syndrome. J. Neurosurg. *125*, 648–660.

Mutch, W.A.C., Ellis, M.J., Ryner, L.N., Morissette, M.P., Pries, P.J., Dufault, B., Essig, M., Mikulis, D.J., Duffin, J., and Fisher, J.A. (2016b). Longitudinal Brain Magnetic

Resonance Imaging CO2 Stress Testing in Individual Adolescent Sports-Related Concussion Patients: A Pilot Study. Front. Neurol. *7*, 1–8.

Myburgh, J.A., Cooper, D.J., Finfer, S., Venkatesh, B., Jones, D., Higgins, A., Bishop, N., Higlett, T., and Myburgh, J. (2008). Epidemiology and 12-month outcomes from traumatic brain injury in Australia and New Zealand. J. Trauma - Inj. Infect. Crit. Care *64*, 854–862.

Myer, D.J., Gurkoff, G.G., Lee, S.M., Hovda, D.A., and Sofroniew, M. V. (2006). Essential protective roles of reactive astrocytes in traumatic brain injury. Brain *129*, 2761–2772.

Myerson, J., Green, L., and Warusawitharana, M. (2001). Area under the curve as a measure of discounting. J. Exp. Anal. Behav. *76*, 235–243.

Najjar, S., Pearlman, D.M., Alper, K., Najjar, A., and Devinsky, O. (2013). Neuroinflammation and psychiatric illness. J. Neuroinflammation *10*, 1–24.

Namjoshi, D.R., Martin, G., Donkin, J., Wilkinson, A., Stukas, S., Fan, J., Carr, M., Tabarestani, S., Wuerth, K., Hancock, R.E.W., et al. (2013). The Liver X Receptor Agonist GW3965 Improves Recovery from Mild Repetitive Traumatic Brain Injury in Mice Partly through Apolipoprotein E. PLoS One *8*, 1–14.

Namjoshi, D.R., Cheng, W.H. an., McInnes, K.A., Martens, K.M., Carr, M., Wilkinson, A., Fan, J., Robert, J., Hayat, A., Cripton, P.A., et al. (2014). Merging pathology with biomechanics using CHIMERA (Closed-Head Impact Model of Engineered Rotational Acceleration): a novel, surgery-free model of traumatic brain injury. Mol. Neurodegener. *9*, 1–18.

Namjoshi, D.R., Cheng, W.H., Carr, M., Martens, K.M., Zareyan, S., Wilkinson, A., McInnes, K.A., Cripton, P.A., and Wellington, C.L. (2016). Chronic exposure to androgenic-

anabolic steroids exacerbates axonal injury and microgliosis in the CHIMERA mouse model of repetitive concussion. PLoS One *11*, 1–21.

Namjoshi, D.R., Cheng, W.H., Bashir, A., Wilkinson, A., Stukas, S., Martens, K.M., Whyte, T., Abebe, Z.A., McInnes, K.A., Cripton, P.A., et al. (2017). Defining the biomechanical and biological threshold of murine mild traumatic brain injury using CHIMERA (Closed Head Impact Model of Engineered Rotational Acceleration). Exp. Neurol. *292*, 80–91.

Nation, D.A., Sweeney, M.D., Montagne, A., Sagare, A.P., D'orazio, L.M., Pachicano, M., Sepehrband, F., Nelson, A.R., Buennagel, D.P., Harrington, M.G., et al. (2019). Blood-brain barrier breakdown is an early biomarker of human cognitive dysfunction. Nat. Med. *25*, 270–276.

Nordström, P., Michaëlsson, K., Gustafson, Y., and Nordström, A. (2014). Traumatic brain injury and young onset dementia: a nationwide cohort study. Ann. Neurol. *75*, 374–381.

Oertel, M., Boscardin, W.J., Obrist, W.D., Glenn, T.C., McArthur, D.L., Gravori, T., Lee, J.H., and Martin, N.A. (2005). Posttraumatic vasospasm: the epidemiology, severity, and time course of an underestimated phenomenon: a prospective study performed in 299 patients. J. Neurosurg. *103*, 812–824.

Olesen, J., Gustavsson, A., Svensson, M., Wittchen, H.U., and Jönsson, B. (2012). The economic cost of brain disorders in Europe. Eur. J. Neurol. *19*, 155–162.

Ommaya, A., Faas, F., and Yarnell, P. (1968). Whiplash Injury and Brain Damage. JAMA - J. Am. Med. Assoc. *204*, 285–289.

Osier, N., and Dixon, C.E. (2017). Mini review of controlled cortical impact: A well-suited device for concussion research. Brain Sci. *7*.

Ouyang, Y., Voloboueva, L.A., Xu, L., and Giffard, R.G. (2007). Selective Dysfunction of

Hippocampal CA1 Astrocytes Contributes to Delayed Neuronal Damage after Transient Forebrain Ischemia. *27*, 4253–4260.

Ozga, J.E., Povroznik, J.M., Engler-Chiurazzi, E.B., and Haar, C.V. (2018). Executive (dys)function after traumatic brain injury. Behav. Pharmacol. *29*, 617–637.

Panzer, M.B., Wood, G.W., and Bass, C.R. (2014). Scaling in neurotrauma: How do we apply animal experiments to people? Exp. Neurol. *261*, 120–126.

Papa, L., Ramia, M.M., Edwards, D., Johnson, B.D., and Slobounov, S.M. (2015). Systematic review of clinical studies examining biomarkers of brain injury in athletes after sports-related concussion. J. Neurotrauma *32*, 661–673.

Pitkänen, A., and Bolkvadze, T. (2010). Head trauma and epilepsy. Epilepsia *51*, 31.

Plassman, B.L., Havlik, R.J., Steffens, D.C., Helms, M.J., Newman, T.N., Drosdick, D., Phillips, C., Gau, B.A., Welsh-Bohmer, K.A., Burke, J.R., et al. (2000). Documented head injury in early adulthood and risk of Alzheimer's disease and other dementias. Neurology *55*, 1158–1166.

Raji, C.A., Tarzwell, R., Pavel, D., Schneider, H., Uszler, M., Thornton, J., van Lierop, M., Cohen, P., Amen, D.G., and Henderson, T. (2014). Clinical utility of SPECT neuroimaging in the diagnosis and treatment of traumatic brain injury: a systematic review. PLoS One *9*, e91088.

Ransohoff, R.M. (2016). A polarizing question: do M1 and M2 microglia exist? *19*, 987–991.

Rao, D.P., McFaull, S., Thompson, W., and Jayaraman, G.C. (2017). Trends in self-reported traumatic brain injury among Canadians, 2005-2014: a repeated cross-sectional analysis. C. Open *5*, E301–E307.

Rapp, P.E., Keyser, D.O., Albano, A., Hernandez, R., Gibson, D.B., Zambon, R.A., Hairston,

W.D., Hughes, J.D., Krystal, A., and Nichols, A.S. (2015). Traumatic Brain Injury Detection Using Electrophysiological Methods. Front. Hum. Neurosci. *9*, 1–32.

Rizzi, G., and Tan, K.R. (2017). Dopamine and Acetylcholine, a Circuit Point of View in Parkinson's Disease. Front. Neural Circuits *11*.

Rochat, L., Beni, C., Billieux, J., Azouvi, P., Annoni, J.M., and Van Der Linden, M. (2010). Assessment of impulsivity after moderate to severe traumatic brain injury. Neuropsychol. Rehabil. *20*, 778–797.

Rodríguez-Baeza, A., Reina-de la Torre, F., Poca, A., Martí, M., and Garnacho, A. (2003). Morphological features in human cortical brain microvessels after head injury: A three-dimensional and immunocytochemical study. Anat. Rec. Part A Discov. Mol. Cell. Evol. Biol. *273A*, 583–593.

Rodriguez Merzagora, A.C., Izzetoglu, M., Onaral, B., and Schultheis, M.T. (2014). Verbal working memory impairments following traumatic brain injury: an fNIRS investigation. Brain Imaging Behav. *8*, 446–459.

Rosenthal, J.A., Foraker, R.E., Collins, C.L., and Comstock, R.D. (2014). National high school athlete concussion rates from 2005-2006 to 2011-2012. Am. J. Sports Med. *42*, 1710–1715.

Rowson, S., Duma, S.M., Beckwith, J.G., Chu, J.J., Greenwald, R.M., Crisco, J.J., Brolinson, P.G., Duhaime, A.C., McAllister, T.W., and Maerlender, A.C. (2012). Rotational head kinematics in football impacts: An injury risk function for concussion. Ann. Biomed. Eng. *40*, 1–13.

Rusnak, M. (2013). Traumatic brain injury: Giving voice to a silent epidemic. Nat. Rev. Neurol. *9*, 186–187.

Saatman, K.E., Duhaime, A.-C., Bullock, R., Maas, A.I.R., Valadka, A., Manley, G.T., and Workshop Scientific Team and Advisory Panel Members (2008). Classification of Traumatic Brain Injury for Targeted Therapies. J. Neurotrauma *25*, 719–738.

Sagare, A.P., Sweeney, M.D., Makshanoff, J., and Zlokovic, B. V (2015). Shedding of soluble platelet-derived growth factor receptor-β from human brain pericytes. Neurosci. Lett. *607*, 97–101.

Saing, T., Dick, M., Nelson, P.T., Kim, R.C., Cribbs, D.H., and Head, E. (2011). Frontal Cortex Neuropathology in Dementia Pugilistica. J. Neurotrauma *29*, 1054–1070.

Sariaslan, A., Sharp, D.J., D'Onofrio, B.M., Larsson, H., and Fazel, S. (2016). Long-Term Outcomes Associated with Traumatic Brain Injury in Childhood and Adolescence: A Nationwide Swedish Cohort Study of a Wide Range of Medical and Social Outcomes. PLoS Med. *13*, 15–19.

Sauerbeck, A.D., Fanizzi, C., Kim, J.H., Gangolli, M., Bayly, P. V., Wellington, C.L., Brody, D.L., and Kummer, T.T. (2018). ModCHIMERA: A novel murine closed-head model of moderate traumatic brain injury. Sci. Rep. *8*, 1–17.

Saw, M.M., Chamberlain, J., Barr, M., Morgan, M.P.G., Burnett, J.R., and Ho, K.M. (2014). Differential disruption of blood–brain barrier in severe traumatic brain injury. Neurocrit. Care *20*, 209–216.

Schwarzbold, M., Diaz, A., Martins, E.T., Rufino, A., Amante, L.N., Thais, M.E., Quevedo, J., Hohl, A., Linhares, M.N., and Walz, R. (2008). Psychiatric disorders and traumatic brain injury. Neuropsychiatr. Dis. Treat. *4*, 797–816.

Scott, C., McKinlay, A., McLellan, T., Britt, E., Grace, R., and MacFarlane, M. (2015). A comparison of adult outcomes for males compared to females following pediatric

traumatic brain injury. Neuropsychology *29*, 501–508.

Selassie, A.W., Wilson, D.A., Pickelsimer, E.E., Voronca, D.C., Williams, N.R., and Edwards, J.C. (2013). Incidence of sport-related traumatic brain injury and risk factors of severity: A population-based epidemiologic study. Ann. Epidemiol. *23*, 750–756.

Semple, B.D., Dixit, S., Shultz, S.R., Boon, W.C., and O'Brien, T.J. (2017). Sex-dependent changes in neuronal morphology and psychosocial behaviors after pediatric brain injury. Behav. Brain Res. *319*, 48–62.

Sener, S., Van Hecke, W., Feyen, B.F.E., Van der Steen, G., Pullens, P., Van de Hauwe, L., Menovsky, T., Parizel, P.M., Jorens, P.G., and Maas, A.I.R. (2016). Diffusion Tensor Imaging: A Possible Biomarker in Severe Traumatic Brain Injury and Aneurysmal Subarachnoid Hemorrhage? Neurosurgery *79*, 786–793.

Shahim, P., Gren, M., Liman, V., Andreasson, U., Norgren, N., Tegner, Y., Mattsson, N., Andreasen, N., Öst, M., Zetterberg, H., et al. (2016). Serum neurofilament light protein predicts clinical outcome in traumatic brain injury. Sci. Rep. *6*, 1–9.

Shenton, M.E., Hamoda, H.M., Schneiderman, J.S., Bouix, S., Pasternak, O., Rathi, Y., Vu, M.A., Purohit, M.P., Helmer, K., Koerte, I., et al. (2012). A review of magnetic resonance imaging and diffusion tensor imaging findings in mild traumatic brain injury. Brain Imaging Behav. *6*, 137–192.

Shewchenko, N., Withnall, C., Keown, M., Gittens, R., and Dvorak, J. (2005). Heading in football. Part 1: Development of biomechanical methods to investigate head response. Br. J. Sports Med. *39*, 10–25.

Shlosberg, D., Benifla, M., Kaufer, D., and Friedman, A. (2010). Blood–brain barrier breakdown as a therapeutic target in traumatic brain injury. Nat. Rev. Neurol. *6*, 393–403.

Shultz, S.R., McDonald, S.J., Vonder Haar, C., Meconi, A., Vink, R., van Donkelaar, P., Taneja, C., Iverson, G.L., and Christie, B.R. (2017). The potential for animal models to provide insight into mild traumatic brain injury: Translational challenges and strategies. Neurosci. Biobehav. Rev. *76*, 396–414.

Siedler, D.G., Chuah, M.I., Kirkcaldie, M.T.K., Vickers, J.C., and King, A.E. (2014). Diffuse axonal injury in brain trauma: insights from alterations in neurofilaments. Front. Cell. Neurosci. *8*, 1–10.

Silver, J.K., and Lux, W.E. (1994). Early onset dystonia following traumatic brain injury. Arch. Phys. Med. Rehabil. *75*, 885–888.

Skolnick, B.E., Maas, A.I., Narayan, R.K., van der Hoop, R.G., MacAllister, T., Ward, J.D., Nelson, N.R., and Stocchetti, N. (2014). A Clinical Trial of Progesterone for Severe Traumatic Brain Injury. N. Engl. J. Med. *371*, 2467–2476.

Stein, D.G. (2015). Embracing failure: What the Phase III progesterone studies can teach about TBI clinical trials. Brain Inj *29*, 1362–301.

Stewart, W., Allinson, K., Al-Sarraj, S., Bachmeier, C., Barlow, K., Belli, A., Burns, M.P., Carson, A., Crawford, F., Dams-O'Connor, K., et al. (2019). Primum non nocere: a call for balance when reporting on CTE. Lancet Neurol. *18*, 231–233.

Streit, W.J. (2000). Microglial Response to Brain Injury : A brief synopsis. Toxicol. Pathol. *28*, 28–30.

Stukas, S., Higgins, V., Frndova, H., Gill, J., Hubara, E., Guerguerian, A.-M., Boutis, K., Beauchamp, M., Farrell, C., Babl, F.E., et al. (2019). Characterisation of serum total tau following paediatric traumatic brain injury: a case-control study. Lancet Child Adolesc. Heal. *3*, 558–567.

Sweeney, M.D., Sagare, A.P., and Zlokovic, B. V. (2018a). Blood-brain barrier breakdown in Alzheimer disease and other neurodegenerative disorders. Nat. Rev. Neurol. *14*, 133–150.

Sweeney, M.D., Kisler, K., Montagne, A., Toga, A.W., and Zlokovic, B. V. (2018b). The role of brain vasculature in neurodegenerative disorders. Nat. Neurosci. *21*, 1318–1331.

Szabo, T.J., and Welcher, J.B. (1996). Human Subject Kinematics and Electromyographic Activity During Low Speed Rear Impacts. SAE Trans. *105*, 1924–1944.

Tagge, C.A., Fisher, A.M., Minaeva, O. V., Gaudreau-Balderrama, A., Moncaster, J.A., Zhang, X.L., Wojnarowicz, M.W., Casey, N., Lu, H., Kokiko-Cochran, O.N., et al. (2018). Concussion, microvascular injury, and early tauopathy in young athletes after impact head injury and an impact concussion mouse model. Brain *141*, 422–458.

Tang, Y., and Le, W. (2016). Differential Roles of M1 and M2 Microglia in Neurodegenerative Diseases. 1181–1194.

Thomsen, G.M., Ma, A.M., Ko, A., Harada, M.Y., Wyss, L., Haro, P.S., Vit, J.P., Shelest, O., Rhee, P., Svendsen, C.N., et al. (2016). A model of recurrent concussion that leads to long-term motor deficits, CTE-like tauopathy and exacerbation of an ALS phenotype. J. Trauma Acute Care Surg. *81*, 1070–1078.

Thomsen, G.M., Ko, A., Harada, M.Y., Ma, A., Wyss, L., Haro, P., Vit, J.P., Avalos, P., Dhillon, N.K., Cho, N., et al. (2017). Clinical correlates to assist with chronic traumatic encephalopathy diagnosis: Insights from a novel rodent repeat concussion model. J. Trauma Acute Care Surg. *82*, 1039–1048.

Tomkins, O., Feintuch, A., Benifla, M., Cohen, A., Friedman, A., and Shelef, I. (2011). Blood-brain barrier breakdown following traumatic brain injury: a possible role in posttraumatic epilepsy. Cardiovasc. Psychiatry Neurol. *2011*, 1–11.

Tucker, L.B., Velosky, A.G., Fu, A.H., and McCabe, J.T. (2019). Chronic neurobehavioral sex differences in a murine model of repetitive concussive brain injury. Front. Neurol. *10*, 1–14.

Velosky, A.G., Tucker, L.B., Fu, A.H., Liu, J., and McCabe, J.T. (2017). Cognitive performance of male and female C57BL/6J mice after repetitive concussive brain injuries. Behav. Brain Res. *324*, 115–124.

Verellen, R.M., and Cavazos, J.E. (2010). Post-traumatic epilepsy: An overview. Therapy *7*, 527–531.

Villapol, S., Loane, D.J., and Burns, M.P. (2017). Sexual dimorphism in the inflammatory response to traumatic brain injury. Glia *65*, 1423–1438.

Vonder Haar, C., Lam, F.C.W., Adams, W.K., Riparip, L.K., Kaur, S., Muthukrishna, M., Rosi, S., and Winstanley, C.A. (2016). Frontal Traumatic Brain Injury in Rats Causes Long-Lasting Impairments in Impulse Control That Are Differentially Sensitive to Pharmacotherapeutics and Associated with Chronic Neuroinflammation. ACS Chem. Neurosci. *7*, 1531–1542.

Vonder Haar, C., Martens, K.M., Riparip, L.-K., Rosi, S., Wellington, C.L., and Winstanley, C.A. (2017). Frontal Traumatic Brain Injury Increases Impulsive Decision Making in Rats: A Potential Role for the Inflammatory Cytokine Interleukin-12. J. Neurotrauma *34*, 2790–2800.

Wagner, A.K., Scanlon, J.M., Becker, C.R., Ritter, A.C., Niyonkuru, C., Dixon, C.E., Conley, Y.P., and Price, J.C. (2014). The influence of genetic variants on striatal dopamine transporter and D2 receptor binding after TBI. J. Cereb. Blood Flow Metab. *34*, 1328–1339.

Walhovd, K.B., Fjell, A.M., Brewer, J., McEvoy, L.K., Fennema-Notestine, C., Hagler, D.J., Jennings, R.G., Karow, D., Dale, A.M., and Alzheimer's Disease Neuroimaging Initiative (2010). Combining MR imaging, positron-emission tomography, and CSF biomarkers in the diagnosis and prognosis of Alzheimer Disease. Am. J. Neuroradiol. *31*, 347–354.

Wang, H.-K., Lin, S.-H., Sung, P.-S., Wu, M.-H., Hung, K.-W., Wang, L.-C., Huang, C.-Y., Lu, K., Chen, H.-J., and Tsai, K.-J. (2012). Population based study on patients with traumatic brain injury suggests increased risk of dementia. J. Neurol. Neurosurg. Psychiatry *83*, 1080–1085.

Weafer, J., Baggott, M.J., and De Wit, H. (2013). Test-retest reliability of behavioral measures of impulsive choice, impulsive action, and inattention. Exp. Clin. Psychopharmacol. *21*, 475–481.

Weil, Z.M., and Karelina, K. (2017). Traumatic Brain Injuries during Development: Implications for Alcohol Abuse. Front. Behav. Neurosci. *11*, 1–8.

Weiner, M.W., Crane, P.K., Montine, T.J., Bennett, D.A., and Veitch, D.P. (2017). Traumatic brain injury may not increase the risk of Alzheimer disease. Neurology *89*, 1923–1925.

Whyte, T., Liu, J., Chung, V., McErlane, S.A., Abebe, Z.A., McInness, K.A., Wellington, C.L., and Cripton, P.A. (2019). Technique and preliminary findings for in vivo quantification of brain motion during injurious head impacts. J. Biomech. *In press*.

Wilk, J.E., Herrell, R.K., Wynn, G.H., Riviere, L.A., and Hoge, C.W. (2012). Mild traumatic brain injury (concussion), posttraumatic stress disorder, and depression in U.S. soldiers involved in combat deployments: Association with postdeployment symptoms. Psychosom. Med. *74*, 249–257.

Williams, R.M., Puetz, T.W., Giza, C.C., and Broglio, S.P. (2015). Concussion Recovery Time

Among High School and Collegiate Athletes: A Systematic Review and Meta-Analysis. Sport. Med. *45*, 893–903.

Wilson, L., Stewart, W., Dams-O'Connor, K., Diaz-Arrastia, R., Horton, L., Menon, D.K., and Polinder, S. (2017). The chronic and evolving neurological consequences of traumatic brain injury. Lancet Neurol *16*, 813–825.

Winstanley, C.A. (2007). The orbitofrontal cortex, impulsivity, and addiction. Ann. N. Y. Acad. Sci. *1121*, 639–655.

Winstanley, C.A. (2010). The neural and neurochemical basis of delay discounting. Impuls. Behav. Neurol. Sci. Discount. 95–121.

Winstanley, C.A., Eagle, D.M., and Robbins, T.W. (2006). Behavioral models of impulsivity in relation to ADHD: Translation between clinical and preclinical studies. Clin. Psychol. Rev. *26*, 379–395.

Yamaki, T., Uchino, Y., Henmi, H., Kamezawa, M., Hayakawa, M., Uchida, T., Ozaki, Y., Onodera, S., Oka, N., Odaki, M., et al. (2018). Increased brain glucose metabolism in chronic severe traumatic brain injury as determined by longitudinal 18F-FDG PET/CT. J. Clin. Neurosci. *57*, 20–25.

Zetterberg, H., and Blennow, K. (2016). Fluid biomarkers for mild traumatic brain injury and related conditions. Nat. Rev. Neurol. *12*, 563–574.

Zetterberg, H., and Burnham, S.C. (2019). Blood-based molecular biomarkers for Alzheimer's disease. Mol. Brain *12*, 1–7.

Zgaljardic, D.J., Seale, G.S., Schaefer, L.A., Temple, R.O., Foreman, J., and Elliott, T.R. (2015). Psychiatric Disease and Post-Acute Traumatic Brain Injury. J. Neurotrauma *32*, 1911–1925.

Zlokovic, B. V. (2011). Neurovascular pathways to neurodegeneration in Alzheimer's disease and other disorders. Nat. Rev. Neurosci. *12*, 723–738.

Zweifel, C., Castellani, G., Czosnyka, M., Carrera, E., Brady, K.M., Kirkpatrick, P.J., Pickard, J.D., and Smielewski, P. (2010a). Continuous assessment of cerebral autoregulation with near-infrared spectroscopy in adults after subarachnoid hemorrhage. Stroke *41*, 1963–1968.

Zweifel, C., Castellani, G., Czosnyka, M., Helmy, A., Manktelow, A., Carrera, E., Brady, K.M., Hutchinson, P.J.A., Menon, D.K., Pickard, J.D., et al. (2010b). Noninvasive monitoring of cerebrovascular reactivity with near infrared spectroscopy in head-injured patients. J. Neurotrauma *27*, 1951–1958.

Appendices

Appendix A List of Publications

Bashir, A*, Abebe, ZA, McInnes, KA, Button, EB, Tatarnikov, I, Cheng, WH, Haber, M, Wilkinson, A, Barron, C, Diaz-Arrastia, R, Stukas, S, Cripton, PA, Wellington, CL. Increased severity of the CHIMERA model induces acute vascular injury, sub-acute deficits in memory recall, and chronic white matter gliosis. (2020). Exp Neurol 324.

Sandsmark, D*, Bashir, A*, Wellington, C[$], Diaz-Arrastia, R[$]. Cerebral microvascular injury: a potentially treatable mechanism of trauma-induced neurodegeneration. (2019). Neuron 103(3):367-379

Vonder Haar, C*, Martens, KM*, Bashir, A*, McInnes, KA, Cheng, WH, Cheung, H, Stukas, S, Barron, C, Ladner, T, Welch, K, Cripton, PA, Winstanley, CA, Wellington, CL. (2019). Repetitive closed-head impact model of engineered rotational acceleration (CHIMERA) injury in rats increases impulsivity, decreases dopaminergic innervation in the ventral striatum and generates white matter inflammation, tau phosphorylation and degeneration. Exp Neurol 317:87-99.

Cheng, WH*, Martens, KM, Bashir, A, Cheung, H, Stukas, S, Button, EB, Wilkinson, A, Barron, C, Cripton, PA, Wellington, CL. (2019). CHIMERA repetitive mild traumatic brain injury induces chronic behavioral and neuropathological phenotypes in wild-type and APP/PS1 mice. Alzheimer's Research and Therapy 11(6): 1-21.

Kyriazis, AD*, Noroozizadeh, S*, Refaee, A*, Choi, W*, Chu, L*, Bashir, A, Cheng, WH, Zhao, R, Namjoshi, DR, Salcudean, SE, Wellington, CL, Nir, G. (2018). An end-to-end system for automatic characterization of iba1 immuno-positive microglia in whole slide imaging. Neuroinformatics, 1-17.

Cheng WH*, Stukas S, Martens KM, Namjoshi DR, Button EB, Wilkinson A, Bashir A, Robert J, Cripton PA, Wellington CL. (2018). Age at injury and genotype modify acute inflammatory and neurofilament-light responses to mild CHIMERA traumatic brain injury in wild-type and APP/PS1 mice. Exp Neurol 301:26-38.

Namjoshi DR*, Cheng WH, Bashir A, Wilkinson A, Stukas S, Martens KM, Whyte T, Abebe ZA, McInnes KA, Cripton PA, Wellington CL. (2017). Defining the biomechanical and biological threshold of murine mild traumatic brain injury using CHIMERA (Closed Head Impact Model of Engineered Rotational Acceleration). Exp Neurol 292:80-91.

*indicates first/co-first authorship